Using Digital Television Signals for Radar Imaging

by

George Atkinson

A thesis submitted to the
School of Engineering
of the
University of Birmingham
For the degree of
DOCTOR OF PHILOSOPHY

September 2020

Abstract

This thesis presents the first systematic theoretical and experimental study of passive bistatic Synthetic Aperture Radar (SAR) imaging utilising Digital Television Broadcasting - Terrestrial (DVB-T) as an illuminator of opportunity. It presents the theoretical background for radar, SAR, and DVB-T transmissions, and studies the waveform on the basis of its ambiguity function. It considers the theoretical constraints of DVB-T SAR, including the impact of multiple transmitters and the properties of the DVB-T signal on image formation. It tracks the development and evolution of a receiver system and image formation algorithm, which is then validated through a series of ground-based and airborne experimental campaigns. From these campaigns, a catalogue of images are produced and analysed in order to establish the informational potential of DVB-T SAR imagery in both quasi-monostatic and bistatic environments. Specifically, the quality of images formed from a range of bistatic angles from 4 to 140 degrees is considered.

Dedication

To my wonderful partner, Frances, and my loving family

Acknowledgements

I would like to thank my supervisors, Dr. M. Antoniou and Prof. M. Cherniakov, for their help and guidance through the course of the PhD. I have learned a lot during my time in the department, and it has been a pleasure working with them.

I am also grateful to the University of Birmingham and the School of Engineering for providing me with the scholarship with which to undertake this PhD.

My thanks to the many colleagues and the friends I have made in the department who have made my time here enjoyable. A special thanks to Alp Sayin for his help and insight on the project and a thank you to my friend Jack Lindon for all the good times that kept me sane during this process.

Finally, I would like to thank my partner, Frances Cadd, and my parents, Jon and Zoe Atkinson, for their continual love and support.

List of Publications

H Ma et al, “Passive SAR Using Small Satellite Receivers for Persistent Earth Observation", IET Radar Conference, Belfast, October 2017

C. Underwood et al, “PASSAT: Passive Imaging Radar Constellation for Near-Persistent Earth Observation”, 68th International Astronautical Congress (IAC-17), Adelaide, September 2017

C. Underwood et al, “PASSAT: Passive Bi-static Radar Imaging Constellation – Airborne Trials and In-orbit Demonstrator Design,” 69th International Astronautical Congress (IAC-18), Bremen, October 2018

M Antoniou et al, “Passive SAR satellite constellation for near-persistent earth observation: Prospects and issues”, IEEE Aerospace and Electronic Systems Magazine, Volume 33, Issue 12, December 2018

G. Atkinson et al, “Passive SAR Satellite System (PASSAT): Ground Trials”, International Conference on Radar, Brisbane, August 2018

G. Atkinson et al, “Passive SAR Satellite System (PASSAT): Airborne demonstrator and first results”, IET RSN Special Issue on Passive Radar, June 2018

G. Atkinson et al, “Passive SAR Satellite System (PASSAT): First Airborne Trials”, International Radar Symposium, Ulm, June 2019

G.Atkinson et al. "Passive DVB-T SAR Phenomenology: First Results from a Bistatic Campaign", EuRad, 17th European Radar Conference (EuRAD), Utrecht, January 2021 (Paper accepted for September 2020, but conference postponed to January 2021 due to the COVID-19 pandemic).

Table of Contents

List of Figures

List of Tables

List of Abbreviations

ADC	Analog to Digital Converter
AIS	Automated Identification System
AM	Amplitude Modulation
AMF	Average Matched Filter
ASDEC	Advanced Structural Dynamics Evaluation Centre
BPF	Bass-Pass Filter
CSV	Comma Separated Value
DDC	Digitally Down-Converted
DVB-S	Digital Video Broadcasting – Satellite
DVB-T	Digital Video Broadcasting – Terrestrial
ECEF	Earth Centred Earth Fixed
EIRP	Effective Isotropic Radiated Power
EM	Electromagnetic
FFT	Fast Fourier Transform
FM	Frequency Modulation
GNSS	Global Navigation Satellite System
GSM	Global System for Mobile Communications
LFM	Linear Frequency Modulation

LNA	Low-Noise Amplifier
MUX	Multiplex
NESZ	Noise Equivalent Sigma Zero
NI	National Instruments
OFDM	Orthogonal Frequency-Division Multiplexing
PCIe	Peripheral Component Interconnect Express
PM	Phase Modulation
PRBS	Pseudo Random Binary Sequence
PSF	Point Spread Function
QAM	Quadrature Amplitude Modulation
RCS	Radar Cross-Section
RF	Radio Frequency
RFI	Radio-Frequency Interference
RTK	Real-Time Kinematics
SAR	Synthetic Aperture Radar
SIR	Signal to Interference Ratio
SNR	Signal to Noise Ratio
SSD	Solid-State Drive
TPS	Transmission Parameter Signalling
UHF	Ultra High Frequency
USRP	Universal Software Radio Peripheral
VHF	Very High Frequency

Chapter 1

Introduction

1.1 Introduction

1.1.1 Radar Concept

Radar is a sensing system that utilises radio waves to determine properties of detected targets. The word Radar comes from the abbreviation Radio Detection and Ranging, however, modern radar systems are not limited to detection and ranging, but are capable of tracking, identification, classification and imaging of targets. Modern radar can detect aircraft, ships, vehicles, spacecraft, missiles, weather formations, and even terrain, and have a diverse variety of uses including guidance, surveillance, flight-control systems, fire-control systems, mapping, and remote sensing, to name a few [1].

There are two main types of radar configuration, monostatic and bistatic. Figure 1.1a demonstrates the typical operation of a monostatic radar. In a typical

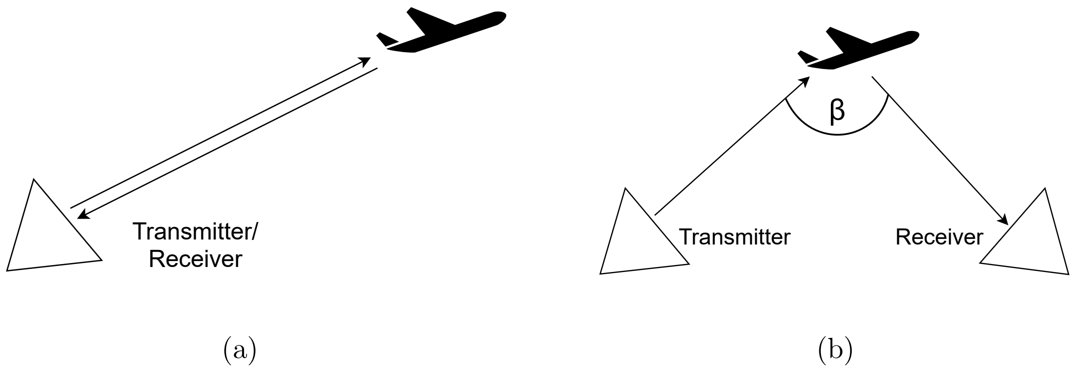

Figure 1.1: Diagrams of the basic typologies of a radar system: (a) Monostatic, (b) Bistatic

monostatic configuration, a single transmitter and receiver pair are co-located and detection is achieved by transmitting radio waves and then receiving the reflected radio waves from targets of interest, a process called backscattering. A processing system is then used to transform the received echo signals into information about the properties of the detected targets such as their ranges and velocities.

Figure 1.1b demonstrates one possible configuration for a bistatic radar. A typical bistatic radar system also utilises a single transmitter and receiver pair but, unlike the monostatic case, they are not co-located. The separation of the transmitter and receiver permits a bistatic radar to operate in different ways depending on the angle between the transmitter target and receiver, known as the bistatic angle, β. There is no standard which defines what bistatic angle is required to class a radar system as bistatic. This thesis will use the convention that a system with a bistatic angle less than 20 degrees can be considered quasi-monostatic in name and monostatic when considering radar properties such as resolution.

1.1.2 Synthetic Aperture Radar

Synthetic Aperture Radar (SAR) is a radar system which is used to create images of a static target scene, usually terrain, using radio signals. Since its inception in 1951 by Carl Wiley, SAR imaging has proven itself as a popular, well-established, and highly capable remote sensing technique [2]. Today, SAR systems are used for a wide range of land [3–7] and sea [8–10] monitoring applications from a variety of moving platforms, such as ground-based vehicles, aircraft, and satellites. In particular, a number of very precise state of the art SAR imaging systems, developed for space-borne orbital use, are in operation today such as RADARSAT, TerraSAR-X, Sentinel-1, and COSMO-SkyMed [11–14].

Synthetic Aperture Radar works by simulating a large phased array antenna over time, known as time-multiplex. Whereas a typical phased array antenna contains a large number of static parallel antenna elements, creating a spatial aperture, a SAR array uses a single moving antenna to construct an aperture over a particular time period as the antenna moves from the start point to the end point.

Successive radio wave pulses are transmitted in order to illuminate a target scene, and the reflected echo pulses are received and recorded. Traditional monostatic SAR uses a moving platform which houses both the radar transmitter and receiver. As the platform moves, the distance between the receiver and any point within the target scene changes as a function of time. An image formation algorithm is then used to coherently combine the recorded pulses from multiple receiver positions, forming a synthetic aperture in time which is larger than the physical aperture of the receiving antenna, and in doing so allows for the creation of higher-resolution imagery.

1.2 Motivation

At present, most SAR systems are active, which means that they both transmit and receive radio signals, usually from the same platform. Active systems have full control over the transmitted signal which includes, the waveform, the transmit power, and the antenna beam pattern. The ability to control these parameters allows the radar to enhance imaging performance, for example by improving range and resolution. However, for an active system licenses must be obtained for the frequency band used for transmission, and many bands within the already congested frequency spectrum are reserved, already in use, or lack the bandwidth necessary for performing imaging.

Owing to these limitations, in recent decades there has been a growing interest in passive radar. A passive system is one that utilises radio signals which are already present from transmitters of opportunity, also known as non-cooperative transmitters, originally designed for broadcasting, communications, and navigation. These include, but are not limited to, FM radio, the Global System for Mobile Communications (GSM), the Global Navigation Satellite System (GNSS), analogue television, Digital Video Broadcasting - Satellite (DVB-S), and Digital Video Broadcasting - Terrestrial (DVB-T) [15–24]. Since a passive system does not contain a dedicated transmitter, frequency allocation is not required and no licenses must be obtained to receive already existing signals. In addition, a passive system has the advantage of reduced detectability. Whereas an active system could be located by tracking the output signal from its transmitter, a passive system has no such weakness.

Recently, scholars have demonstrated the feasibility of utilising these non-cooperative transmissions for passive SAR, for example see [25–30]. Specifically, digital television transmissions have been considered as an ideal candidate for passive SAR, due to the high radiating power and large coverage areas of DVB-T transmission stations, as well as possessing a sufficient bandwidth for passive radar imaging applications, as will be discussed in the literature review in the following section. DVB-T uses a multiplex signal to transmit video and audio data on Ultra High Frequency (UHF) carrier waves. Multiplexing refers to the combination of multiple signals into one single signal to increase the amount of information that can be transmitted. DVB-T utilises Orthogonal Frequency-Division Multiplexing (OFDM) in which data is split between multiple sub-carrier waves with differing frequencies before being combined into the final transmitted signal. Since DVB-T is transmitted from fixed ground-based stations, a passive SAR system is likely to be in a bistatic configuration. For SAR imaging, a bistatic geometry can provide additional information about the targets within a scene, however, larger bistatic angles also degrade resolution and potentially reduce the Signal-to-Noise Ratio (SNR), and hence the ability to distinguish targets from the background in imagery.

1.3 Literature Review

Evers et al. presented a paper investigating the utility of passive OFDM-based digital signals, including digital television, for producing SAR imagery [31]. The research presented builds upon the work of Gutiérrez del Arroyo et al., utilising an Averaged Matched Filter (AMF) technique. As stated in the paper, AMF coherently averages over segments of each received pulse of the synthetic aperture, which reduces the effects of noise and clutter. The authors used a segment length equal to the DVB-T symbol duration for their matched filtering. Rather than using signals from broadcasting stations, the authors instead generated their own OFDM signals with an artificially high 300 MHz bandwidth in order to conduct small-scale experiments. A small-scale experiment was conducted using a 2 m long aperture, producing 33 pulses, and with a bistatic angle of just 3 degrees. Given the bandwidth and aperture length, the range and cross-range resolutions were calculated to be 0.5 m and 0.83 m respectively. Four targets, with an area of 0.4 m^2 were placed within the target scene and are clearly distinguishable in the resulting SAR imagery generated using convolutional backprojection of the averaged matched filtered data. A scaled version of the SAR image results, depicting the reflectivity function for a real system with a bandwidth of one DVB-T symbol, B = 7.61 MHz, is also shown. The results demonstrate the possibility of using OFDM signals, such as DVB-T for SAR imaging, however, the small-scale controlled experimental environment using generated signals does not address any of the potential problems which could result from a fully passive non-cooperative DVB-T transmitter or a system with a high bistatic angle.

In 2014, Gromek et al. published a paper presenting a range-Doppler map of an observed ground area using a DVB-T based passive radar receiver [32]. A receiver was mounted on an airborne platform and was used to measure the direct signals from a DVB-T transmitter 2 km away, as well as the reflected signals from an area of the ground. A series of signal processing steps were performed on the measured data, including an algorithm to remove the direct signal from the measurement channel and range compression. The raw data after range compression is shown, as well as a range-Doppler map produced with a short Fast Fourier Transform (FFT) compression. The authors conclude that the radar had a range of 30 km and identify geometric distortion due to the bistatic geometry, however the exact bistatic angle is not stated. The resulting image shows returns with clear structure which are attributed to reflections from strong ground scatterers, but no ground truth imagery is presented to explain the origins of bright spots within the image. These initial results showed that it is possible to form ground imagery with a passive DVB-T radar.

In 2015, Ulander et al describe two unique experiments, the first of which investigated passive synthetic aperture radar using DVB-T signals with the use of an airborne receiver, and the second investigating a passive Very High Frequency (VHF) SAR with a transmitting airborne radar [33]. A DVB-T receiver with a single receiving channel was flown aboard an aircraft. The collected data was processed with a Radio-Frequency Interference filter (RFI) and then the backprojection algorithm was used to form a SAR image with a 13 second integration time, corresponding to a 2 km aperture. Results showed SAR imagery with a bistatic angle of 20 degrees, with ranges up to 15 km, and with a dynamic range of 70 dB, consistent with the 1 second integration period used. The DVB-T transmitter, located atop a 300 m tall mast, was present in the SAR imagery, and there was strong direct signal interference. These are likely the first results to show the first airborne passive DVB-T SAR imagery, although with a short integration time and a low signal-to-noise ratio.

Gromek et al. published another paper in 2016 presenting pioneering experimental results of a passive DVB-T SAR receiver, verifying the feasibility of ground imaging which was previously shown only theoretically or with short integration times [34]. The authors developed a DVB-T SAR demonstrator with two channels, one for the direct reference signal and the other for the surveillance ground echo signal. The demonstrator was flown on an aircraft at an altitude of 300 m along a path with the receiver and target scene in a quasi-monostatic configuration. Backprojection was used to generate two SAR images with a 40 s integration time, and a form of adaptive filtering was used to remove the direct signal from the surveillance channel. The two images were shown with corresponding ground truth imagery of the target areas, the first covering a region 3.3 km by 2.7 km and the second covering a region 2.5 km by 1.5 km, both of which were of rural areas containing fields, forests, and roads. The authors concluded that most of the targets visible in the ground truth imagery were visible in some form in the passive SAR images, but also that some targets visible in the optical images were not present in the SAR imagery and vice versa. This was attributed in part to shadowing resulting from the shallow grazing angle of the illumination. The authors identified the possible drawbacks of passive SAR, including the effects of shadowing, strong direct signal leakage masking weaker targets, and the complex signal processing required for image formation. While the paper proves the fundamental feasibility of DVB-T SAR and identifies some of the potential issues, the authors provided only a limited example scenario in which the receiver is optimally positioned relative to the transmitter for quasi-monostatic image formation.

In the same year, Frölind showed results of airborne SAR using DVB-T signals [35]. Imagery was generated, using backprojection, of a 40 by 50 km area up to 60 km in range from an airborne receiver with an altitude of 3 km. The DVB-T transmitter was atop a 300 m tall mast and had an average transmit power of 50 kW. The focus of the research was on the characteristics of ground and sea targets in DVB-T SAR imagery. A 30 second data segment was used, corresponding to a 5 km aperture, giving a theoretical azimuth resolution of about 2 m. The author identifies the location of sea targets in the form of large ships within the DVB-T SAR imagery, confirmed with positional data from the Automated Identification System (AIS). The SNR of the ships is approximately 24 dB while the dynamic range of the image is approximately 80 dB. These initial results show that target characteristics can be extracted from DVB-T SAR imagery. However, due to the movement of the ships during the integration time, the returns are not completely in-focus.

In 2017 Ulander et al. presented experimental results of an airborne DVB-T SAR using a single channel receiver tuned to accommodate a single DVB-T channel with a centre frequency of 634 MHz [36]. The aircraft flew a total distance of 50 km at altitudes of 1.5 and 3 km, about 15 km from the DVB-T transmission station used, which had a mast of 260 m and is located 80 m above sea level. The receiver used was initially an active radar, modified to a receive-only passive mode, resulting in 1.5 microsecond gaps in the recorded data stream every 160 microseconds, which was accounted for during signal processing but limited the improvements in azimuth resolution when increasing integration time. The authors present a DVB-T SAR image with an integration time of 13 seconds, corresponding to a 2 km aperture, with an aircraft altitude of 3 km. A simple matched filter followed by backprojection was used for image formation. The authors also state that SAR imagery was generated for target ground scenes up to 40 km from the transmitter and receiver but are not shown. The SAR image was presented with a map of the same area, and ground-truth targets were identified in the imagery based on their locations. Thus demonstrating an initial analysis in order to ascertain the informational potential of DVB-T SAR imagery.

1.4 Problem Statement

The research presented in the literature review has demonstrated the fundamental feasibility of DVB-T SAR. This thesis builds upon this previous scholarship by providing a more systematic theoretical and experimental study of the challenges and potentialities of DVB-T SAR image formation. Firstly, to achieve this goal, theoretical calculations on system performance, including power budget, resolution, and sensitivity are considered. In addition, the development of a simulation environment operating with DVB-T signals, constructed for the purpose of creating and testing different iterations of an imaging algorithm, is then shown. Notably, through this simulation, the influence of both multiple transmitters and the properties of DVB-T pilot signals on the quality of images produced, is assessed.

Secondly, this thesis presents the development of a series of experimental campaigns, which put the theoretical considerations, outlined above, into practice. It shows how an experimental system, comprised of receiving hardware and signal processing algorithms, was designed and built to provide experimental data. Chapters 3 to 5 show this experimental system on a variety of platforms and at different bistatic angles, tracking the progression and development of three campaigns from a ground-based trial (presented in Chapter 3), to an airborne trial in optimal quasi-monostatic environments (shown in Chapter 4), to finally, an airborne trial using a wider range of bistatic geometries (demonstrated in Chapter 5). Throughout, the resulting images of target scenes are qualitatively analysed, compared, and contrasted, in order to assess the informational potential of DVB-T SAR imaging i.e. what can be inferred from SAR imagery of a variety of different real-world targets.

The work carried out includes:

- A thorough investigation of the theoretical constraints of a passive bistatic radar system utilising DVB-T signals.

- The development of a DVB-T based SAR system simulation to investigate the effects of multiple transmitter interference which cannot easily be investigated via a real-world experimentation.
- The investigation of the effects of DVB-T pilot signal ambiguities and their suppression during backprojection image formation.
- The design and development of a receiver system and image formation algorithm for DVB-T SAR imagery.
- The planning and execution of a series of experimental campaigns, both ground-based and airborne, to provide a comprehensive set of images from multiple scenarios with varying bistatic angles, allowing for the analysis of UHF image features, as well as the validation of the developed receiver system.
- The visual and numerical analysis of bistatic DVB-T SAR imagery as a foundational step towards understanding the information that can extracted from such imagery for multiple possible applications.

1.5 Thesis Outline

Chapter 2 presents the theoretical background for radar, DVB-T, and SAR image formation in both monostatic and bistatic configurations. The generation of SAR imagery through the reconstruction of the ideal target function is reviewed and the formulation of the backprojection algorithm is derived. The construction of DVB-T transmission signals is shown, as well as the generation of a simulated DVB-T signal and the study of its ambiguity function. Chapter 3 covers the theoretical constraints of a DVB-T SAR system, including the power budget, resolution, and sensitivity. In addition, it investigates the problems of multiple transmitter interference and DVB-T signal properties on image quality, presents the design and development of an initial DVB-T SAR receiver system and imaging algorithm, and shows the execution and results of a ground-based measurement campaign. Chapter 4 shows the evolution of the initial DVB-T SAR receiver into a flight-ready demonstrator system and presents the results of an airborne quasi-monostatic experimental campaign, designed to evaluate the returns from a variety of known targets. Chapter 5 describes a second airborne experimental campaign, concentrating on the analysis of DVB-T SAR imagery produced in primarily bistatic configurations. In addition, crucially, it also provides an initial assessment on the attributes of images formed from measurements at high bistatic angles. The thesis conclusions are presented in Chapter 6 as well as suggestions for possible future research. Appendix A is an extension of Chapter 4, presenting the results and analysis of quasi-monostatic DVB-T SAR imagery for three additional target areas.

Chapter 2

Background

Building on the introductions to radar, SAR, and DVB-T provided in Chapter 1, this chapter presents the relevant background information and theory behind the study of DVB-T SAR imaging, shown in this thesis. A number of scholars have provided comprehensive explanatory texts on the fundamentals of radar, SAR, and DVB-T [37, 38]. The aim of this chapter is to summarise these research areas in order to obtain a greater understanding of the principles of DVB-T SAR.

2.1 Radar Fundamentals

2.1.1 Basic Radar Configuration

Figure 2.1 shows a block diagram showing the essential processes of typical radar system and the interrelationships between them. The operation of a typical radar can be broken down into three basic stages:

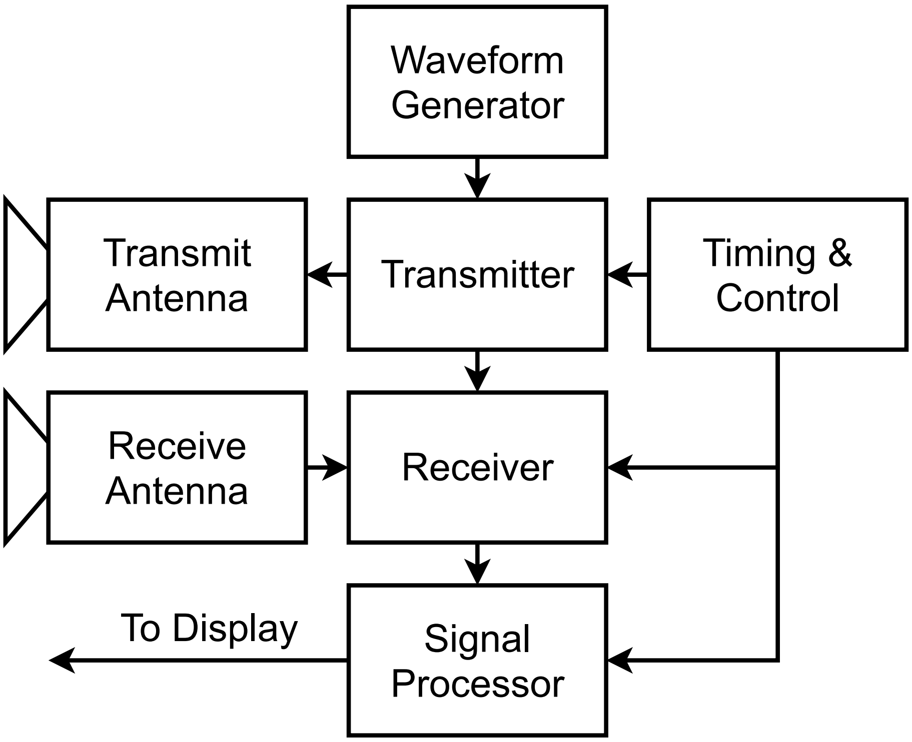

Figure 2.1: Basic radar system block diagram

1. Transmission
2. Interaction
3. Reception

Transmission

Transmission is concerned with both the generation and transmission of radio waves towards a target. The timing and control circuitry, in conjunction with a waveform generator, produce a radio signal with a particular carrier frequency. Although some forms of radar, such as a Doppler radar, can use a constant frequency signal to measure target properties such as velocity, in general, to determine a target's range or to image a target, some form of modulation of the transmit signal is required.

Modulation refers to the varying of the properties of a waveform with a modulating signal in order to disambiguate the return signal, improve resolution, as well as to reduce interference. The three primary ways of modulating a radar waveform are to vary its amplitude, called Amplitude Modulation (AM), its frequency, called Frequency Modulation (FM), or its phase, called Phase Modulation (PM). The most common form of amplitude modulation used in radar is to periodically switch the amplitude of the signal from high to low (on to off), creating a pulsed waveform as shown in Figure 2.2. Frequency modulation is also commonly used in radar, usually in the form of a Linear Frequency Modulation (LFM) where the frequency of the signal is increased linearly over a period of time. Frequency modulation in combination with a pulsed waveform is known as a pulse compressed waveform. After modulation, the signal is then amplified before being sent to one or more transmitting antennae. The transmitting antenna directs the radio wave energy towards the targets whose properties are to be measured.

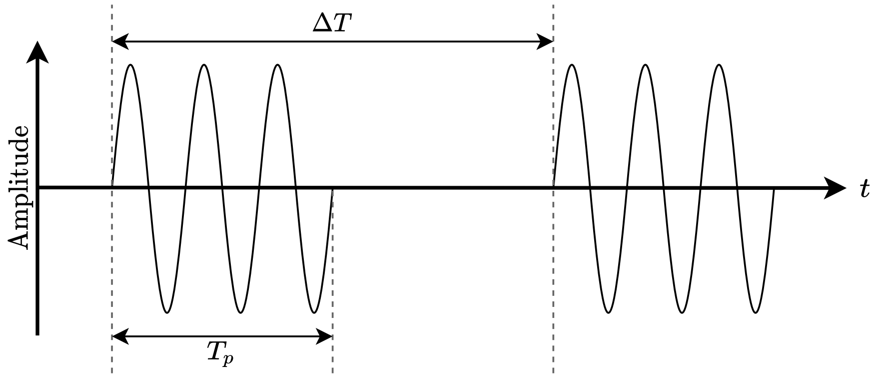

Figure 2.2: Diagram showing a pulsed waveform

Interaction

Interaction describes the behaviour of radio waves as they travel from the transmitter to a target, and how the radio waves interact with matter, including both the target and the medium the waves have to travel through, which is usually the atmosphere. In a vacuum, radio waves travel at the speed of light and obey the inverse square law which attenuates the waves according to the equation:

$$\rho = \frac{1}{r^2} \tag{2.1}$$

where ρ is the power density of an Electromagnetic (EM) wave and r is the distance from a point source which emits the radio waves. Radio waves can interact with matter in several different ways, including:

- Reflection
- Refraction
- Diffraction
- Absorption
- Polarisation
- Scattering

Reflection occurs when a proportion of the EM energy incident on a medium is rebounded. Refraction refers to the apparent bending of EM waves due to retardation when passing between mediums with differing densities. Diffraction is the process by which a beam of EM radiation is spread out as a result of passing through a narrow aperture or across an edge. Absorption occurs when an object converts the incident EM energy into another form of energy, usually heat. Polarisation refers to the transverse direction of the EM wave, whose direction can be altered by interacting with an object. Scattering occurs when EM waves are absorbed by matter and then re-emitted in multiple directions, causing a deviation of the trajectory of the EM wave from a straight path.

For a radar system, although all interactions can occur to some degree, the primary interactions which must be considered for radar purposes are attenuation and reflection. At this stage, the EM signal propagates towards the target, losing energy due to attenuation and atmospheric absorption, before interacting with a target object. Some of the EM energy incident on the object is reflected back towards the radar receiver. The amount of reflected energy from a target is encapsulated by its Radar Cross-Section (RCS), which is a measure of the target's ability to reflect radar signals in the direction of the radar receiver, and which is not, in general, the same as the physical cross-sectional area of the object. The RCS is dependant on a number of physical factors of the target, including its size, shape, material, and orientation, as well as some of the properties of the incident radar signal, including its wavelength.

Reception

The reflected signal is then received by one or more receiving antennas before being amplified. The carrier wave is removed from the received signal, leaving the baseband signal. For a coherent radar, the phase of the signal is required. Therefore, when the baseband signal is recorded, the signal is split into two components, an in-phase component, I, and a quadrature component, Q, so that the phase of the baseband signal can be recorded and not just the amplitude. The receiver converts the baseband signal components into a digital signal and then the signal processor extracts the desired information about the target that has been encoded onto the baseband signal by the interaction of the signal with the target.

2.1.2 Radar Range Equation

The radar range equation gives the power returned from a single target, determined from the properties of the transmitter, the receiver, the target, and the effects from the operating environment, such as attenuation [1, 37]. The power at the output of the receiving antenna from a single target is given by:

$$P_R = \frac{P_T G_T G_R \lambda^2 \sigma L}{(4\pi)^3 R_T^2 R_R^2} \tag{2.2}$$

where

- P_T is the power of the transmitted signal;
- G_T is the gain of the transmit antenna;
- G_R is the gain of the receiver antenna;
- λ is the wavelength of the transmitted signal;
- σ is the bistatic RCS of the target;
- L is a loss factor which represents additional losses due to propagation through a medium other than free space;
- R_T is the range from the transmitting antenna to the target;
- R_R is the range from the receiving antenna to the target;

For the case of monostatic radar receivers, $R_T = R_R$ and is usually expressed by a single parameter, R, raised to the power of 4, and $G_T = G_R$. The noise at the output of the receiving antenna is the accumulation of two primary noise sources; environmental noise picked up by the receiving antenna, and the thermal noise produced by the components of the receiver. The equation for thermal noise power is given by:

$$P_N = k_B T_0 B N_f \tag{2.3}$$

where k_B is Boltzmann's constant, T_0 is the temperature of the receiver measured in Kelvin, B is the receiver bandwidth, and N_f is the receiver noise figure. The radar range equation is the ratio of the power of the target signal, Equation 2.2, (the signal coming from the target of interest) to the power of the interference signal (any signals other than the target signal such as those generated by noise or clutter), otherwise known as the Signal to Interference Ratio (SIR). If the dominant interference is from noise, described by Equation 2.3, this ratio is referred to as the Signal to Noise Ratio (SNR), and is often used to describe the performance of a radar system.

$$SNR = \frac{P_R}{P_N} = \frac{P_T G_T G_R \lambda^2 \sigma L}{(4\pi)^3 R_T^2 R_R^2 k_B T_0 B} \tag{2.4}$$

2.1.3 Maximum Unambiguous Range

For a pulsed radar, the detection and ranging of a target is determined by calculating the time between the transmission of a single pulse and the reception of the reflected signal some amount of time later. Therefore, if the time taken for a pulse to return to the radar receiver is longer than the time between consecutive pulses, there is not enough information to determine which of the transmitted pulses is the origin of the reflected signal, and thus the time between transmission and reception is ambiguous. Therefore, the maximum unambiguous range is given by:

$$R_{max} = \frac{c(\Delta T - T_p)}{2} \tag{2.5}$$

where ΔT is the time between consecutive pulses, as measured from the start of each pulse as shown in Figure 2.2, and T_p is the length of the pulse, or pulse width. Targets beyond the maximum unambiguous range appear as targets with incorrect range estimation and therefore incorrect positions on a radar image. Such targets are referred to as "ghost targets", since they are visible but do not correspond to an actual reflector at the determined position.

While Equation 2.5 gives the maximum unambiguous range based on the signal pulse width and pulse repetition frequency, the maximum detection range is determined by the minimum SNR such that the receiver can still perform an accurate detection. Rearranging Equation 2.4, the maximum range is expressed as:

$$R_{max} = \left[\frac{P_T G^2 \lambda^2 \sigma}{(4\pi)^3 S_{min}} \right]^{1/4} \tag{2.6}$$

where S_{min} is the minimum detectable SNR.

2.1.4 Bistatic Radar Geometric Relationships

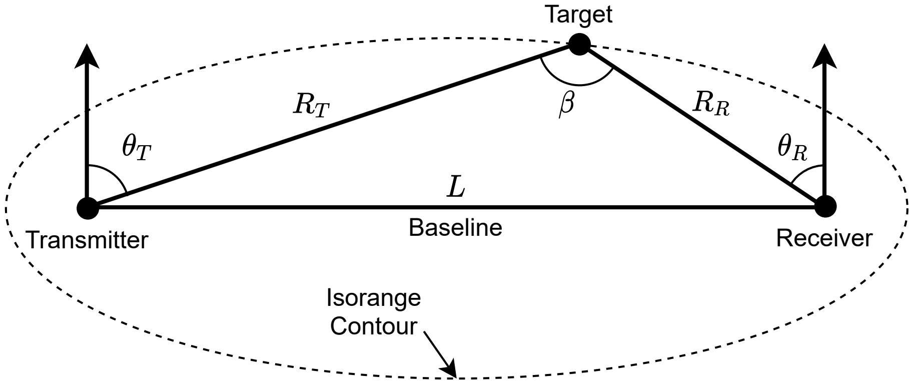

Figure 2.3: Geometry of a bistatic radar system

Figure 2.3 shows a plan view of the geometry of a typical bistatic radar configuration. The transmitter is separated from the receiver by a distance L, measured along the baseline, which is defined as the line joining the transmitter and the receiver. A target is located at a distance R_T from the transmitter and R_R from the receiver. The bistatic angle is defined as the angle between the line joining the transmitter to the target, and the line joining the receiver to the target. While a monostatic radar measures the range from the co-located transmitter and receiver to the target, a bistatic radar typically measures the target range sum, $R_T + R_R$.

A particular range sum defines a surface in space, which in two dimensions is called an isorange contour, such that all points on the surface share the same range. For bistatic geometry, this is equivalent to the locus of points such that the sum of the distances from the transmitter and receiver are constant. This defines an ellipsoidal isorange surface, or an elliptic isorange contour, where the two foci are the transmitter and receiver locations. For a monostatic radar, since $R_T = R_R$, the isorange surfaces are spheres with the transmitter and receiver co-located at the centre, or circles in two dimensions.

2.1.5 Doppler

Relative motion between the source of an EM wave and the reflecting target causes a frequency difference to occur called Doppler frequency. The bistatic Doppler frequency shift is defined as the rate of change of the total path length from transmitter to target to receiver, normalised by the wavelength, given by[39]:

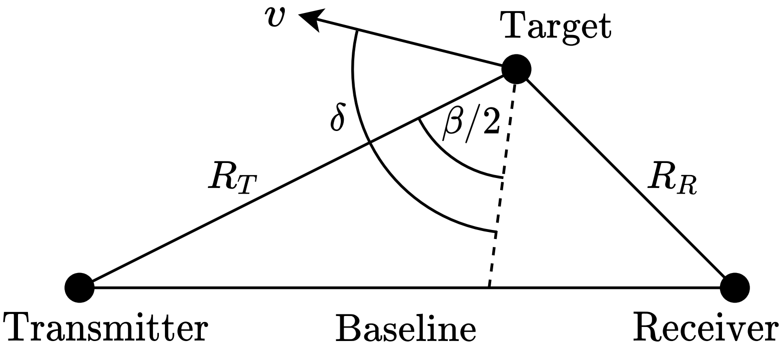

Figure 2.4: Diagram showing the Doppler properties of a moving target

$$f_D = \frac{1}{\lambda}\left[\frac{d}{dt}(R_T + R_R)\right] \tag{2.7}$$

For a static transmitter and receiver but a moving target, the relationship between target velocity, V, and the Doppler shift, f_D, can be expressed as:

$$f_D = \frac{2V}{\lambda}\cos(\delta)\cos(\beta/2) \tag{2.8}$$

where δ is the angle between the velocity vector and the bistatic bisector, see Figure 2.4. For a target on the baseline, $\beta = 180°$, the Doppler shift becomes, $f_D = 0$, and the target velocity cannot be determined. For a monostatic radar, $\beta = 0$, and the equation reduces to the monostatic Doppler frequency:

$$f_D = \frac{2V}{\lambda}\cos(\delta) \tag{2.9}$$

where δ is now the angle between the velocity vector and the radial line from the co-located transmitter and receiver to the target.

2.1.6 Resolution

Range Resolution

The range resolution of a radar system is its ability to distinguish between two or more targets at different ranges. For a pulsed radar system with a pulse width of T_p, and a pulse repetition interval of ΔT, received echo pulses from two different targets are resolvable if the interval between the pulses is greater than or equal to the pulse width, i.e. $\Delta T \geq T_p$. Therefore, T_p is the minimum unambiguous round-trip time, which when converted to range, gives the formula for range resolution:

$$\Delta R = \frac{cT_p}{2} \tag{2.10}$$

For a pulsed radar with a short pulse duration, the relationship between frequency bandwidth, B, and pulse duration, T_p, for small T_p, is represented as:

$$B \approx \frac{1}{T_p} \tag{2.11}$$

From Equation 2.10, the range resolution then becomes:

$$\Delta R = \frac{c}{2B} \tag{2.12}$$

This represents the range resolution for a monostatic radar. For a bistatic radar the range resolution varies with bistatic angle and is given by:

$$\Delta R = \frac{c}{2B\cos(\beta/2)} \tag{2.13}$$

The bistatic range resolution is therefore a minimum when $\beta = 0$, i.e a monostatic configuration, and increases towards infinity when $\beta = 180°$, also known as a forward scatter configuration, which represents a complete loss of range resolution. The monostatic range resolution therefore represents the best case range resolution. The range resolution defines the separation between two concentric isorange contours, also known as the range cell. Figure 2.5 depicts the range cell for a bistatic geometry with two confocal concentric isorange ellipses.

Doppler Resolution

For both monostatic and bistatic radar configurations, the Doppler frequency resolution is conventionally taken to be the reciprocal of the integration time, i.e., the time for which the radar is looking at the target, given by:

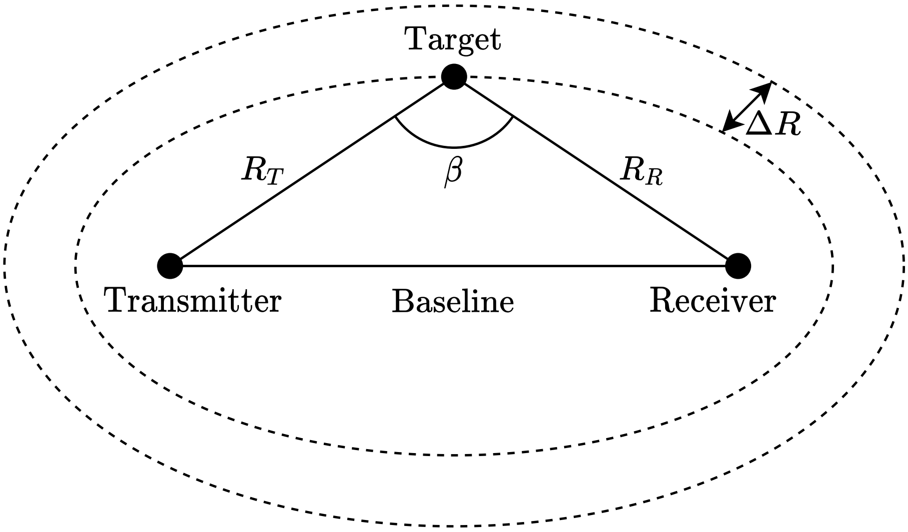

Figure 2.5: Diagram showing the isorange contours of a bistatic radar system

$$\Delta f_D = \frac{1}{T_c} \tag{2.14}$$

where T_c is the integration time. Using Equation 2.8, the required separation in velocity of two targets such that their Doppler frequencies can be resolved is:

$$\Delta V = \frac{\lambda}{2T_c \cos(\beta/2)\cos(\delta)} \tag{2.15}$$

At $\beta = 180°$, representing a forward scatter geometry, there is a complete loss of velocity resolution. At $\beta = 0°$, the equation reduces to the monostatic case:

$$\Delta V = \frac{\lambda}{2T_c} \tag{2.16}$$

2.2 Synthetic Aperture Radar Fundamentals

2.2.1 SAR Geometry

There are three major modes of SAR system configuration:

1. **stripmap** SAR uses a fixed antenna and images the ground in a long strip of terrain during the entire measurement duration.
2. **scan** SAR varies the elevation angle of the antenna to cover a wider ground swath.
3. **spotlight** SAR varies the elevation and azimuth angles of the antenna to image a single area at multiple viewing angles.

Figure 2.6 depicts an imaging radar mounted to a moving platform, such as a satellite or aircraft, configured to image the ground. The configuration is a broadside-mode side-looking radar system, where the antenna, and thus the radar main beam, is pointed perpendicular to the flight path. The experimental campaigns described in this thesis utilise a broadside-mode SAR system. The platform is moving at a constant velocity, v, and is a height, H, above the ground. The distance between the radar receiver and the target is denoted R_s, which is the slant range of the target, while R_g is the ground range of the target. The look angle, or angle of incidence, is denoted θ_i, while the beamwidth is denoted by the angle θ_H. The physical length of the receiving antenna is denoted D, while the full synthetic aperture length is L. The radar transmits pulses with duration T_p towards the ground with a pulse repetition interval T. The area of the ground illuminated by the antenna is called the antenna footprint. The swath is the ground area illuminated by consecutive radar pulses for the entire duration of a measurement.

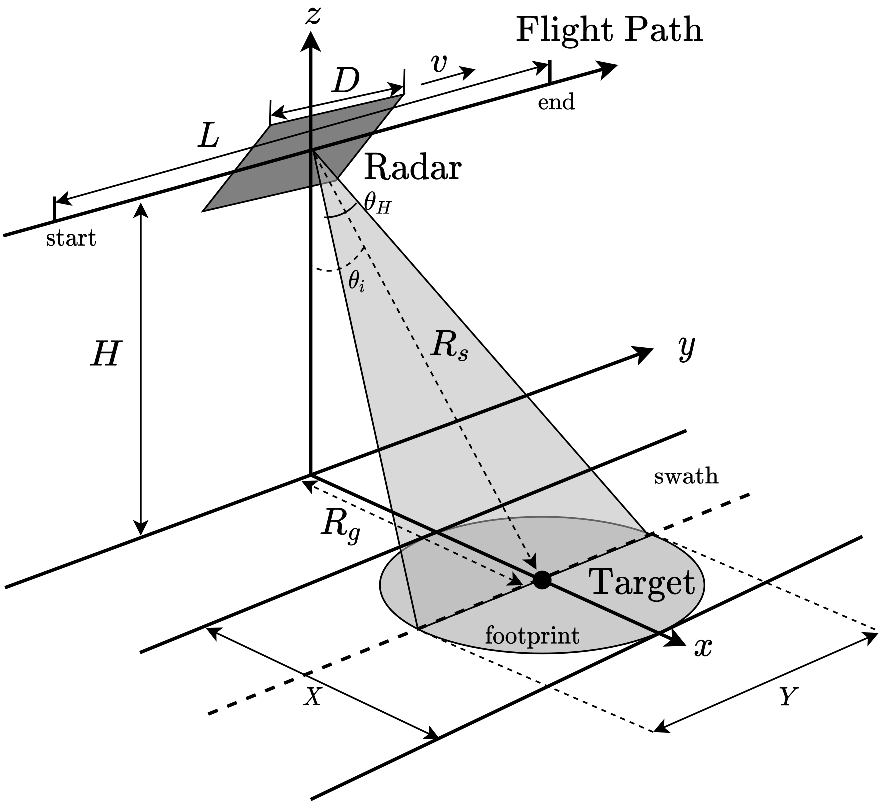

Figure 2.6: Geometry of a broadside SAR system

2.2.2 SAR Data

As the platform moves, the radar beam scans across a large ground swath and reflections from illuminated scatterers interfere with each other causing phase and amplitude modulation of the signal. The received signal is recorded and the reception of a single pulse produces a stream of I and Q samples.

For simplification in processing, the receiver can be considered stationary during the transmission and reception of a pulse, which is known as the "stop-and-go" technique. In reality the receiver is in constant motion, but the speed of propagation of the wave from transmitter to target, and then back to the receiver, is many orders of magnitude faster than the speed of the SAR platform. This difference in speeds forms a separation of timescales, where fast-time refers to the timescale of a single pulse, and slow-time refers to the timescale of the motion of the platform. The collected data forms a two-dimensional data matrix with a one-dimensional array of samples in fast-time, t, for each aperture position of the receiver in slow-time, u. For unambiguous imaging, the fast-time and slow-time domains must be sampled at a sufficient rate governed by the Nyquist theorem [40]. In fast-time, t, this equates to a sample spacing given by:

$$\Delta t \leq \frac{\pi}{\omega_0} \tag{2.17}$$

where ω_0 is the radar signal half bandwidth measured in radians. For a broadside SAR, the sample spacing in slow-time, u, is given by:

$$\Delta u \leq \frac{R_c \lambda}{4(Y_0 + L)} \tag{2.18}$$

where R_s is the radial distance from the centre of the aperture to the centre of the target scene, $Y_0 = Y/2$ is the half-width of the target area in cross-range, and L is the synthetic aperture length.

2.2.3 SAR Imaging

A SAR image is a two-dimensional, or sometimes three-dimensional, array of cells, usually pixels, where each cell represents a spatial area (or volume) and contains a value which represents the response of any reflective objects within that area when illuminated by radio waves. SAR image formation can be considered as the transformation from object space, which is defined by the physical properties of the objects in the scene of interest, to the data space of raw radar measurement, and then finally to the image space, the array of cells depicting the scene. The interaction of the radar signal with the environment encodes information about the targets onto the signal. After the reception of the signal and acquisition of the raw data, the signal processor transforms the data from the signal space, (t, u), to image space, (x, y), resulting in the final SAR image. A conceptual diagram of the SAR imaging process is shown in Figure 2.7.

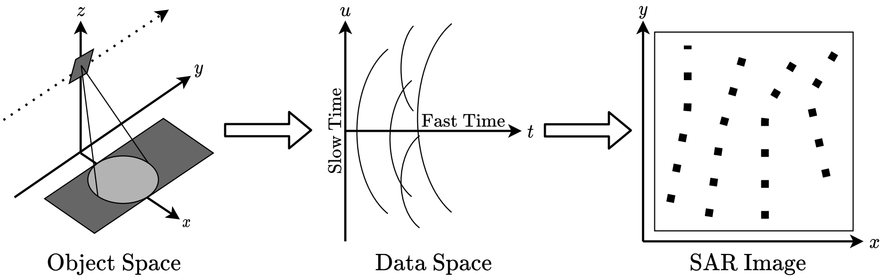

Figure 2.7: Diagram showing SAR image formation as the transformation of information from object space, to data/signal space, and finally, to image space

System Model

The target function is a function which describes the reflectivity of targets in a scene. Therefore, a SAR image can be thought of as a two-dimensional sampled reconstruction of the target function of a scene. For a set of N targets in a scene, the ideal SAR target function, which identifies the location of each target, is given by:

$$f(x, y) = \sum_{n=0}^{N-1} \sigma_n \delta\left(x - x_n, y - y_n\right) \tag{2.19}$$

where σ_n is the target reflectivity of the nth target, and x_n, y_n is the position of the centre of mass of the nth target in range and cross-range respectively. The distance between the radar and the nth target in slant range is:

$$R_n(u) = \sqrt{x_n^2 + (y_n - u)^2} \tag{2.20}$$

where u is the position of the receiver along the aperture (see Figure 2.8).

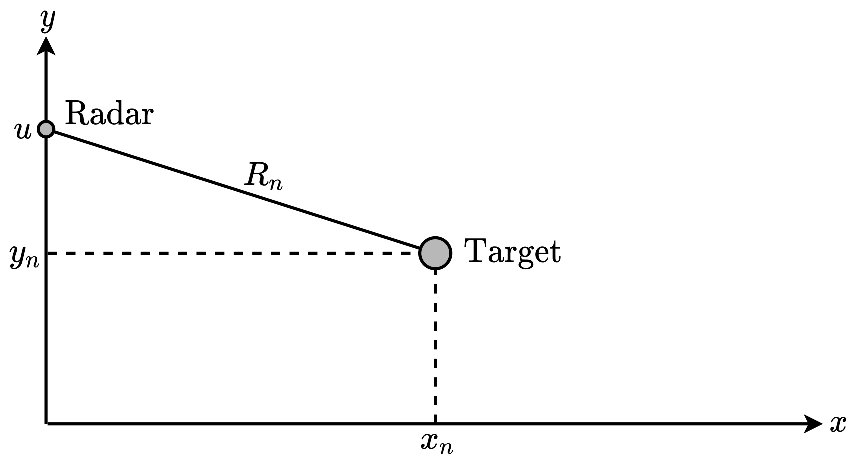

Figure 2.8: Range from radar to target

Let $p(t)$ represent the transmitted radar signal illuminating the target scene containing N targets. The returned echo signal, henceforth referred to as the SAR signal, is then:

$$\begin{aligned} s(t,u) &= \sum_{n=0}^{N-1} \sigma_n p(t - t_n) \\ &= \sum_{n=0}^{N-1} \sigma_n p \left[t - \frac{2R_n(u)}{c} \right] \\ &= \sum_{n=0}^{N-1} \sigma_n p \left[t - \frac{2\sqrt{x_n^2 + (y_n - u)^2}}{c} \right] \end{aligned} \tag{2.21}$$

The fast-time Fourier transform of the SAR signal in Equation 2.21 is:

$$s(\omega, u) = P(\omega) \sum_n \sigma_n \exp\left[-i2k\sqrt{x_n^2 + (y_n - u)^2} \right] \tag{2.22}$$

The spatial transform of Equation 2.22 with respect to slow-time, u is:

$$S(\omega, k_u) = P(\omega) \sum_n \sigma_n \exp(-i\sqrt{4k^2 - k_u^2}x_n - ik_u y_n) \tag{2.23}$$

Substituting $k_x(\omega, k_u) = \sqrt{4k^2 - k_u^2}$ and $k_y(\omega, k_u) = k_u$ into Equation 2.23 we can rewrite the SAR signal in the (ω, k_u) domain as:

$$S(\omega, k_u) = P(\omega) \sum_n \exp[-ik_x(\omega, k_u)x_n - ik_y(\omega, k_u)y_n] \tag{2.24}$$

The two-dimensional spatial transform of the ideal target function, Equation 2.19, is given by:

$$F_0(k_x, k_y) = \sum_n \sigma_n \exp(-ik_x x_n - ik_y y_n) \tag{2.25}$$

Substituting Equation 2.25 into Equation 2.24 yields:

$$S(\omega, k_u) = P(\omega)F_0[k_x(\omega, k_u), k_y(\omega, k_u)] \tag{2.26}$$

Therefore, the SAR signal can be expressed as the convolution of the transmitted signal with the ideal target function.

Reconstruction

Given a transmit signal, $p(t)$, and the received echo signal, $s(t)$, the goal of SAR image formation is to reconstruct the target function, $f(x, y)$, for a scene. For an ideal radar system the ideal target function can be derived as the two-dimensional inverse spatial Fourier transform of the SAR signal in the (ω, k_u) domain, divided by the Fourier transform of the transmission signal:

$$f_0(x, y) = \mathcal{F}^{-1}\left[\frac{S(\omega, k_u)}{P(\omega)}\right] \tag{2.27}$$

Whilst Equation 2.27 would provide a perfect reconstruction of the ideal target function, it also requires that the function $P(\omega)$ have an infinite bandwidth as well as to never go to zero for all ω. These conditions are not possible for a finite signal in time, such as a pulse, which has a sinc-like Doppler spectrum. An infinite bandwidth would require an infinitesimal pulse duration. One method for practical reconstruction is via fast-time matched filtering, defined by:

$$s_M(t,u) = s(t,u) * p^*(-t) \tag{2.28}$$

which can be expressed in the Frequency domain as:

$$S_M(\omega) = S(\omega)P^*(\omega) \tag{2.29}$$

Matched filtering is the process of correlating the transmitted signal with the received signal in order to form a range profile. This has the effect of detecting the presence of the transmitted signal within the received signal while maximising the SNR. The result is a function of delay time, which when interpreted as range produces a range profile, where the peaks in intensity correspond to targets at a given range. The evolution of the range of a target as a function of the aperture position u is called the targets range history. Applying this to Equation 2.27 gives:

$$F[k_x(\omega,k_u),k_y(\omega,k_u)] = P^*(\omega)S(\omega,k_u) \tag{2.30}$$

which is the convolution of the SAR signal, $s(t,u)$, with the conjugate of the transmit signal, $p(t)$. This can be expressed in the (t,u) domain as:

$$f(x,y) = \sum_n \int_u \int_t s(t,u) p^* \left[t - \frac{2\sqrt{x_n^2 + (y_n - u)^2}}{c} \right] dt du \tag{2.31}$$

Backprojection

As previously shown, SAR image formation can be considered as a transformation from signal space to image space via a two-dimensional convolution of the received SAR signal with a reference signal, followed by a mapping from the frequency domain to the spatial frequency domain. Backprojection is one of many possible algorithms for constructing an image from SAR signal data. The algorithm first defines a grid of discrete cells, where each cell corresponds to a two-dimensional sample point (x_i, y_j) in the spatial domain, or object space. As shown in Equation 2.31, the target function for a particular grid point is the correlation of the SAR signature at the given grid point with the measured SAR signal, $s(t,u)$, given by:

$$\begin{aligned} f(x_i, y_j) &= \int_u \int_t s(t,u) p^* \left[t - \frac{2\sqrt{x_i^2 + (y_j - u)^2}}{c} \right] dt du \\ &= \int_u \int_t s(t,u) p^* [t - t_{ij}(u)] dt du \end{aligned} \tag{2.32}$$

where $t_{ij}(u)$ is the round trip delay of the echo signal from a target located at grid point (x_i, y_j), and where the SAR signature, or reference signature, at a particular grid point is given by:

$$p \left[t - \frac{2\sqrt{x_i^2 + (y_j - u)^2}}{c} \right] \tag{2.33}$$

which is a time shifted version of the transmitted signal, $p(t)$. Using the definition of a matched filter from Equation 2.28, the reconstruction of the target function can be expressed as:

$$f(x_i, y_i) = \int_u s_M[t_{ij}(u), u] du \tag{2.34}$$

For a given synthetic aperture position, u, the fast time range history, s_M, are projected into the spatial domain to determine the return from a reflector at position (x_i, y_i), giving backprojection its name. This process requires an interpolation step to convert the discrete sampled matched filtered signal $s_M(t, u)$, to $s_M[t_{ij}(u), u]$, since the discrete samples of the signal will not, in general, align with the required samples at position (x_i, y_i). Figure 2.9 shows a block diagram depicting the backprojection algorithm and how it transforms a signal into an image. The process is repeated for each cell (i, j) in the image. The resulting target function formed via backprojection must then be multiplied with a phase function, $exp(-jk_c r)$, for baseband conversion, where k_c is the carrier frequency wavenumber in the range domain and r is the range to the target[41].

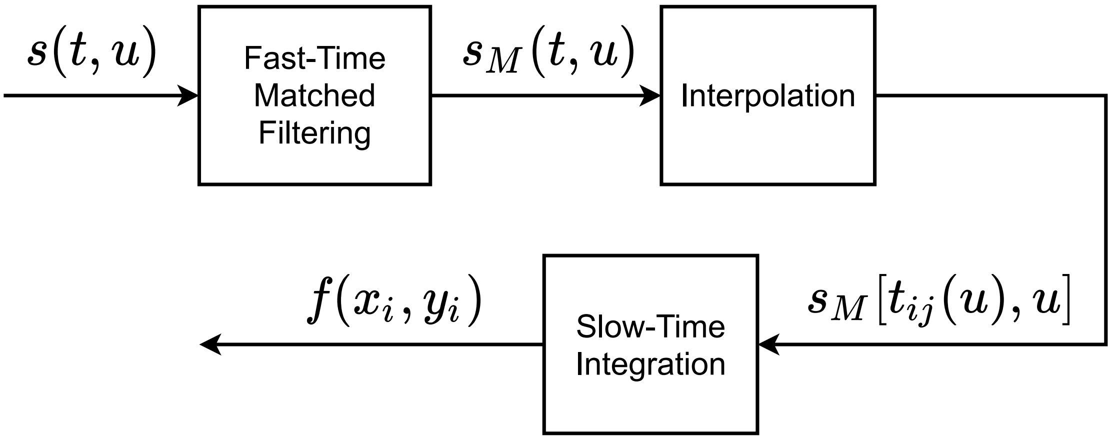

Figure 2.9: Block diagram of SAR reconstruction via backprojection algorithm, adapted from [41]

2.2.4 SAR Resolution

From Equation 2.10 the slant range resolution is given by:

$$\Delta R_s = \frac{c}{2B\cos(\beta/2)} \tag{2.35}$$

where β is the bistatic angle. The corresponding ground range resolution is then:

$$\Delta R_g = \frac{c}{2B\sin(\theta)cos(\beta/2)} \tag{2.36}$$

where θ is the incident angle of the radar beam.

The cross-range resolution is the minimum distance in the cross-range direction that two or more targets can be separately distinguished in a SAR image. More specifically, the cross-range resolution is the horizontal beamwidth of the receiving antenna at range R, where for SAR we use the length of the synthetic aperture rather than the physical antenna.The cross-range resolution for a physical aperture is given by:

$$\Delta CR = R\theta_B = \frac{\lambda R}{L} \tag{2.37}$$

where R is the range to the target, θ_B is the azimuth -3 dB beamwidth, λ is the carrier wavelength, and L is the size of the antenna aperture. It is clear from Equation 2.37 that increasing the aperture length will decrease (improve) the cross-range resolution, which is the premise of synthetic aperture imaging, and that the resolution degrades with increasing range. Equation 2.37 seems to suggest that arbitrarily fine resolutions can be obtained by increasing the aperture length. However, this presumes that the target is illuminated by the beam for the entire length of the aperture, such as a spotlight mode SAR. For a stripmap mode SAR, where the target enters and exits the main beam of the receive antenna as the platform moves, the equation for cross-range resolution becomes [42]:

$$\Delta CR = \frac{D}{2} \tag{2.38}$$

where D is the length of the physical aperture, independent of the synthetic aperture length.

The general equation for cross-range azimuth resolution in bistatic SAR system is given by:

$$\delta_{az} = \frac{\lambda}{2\omega_E T_d} \tag{2.39}$$

where ω_E is the effective angular speed of the platform and T_d is the dwell time on target. For a quasi-monostatic configuration, δ_{az} simplifies to:

$$\delta_{az} = \frac{\lambda}{\theta_{az}} \tag{2.40}$$

where θ_{az}, measured in radians, is the beamwidth of the SAR receiving antenna in the azimuth direction.

2.2.5 Sources of Error

Range Migration

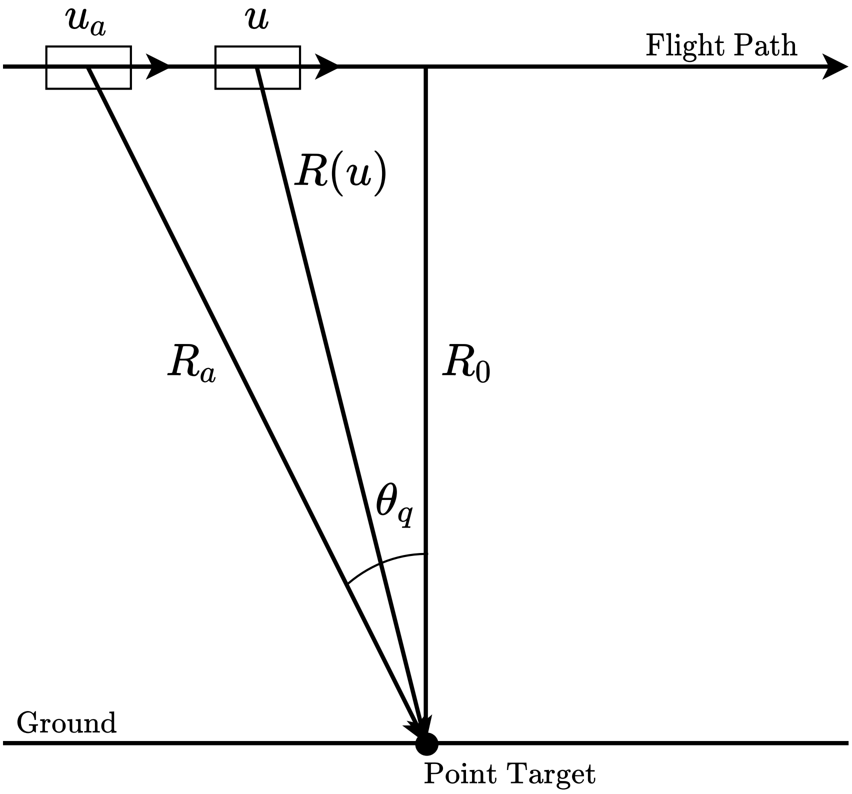

Figure 2.10: Diagram showing a top-down view of a simplified single-target squint SAR system

Range migration refers to the difference in range between successive aperture steps. Figure 2.10 shows a diagram of a top-down view of a broadside synthetic aperture radar. Let the point u be the current position of the radar, u_a be the previous position of the radar, and with the position of a point target indicated. The range from the radar at a position u along the aperture to the point target, $R(u)$ is given by:

$$R(u) = \sqrt{R_a^2 + (u_a - u)^2 - 2R_a\,(u_a - u)\cos\theta_q} \tag{2.41}$$

where R_a is the range from the radar at point u_a to the target, and θ_q is the squint angle. Using Taylor's theorem we can express the square-root as a Taylor series expansion. For a sufficiently small distance between successive aperture steps, $u - u_a$, the higher order terms can be ignored, and Equation 2.41 becomes:

$$R(u) \approx R_a + (u - u_a)\sin\theta_q + \frac{(u - u_a)^2}{2R_a} \tag{2.42}$$

Range migration, ΔR, is defined as the difference between the range at position u, R_u, and the range at the previous step, R_a:

$$\Delta R = R(u) - R_a \tag{2.43}$$

For a range resolution, ΔR_s, there will be no required range migration correction if $\Delta R_{max} < \Delta R_s/4$. Since $|u - u_a| < L/2$, the criteria for range migration correction is given by:

$$\frac{2\lambda R_a}{L}\left(|\sin\theta_q| + \frac{\lambda}{4L}\right) < \Delta R_s \tag{2.44}$$

which for a broadside SAR with no squint angle, i.e. $\theta_q = 0$ and $R_a = R_0$, simplifies to:

$$\frac{R_0\lambda^2}{2L^2} < \Delta R_s \tag{2.45}$$

Geometric Distortion

The range to a target feature is measured in slant range, R_s, rather than the true horizontal ground range, R_g. The relationship between slant range and horizontal ground range is given by:

$$R_s = R_g \sin\theta \tag{2.46}$$

where θ is the radar incident angle.

The difference between the slant range and horizontal ground range results in a distortion of relative distances between objects in the resulting SAR imagery which needs to be accounted for when comparing SAR imagery to ground truth positions. The discrepancy between slant range and ground range also results in a number of further possible geometric distortions of image features which depend on the slant angle, as well as the geometric properties of the features themselves, and are described below.

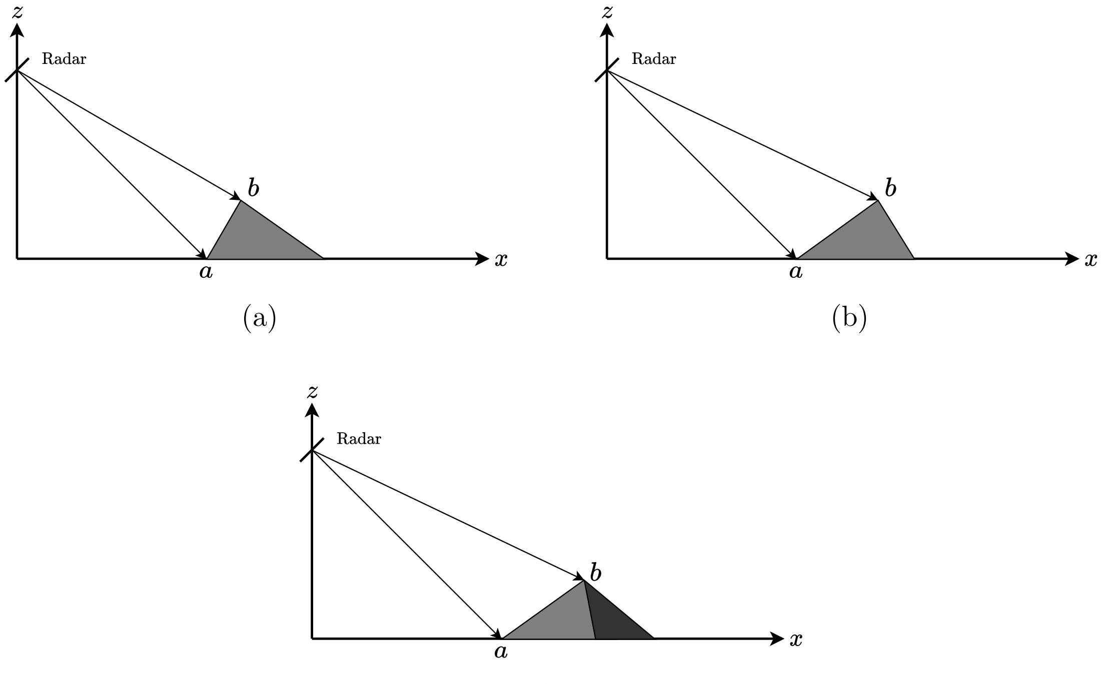

(a)

(b)

(c)

Figure 2.11: Diagrams demonstrating the causes of three possible geometric distortions: (a) Layover, (b) Foreshortening, (c) Shadowing

Layover

Layover describes the result of the radar beam reaching the top of a tall target feature before it reaches the base point. Since the return signal from the top will be received before the return signal from the bottom, the top of the feature will appear displaced towards the radar from its true ground position and will appear to overlay ("lay over") the base of the feature.

Foreshortening

Opposite in effect to layover, foreshortening occurs as a result of the radar beam reaching the base of a target feature before it reaches the top. The length of the slope from the base to the top of the feature appears compressed, or foreshortened, in the radar image.

Shadowing

Shadowing occurs when the radar beam is unable to reach part of a feature due to obstruction by reflecting objects. Any targets in the shadowed region will not appear in the resulting SAR image.

Speckle

A resolution cell which contains multiple reflecting objects can cause random interference from multiple scattering returns which results in random bright and dark areas in the radar image called speckle.

Motion Errors

Image formation via backprojection requires accurate positioning of the receiver in order to calculate the range to a target cell. To model the effect of motion errors, Equation 2.21 for the SAR signal from a particular nth target becomes:

$$s_n(\omega, u) = P(\omega)\sigma_n \exp\left[-i2k\sqrt{[x_n - x_e(u)]^2 + [y_n - u - y_e(u)]^2}\right] \tag{2.47}$$

where $x_e(u)$ and $y_e(u)$ are the motion errors as functions of slow-time, u, in the range and cross-range domains respectively. This signature can be written as:

$$s_n(\omega, u) = a_{en}(\omega, x_n, y_n - u) \exp\left[-i2k\sqrt{x_n^2 + (y_n - u)^2}\right] \tag{2.48}$$

where

$$a_{en}(\omega, x_n, y_n - u) = \exp\left[j2kr_{en}(u)\right] \tag{2.49}$$

and

$$r_{en}(u) = -\sqrt{[x_n - x_e(u)]^2 + [y_n - u - y_e(u)]^2} + \sqrt{x_n^2 + (y_n - u)^2} \tag{2.50}$$

Equation 2.50 describes the radial error for the nth target while Equation 2.49 describes the motion phase error function. This phase error function is equivalent to a spatial frequency, (k_x, k_y), filter which blurs target returns in the resulting SAR imagery.

2.3 DVB-T Signal

DVB-T operates in one of two modes, a "2K mode" suitable for small networks with limited transmitter distances, and an "8K mode" suitable for small and large networks. Each mode has differing parameters as defined by the standard. The different modes determine the number of sub-carriers within an OFDM symbol, as well as the length of the symbol in time. A full list of parameters for each mode is shown in Table 2.1. The transmitted DVB-T signal is organised into frames, where sixty-eight OFDM symbols constitute a frame, and four frames constitute a super-frame.

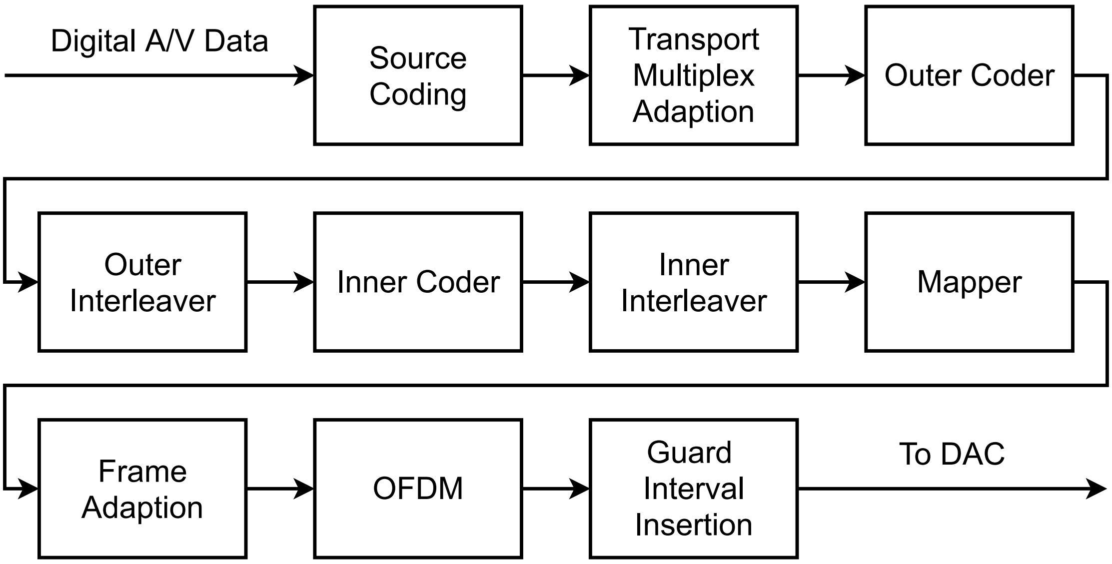

Figure 2.12: Block diagram of DVB-T Signal Construction

The basic construction of a DVB-T signal is shown as a flow diagram in Figure 2.12. The following sub-sections give a brief description of each phase of DVB-T signal construction in order to provide context for the analysis of the properties of DVB-T signals as a radar waveform.

Table 2.1: Table of DVB-T parameters for 8K and 2K modes.

Parameter	**Symbol**	**8K Mode**	**2K Mode**
Number of Carriers	K	6817	1705
Symbol Duration	T_U	896 μs	224 μs
Carrier Spacing	$1/T_U$	1116 Hz	4464 Hz
Bandwidth	$B = (K-1)/T_U$	7.61 MHz	7.61 MHz

2.3.1 Source Coding

The DVB-T standard defines that the video and audio data be encoded via MPEG-2. MPEG-2 is itself a standard which describes the compression and decompression of raw video and audio data to reduce the size of the files to be transmitted. The output of the MPEG-2 encoding is a stream of bytes to be transmitted.

2.3.2 Transport Multiplex Adaption

The first step after source coding is transport Multiplex (MUX) adaption and randomisation for energy dispersal. This is necessary because the DVB-T signal will affect the energy of the resulting transmission wave, and so it is ideal to disperse the energy across the wave. The data stream is randomised by a scrambler using a Pseudo Random Binary Sequence (PRBS).

2.3.3 Coding and Interleaving

After transport multiplex adaption, the data undergoes a series of steps to apply forward error correction, also known as channel coding. This is to ensure that the data can be correctly reconstructed at the receiver in the case of data loss due to a noisy or unreliable transmission. For the purpose of DVB-T SAR, the actual contents of the signal is not required for image formation. Therefore the precise details of coding and interleaving are not presented here but can be found in the standard handbook for digital video broadcasting [43].

2.3.4 Mapping

Mapping refers to the process of transforming binary data into phase and amplitude values which can be used to modulate a carrier wave.

Quadrature Amplitude Modulation

The DVB-T standard uses Quadrature Amplitude Modulation (QAM) to encode digital information onto a carrier wave. Whereas phase modulation keeps the amplitude and the radar frequency of the transmitted signal constant while modulating the phase, QAM modulates both the phase and amplitude of the signal. QAM works by modulating the amplitude of two sinusoidal signals with the same frequency, but a phase difference of 90°, also known as orthogonal or in-quadrature. The output of QAM is the signal resulting from the summation of the two amplitude modulated orthogonal waves. Since sine and cosine are orthogonal functions, a QAM signal can be expressed mathematically as:

$$s(t) = I(t)sin(\omega_c t) + Q(t)cos(\omega_c t) \tag{2.51}$$

where $I(t)$ is the amplitude modulation signal of the first component, known as the in-phase component, $Q(t)$ is the amplitude modulation signal of the quadrature component, and ω_c is the carrier frequency of the waves. Using Euler's formula, QAM can also be expressed as:

$$s(t) = C(t)\mathrm{e}^{i\omega_c t} \tag{2.52}$$

where $C(t) = I(t) + iQ(t)$ is a complex function where the real part corresponds to the in-phase component and imaginary part corresponds to the quadrature component. Since DVB-T is a digital signal, the values of $I(t)$ and $Q(t)$, and thus also $C(t)$, for each sub-carrier are constant discrete values over the transmitted symbol.

At this stage, the video and audio information is still a stream of ones and zeros, or bits. A constellation diagram, as shown for QAM-64 in Figure 2.13, shows how bits are mapped to discrete amplitudes for the in-phase and quadrature components of the carrier. For the case of QAM-64, six bits are mapped to one of sixty-four possible constellation points, which is then used to modulate a sub-carrier. This process is repeated for each sub-carrier within a DVB-T symbol, where the total number of sub-carriers per symbol is determined by the transmission mode, shown in Table 2.1.

2.3.5 Frame Adaption

A DVB-T OFDM frame with duration T_F consists of sixty-eight OFDM symbols (numbered 0 to 67), where each OFDM symbol, with duration T_S, is constituted by K sub-carriers. Whilst the majority of the sub-carriers are modulated with audio and video data via QAM, in addition to transmitted data, an OFDM frame also contains a number of pilot carriers. Pilot signals are inserted into the DVB-T transmission to allow for various types of synchronisation, as well as phase noise estimation. Pilot signals are sub-carriers within a DVB-T symbol modulated with a fixed and predetermined amplitude and frequency offset. There are three types of reference pilot carrier:

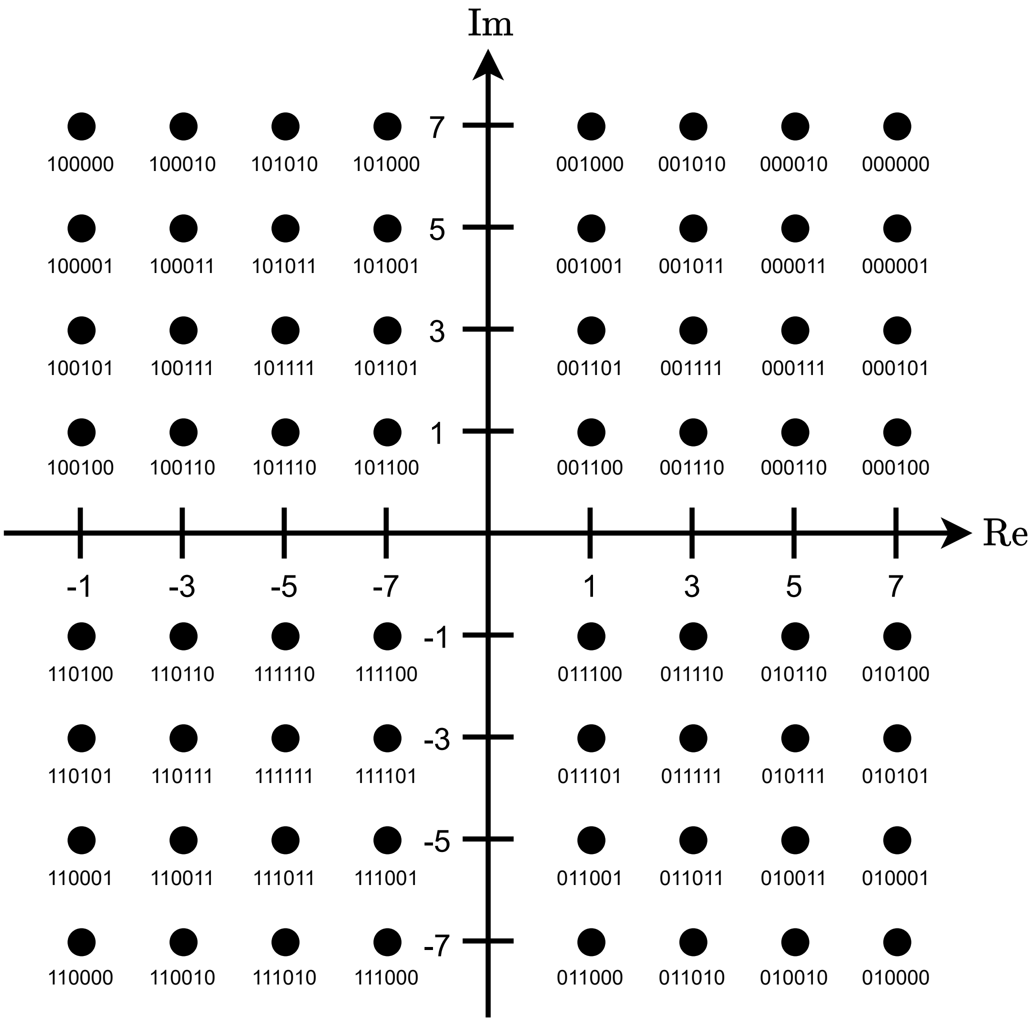

Figure 2.13: QAM-64 Constellation Diagram

1. Continual pilots
2. Scattered pilots
3. Transmission Parameter Signalling (TPS) carriers

Continual Pilots

Continual pilot signals are modulated onto the same sub-carriers within an OFDM symbol across the entire frame. The continual pilot sub-carrier positions, given as an index from 0 to $K - 1$, are defined by the standard for each mode and are also shown in Table B.1 in Appendix B.

The values of the continual pilots are determined by a PRBS, w_k, corresponding to their sub-carrier location k. The generator for the PRBS is defined as:

$$X^{11} + X^2 + 1 \tag{2.53}$$

Continual pilots are transmitted at a boosted power level of 4/3 relative to the power level of non-pilot carriers.

Scattered Pilots

Similarly to continual pilots, scattered pilots are also transmitted at a boosted power level of 4/3 above the power level of non-pilot sub-carriers and have values determined by the same PRBS. However, unlike continual pilots, the locations of scattered pilots are not constant for each OFDM symbol but follow a pattern where the sub-carrier location k is given by:

$$k = K_{min} + 3 \times (l \text{mod} 4) + 12p \tag{2.54}$$

where p is an integer which takes all possible values greater than or equal to zero, such that the resulting value for k does not exceed the range $[K_{min}; K_{max}]$, and where l is the time index of the symbols and and ranges from 0 to 67 for a single OFDM frame. Figure 2.14 shows a diagram representing an OFDM frame, where each circle represents a DVB-T symbol or sub-carrier, and each row represents an OFDM symbol. The locations of continual and scattered pilots coincide every fourth DVB-T symbol, and the pattern for scattered pilots repeats every four OFDM symbols.

TPS Carriers

Transmission Parameter Signalling (TPS) specifies the use of predefined carriers within a DVB-T symbol which are used for transmitting information related to the transmission scheme, such as channel coding and modulation. TPS is transmitted on seventeen carriers for the 2K mode and sixty-eight carriers for the 8K mode. The carrier indices are shown in Table B.2 in Appendix B. Unlike the continual and scattered pilots, the relative power level of TPS carriers is the same as the data carriers.

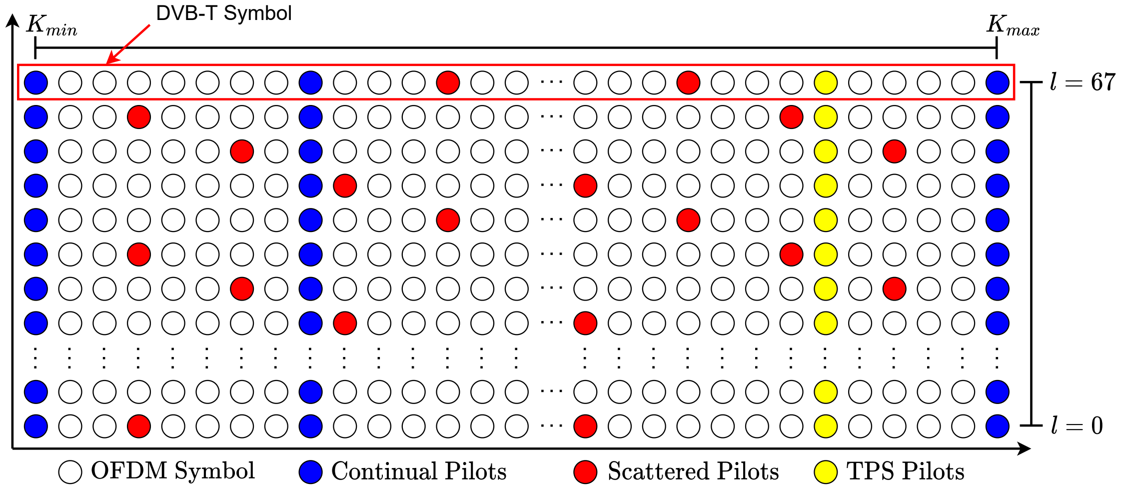

Figure 2.14: DVB-T symbol diagram for a full frame showing the different types of pilot carriers and their relative positions within a frame

2.3.6 Guard Interval Insertion

The normal function of a DVB-T receiver is to record and then decode the signal to retrieve the binary data that makes up the audio and video information. To do this, the receiver needs to be able to determine the start and end of a symbol. For this purpose a fractional section of a DVB-T symbol is copied from the end to the beginning of the symbol and is known as the guard interval.

2.3.7 DVB-T Waveform

The emitted DVB-T signal at the output of the transmitter can be expressed as:

$$s(t) = \mathrm{Re}\{e^{j2\pi f_c t} \sum_{m=0}^{\inf} \sum_{l=0}^{67} \sum_{k=K_{min}}^{K_{max}} c_{m,l,k} \times \psi_{m,l,k}(t)\} \tag{2.55}$$

where

$$\psi_{m,l,k}(t) = \begin{cases} \mathrm{e}^{i2\pi \frac{k'}{T_U}(t-\Delta-lT_s-68mT_s)} & (l+68m)T_s \leq t \leq (l+68m+1)T_s \\ 0 & \text{else} \end{cases} \tag{2.56}$$

where

- k is the carrier number;
- l is the OFDM symbol number;
- m is the frame number;
- K is the number of transmitted carriers;
- T_S is the symbol duration, where $T_S = T_U + \Delta$;
- T_U is the useful symbol duration;
- Δ is the guard interval duration;
- f_c is the carrier frequency;
- k' is the relative carrier index, $k' = k - (K_{max} + K_{min})/2$;
- $C_{m,l,k}$ is the QAM symbol for carrier k, OFDM symbol l, and frame m;

Taking a single DVB-T symbol, where $m = l = 0$, and considering where $0 \leq t \leq T_S$, the single symbol can be expressed as:

$$s(t) = e^{j2\pi f_c t} \sum_{k=K_{min}}^{K_{max}} c_k e^{j2\pi \frac{k}{T_U}(t-\Delta)} \tag{2.57}$$

2.3.8 DVB-T Signal Simulation

For a passive radar receiver system it is important to understand the characteristics of the transmit waveform. This is because, unlike an active radar system, the transmit waveform is not under the control of the radar system. In particular, for transmit waveforms that were not originally intended for use in a radar system, such as DVB-T signals, it is important to investigate and suppress any artefacts that may be introduced by the properties of the transmit signal.

Ambiguity Function Analysis

The ambiguity function allows for the analysis of the characteristics of a radar waveform independent of any target reflections and is specified by the parameters of the system.

The equation describing the ambiguity function is given by[44]:

$$\chi(\tau, \nu) = \int_{-\infty}^{\infty} s(t) s^*(t-\tau) \mathrm{e}^{2\pi i \nu t} dt \tag{2.58}$$

where $s(t)$ is the complex transmitted signal, τ represents a time delay and ν represents a frequency shift. Thus the ambiguity function is a two-dimensional complex function representing the correlation of the transmitted waveform with a time-delayed and frequency-shifted copy of itself.

The ambiguity function can be used to identify artefacts that result from the auto-correlation of deterministic and repeating structures within a signal. For example, if part of a signal is repeated within the transmit waveform, the repeating section will correlate with itself at least twice, resulting in an ambiguous measurement of range which, when combined with SAR image formation, could result in the presence of artificial targets, or ghost targets, in processed SAR imagery.

Figure 2.15 shows a plot of the ambiguity function of a simulated DVB-T signal with six OFDM symbols and with a frequency-shift range from 0 to 16 KHz. The DVB-T signal contains continual, scattered and TPS pilots and each OFDM symbol includes a 1/16 guard interval. From the figure, it is clear that the pilot carriers and the guard interval introduce ambiguities in the ambiguity function. Previous research has focused on the mitigation or removal of these ambiguities for use in radar [45–47]. However, as will be shown in Section 3.7, this is not necessary for use in synthetic aperture radar due to the suppression of these ambiguities during coherent integration.

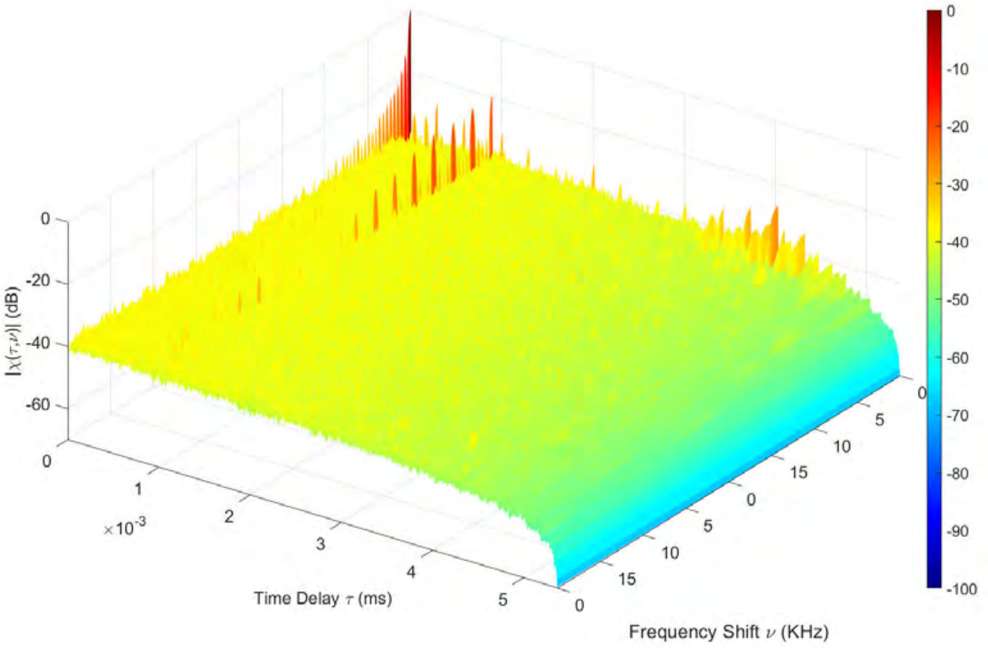

Figure 2.15: Ambiguity function of a six symbol DVB-T signal with 1/16 guard interval.

The MPEG-2 encoding removes similarities between video frames and, combined with the randomisation during transport multiplex adaption, results in a randomised signal. To simulate this effect, the computer simulation of the DVB-T signal uses a random distribution of QAM-64 complex symbols to modulate the OFDM sub-carriers. The ambiguity function of a random signal does not contain any ambiguities as the signal does not correlate except for at zero delay in time. Figure 2.16 shows a comparison of the ambiguity function for six DVB-T symbols of a DVB-T signal with only particular pilots present and the rest removed. The axes for each sub-figure are the same as those shown in figure 2.15. The signals shown in each ambiguity plot do not occur in isolation but have been separated out to highlight the different contributions to the full ambiguity function.

In Figure 2.16a the continual, scattered, and TPS carriers have been replaced with random QAM symbols which replicate encoded data. A 1/16th guard interval is included on each DVB-T symbol which causes a correlation of the signal at a time delay equal to the symbol useful duration, $T_U = 896\mu s$.

Figure 2.16b shows the ambiguity function for a DVB-T signal with only continual pilot carriers included, no scattered or TPS pilots, and no guard interval insertion. While the index locations of the continual pilot sub-carriers are somewhat random, continual pilots are the same for each DVB-T symbol and thus correlate strongly when integrating over more than one symbol, causing ambiguities to appear in the ambiguity function.

Figure 2.16c shows the ambiguity function for a DVB-T signal with only scattered pilot carriers included. Continual pilots, TPS pilots, and the guard interval have been replaced with random QAM symbols to preserve the signal length for comparison. Scattered pilot index locations follow a pattern which repeats every four DVB-T symbols and is given by Equation 2.54. Because of this repetition, the scattered pilots correlate, causing ambiguities in the ambiguity function.

Figure 2.16d shows the ambiguity function for a DVB-T signal with only the TPS carriers included. All other pilots and the guard interval have been replaced with random QAM symbols to replicate non-correlating data. Because the locations of TPS carriers within a DVB-T symbol are essentially random, the TPS carriers do not correlate with each other, and therefore do not produce any ambiguities.

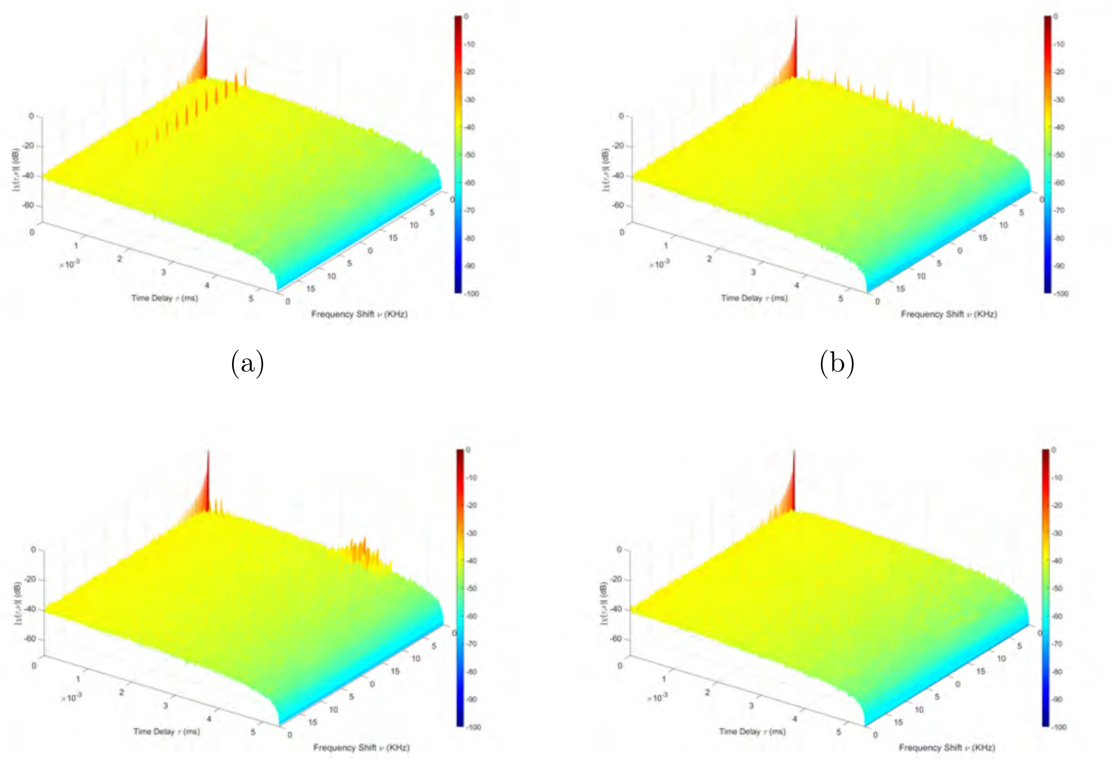

(a) (b)

(c) (d)

Figure 2.16: Comparison of ambiguity functions of a 6 symbol DVB-T signal with different pilot carriers or guard interval included. (a) guard interval only, (b) continual pilots only, (c) scattered pilots only, (d) TPS pilots only.

Chapter 3

DVB-T SAR System Overview

3.1 Introduction

Having presented the background and theory of SAR and DVB-T fundamentals in Chapter 2, this chapter will now provide an overview of both the theoretical constraints and the practical design and development of a general DVB-T SAR system. Firstly, the theoretical constraints explored include an investigation of the power budget, resolution, and sensitivity, as the operating range and bistatic angles are increased. Secondly, the potential issues of multiple transmitter interference and pilot ambiguities are considered and investigated with the use of a DVB-T SAR computer simulation. Thirdly, an image formation algorithm for DVB-T SAR, based on the backprojection algorithm, is presented as well as the signal processing steps required to transform measured data into imagery. Finally, the design and development of an initial demonstrator receiver system is shown, as well as the execution and results of a ground-based experimental campaign, the purpose of which was to validate the initial receiver system and image formation algorithm.

3.2 DVB-T Transmitter

The UK uses a multi-frequency network to transmit digital television. In a multi-frequency network, multiple radio frequency bands are used to transmit media content to an area, while neighbouring areas use a different distribution of radio frequencies to avoid interference from other transmitters. For the measurement campaigns shown in this thesis, the Sutton Coldfield transmitting station was used as the illuminator of opportunity.

Digital television signals are broadcast in the UHF frequency band from 400 MHz to 800 MHz. While this is in contrast to modern state-of-the-art systems, which usually operate in the L- to X-band regions of the spectrum, UHF radar is known for foliage penetration and non line-of-sight properties that could compliment current SAR systems [48–50]. Therefore, these unique properties of UHF, and their effect on SAR imagery, require exploration.

The Sutton Coldfield transmitting station broadcasts digital television signals, as well as analogue (FM) and digital (DAB) radio signals, and has a coverage area which encompasses the majority of the west-midlands, making it the second most important transmitter by coverage after the crystal palace transmitter in London[51]. Figure 3.1 shows the coverage area for the Sutton Coldfield transmitter, which encompasses all of Birmingham, Coventry, and Leicestershire where the ground and airborne trials were conducted [52]. The Sutton Coldfield transmitting station has a single mast with a height of 270.5 meters and is located at a point with an elevation of 169 meters above mean sea level, making the top of the mast 439.5 meters above mean sea level [53, 54]. The transmitter has a maximum output power of 250 kW for FM radio, and a 200 kW maximum output power for digital DVB-T television signals.

Table 3.2 lists the digital television signal channels transmitted from the Sutton

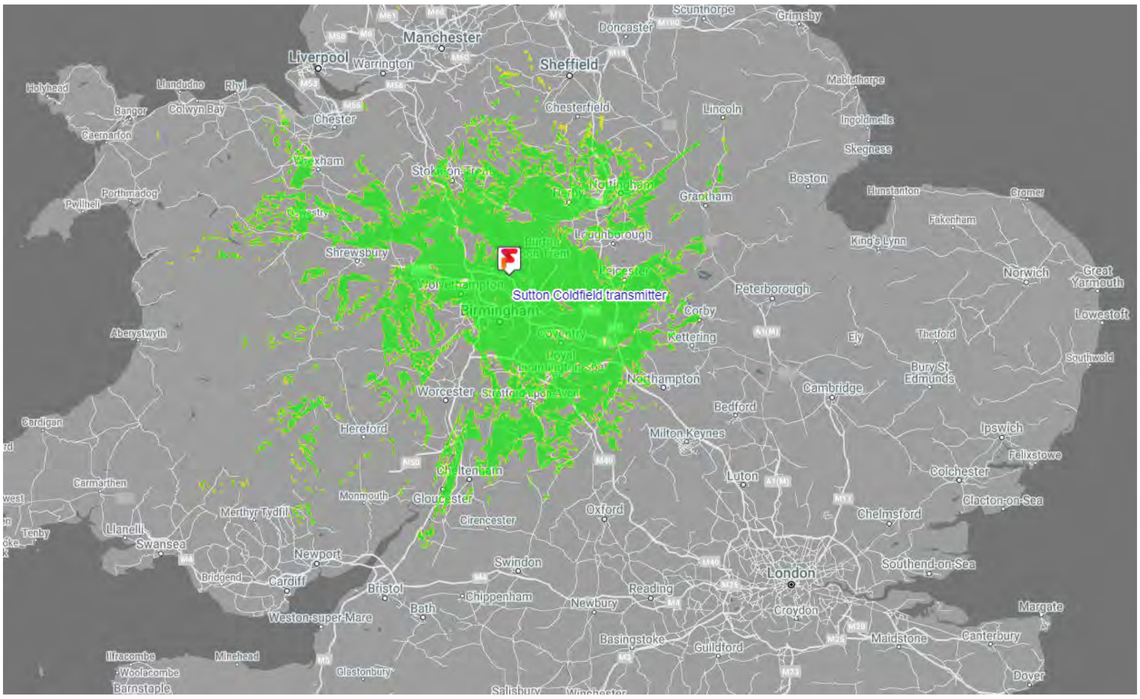

Figure 3.1: Image showing the coverage area of the Sutton Coldfield transmitter

Table 3.1: Table of Sutton Coldfield transmitting station properties

Property	Value	Unit
Latitude	52.600556	degrees
Longitude	-1.833889	degrees
Altitude	169	meters
Mast Height	270.5	meters

Table 3.2: Table of digital television channels transmitted from Sutton Coldfield transmission station.

Channel	Frequency	Power	Polarisation	System
33	570.0 MHz	89.2 kW	H -3.5dB	DVB-T2
35	586.0 MHz	86 kW	H -3.7dB	DVB-T2
39+	618.2 MHz	200 kW	H max	DVB-T
40+	626.2 MHz	200 kW	H max	DVB-T2
42	642.0 MHz	200 kW	H max	DVB-T
43	650.0 MHz	200 kW	H max	DVB-T
45	666.0 MHz	200 kW	H max	DVB-T
46	674.0 MHz	200 kW	H max	DVB-T
51	714.0 MHz	10 kW	H -13dB	DVB-T

Coldfield transmitting station, including their carrier frequency, output power, polarisation, and DVB-T specification [52].

Of these channels, five are transmitted via DVB-T at the maximum output power of 200 kW. Channel 40+ is also transmitted at 200 kW but uses the newer but less widely used version of the DVB-T standard called DVB-T2, which uses the same underlying OFDM structure. Channel 43, with a carrier frequency of 650 MHz, was chosen somewhat arbitrarily from the list of possible DVB-T transmission channels with the maximum output of 200 kW Effective Isotropic Radiated Power (EIRP) for reception and use in image formation.

3.3 Power Budget

For a DVB-T SAR receiver, both the direct signal from the transmitter and the reflected signal from the terrain being imaged must be recorded in order to maintain the coherence required for imaging. For image formation a sufficient SNR is required, and so presented here is a power budget calculation for a hypothetical DVB-T SAR receiver system in a low-earth orbit. A low-earth orbital system was chosen as the maximal range system, since a sufficient SNR for orbital use qualifies it for shorter range use, such as on-board an aircraft or within a ground-based vehicle.

Table 3.3: Table of Sutton Coldfield transmitting station properties

Parameter	**Symbol**	**Value**	**Unit**
Effective Radiated Power (ERP)	P_T	200	kW
Wavelength	λ	0.46	m
Bandwidth	B	7.61	MHz
Receiver Antenna Gain	G_r	15	dB
Receiver Antenna Effective Area	A_e	0.4	m^2
Receiver Noise Figure	N_f	5	dB
Receiver Altitude	r_d	400	km
Receiver Velocity	v	7626	m/s

The SNR at the receiving antenna output for the direct signal is given by:

$$SNR_D = \frac{P_T G_R \lambda^2}{(4\pi)^3 r_d^2 k T_0 B N_f} \tag{3.1}$$

where k is Boltzmann's constant and T_0 is the receiver temperature, assumed to be 300 Kelvin. The other parameters of the hypothetical orbital system are shown in Table 3.3. The radiated power of 200 kW and wavelength of 0.46 m, corresponding to a centre frequency of 650 MHz, are taken from the table of transmission channels for the Sutton Coldfield transmitter. The receiver altitude is chosen as the approximate altitude of the international space station which operates in a low-earth orbit, while the speed of the receiver platform is calculated from the orbital speed equation:

$$v = \sqrt{\frac{GM}{R}} \tag{3.2}$$

where G is the gravitational constant, M is the mass of the earth, and R is the radius of the orbit measured from the centre of the earth. Substituting the parameters in Table 3.3 into Equation 3.1 gives $SNR_D = 46.26$ dB, which demonstrates the viability of an orbital system for image formation. This value does not take into account atmospheric attenuation or transmit antenna directivity. Since DVB-T is designed for use on the ground, for an orbital system, it is highly likely that the direct signal would be received through the side-lobes of the transmit antenna. Figure 3.2 shows how the SNR varies as a function of the distance, r_d.

3.4 Spatial Resolution

A single DVB-T channel, with a bandwidth of 7.61 MHz, can be used with Equation 2.10 to determine a baseline range resolution. For a quasi-monostatic configuration

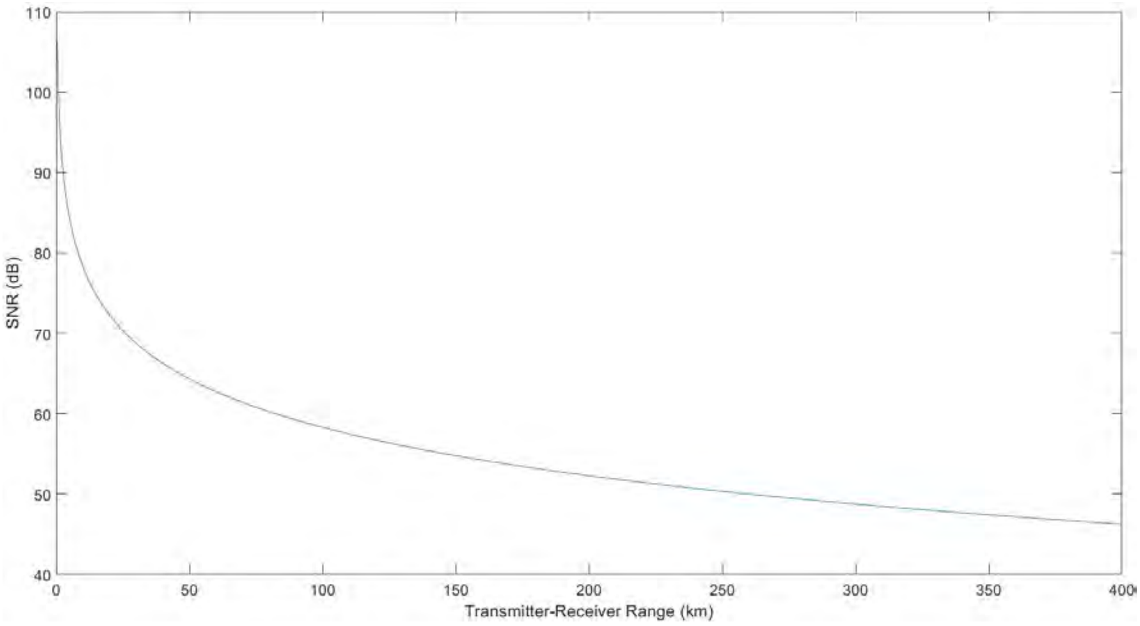

Figure 3.2: Graph of system SNR against transmitter-receiver range

($\beta = 0$), the range resolution is $\delta_r = 19.7$ m. As the bistatic angle increases, the range resolution degrades. Figure 3.3 shows a graph of the range resolution against the bistatic angle. As the bistatic angle approaches 180 degrees, the range resolution approaches infinity, representing a complete loss of resolution and hence a loss of imaging ability.

The general equation for cross-range resolution in bistatic SAR is given by Equation 2.40. For the 15 dB gain receiving antenna from Table 3.3, the antenna beamwidth is $\theta_{az} = 36°$, giving a maximum resolution of approximately 0.74 m.

3.5 Sensitivity

The sensitivity of a hypothetical passive DVB-T SAR system can be determined using the Noise Equivalent Sigma Zero (NESZ), which for a bistatic system can be derived as:

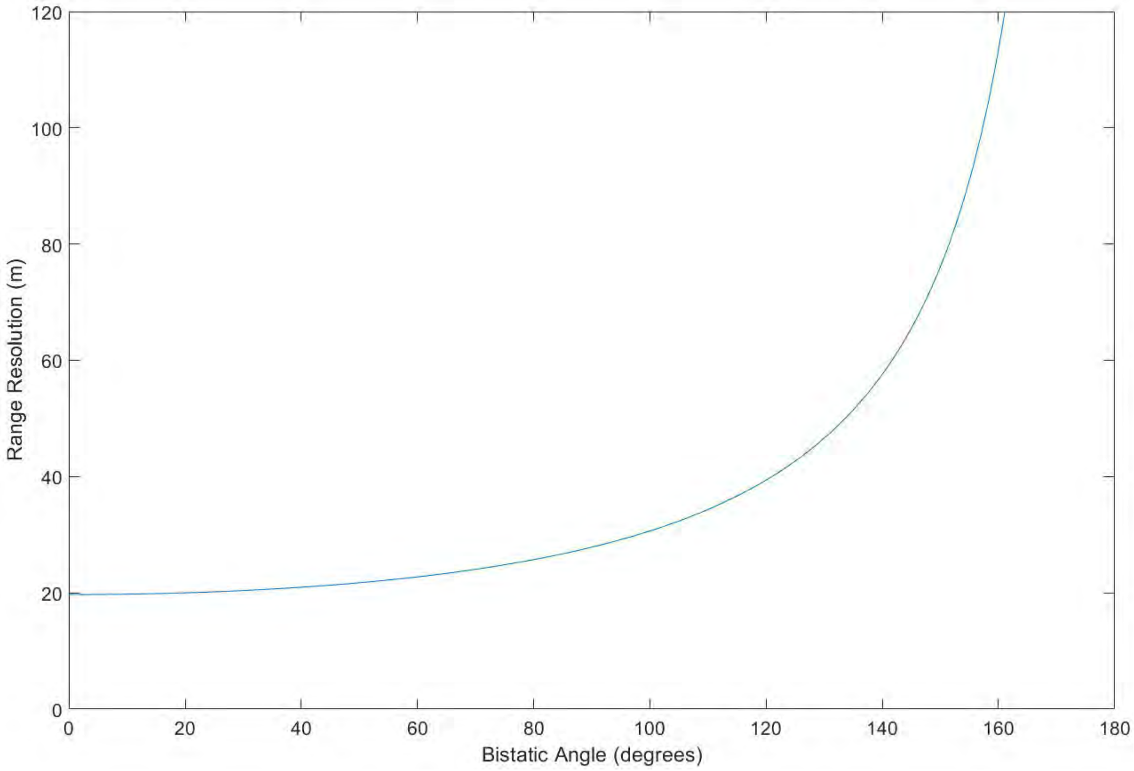

Figure 3.3: Graph of range resolution against bistatic angle

$$NESZ = \frac{(4\pi)^2 r_t^2 r_r k T_0 \nu N}{P_T A_e \delta_r \lambda} \tag{3.3}$$

where r_t is the transmitter to target range, r_r is the receiver to target range, v is the speed of the SAR moving platform, and A_e is the effective area of the receiving antenna. Table 3.3 shows the values for each parameter for a hypothetical orbital satellite SAR receiver system, which represents the limiting real-world case for receiver to target range. The satellite is modelled to be in a low-earth orbit with an altitude of 400 km, the transmit power, P_t, is set to the maximum power of the Sutton Coldfield transmitter at 200 kW, and A_e, is set to the effective area of a 15 dB gain antenna. NESZ, also known as noise-equivalent backscatter coefficient, is the clutter reflectivity which generates a power level in a SAR image equal to that of thermal noise [1].

Figure 3.4 shows the NESZ plotted against the transmitter to target distance, r_t.

At an r_t of 200 km from the transmitter, the NESZ is -34 dB, which demonstrates the viability of such a system for long-range operation. However, since DVB-T broadcasting stations are typically only a few hundred meters from the ground, the grazing angle of the incident signal is very small. Figure 3.5 shows how the grazing angle changes with increasing transmitter to target distance for a flat ground plane model and a 270 m tall transmitter. The lower the grazing angle, the higher the likelihood of the effects of shadowing and layover, which results in distorted imagery. The point at which the grazing angle results in geometric distortion is dependent on the geometry of the system and the relative locations of targets.

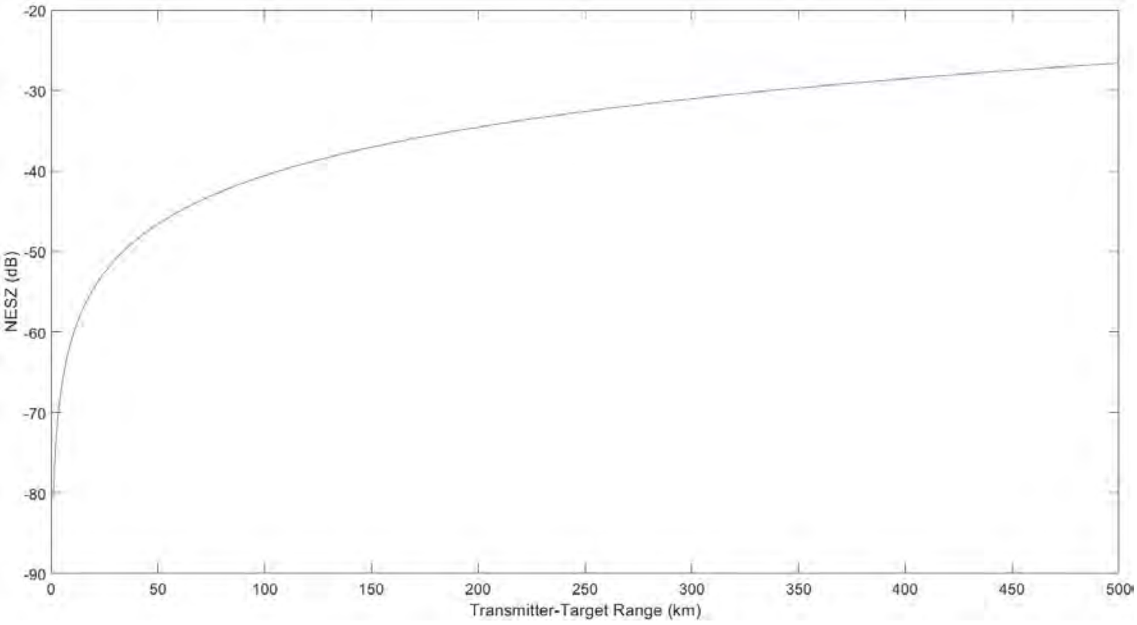

Figure 3.4: Graph of system sensitivity against transmitter-target range

3.6 Multiple Transmitter Interference

Different DVB-T transmission stations spaced sufficiently far apart may reuse the same frequency band for the transmission of different television signals. While a ground-based receiver is unlikely to receive significant direct signal interference from multiple transmitters, an airborne or space-borne system, due to their larger receiver antenna ground footprints, are likely to receive signals originating from mul-

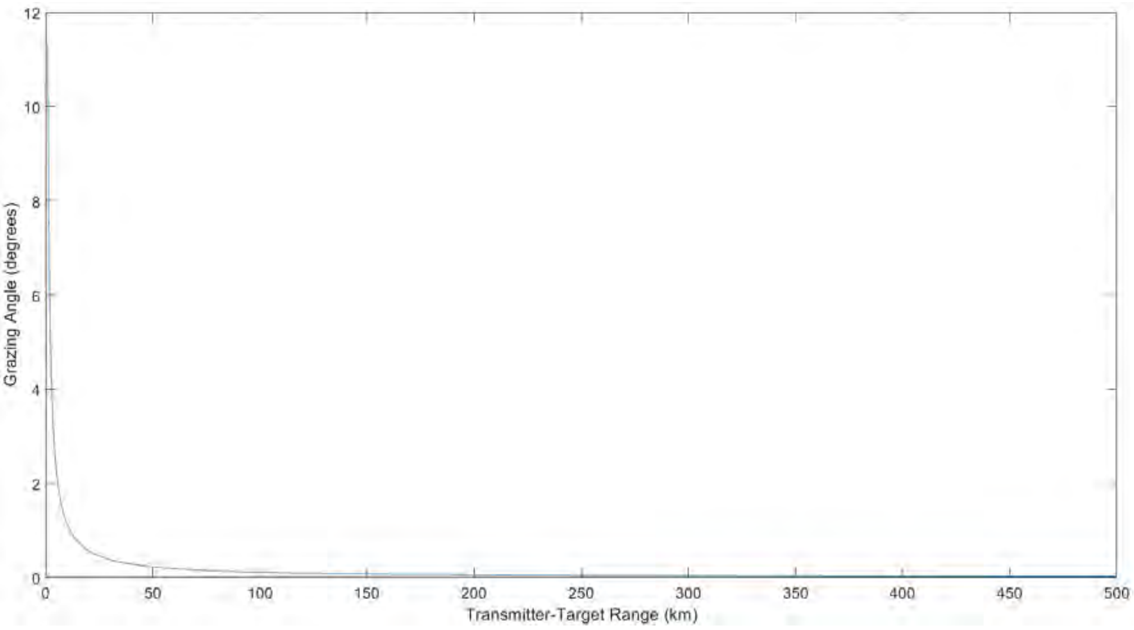

Figure 3.5: Graph of grazing angle against transmitter-target range

tiple transmitters with the same centre frequency. Multiple transmitter interference has the potential to cause ghost targets to appear in processed SAR imagery. For this reason, a DVB-T SAR simulation with multiple transmitters was developed to investigate the effects of multiple transmitter interference on SAR imagery.

Two real DVB-T transmitters located in the UK, which both transmit at the same centre frequency of 650MHz, but with differing power outputs, were chosen for simulation. Figure 3.6 shows the real world transmitters selected (Sutton Coldfield and Chesterfield), and the 75 km distance between them. There is a 30 dB difference in power, and a different polarisation between the two transmitters, but for the simulation we assume the power and polarisation to be the same.

For the simulation, the relative transmitter locations were modelled and the same DVB-T signal was transmitted at the same power level for each transmitter. A simulated receiver was positioned half-way between the two transmitters and a simulated point target. Figure 3.7 shows the geometry used for the simulation, as well as the distances involved.

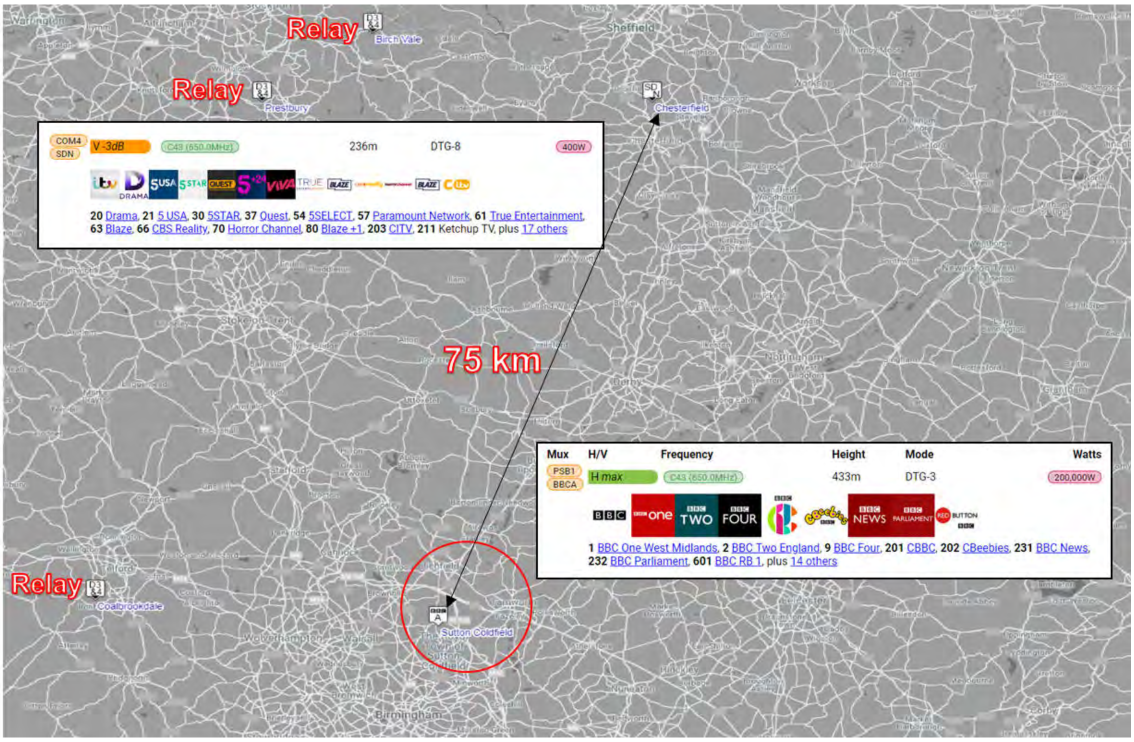

Figure 3.6: Real world location of two transmitters which operate at the same frequency to provide an example of the typical distances between co-frequency transmitters

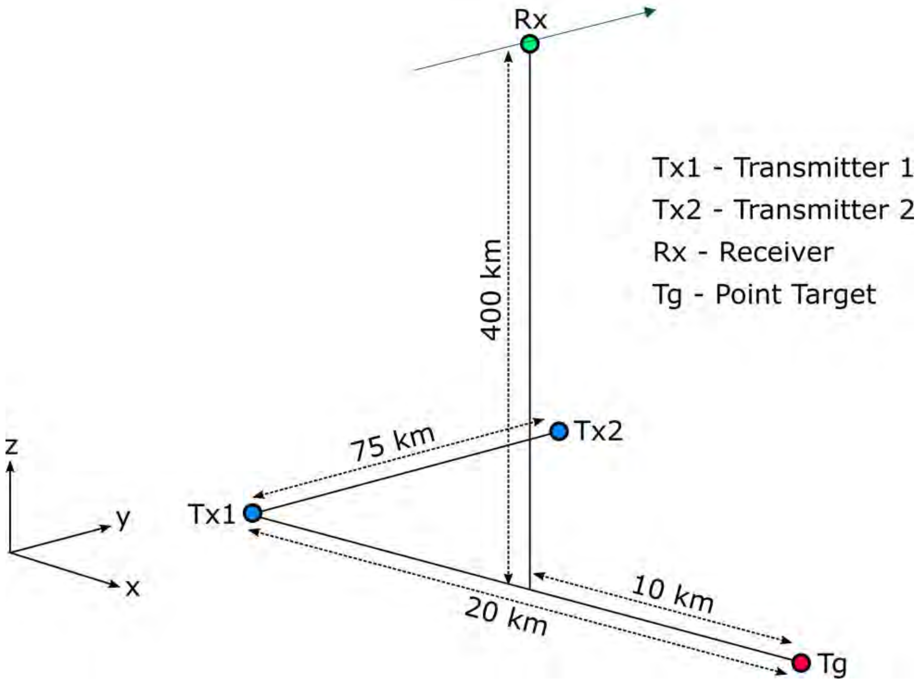

Figure 3.7: Diagram of the geometry of the multiple transmitter simulation with distances labelled

Table 3.4 shows the parameters of the simulation. An aperture time of 40 seconds was chosen to more accurately simulate the kind of aperture time that would be recorded by a low-orbit satellite. However, the receiver speed is an order of magnitude smaller than the actual orbital speed of a low orbit satellite (approximately 8 km/s) so that the amount of simulated data generated could be processed in a reasonable time. The simulation was performed with a single transmitter and multiple transmitters for comparison, and the results of these simulations are shown in Figures 3.8a and 3.8b respectively. Any difference in the intensity of the simulated point spread function is not visible with the naked eye.

Table 3.4: Table of parameters for multiple transmitter simulation

Parameter	**Symbol**	**Value**	**Unit**
Transmitter1 Centre Frequency	f_c1	650	MHz
Transmitter2 Centre Frequency	f_c2	650	MHz
Synthetic Aperture Length	d	4000	m
Synthetic Aperture Time	t	40	s
Receiver Platform Speed	v	100	m/s
Effective Pulse Width	T	1.8	ms
Distance Transmitter1 - Transmitter 2	T_x1T_x2	75	km
Distance Transmitter1 - Target	T_x1T_g	20	km
Distance Transmitter2 - Target	T_x2T_g	77.61	km
Distance Receiver - Target	R_xT_g	400.13	km
Range Resolution	δR	20	m
Cross-Range Resolution	δCR		m

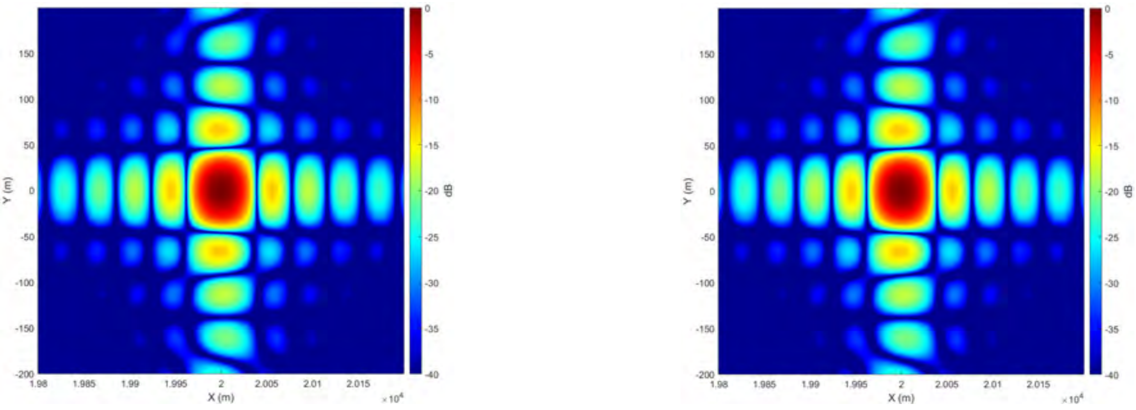

(a) (b)

Figure 3.8: Point spread function of simulated point targets for single and multiple transmitters. (a) single transmitter, (b) multiple transmitters operating at the same centre frequency

Figure 3.10 shows the range profile after cross-correlation for a single DVB-T symbol with the two transmitters. The range profile clearly shows that there are ambiguous peaks that occur due to the second transmitter, with only one of the peaks belonging to the actual simulated point target. The peaks shown in Figure 3.10 can all be explained in relation to the distances between the two transmitters and the target, shown in Figure 3.9, and the paths of either the direct signal or the reflected signal:

1. $T_x2R_x - R_xT_g = 407.1 \text{ km} - 400.5 \text{ km} = 6.6 \text{ km}$
2. $T_x1T_g + R_xT_g - T_x2R_x = 20 \text{ km} + 400.5 \text{ km} - 407.1 \text{ km} = 13.4 \text{ km}$
3. $T_x1T_g + R_xT_g - T_x1R_x = 20 \text{ km} + 400.5 \text{ km} - 400.5 \text{ km} = 20 \text{ km}$
4. $T_x2T_g - T_x1T_g = 77.62 \text{ km} - 20 \text{ km} = 57.62 \text{ km}$
5. $T_x2T_g + R_xT_g - T_x2R_x = 77.62 \text{ km} + 400.5 \text{ km} - 407.1 \text{ km} = 71.02 \text{ km}$
6. $T_x2T_g + R_xT_g - T_x1R_x = 77.62 \text{ km} + 400.5 \text{ km} - 400.5 \text{ km} = 77.62 \text{ km}$

Only the peak labelled (3), corresponding to the bistatic range of the target, is integrated during image formation. The rest are suppressed by the image formation algorithm, which is a spatial filter tuned to the location of the transmitter and receiver, which are both known locations, as well as the target image pixel, which is at a known distance from the transmitter and receiver.

Figure 3.11a again shows the point target at 20 km, this time with a higher dynamic range. To demonstrate that the image formation algorithm does not compress the ambiguous peaks in cross-range, Figure 3.11b, shows a SAR image focused at the distance of the peak labelled (1) in Figure 3.10, with the intensity normalised to the peak intensity of the point target in Figure 3.11a. While the side-lobes of the point target at 20 km are visible in the image in Figure 3.11b, they appear 50 dB below the peak intensity, within the threshold of the noise level.

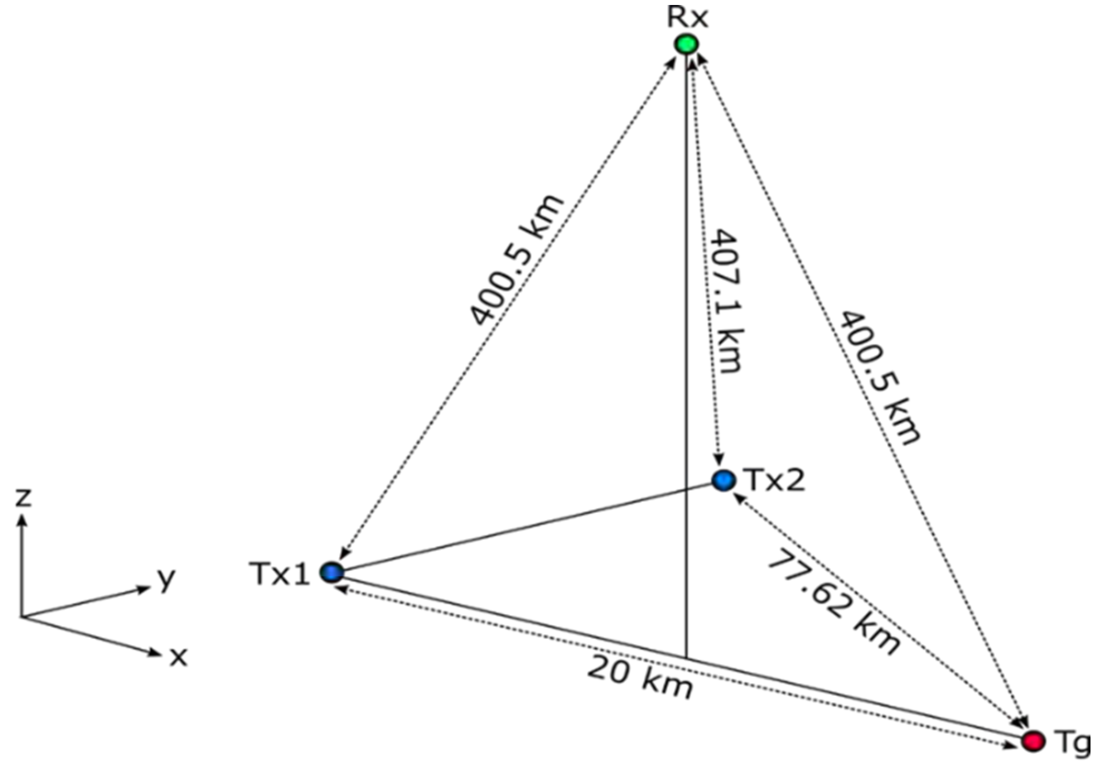

Figure 3.9: Diagram showing the the geometry of the multiple transmitter simulation with distances between the transmitter, receiver, and target labelled

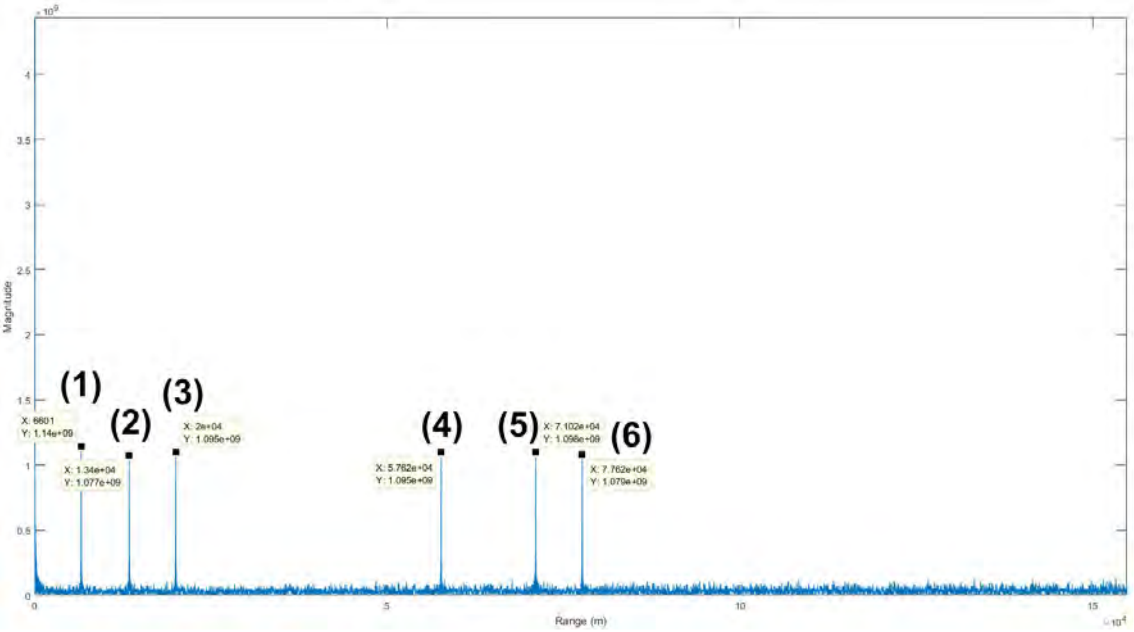

Figure 3.10: Range profile of a typical DVB-T symbol via cross-correlation with a simulated point target at 20 km and two simulated transmitters with the same centre frequency positioned according to Figure 3.7

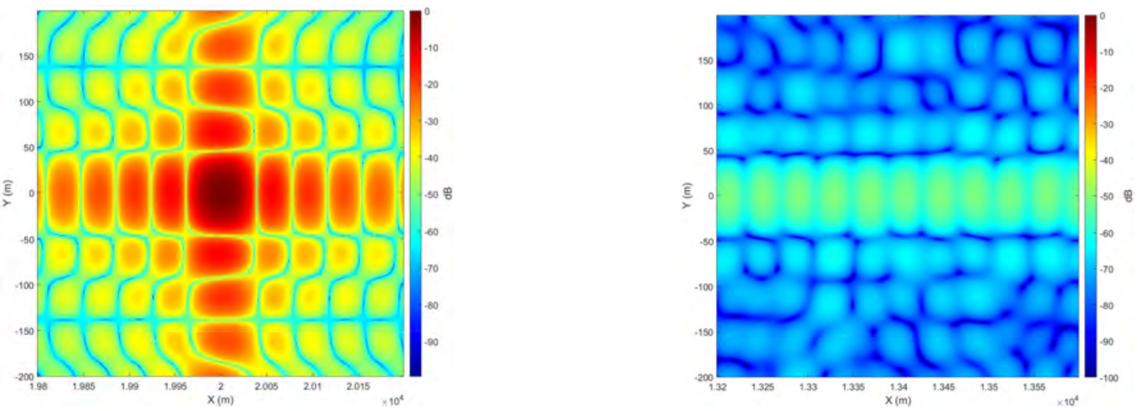

(a)

(b)

Figure 3.11: Simulated point target at 20 km with two transmitters. (a) Image of simulated point target. (b) Image focused at the location of an ambiguity caused by multiple transmitters.

3.7 DVB-T Pilot Ambiguities

As shown in Section 2.3.5, the transmitted DVB-T signal contains deterministic components called pilots which are used for synchronisation during decoding. It was shown in Section 2.3.8 how these pilot carriers cause ambiguities in the ambiguity function for the DVB-T signal, and previous research has investigated and developed ways to mitigate these ambiguities for passive radar [45, 55, 56]. For SAR imaging, the effects of pilot ambiguities on processed SAR images was investigated.

The transmitted DVB-T signal can be expressed as:

$$s(t) = \mathrm{Re}\{\mathrm{e}^{j2\pi f_c t} \sum_{m=0}^{\mathrm{inf}} \sum_{l=0}^{67} \sum_{k=K_{min}}^{K_{max}} c_{m,l,k} \times \mathrm{e}^{i2\pi \frac{k'}{T_U}(t-\Delta-lT_s-68mT_s)}\} \tag{3.4}$$

where the definitions of each term are shown in Section 2.3.7. The direct signal recorded by the receiver can be expressed as:

$$d(t) = s(t-\tau_0) \tag{3.5}$$

where $\tau_0 = R_B/c$, and R_B denotes the baseline range from the receiver to the transmitter. The reflected signal can be expressed as:

$$r(t) = s(t - \tau_1) \tag{3.6}$$

where $\tau_1 = (R_T + R_R)/c$, and R_T is the range from the transmitter to the target, and R_R is the range from the receiver to the target, as shown in Figure 2.3. Range compression is performed with the correlation of the direct and reflected signals giving:

$$s(\tau) = R_{dr}(\tau) + R_{rd}(\tau) \tag{3.7}$$

where $R_{dr}(\tau) = d(r) \star r(t)$ is the cross-correlation of the direct signal with the reflected signal, and $R_{rd}(\tau) = r(t) \star d(t)$ is the cross-correlation of the reflected signal with the direct signals. The first term in Equation 3.7 is given by:

$$R_{dr}(\tau) = \int_{-\infty}^{\infty} d(t) \cdot r^*(t - \tau) dt \tag{3.8}$$

Substituting the definitions of $d(t)$ and $r(t)$ into Equation 3.8, and setting $t = t - \tau$, gives:

$$R_{dr}(\tau) = \int_{-\infty}^{\infty} s(t) \cdot s^*(t - \Delta - \tau) dt \tag{3.9}$$

where $\Delta = \tau_1 - \tau_0 = R_T + R_R - R_B$. Comparison with the definition of the ambiguity function, $\chi(\tau, \nu)$, shown in Equation 2.58, shows that R_{dr} can be expressed as:

$$R_{dr} = \chi(\tau + \Delta, 0) \tag{3.10}$$

Similarly, it can be shown that $R_{rd} = \chi(\tau - \Delta, 0)$. Therefore, the location of range-compressed pilot carrier ambiguities will be located at a delay according to:

$$\tau = \Delta \pm \{0, \frac{k}{12}T_U, T_S\} \tag{3.11}$$

Equation 3.11 shows the location of ambiguous peaks in the ambiguity function which are separated by $KT_U/12$ in time. However, after image formation these ambiguities are suppressed by the integration over slow time. More specifically, because the location of the pilot peak ambiguities is independent of the slow time position of the receiver, u, the range and phase histories of the ambiguities will not be integrated by the backprojection algorithm [57]. Figure 3.12 demonstrates the mismatch between target range histories (black lines), which are integrated during backprojection, and pilot range histories (red lines), which are not. Because the delay of the pilot carriers remains constant, the corresponding range remains constant for each azimuth position of the receiver, resulting in a straight-line range history. In contrast, a real target with a fixed spatial position will have a non-constant range as the receiver moved along the aperture in the azimuth direction, resulting in a curved range history. The image formation process integrates along the range history for a target, and therefore does not coherently integrate the pilot signal range histories.

3.8 Image Formation

To generate a SAR image of the scene under study, an image formation algorithm is required. The purpose of an image formation algorithm is to transform raw data

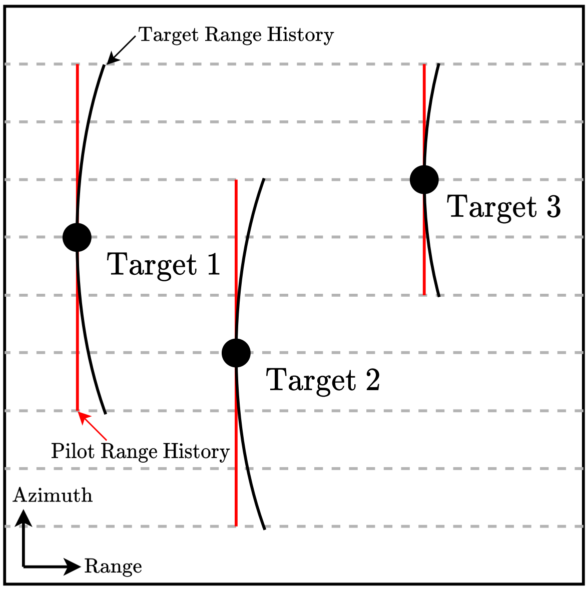

Figure 3.12: Diagram demonstrating the mismatch between the range histories of pilot ambiguities compared to target range histories

collected in object space into an image which represents the scene in image space. For the case of DVB-T passive SAR, the transmitter is at a fixed location, while the receiving platform moves along an ideally straight path. As the receiver moves it records the direct and reflected signals continuously throughout the aperture. However, for simplicity when describing the image formation process, the receiver system can be considered as a stop-and-go system where the receiver moves a particular distance, stops to record the signals for a particular time, then proceeds to move to the next recording point. In this way the receiver is not recording while in motion and is not moving while recording. This process is performed implicitly by splitting the continuously recorded data into a number of sections of equal length and processing the data as if these sections were individual radar pulses, where each section corresponds to a particular aperture position, u. A natural choice of partition, and the one used in this thesis, is the length of a single DVB-T symbol. The transmit signal is then given by:

$$p(t) = \mathrm{e}^{j2\pi f_c t} \sum_{k=K_{min}}^{K_{max}} C_k \mathrm{e}^{j2\pi \frac{k}{T_u}(t-\Delta)} \tag{3.12}$$

where the definition of each symbol is described in Section 2.3.7.

For image formation, the backprojection algorithm (described in Section 2.2.3) was used. For each aperture position, u, the sampled radar and reference signals were used to perform a matched filter by cross-correlating the signals, resulting in a range profile, $S_M(t,u)$. It is also possible, in the case of a single receiver channel, to auto-correlate the radar signal, which contains both the reflected signals from the target scene as well as the direct signal from the transmitter, as will be shown in Section 4.5.3.

The process of matched filtering is followed by an interpolation step with the bistatic range to each cell in the image scene. First a target scene is defined by a rectangular area given by width and height in meters, and a corresponding image scene is defined with a width, W and height H in pixels. This is combined with elevation data, extracted from online DEM's, and is used to create a two-dimensional W by H target scene matrix representing the terrain surface of the target scene, where each cell of the matrix contains a vector representing the position of the centre of the cell [58].

The range from the transmitter to the centre of a cell is given by:

$$R_T[i,j] = \sqrt{(x_T - x[i,j])^2 + (y_T - y[i,j])^2 + (z_T - z[i,j])^2} \tag{3.13}$$

where (x_T, y_T, z_T) is the position of the transmitter and $(x[i,j], y[i,j], z[i,j])$ is the position of a grid cell sampled with indices i and j from the target scene matrix. Since the transmitter and target scene are stationary relative to each other, R_T does not depend on the aperture position u. The range from the receiver to the centre of a cell is given by:

$$R_R[i,j](u) = \sqrt{(x_R(u) - x[i,j])^2 + (y_R(u) - y[i,j])^2 + (z_R(u) - z[i,j])^2} \tag{3.14}$$

In this case, the range is a function of the receiver position along the aperture. Similarly, the range between the transmitter and receiver is given by:

$$R_B(u) = \sqrt{(x_R(u) - x_T)^2 + (y_R(u) - y_T)^2 + (z_R(u) - z_T)^2} \tag{3.15}$$

which is a function of u but does not depend on any particular target matrix cell position. The bistatic range for a particular grid cell position, (i,j), is then defined as:

$$R[i,j](u) = R_T[i,j] + R_R[i,j](u) - R_B(u) \tag{3.16}$$

Substituting this and the transmit signal, Equation 3.12, into Equation 2.21, gives the signal measured by the receiver at grid cell, (i,j), where propagation and attenuation effects are encapsulated by the multiplication of an amplitude term, α:

$$s(t,u)[i,j] = \alpha \mathrm{e}^{j2\pi f_c\left(t - \frac{2R(u)[i,j]}{c}\right)} \sum_{k=K_{min}}^{K_{max}} C_k \mathrm{e}^{j2\pi \frac{k}{T_u}\left(t - \Delta - \frac{2R(u)[i,j]}{c}\right)} \tag{3.17}$$

The received signal is cross-correlated with the transmit signal to give the range profile, $S_M(t,u)$, which is then sampled by the bistatic range, using linear interpolation for points that do not correspond directly to the sample points of the range profile. The last step of the backprojection algorithm is the integration of the range compressed data over the slow-time, u, domain. This compresses the data in the aperture direction, reconstructing the target function for the specified area, resulting in a SAR image. The last step is to multiply by a phase function, $\mathrm{e}^{-j\omega_c\Delta}$, which corrects the phase error resulting from the baseband conversion of the reflected signal.

The full process as performed by a computer can be summarised as follows:

- For each slow-time position u:
    - Perform range compression via matched filtering by cross-correlating the direct and reflected signals recorded at position u along the aperture, giving a range profile, $S_M(\tau)$.
    - Calculate R_B, the baseline distance from the transmitter to the receiver at position u along the aperture.
    - Define a target scene and a grid of cells representing the target scene.
    - For each cell, i, j, in the grid:
        - Compute the range from the grid cell to the transmitter, $R_T[ij]$, and to the receiver, $R_R[ij](u)$.
        - Calculate the sampling time, $\Delta_{ij}(u) = (R_T[ij] + R_R[ij](u) - R_B)/c$.
        - Use the sampling time to sample the range profile using linear interpolation.
        - Apply the phase function correction $\mathrm{e}^{-j\omega_c\Delta}$.
    - Coherently sum the resulting image with the image produced at the previous u position.

3.9 Experimental Ground Campaign

An experimental ground campaign was designed for DVB-T SAR image formation. The purpose of the ground campaign was to verify the ability of the receiver and image formation algorithms to produce SAR imagery from DVB-T signals, as well as the preliminary investigation of SAR imagery, by visually identifying returns from known objects within the image scene, forming the basis of a qualitative analysis. The human brain is remarkably good at segmenting and characterising image textures within an image given the appropriate context [38], i.e. given an aerial image of the target scene with known and recognisable targets, returns in the corresponding SAR imagery can usually be classified.

3.9.1 Scene Location

The location chosen for the ground trials was Bartley Reservoir due to its ideal imaging geometry, as well as its close proximity to the University of Birmingham. Figure 3.13 shows an aerial view of the reservoir with the aperture, transmitter direction, and imaging direction indicated. The total track length provided by the straight road running along the reservoir is approximately 500 m, while the full length of the reservoir is 1.05 km, and the widest point is 540 m across. The Sutton Coldfield transmitter, used for these trials, is 21.67 km away from the centre of the track. By taking measurements along the straight road running perpendicular to the reservoir, this location provided a near quasi-monostatic geometry with an angle between the aperture and a line connecting the transmitter to the aperture centre of 73 degrees, corresponding to a bistatic angle of 16 degrees at the centre of the reservoir.

Since the aim for this first measurement campaign with the DVB-T receiver was to verify the functionality of the receiver system and validity of the image formation

Figure 3.13: Image showing the synthetic aperture relative to the transmitter and Bartley Reservoir

algorithm, the measurement scenario was kept as simple as possible to mitigate errors. A quasi-monostatic geometry was chosen with a straight aperture which could be easily replicated by the vehicle for multiple measurements. The straight road used as the aperture also allowed for some form of verification of the positioning system, which was expected to record a straight line trajectory with a near-constant velocity. The Bartley Reservoir location, as well as providing a straight track for the aperture, was chosen as it presented a number of potential targets immediately surrounding the reservoir, as shown in Figure 3.14.

The proposed image scene is a 5 km by 4 km rectangular area, centred around the point (52.4151, -2.0166) in latitude, longitude coordinates. Using a Cartesian coordinate system, where the x-axis aligns with the down-range direction, and the y-axis aligns with the track/ cross-range direction, with the centre of the track at the origin, the proposed image scene can be defined as a rectangle with the coordinates shown in Table 3.5. These dimensions were chosen so as to encompass the reservoir, as well as a significant area around the reservoir, so that a variety of potential reflectors could be imaged and analysed.

Figure 3.14: Image showing the target scene containing Bartley Reservoir as well as the surrounding area

Figure 3.15 shows an elevation map of the target scene with the reservoir location indicated with a black outline. The track is at an elevation of 186 m above mean sea level, while the average elevation is 192 m and the maximum elevation is 282 m at the coordinates (52.4164, -2.0128). Because the accuracy of the elevation map was unknown, the data was verified by cross-checking multiple elevation points with a second source, in this case Google Earth. It was found that the tested elevation map points points were within 1 meter of those reported by the second source, verifying the validity of the elevation map.

The elevation data was extracted from Bing Maps using http requests to their REST API [**noauthor_get_nodate**]. Each request allowed the download of 1024 evenly spaced elevation points in a 32 by 32 grid defined by a bounding box using latitude and longitude coordinates. To increase the resolution of the elevation map, the scene was split into a 4 by 4 grid of 16 sub-regions and elevation data was downloaded for each region and then combined together for a map with 128 by 128 elevation points. Since this is below the resolution of a typical processed SAR image, the elevation map was up-scaled by interpolating the points.

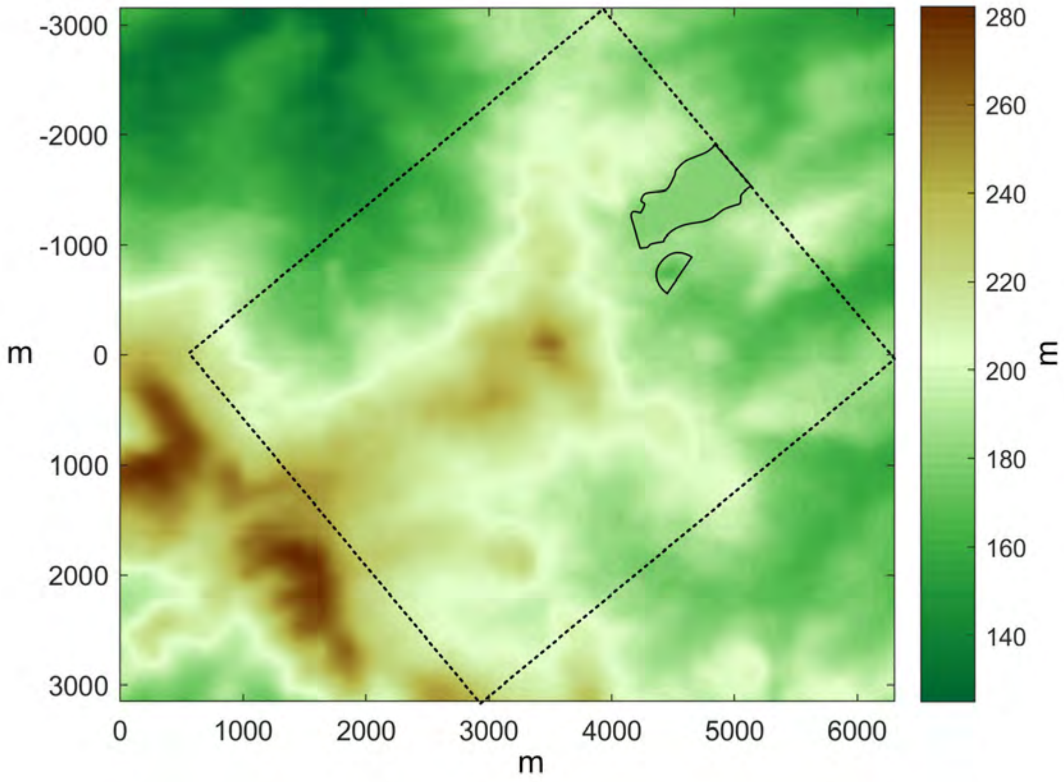

Figure 3.15: Elevation map of the area surrounding the target scene. The target scene location is outlined with a dashed black line while the reservoir location is outlined in a solid black line.

Table 3.5 outlines the important parameters of the target area, while Figure 3.16 shows an aerial image of Birmingham, with markers indicating the locations of the Sutton Coldfield transmitter and Bartley reservoir. The distance and angle from the aperture centre to the transmitter is indicated, as is the image scene area.

Table 3.5: Table of image scene parameters

Parameter	**Value**	**Units**
Width	5	km
Height	4	km
Bottom Left	(52.443, -2.011)	(lat, lon)
Top Right	(52.387, -2.022)	(lat, lon)
Aperture Start	(52.432, -1.993)	(lat, lon)
Aperture End	(52.429, -1.988)	(lat, lon)
Aperture Centre	(52.430, -1.990)	(lat, lon)
Distance to Transmitter	21.67	km
Angle to Transmitter	73	degrees

Figure 3.16: Aerial image showing the location of the target scene and transmitter, with a distance between them of 21.67 km

3.9.2 Receiver System

At the heart of the radar receiver used for the first ground trials was a National Instruments (NI) Universal Software Radio Peripheral (USRP) 2950R. This is a software defined radio that was controlled by a laptop and was programmed to receive a single DVB-T channel with a carrier frequency of 650 MHz on two receiving channels, with an internal clock synchronised to a 10MHz reference provided by GPS. For each receiving channel the input signals were Digitally Down-Converted (DDC) through a 200 MHz Analog to Digital Convertor (ADC) to an I/Q baseband with a 40 MHz bandwidth. The digital baseband signals were transferred to the control laptop via a high-speed Peripheral Component Interconnect Express (PCIe) connector (250 MBps) and then recorded to a Solid-State Drive (SSD) as complex values with single-precision floating point numbers for the real and imaginary parts. The signals from the two input channels were recorded to the SSD in an interleaved format, and the drive was set up in a RAID 0 configuration for fast recording, but no backup partition for data recovery.

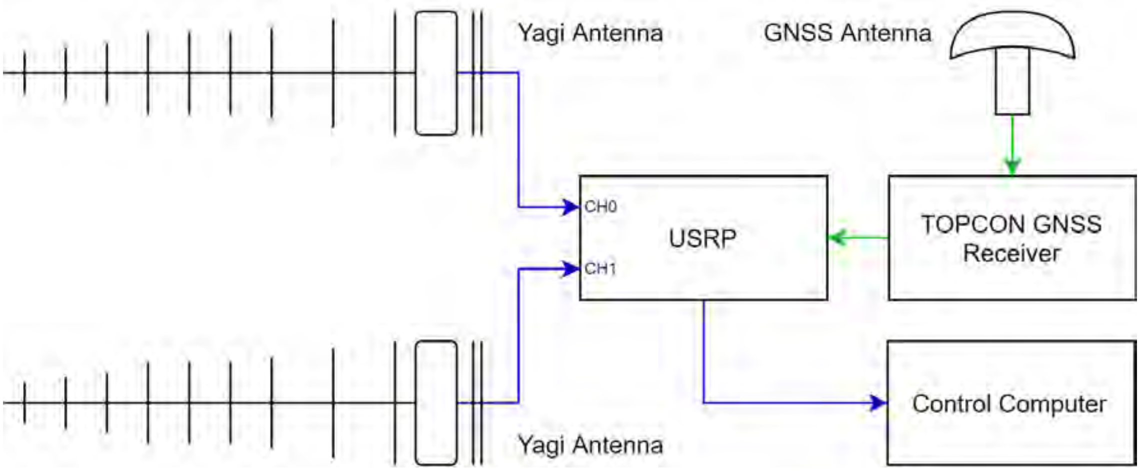

Figure 3.17: Hardware block diagram for the initial receiver system

This meant that recorded data needed to be manually backed-up during trials to reduce the risk of data loss. The control software, used to take measurements, was developed to allow for the sampling frequency, input gain, and centre frequency to be set by the user. In the first iteration of the control software, a measurement was recorded by starting the measurement process with a button and then stopping the process after the desired time had passed. The software would then allow the user to name the produced data file and also provided a timestamp which was then recorded manually in a log book. For later iterations of the software, the start time and duration of a measurement were recorded into the filename of the recorded data.

Table 3.6: Table of specification parameters for the NI USRP 2950R.

Parameter	**Value**
Number of channels	2
Frequency range	50 MHz to 2.2 GHz
Frequency Step	$<$ 1 KHz
Gain range	0 dB to 37.5 dB
Gain step	0.5 dB
Maximum input power (P_{in})	-15 dB

Receiver Antennas and Positioning System

The initial choice of receiver antennas were two Yagi-Uda antennas with a gain of 8 dBi, a -3dB beamwidth of 20 degrees, and an overall length of 1.2 m per antenna. The antennas were connected to the receiver via two 7.5 m long Radio Frequency (RF) cables with a measured loss of 3 dB at DVB-T frequencies.

The method of backprojection for SAR image formation requires accurate positioning of the radar platform in relation to the scene. For the first set of ground trials a TOPCON NET-3GA full-spectrum GNSS receiver was used in conjunction with a separate GNSS antenna mounted to the roof of the vehicle. The TOPCON device provided accurate positioning data from GPS, GLONASS and Galileo satellite constellations at a 100 Hz refresh rate, and was battery operated. This positioning data was stored on the internal memory of the device to be extracted, matched to the received radar data, and used for image formation.

During the measurement process, the GNSS receiver was set up to record throughout the whole trial, while the individual radar receiver measurements were manually triggered and timestamped due to the size of the recorded data files and the constraint on the memory available for storage. Because the positioning data was recorded separately to the radar data, measurements had to be matched to the corresponding positioning data using the recorded timestamps. While the positioning timestamps were accurate to the nearest 100th of a second, the radar receiver control software produced timestamps to the nearest second, resulting in a precision error of ±0.5 s.

3.9.3 Vehicle Demonstrator

Figure 3.18 shows a diagram of the vehicle demonstrator. Two Yagi antennas, one for the radar channel and another for the reference channel, were mounted on 2 m poles atop the vehicle, a Land Rover Discovery 2, providing a total antenna height of 4 m above ground level. This height was necessary as the location chosen has a 2 m wall along the roadside in the imaging direction. Due to the quasi-monostatic nature of the scene geometry, the antennas were mounted back-to-back and in such a way as to not protrude from the vehicle. Therefore, no matter which direction travelled along the road, one antenna pointed towards the imaging direction for the radar channel while the other pointed towards the Sutton Coldfield Transmitter for reference channel. The direction of travel and which of the antennas was recording the direct signal was recorded in a log book.

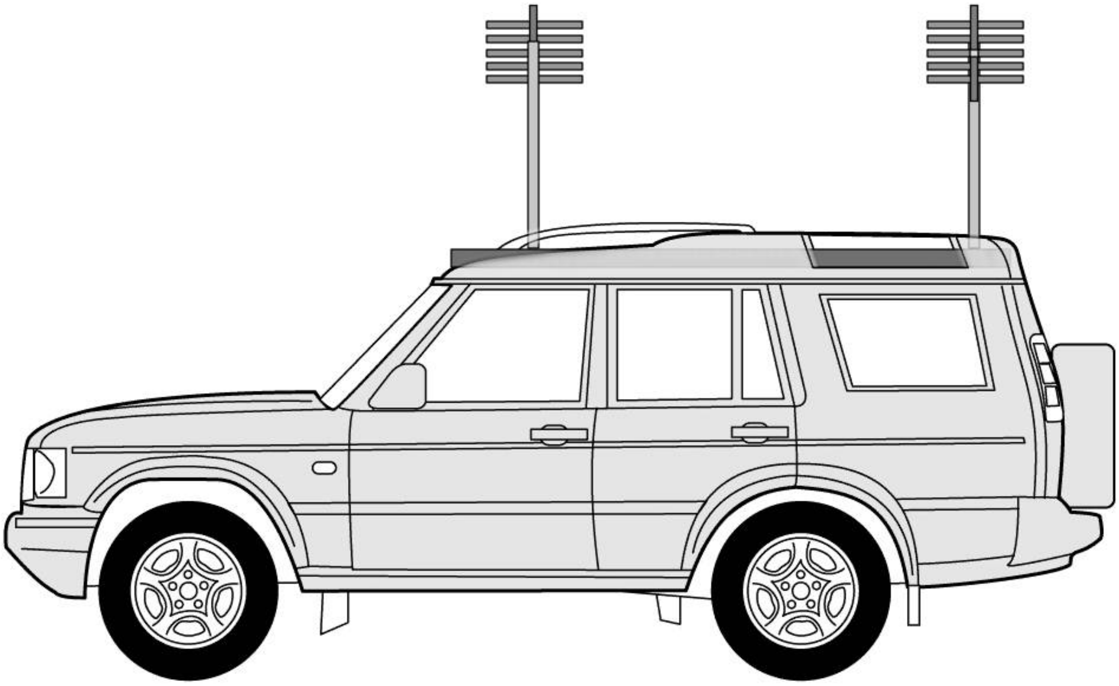

Figure 3.18: Diagram showing the side-view of the vehicle demonstrator

3.10 Data Acquisition

The Land Rover Discovery with the mounted antennas and receiver system were driven along the Bartley Reservoir road at a speed of 30 mph (48 kph) and as straight as possible, while a second person operated the control laptop to start and stop the recording of a measurement. The vehicle was then turned around and the process repeated, but with the vehicle travelling in the opposite direction. This meant that the antenna recording the direct signal and the antenna recording the reflected signal would swap for each measurement. In total, four different measurements were recorded on 17 March 2017 in good clear weather conditions. Table 4.4 summarises the measurements, including which input channel received the direct signal and which input channel received the reflected signal.

Table 3.7: Table of measurements.

Measurement	**Start Time**	**Recording Length (s)**	**Direct Signal Channel**
1	16:40:12	46.19	CH 0
2	16:41:47	35.86	CH 1
3	16:43:32	42.55	CH 0
4	16:45:17	46.83	CH 1

The start times and recording lengths were extracted from the USRP, which uses a GPS disciplined temperature-controlled crystal oscillator, and gives a readout to the nearest second. The direct signal channel indicates which of the USRP input channels, and thus which receiving antenna, was pointed towards the DVB-T transmitter, and by inference which receiving antenna was pointed towards the scene. The TOPCON GNNS receiver was set-up and started before the radar measurements were taken, and positioning data was recorded to the internal memory of the TOPCON receiver for the entire duration of the campaign.

3.11 Data Processing

For each measurement, the radar data required a series of data processing steps before the image formation algorithm could be used. A block diagram describing the data processing stages is shown in Figure 3.19. The first stage of data processing after acquisition was to crop the recorded measurements. For each measurement, the date, time, and duration of the measurement are stored in the file name. This information is parsed from the filename and used to extract the relevant positioning data for the measurement from the full set of positioning data from the GNSS receiver. A sub-aperture is extracted from a measurement by specifying a centre time, relative to the start of the measurement, and a duration. For example, a centre time of 20 seconds and a duration of 4 seconds specifies an aperture which begins at 18 seconds into the measurement and ends at 22 seconds. The data from the radar receiver is stored as interleaved double precision values for I and Q for each receiving channel. So in every block of four values, representing a two-channel complex sample, the first value is the in-phase component of channel 1, the second is the quadrature component of channel 1, followed by the in-phase component of channel 2 and the quadrature component of channel 2. The I and Q components are combined into a complex sample and the samples are extracted into two identical length arrays, one for each channel. The setup of the receiver and the direction of the antennas determines which channel corresponds to the reference and which one correspond to the surveillance.

The second stage of data processing after cropping was the synchronisation of the measurements with the corresponding positional data from the TOPCON GNSS receiver. Proprietary software was used to extract the positioning data in tabular format into text files. The data table contained columns for time, recorded as a timestamp, and position, recorded as x, y, z coordinates in an Earth Centred Earth Fixed (ECEF) coordinate system. The start time and duration of the radar data, recorded from the USRP, was used to extract the corresponding positioning data. The recorded timestamps were then used to synchronise the radar measurements with the positioning measurements. This was possible because both the radar receiver clock and the GNSS receiver clock were synchronised via a 10 MHz reference provided by GPS.

The third stage of data processing was the transformation of the positioning data from ECEF to a local coordinate system which was defined by the chosen sub-aperture. For a particular aperture, the extracted positional data is used to define a local coordinate system where the aperture direction is defined as the cross-range direction, the altitude direction is unchanged from the geodesic coordinate system used by the GNSS receiver, and the down-range direction is perpendicular to the cross-range and altitude directions. Positional data is then converted via an affine transform into the local coordinate space with the aperture centre as the origin. Figure 3.20 shows a side-by-side comparison of the aperture, from a top-down perspective, as recorded from the GNSS receiver in geodesic coordinates, and after the transformation to the local coordinate frame.

The fourth and final stage of data processing before backprojection was the smoothing of positioning data. Positional errors from the GNSS receiver can be mitigated by smoothing the recorded positional data and assuming that the radar receiver moved along a straight track. Figure 3.21 shows a side-by-side comparison of the platform trajectory in the aperture direction as a function of time before and after the process of smoothing. The smoothing was performed by fitting the aperture trajectory with a straight line and using the line as the aperture.

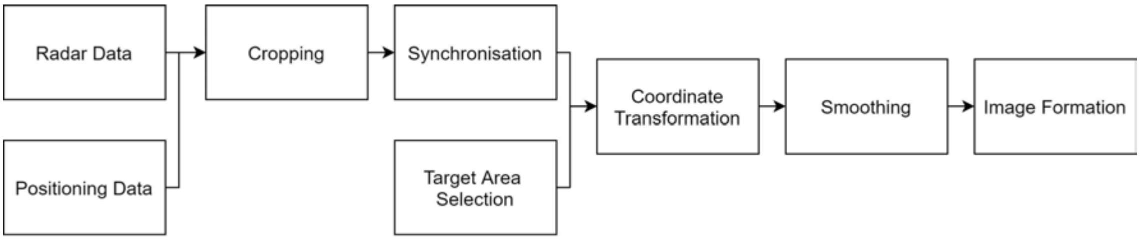

Figure 3.19: Block diagram showing the data processing stages

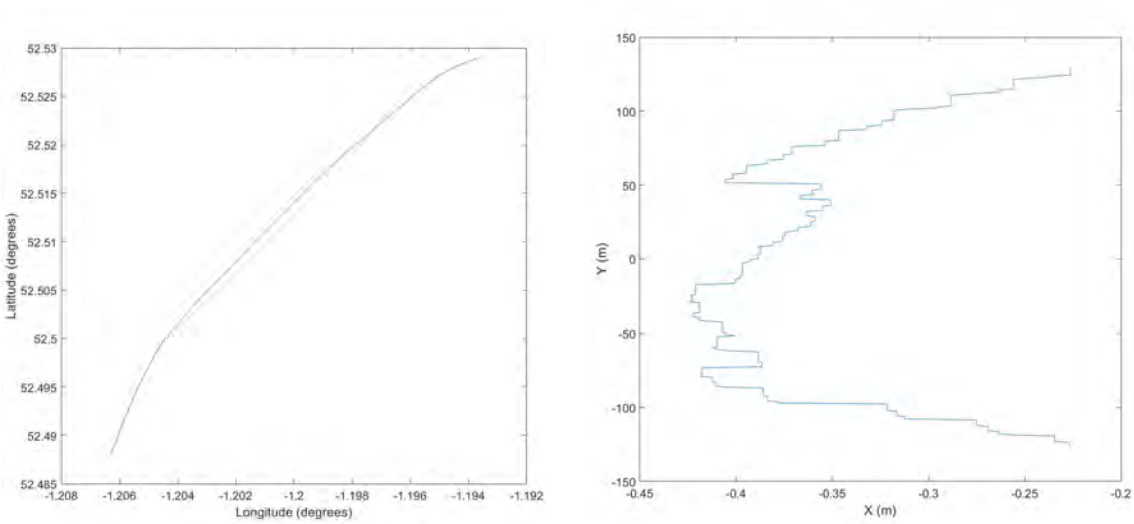

(a) (b)

Figure 3.20: Graphs showing a top-down view of the synthetic aperture in (a) a global geodesic coordinate system, and (b) in a local coordinate frame

3.12 Ground Trial Results

Due to the accumulation of motion errors over long apertures, only a quarter of the full aperture could be processed into a focused image. Figure 3.22 shows an example SAR image produced from the full data set, which corresponds to the last quarter of the aperture from measurement 4 from Table 4.4, corresponding to an aperture of approximately 100 m. Table 3.8 shows the aperture parameters. For this measurement, the vehicle was travelling from left to right with respect to the aperture in Figure 3.13.

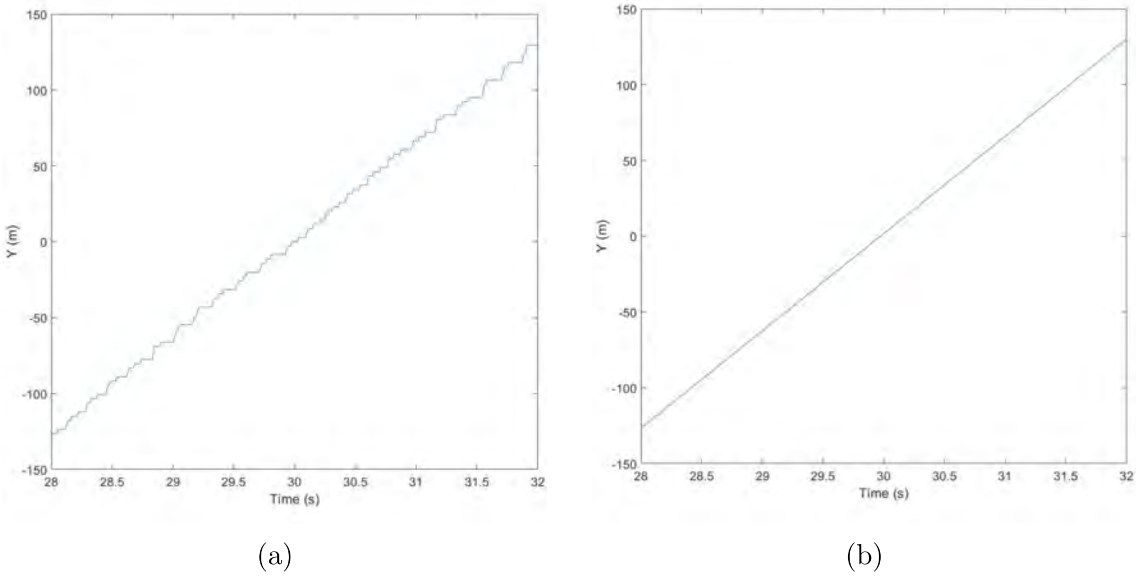

(a) (b)

Figure 3.21: Graphs showing the local y position of the receiver (a) before smoothing, and (b) after smoothing

3.12.1 Ground Truth Verification

The SAR images were evaluated by visually inspecting known objects to determine how well the image was focused. Figure 3.23 shows the same SAR image superimposed onto an aerial photograph of the image scene extracted from Google Earth. An initial visual inspection reveals a good coincidence between reflectors in the SAR image and objects within the scene. Figure 3.23 also shows six sub-regions of the SAR image, each corresponding to an object or group of objects with distinct reflection properties making them distinguishable in the SAR image.

There are a number of clearly visible large scale features present in the image result. Firstly, a partial outline of the reservoir can be seen, with the lower section of the reservoir having a lower intensity than the upper section. This is expected due to the position of the sub-aperture and the relatively narrow 20 degree beamwidth of the Yagi antennas.

Secondly, between 0 - 2.5 km, returns appear to follow the boundaries of fields within the scene. This is due to the presence of trees and hedge rows that often line the

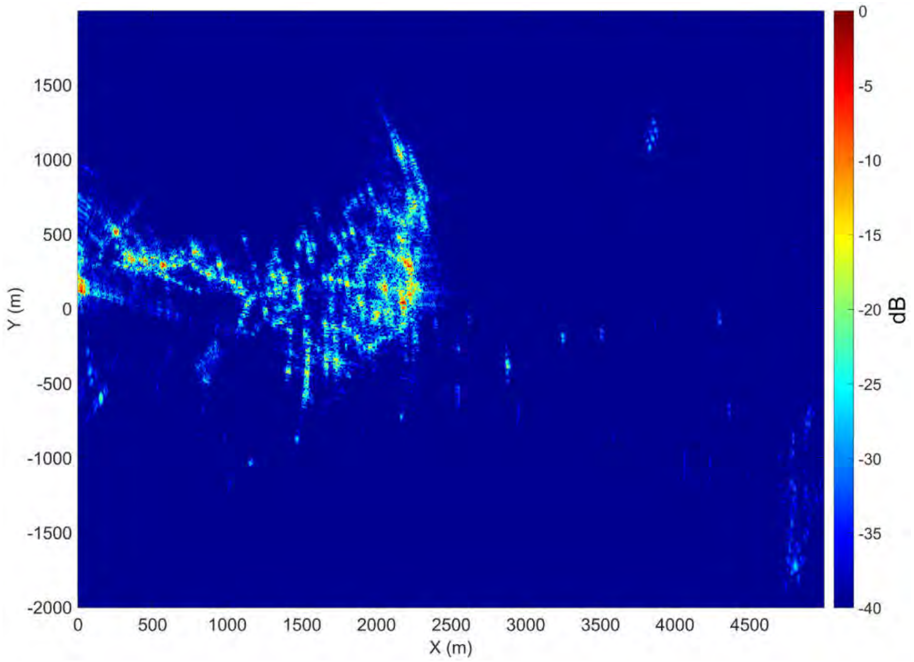

Figure 3.22: SAR image of last quarter aperture from measurement 4

boundaries between adjacent fields. As can be seen in Figure 3.24c, which shows an enlarged view of a sub-region of the image, the returns from a small forested area are some of the strongest returns in the image.

For each result, the origin of the coordinate system used for image formation was taken as the centre of the aperture, with the x-axis pointing perpendicular to the track in the range direction, and with the y-axis pointing along the track in the cross-range direction. The dynamic range of the images was clipped to -40 dB for easier visual inspection of the results.

Table 3.8: Table of aperture parameters

Parameter	**Value**	**Units**
Aperture Length	100	m
Distance to Transmitter	21.67	km
Aperture Start Location	52.4293, -1.9876	latitude, longitude
Aperture End Location	52.4300, -1.9888	latitude, longitude

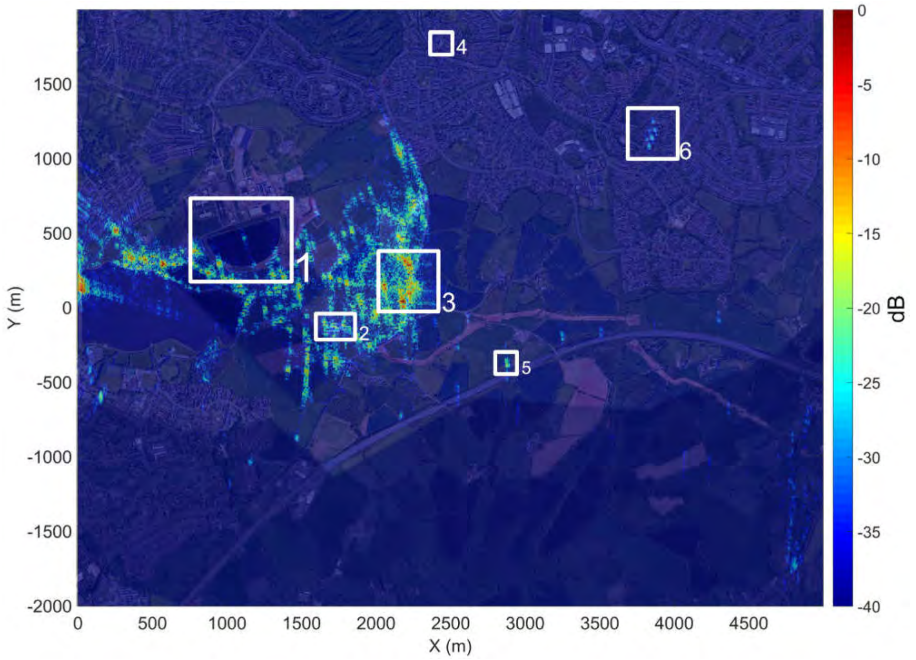

Figure 3.23: SAR image overlaid with aerial image and with six regions highlighted (white rectangles)

3.12.2 Imaging Algorithm Validation

The results from the first set of ground trials were used to experimentally verify the imaging algorithm described in Section 3.8. While the overall image appears to have a good correspondence with the ground truth provided by the aerial imagery, a series of smaller regions were identified and digitally magnified for a closer inspection. Figure 3.24 (a)-(f) shows magnified views of the six regions of interest, numbered 1 to 6, each presented adjacent to the corresponding close-up aerial view of the same area.

(a) Small reservoir (b) Farmhouse

(c) Forest (d) Church

(e) Pylon (f) High-rise buildings

Figure 3.24: Sub-regions of figure 3.23

(a) The first area encompasses a smaller reservoir located next to the Bartley reservoir. This smaller body of water is distinctively man-made in shape, and contains a walkway or land bridge splitting it in two. The distinctive shape makes it easy to identify on SAR imagery and can thus be used for verification and alignment when superimposing aerial imagery atop of SAR imagery for comparison purposes.

(b) The second area is a group of farm buildings surrounded by fields. This target area can be used to investigate the contrast between large building structures which are expected to be quite reflective to DVB-T signals, and rural fields which are expected to be less reflective.

(c) The third area is a region of forest next to a road and also surrounded by fields. This area allows for the investigation of returns from wooded areas in contrast to fields and buildings.

(d) The fourth area is a built-up region with a church, representing one of the few tall structures present in the imaging scene. Due to the shape and size of the church spire, it is expected to be highly visible in a SAR image.

(e) The fifth area contains an electricity pylon within a field and next to a motorway. Due to the size and metallic material of an electricity pylon, the region is expected to be highly visible in a SAR image. There are a row of electricity pylons within the image scene that run nearly parallel to the motorway.

(f) The sixth region contains three high-rise buildings in an urban environment. The unique architecture of these building provides an almost corner-reflector-like target and is expected to be visible within a SAR image of the scene.

Due to the UHF frequencies of DVB-T, it is possible that the transmitted or reflected signals could diffract and allow the imaging of objects in regions of the imaging scene that would otherwise be obscured by terrain or even buildings. Using elevation data, the possibility of signal diffraction was investigated by comparing the elevation of the receiver to the topography of the target scene. Figure 3.25 shows a DVB-T SAR image from another measurement of the ground campaign projected onto a surface plot of the topography of the landscape. From the elevation map in Figure 3.15, the highest point, which is a hill located approximately 2 km down range from the aperture, is at an elevation of 280 m. The landscape behind the hill is 40 to 60 meters lower in elevation and therefore explains the lack of returns in this region of the corresponding SAR imagery. However, some targets, including a line of electricity pylons can still be observed, demonstrating the potential for "beyond the hill" vision due to diffraction of the UHF DVB-T waves.

3.13 Conclusions

This chapter has investigated the theoretical properties of a DVB-T SAR system in order to ascertain its practical feasibility. A power budget analysis was performed

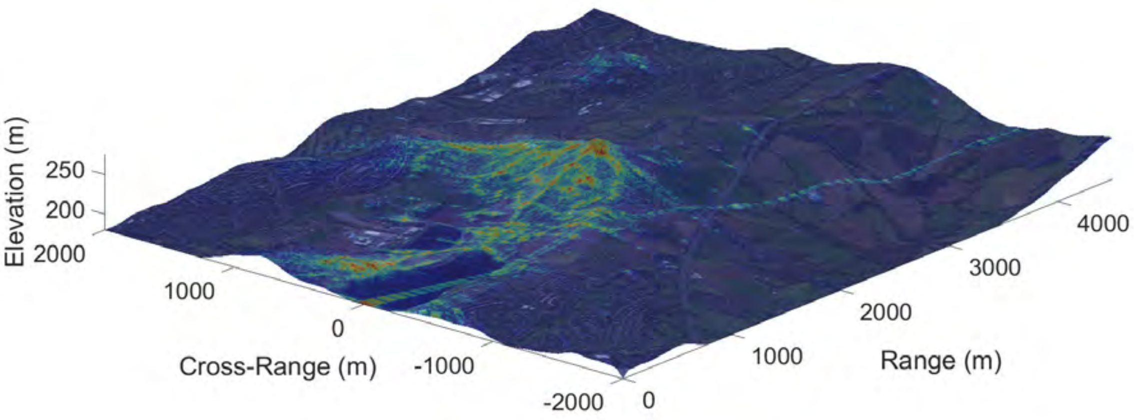

Figure 3.25: DVB-T SAR image of Bartley Reservoir projected onto a topographic surface plot of the target area

and showed that, due to the power of DVB-T transmitters, a SAR receiver can operate on a ground-based platform, an airborne platform, and a satellite platform in low-earth orbit. The theoretical parameters of a DVB-T SAR system were investigated by plotting the range resolution as a function of the range from the receiver to the target, and the system SNR and sensitivity as a function of the range from the transmitter to the receiver. In addition, the sensitivity of a DVB-T SAR system was shown as a function of transmitter to target range.

The effects of multiple transmitter interference were investigated with the use of a DVB-T SAR computer simulation of a point target illuminated by two transmitters, the parameters of which were taken from real-world examples. It was found that, in the UK where a multifrequency network is used, multiple transmitters do not affect the resulting SAR imagery in comparison to a single transmitter. Additionally, the properties of DVB-T signals and their effects on SAR imagery, specifically the presence of pilot carriers in DVB-T signals, were investigated. Through a mathematical analysis, it was shown that the process of image formation suppresses the ambiguities caused by the pilot carries, and thus does not affect the resulting SAR imagery.

This chapter also showed the development of a DVB-T SAR receiver system, as well as an algorithm for DVB-T SAR image formation, both verified with a ground-based measurement campaign. The Bartley Reservoir was chosen as a suitable target location, providing a straight road as a synthetic aperture for a vehicle platform, as well as a quasi-monostatic configuration with the Sutton Coldfield transmission station 21.67 km away. The receiver system, including a TOPCON GNSS receiver, was placed within a vehicle, with two connecting Yagi antennas mounted to the roof. A series of four measurements were conducted at the target location and DVB-T SAR images were formed via a series of post-processing steps followed by an image formation algorithm based on backprojection. The generated DVB-T SAR imagery was verified against ground truth aerial imagery of the target scene and sub-regions of the scene were magnified and compared. The strong correspondence between SAR and ground truth imagery provided validation of the receiver system and the image formation algorithm. In addition, with the use of an elevation map of the target area, indirect propagation of the DVB-T signal was demonstrated with the identification of returns from a series of electricity pylons, which are obscured from the receiver by the topography of the scene.

Chapter 4

Quasi-monostatic Airborne Measurements

4.1 Introduction

This chapter presents the next stage in the systematic study of DVB-T SAR. The feasibility of DVB-T SAR and its application to ground-based measurements was shown in Chapter 3. This chapter presents the development and results of a quasi-monostatic airborne measurement campaign for DVB-T SAR image formation. The aim of the campaign was the further understanding of DVB-T SAR image characteristics in an ideal quasi-monostatic geometry. This chapter is split into two parts, the first detailing the development evolution of the initial receiver system, shown in Chapter 3, and the second detailing the planning, execution, and analysis of a quasi-monostatic airborne measurement campaign.

For the analysis of results, the quasi-monostatic DVB-T SAR imagery is compared with ground truth aerial imagery in order to confirm the validity of the results and the airborne receiver system. It also investigates the kinds of returns observable from known ground targets. In addition, a comparison of range compression techniques between auto-correlation and cross-correlation of the direct and reflected signals is shown, as well as a point spread function analysis of a wind-turbine target. Moreover, the effects of noise on the direct signal receiver channel are investigated in order to analyse the long-range performance of the system. Finally, the effect of extending the integration time during image formation, and the corresponding cross-range resolution performance, is shown.

4.2 Airborne Demonstrator Development

The design of the receiver system is based in part on the intended application of the system. An airborne system has different requirements to a system mounted on a vehicle and used on the ground. However, the fundamental components of a DVB-T SAR system are the same. In Chapter 3 the design and development of an initial DVB-T receiver system was shown, which used large Yagi-Uda antennas and a TopCon GPS receiver. The choice of components for the initial receiver design were appropriate for use in a ground-based measurement campaign in which the receiver system could be placed within a vehicle with the antennas mounted to the roof. In contrast, to avoid the need for safety licensing, which would add time and cost to the project, the airborne receiver needed to be mounted entirely within an aircraft. To conduct airborne experiments, a demonstrator system which could be used on a small light aircraft needed to be developed.

4.2.1 Aircraft

The aircraft used for all flight trials described in this thesis was a Cessna 172N SkyHawk, shown in Figure 4.1a. This model of aircraft was chosen due to its high wing placement above the side-windows, allowing for receiving antennas to be mounted within the aircraft pointing down out of the windows and towards the ground. The Cessna 172N aircraft used for both of the airborne campaigns were hired from a company called Almat Aviation, which is based at and operates from Coventry Airport. A typical Cessna 172N has a max range of 1185 km and a top speed of 84 m/s. The aircraft has four available seats, two in the front and two in the rear, as well as a rear luggage compartment behind the rear seats and into the tail of the aircraft. The vibration resistant case, used to house the receiver equipment, was too large to fit within the luggage compartment, and so had to be secured across the rear seats of the aircraft, as shown in Figure 4.1c.

4.2.2 Receiver Requirements

With the type of aircraft chosen, the receiver development began by analysing the resulting system requirements:

1. Self-contained unit that could be carried within the aircraft with both a pilot and an operator.
2. Able to record and store raw radar data from a single DVB-T channel at 650 MHz from two antennas, one for the direct signals from the transmitter and the other for the reflected signals from the scene.
3. Able to record high precision and high accuracy GNSS positioning data at the same time as recording the radar signal data.
4. Should be easy to operate with minimal points of failure.

These requirements guided the design and development process of the airborne demonstrator receiver system. The choice of antennas, front-end chain, and GNSS receiver were all changed for the airborne receiver system. Other than the antennas and control laptop, the receiver equipment was fitted within a vibration resistant box which was chosen to fit on the rear seats of the Cessna aircraft. The patch antennas were affixed to each end of the box using strong suction-cup clamps. These clamps, designed to attach objects to cars, have an adjustable clamp on one end and a strong vacuum clamp on the other, with a hinge joint in the middle, see Figure 4.1d. The clamps were attached to the metal frame of the vibration resistant box and the suction ends were attached to each of the patch antennas. The hinge joints of the clamps allowed the patch antennas' positions to be adjusted to optimise the antenna area visible through the window, and to point the antennas towards the ground.

4.2.3 Patch Antenna Development

Because the entire receiver system had to be mounted within a small Cessna 172N aircraft, the use of large Yagi antennas used for the initial ground trials, with a length of 1.2 m each, was not possible. It was also not possible to mount anything to the outside of the aircraft due to safety regulations and licensing, however, it was determined that a patch antenna would fit within the windows of the aircraft while providing the necessary gain. Therefore, three patch antennas were developed and manufactured by the University of Birmingham antennas group, two to be used during trials and a spare. The patch antenna design was based on a modified version of a broadband patch antenna for DVB-T passive radar presented by Rosado-Sanz et al [59]. Figure 4.2a shows a CST model of the patch antenna design, while Figure 4.2b shows a photograph of one of the three manufactured antennas. The antennas were designed and built to fit the rear-windows of the aircraft and to receive DVB-T signals with a centre frequency of 650 MHz, covering a bandwidth sufficient to

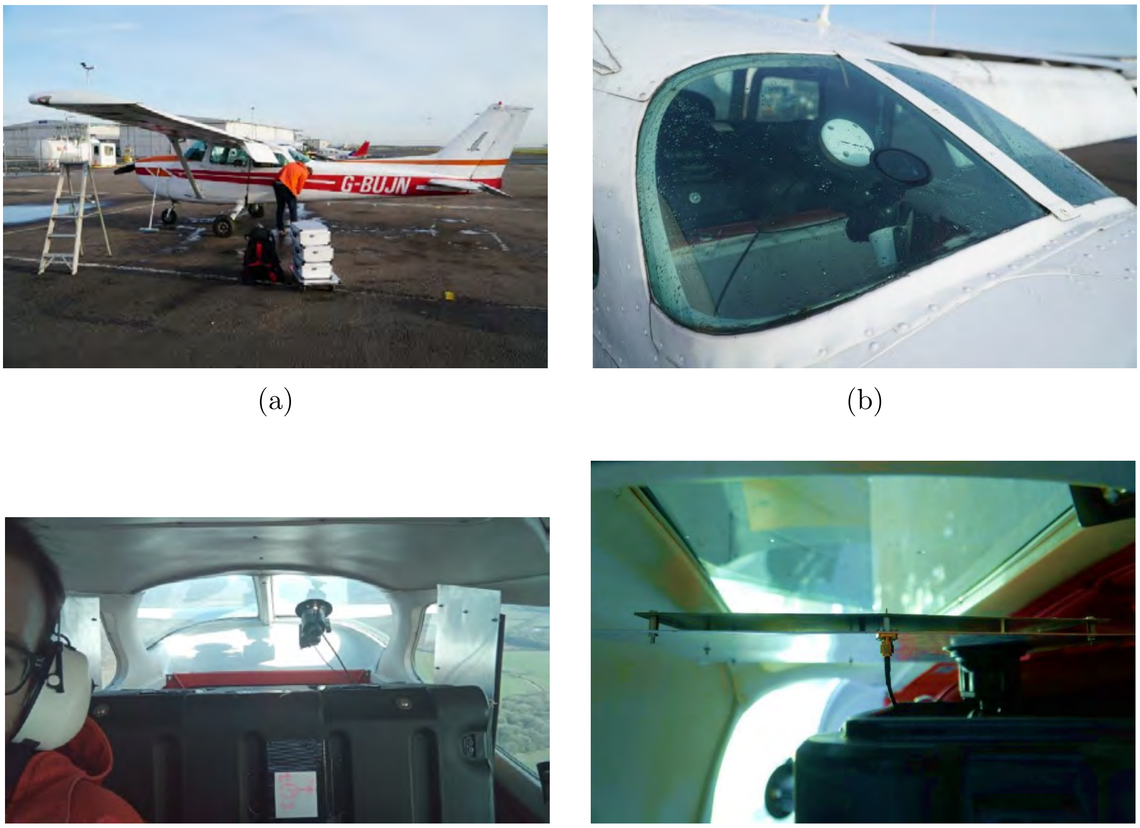

(a) (b) (c) (d)

Figure 4.1: Exterior and interior images of the Cessna 172N Skyhawk aircraft and mounted receiver system used for the quasi-monostatic measurement campaign: (a) Aircraft exterior, (b) GNSS antenna mounted to rear window of aircraft, (c) Receiver system fixed to rear seat of aircraft, (d) Receiver patch antenna looking out of side window of aircraft

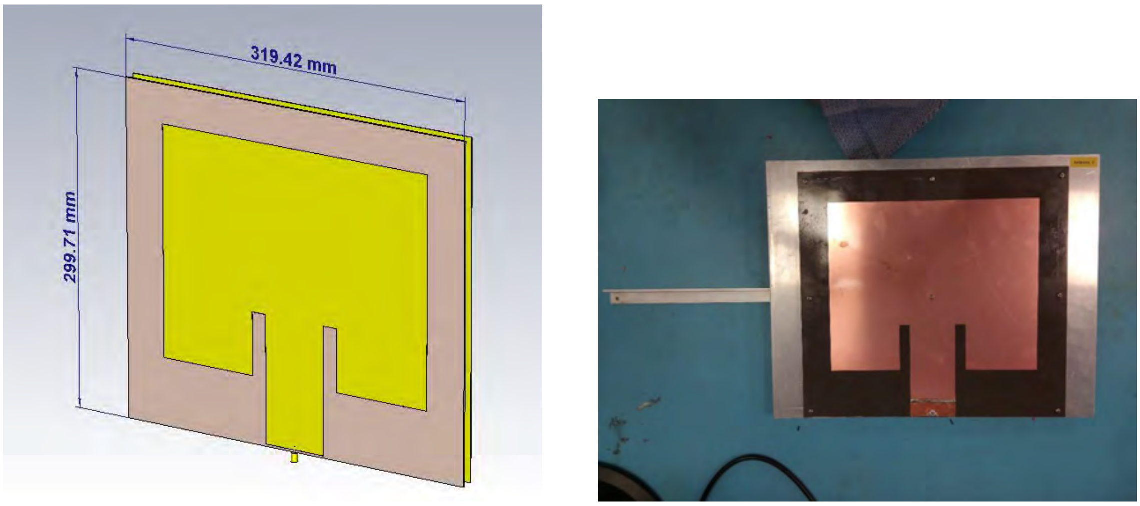

(a) (b)

Figure 4.2: Images showing (a) CST diagram of custom-made patch antenna and (b) an image of one of three constructed patch antennas

receive up to two adjacent DVB-T channels. Whilst the antennas group built the antennas, they did not perform any testing.

Measuring and testing the properties of the constructed patch antennas was non-trivial due to the 650 MHz centre frequency, requiring a large an-echoic environment without any interference signals. Since the University of Birmingham does not possess such an environment, and interference from the Sutton Coldfield Transmitter prevents the possibility of testing the antennas outside, only a relative measurement of gain could be determined by comparing the patch antennas to the Yagi antennas.

Testing of the patch antennas was done outdoors on the roof of the Gisbert Kapp building at the University of Birmingham using the Sutton Coldfield transmitter as a reference signal. Since the environment is not an-echoic, there is a degree of uncertainty in the measurements, and therefore the results shown represent indicative values. Both the new patch antennas and the Yagi antennas were simultaneously pointed towards the transmitter. A portable spectrum analyser was used to measure the DVB-T signal strength from each of the antennas, and by comparing the results, the relative gain of the patch antennas was determined. The obtained results are shown in Table 4.1 and show that the patch antennas have approximately 3 dB more gain than the Yagi antennas. Assuming the quoted gain of 8 dBi from the specification of the Yagi antennas, the patch antennas thus have a gain of approximately 11 dBi. However, it should be noted that the Yagi antennas are matched to a 75 Ohms impedance, while the patch antennas are matched to a 50 Ohms impedance, which may introduce a small error in the power measurements.

Table 4.1: Power measurements of the three patch antennas compared to the gain of a single Yagi antenna.

Antenna	**Patch Gain (dBm)**	**Yagi Gain (dBm)**
1	-31.7000	-34.6542
2	-31.5162	-34.6542
3	-31.2504	-34.6542

The angular pattern of the patch antennas was also measured in the horizontal direction. Each antenna was placed on a rotatable stand and pointed towards the Sutton Coldfield transmitter. A portable spectrum analyser was connected to the antenna being rotated and was used to measure the resulting signal strength. The direction of the transmitter was assumed to be the direction of maximum magnitude as measured by the spectrum analyser. The stand was then rotated in 10 degree increments clockwise and anti-clockwise from the initial position. The results for all three patch antennas are shown in Figure 4.3, where the measured signal strength has been normalised to the maximum value recorded and zero degrees represents the antenna pointed directly towards the transmitter. Using these results, the 3 dB beamwidth of the patch antennas was estimated to be approximately 50 degrees.

From these measurements of relative gain, compared to the yagi antennas already used in the first ground trials, and the 50 degree beamwidth, it was determined that the patch antennas met the requirements for the airborne demonstrator and were incorporated into its design and development.

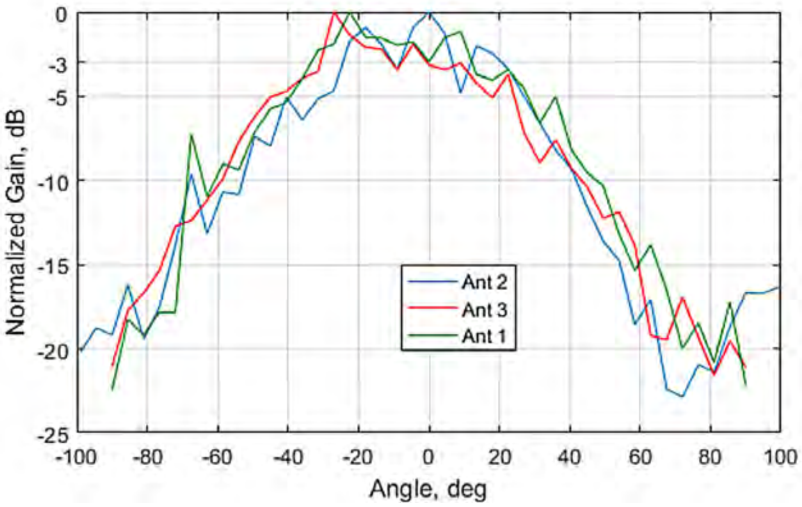

Figure 4.3: Measured angular pattern for the three patch antennas

4.2.4 RF Front-End

For each of the receiving channels of the receiver, an RF front-end chain consisting of a Low-Noise Amplifier (LNA) and a Band-Pass Filter (BPF) were connected at the output of the receiving patch antennas before connecting to the software defined radio. Both the LNAs and BPFs were off the shelf components from Mini-Circuits and were mounted directly to the antenna mounting supports. The LNA was a ZRL-700+, which has a typical gain of 30 dB and a typical noise figure of 2 dB for the DVB-T frequencies received by the patch antenna. The BPF was a RBP-650+, with a pass-band between 624 - 680 MHz with a loss of <7 dB and a stop-band loss of >35 dB. Specifications for the LNA and BPF can be found in Appendix C.

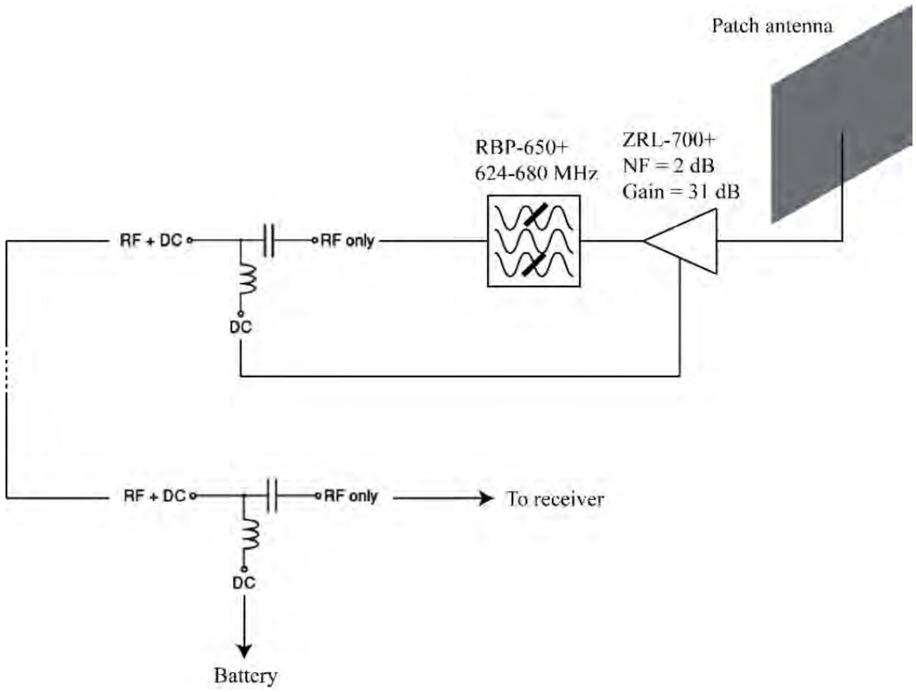

Figure 4.4: Hardware block diagram for RF front-end chain

Figure 4.4 shows a hardware block diagram demonstrating how the RF front-end is connected to the patch antennas, as well as the battery. Two front-end chains were built, one for each of the receiving channels of the USRP. The complete front-end chains were measured using a vector network analyser, and Figure 4.5a shows the magnitude response for each circuit against frequency, while Figure 4.5b shows the phase response.

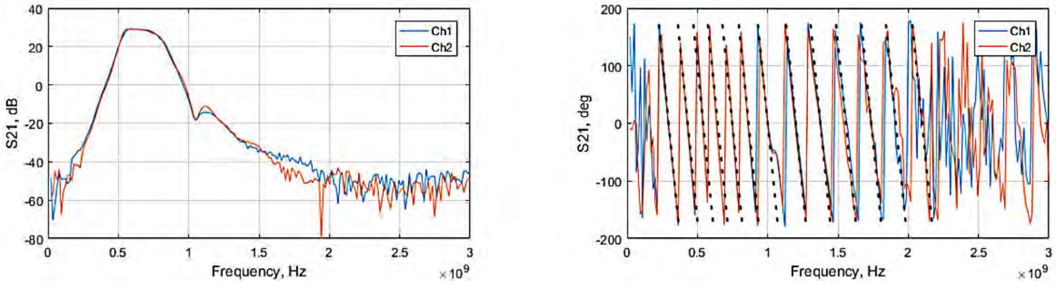

(a) (b)

Figure 4.5: (a) Magnitude response and (b) phase response of the RF front-end chain for two channels

The frequency response of the front-end chain shows a gain of approximately 30 dB across the pass-band region from 624-680 MHz, with the expected 35 dB decrease within the stop band region. The phase response shows a linear relationship from 180 degrees to -180 degrees within the pass-band region of frequencies. These measured values are in agreement with the expected values stated by the manufacturer.

4.2.5 Spatial FOG GNSS Receiver

As well as new receiving antennas, the positioning system used was changed from the TOPCON to the Spatial FOG GNSS receiver built by Advanced Navigation. The primary advantage of the Spatial FOG over the TOPCON receiver used for the first ground trials are its data format, size, and portability. The Spatial FOG receiver transfers positional data via an RS232 connection to the control laptop. The time of the measurement, recorded as a timestamp, and the positional data, recorded as decimal latitude, longitude, and altitude coordinates, are stored in a Comma Separated Value (CSV) format, which is both human readable and easily parsed by the image formation software. As well as positional information, the Spatial FOG also measures and stores kinematic information, including 3-axis velocity, acceleration, and angular velocity, as well as roll, pitch, and heading.

Figure 4.6: Image of the Spatial FOG GNSS IMU receiver

The other main advantage of the Spatial FOG receiver is its accuracy. The Spatial FOG receiver has a horizontal position (latitude, longitude) accuracy of 0.8 m, and a vertical position (altitude) accuracy of 1.5 m, without the use of Real-Time Kinematics (RTK). The receiver has the built in ability to utilise RTK to improve the horizontal accuracy to 0.008 m and the vertical accuracy to 0.015 m. However, RTK requires the use of fixed base-stations which transmit corrections to the receiver. Unfortunately, no public access base stations were available at the locations of the trials and so RTK was not used.

Table 4.2: Table of Spatial FOG parameters

Parameter	**Value**
Horizontal Position Accuracy	0.8 m
Vertical Position Accuracy	1.5 m
Velocity Accuracy	0.007 m/s
Roll and Pitch Accuracy	0.001°
Heading Accuracy	0.05°
Output Data Rate	Up to 1000 kHz
Battery Capacity	> 48 hours

Due to the use of a new positioning system the data processing steps were modified to reflect the different format of the positioning data. As previously stated, the receiver system was synchronised to a 10 MHz reference provided by GPS and produced a timestamp for each measurement to the nearest second. The Spatial FOG receiver produced a more precise timestamp using an internal oscillator, also synchronised to GPS time. Since the timing clocks for each device were synchronised to the same reference, the timestamps could be used to extract the relevant positional information for each measurement.

4.2.6 Airborne Demonstrator Testing and Validation

While the first set of ground trials acted as a test for the initial DVB-T receiver system and image formation processing, the airborne demonstrator receiver was designed to be a robust system with a fast set-up time and a minimal operating difficulty. With the change from Yagi antennas to patch antennas, plus the new RF front-ends, as well as the change from the TOPCON GNSS receiver to the Spatial FOG receiver, a new set of ground based trials was conducted in order to test the airborne demonstrator system.

To test the new system, it was decided that the best approach was to conduct a trial using both the new and old systems for direct comparison. The experimental set-up for the second ground campaign was similar to the first ground campaign. The trial location and target scene was the same, as was the vehicle used, with the same pole mounting points. Two identical Yagi antennas were connected to a USRP via 7.5 m long RF cables, as described in Section 3.9.2, while two identical patch antennas, each with an RF front-end, as described in Section 4.2.3, were connected to a separate but identical USRP with its own control laptop. Both USRP's were synchronised to a 10 MHz reference provided by GPS. The Spatial FOG GNSS receiver was used to record positioning data as it had already been field tested on its own.

Each of the Yagi and patch antennas were mounted onto the same pole atop the Land Rover Discovery, with the antennas facing in opposite directions, as shown in Figure 4.7. This ensured that both antennas would receive DVB-T signals without interfering with the other by recording separate signals. For example, if the Yagi antenna was recording the direct signal, then the patch antenna on the same pole would be recording the radar signal. An identical pole, with a Yagi and Patch antenna mounted to it, was also placed atop the vehicle but facing the opposite direction. This allowed for both the direct and radar signals to be recorded by both the Yagi and patch antennas simultaneously, and without interference.

Figure 4.8 shows the hardware block diagram for the complete setup, showing the configurations for both the patch and Yagi antennas. However, unlike the first ground campaign, the vehicle direction for the second campaign was kept to a single

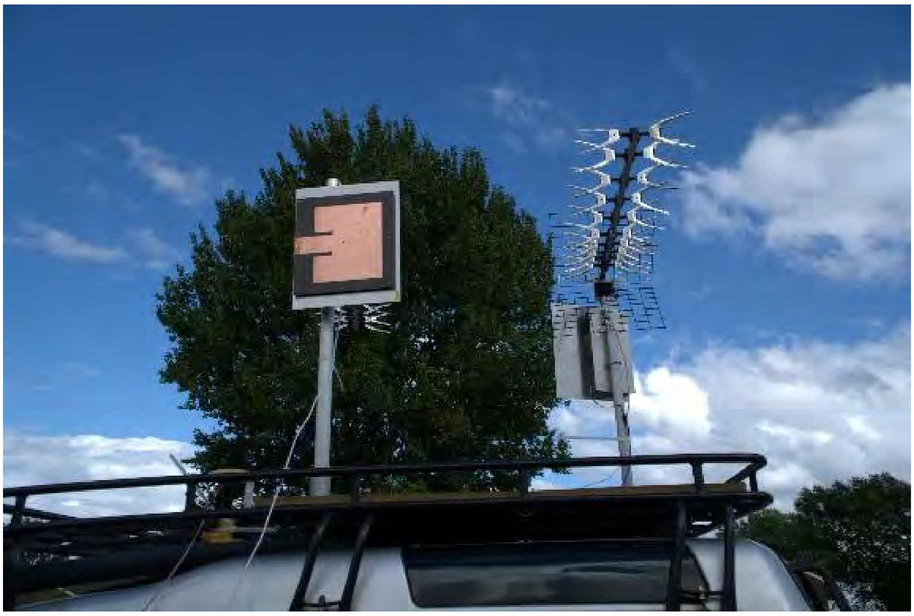

Figure 4.7: Image showing the antenna configuration used to test the airborne receiver system

direction. This allowed the direct channel antenna to be pointed at an angle of 73 degrees, relative to the aperture direction, to stare directly at the transmitting antenna, instead of perpendicular to the vehicle direction of motion, thus ensuring the maximal measured direct signal gain. The Yagi antennas were also fitted with identical front-end chains as the patch antennas, reducing the number of variable parameters, and to ensure that results could be accurately compared.

Figure 4.9 shows a side-by-side comparison of DVB-T SAR images of the Bartley Reservoir target scene. The first image, Figure 4.9a, was generated using the Yagi antennas while the second image, Figure 4.9b, was generated using the patch antennas. The result using the patch antennas appears to produce a sharper image than with the Yagi antennas, i.e. the spread of point-like scatterers within the image is reduced when using the patch antennas as opposed to the Yagi antennas, however this may be coincidental and due to motion inaccuracies. The main difference between the two results is the presence of an artefact within the image produced with the patch antennas. This artefact is due to direct signal interference in which the radar channel receives signals from the transmitter as well as the scene. This effect

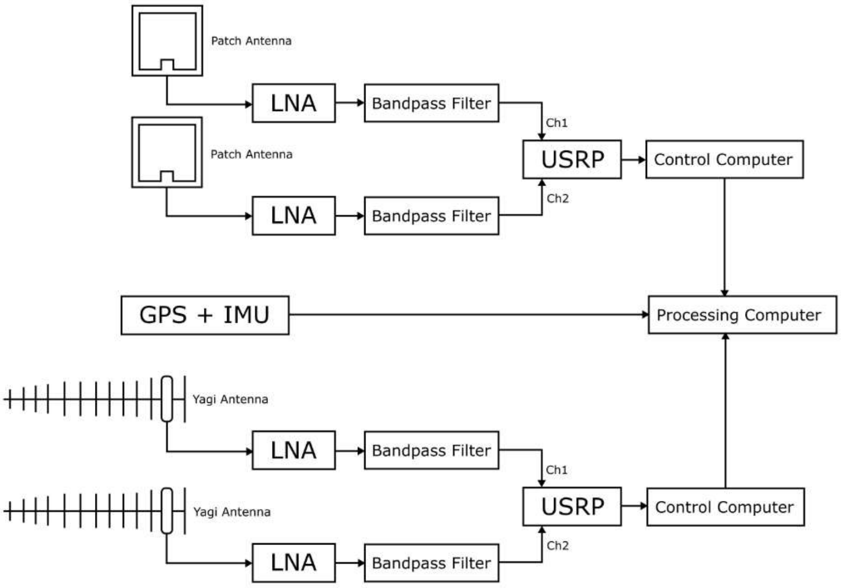

Figure 4.8: Hardware block diagram of dual receiver system used for second ground campaign

is more prominent in images produced with the patch antennas do to the relatively high back-lobe gain in compassion to the Yagi antennas. Overall the images generated with the airborne demonstrator receiver system are comparable to the images generated with the ground-based receiver system and therefore confirm its validity.

4.3 Quasi-monostatic Airborne Experimental Campaign

With a flight-ready receiver system developed, an experimental campaign was designed for quasi-monostatic airborne DVB-T SAR image formation. In this case quasi-monostatic refers to a geometry where the bistatic angle is less than or equal

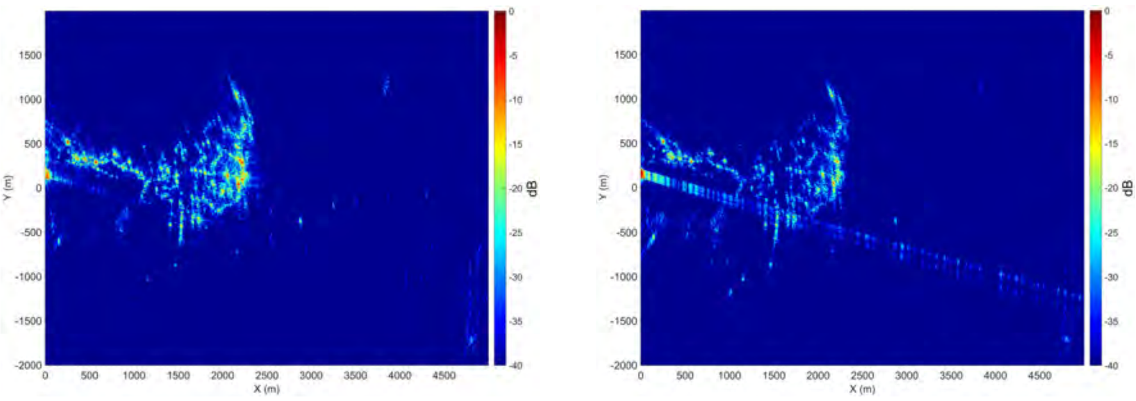

(a) (b)

Figure 4.9: DVB-T images of Bartley reservoir target area using (a) the initial receiver system utilising Yagi antennas and TOPCON GNSS receiver, and (b) the newly developed airborne demonstrator system utilising patch antennas and the Spatial FOG GNSS receiver

to 20 degrees. The aim of this experimental campaign was to produce a data set of quasi-monostatic DVB-T SAR imagery in order to verify the DVB-T SAR imaging system, i.e. the receiving system and signal processing algorithms. The Sutton Coldfield transmission station was again chosen as the DVB-T transmitter for the campaign due to its high power output and proximity to Coventry Airport, where the company operating the Cessna aircraft was based. Table 4.3 shows the main experimental parameters for all the target areas, while specific parameters to a target area are shown in separate tables with the results.

Table 4.3: Quasi-monostatic airborne campaign experimental parameters

Property	**Value**	**Unit**
Carrier Frequency	650	MHz
Bandwidth	7.61	MHz
Transmit Power	200	kW
Average aircraft altitude	600	m

4.3.1 Flight Route

Figure 4.10 shows the planned flight route for the monostatic airborne measurement campaign. The flight route, which started at Coventry airport, was planned such

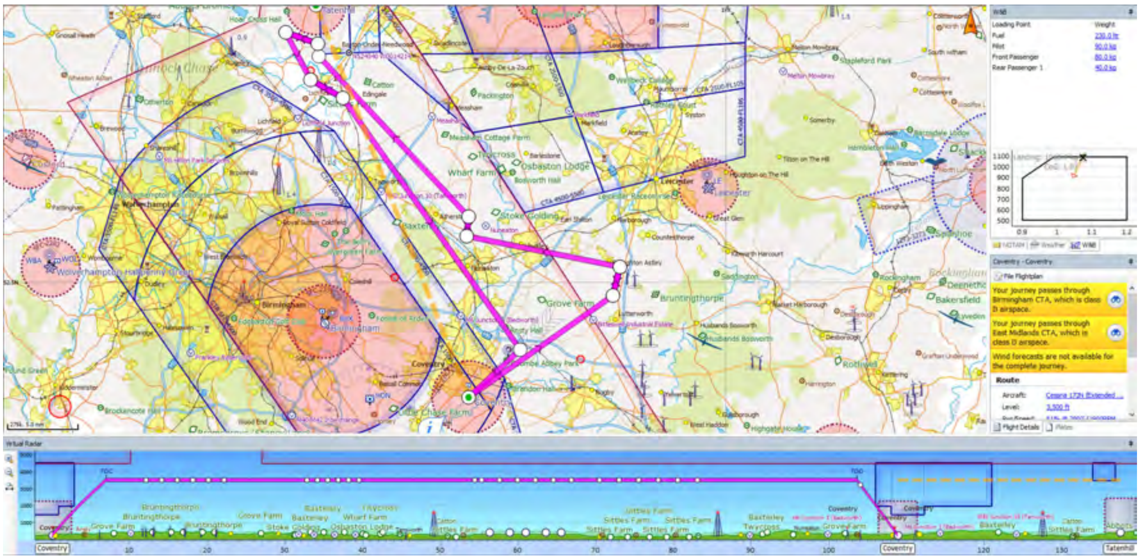

Figure 4.10: Planned SkyDemon flight route and elevation profile of the aircraft for the quasi-monostatic airborne measurement campaign

that measurements could be taken at four target areas which met the following requirements:

- A distance of 20 - 50 km away from the Sutton Coldfield Transmitter, as it was determined during the ground trials, shown in Section 3.12, that images could be generated at these distances.
- A mostly rural environment in case of the need for an emergency landing.
- A variety of different kinds of targets of interest such as fields, farms, forests, pylons, wind turbines, airfields and bodies of water.

The selection process was performed by inspecting aerial imagery from Google Earth which met the above criteria. As a result, the four target areas chosen were:

1. Bruntingthorpe Aerodrome
2. Advanced Structural Dynamics Evaluation Centre (ASDEC)
3. Tatenhill Airfield
4. National Memorial Arboretum

4.3.2 Target Areas

For brevity and to avoid repetition, since many of the results shown appear very similar in the kinds of returns observable, only the Bruntingthorpe target area is presented in this chapter. The target scene descriptions and results, for the ASDEC, Tatenhill, and Memorial target areas, can be found in appendix A.

Bruntingthorpe Aerodrome

Bruntingthorpe Airfield is located at coordinates (52.4906, -1.1314) in latitude and longitude, approximately 16 km south of Leicester and approximately 50 km east of Birmingham. The airfield is approximately 26 km, as the crow flies, from Coventry Airport, the origin point for the flight campaign. The runway at Bruntingthorpe is 3.2 km long, and the largest structure is an aircraft hanger measuring 70 m by 100 m. Figure 4.11 shows an aerial image of the Bruntingthorpe target area with four markers signifying areas with potential targets of interest. The area surrounding the airfield also contains a number of farms and villages with multiple one and two story buildings. As well as the typical potential imaging targets expected from an airfield, such as the runway, parked aircraft, and large buildings and aircraft hangers, Bruntingthorpe Airfield is also completely surrounded by trees, as can be seen in the aerial image shown in Figure 4.11.

Figure 4.11: Aerial image of the Bruntingthorpe target area

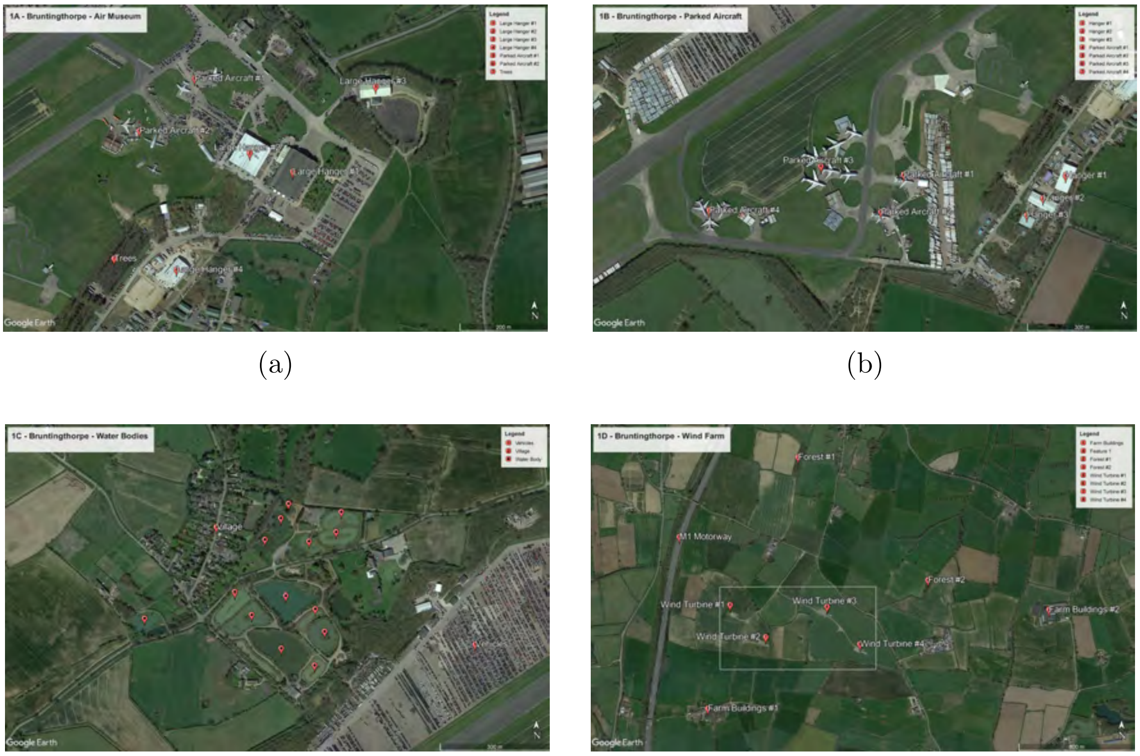

(a) (b)

(c) (d)

Figure 4.12: Four sub-regions of the Bruntingthorpe target area showing different potential targets of interest: (a) the air museum, (b) parked aircraft, (c) bodies of water, (d) four wind turbines

The airfield is also home to the Bruntingthorpe Air Museum, and many larger aircraft are parked next to a pair of large aircraft hangers which house the museum. A close up aerial image of the air museum can be seen in Figure 4.12a, which includes markers depicting the locations of several large aircraft hangers and parked aircraft. The aerial imagery was sourced from Google Earth, which was configured to show imagery from 2016, which was the closest year before the trial date that imagery was available. More recent aerial imagery from after the trial date shows that some of the aircraft have been removed or have changed positions but it is not known whether this was before or after the date of the campaign. Therefore, the locations of aircraft and parked vehicles shown in Figure 4.12a cannot be considered as accurate ground truth but can be used to explain the possible origin of any measured radar signals in the area where aircraft could be stationed.

Figure 4.12b shows an aerial image of another part of the Bruntingthorpe airfield where large aircraft are often parked. As before, the exact locations of the parked aircraft on the date of the measurements cannot be determined accurately from the aerial imagery, but imagery from before and after the trial date shows parked aircraft in at least some of the locations as shown. Three large aircraft hangers are also shown and marked in Figure 4.12b.

Surrounding the airfield are a number of interesting objects for imaging, including a series of water bodies to the north of the runway called Peatling Pools, shown in Figure 4.12c. A total of sixteen bodies of water can be identified next to a small village to the north-west of the pools. To the north-east of the village is a forested region and many of the bodies of water are surrounded by trees, and individual trees can be seen within some of the surrounding fields. To the west of the airfield and east of the M1 motorway is a cluster of four wind turbines, shown in Figure 4.12d.

4.4 Data Acquisition

On 30 January 2018 the Cessna 172N Skyhawk aircraft with mounted airborne DVB-T receiver was flown along the flight route shown in Figure 4.10. Since the equipment was placed on the rear seat, only two people could occupy the aircraft during the trial, including the pilot. A single operator, sat on the adjacent seat to the pilot, operated the equipment with the control laptop. As with the previous ground based trials, positioning data was recorded continuously throughout the whole trial, whereas individual radar measurements were triggered and stopped by the operator. Unlike previous trials, the data was recorded with the time and date as well as the measurement duration automatically within the filename of the raw data. During image formation, the timestamp and duration, which was extracted from the file name, was used to match the measurement with the corresponding positioning data. The positional data is then interpolated to match the pulse data.

Table 4.4 shows the number of measurements taken for each of the four primary imaging areas. Additionally, four extra measurements were recorded between the National Memorial Arboretum and Coventry Airport during the return trip, an area just north of Tamworth. In total, fifteen measurements were recorded over a period of 2 hours in good weather conditions.

The actual flight path of the aircraft, as recorded by the Spatial FOG GNSS receiver, is shown in Figure 4.13. The planned altitude of 600 m above mean sea level, which is approximately 200 m above the height of the Sutton Coldfield transmission antenna and approximately 500 m above mean ground level, could not always be maintained throughout the campaign due to air turbulence. Figure 4.14 shows the actual altitude profile of the flight as recorded by the Spatial FOG receiver.

Table 4.4: Table of quasi-monostatic measurements

Measurement	**Location**	**Start Time**	**Recording Length (s)**
1	Bruntingthorpe Aerodrome	10:44:05	72.9022
2	Bruntingthorpe Aerodrome	10:46:54	79.7180
3	Bruntingthorpe Aerodrome	10:49:04	59.6902
4	ASDEC	10:58:01	41.1042
5	ASDEC	10:59:36	38.7056
6	ASDEC	10:58:01	49.7287
7	Tatenhill Airfield	11:12:27	78.1451
8	Tatenhill Airfield	11:14:32	71.4342
9	National Memorial Arboretum	11:18:29	78.9840
10	National Memorial Arboretum	11:20:56	96.1806
11	National Memorial Arboretum	11:23:47	53.6084
12	Area North of Tamworth	11:25:58	85.2886
13	Area North of Tamworth	11:28:00	60.7388
14	Area North of Tamworth	11:30:13	18.2977
15	Area North of Tamworth	11:31:25	124.0728

4.5 Results and Analysis

This section presents the results of the quasi-monostatic airborne measurement campaign. Firstly, DVB-T SAR imagery from the Bruntingthorpe target areas is shown and compared with ground truth aerial imagery in order to perform an initial visual analysis of the returns from targets within each scene. Results from the ASDEC, Tatenhill, and Memorial target areas can be found in Appendix A. Secondly, a point-like target is identified within the target scene and a point spread function analysis is performed, comparing the measured results with expected results from simulated data. Thirdly, added noise on the reference channel and its effects on image formation are investigated, indirectly demonstrating the long range capabilities of the DVB-T SAR system. Finally, the effects of extending the integration time are investigated, showing the point at which motion inaccuracies cause defocusing within the imagery.

Figure 4.13: Actual flight path of airborne receiver (white) shown on an aerial image of the surrounding area as measured by the GNSS receiver. The four target scene locations are indicated with red markers while the transmitter location is indicated with a yellow marker

Although the SAR images presented in this chapter are shown from an aerial viewpoint, it is important to note that the incident EM waves from the transmitter form a small grazing angle with the ground, and thus the measured intensity of targets within the scene is due to the reflectivity of surfaces which reflect the incoming waves back towards the receiver. For a small grazing angle, as is the case here with a transmitter grazing angle of just 0.34 degrees, the incident waves are almost parallel to the ground, and thus objects with surfaces perpendicular to the ground present the highest reflectively. Figure 4.15 demonstrates approximately the effect of a shallow grazing angle for EM waves incident on an object with sides perpendicular and parallel to ground. However, the exact reflectivity, and the direction of reflectance, is dependant on the target RCS.

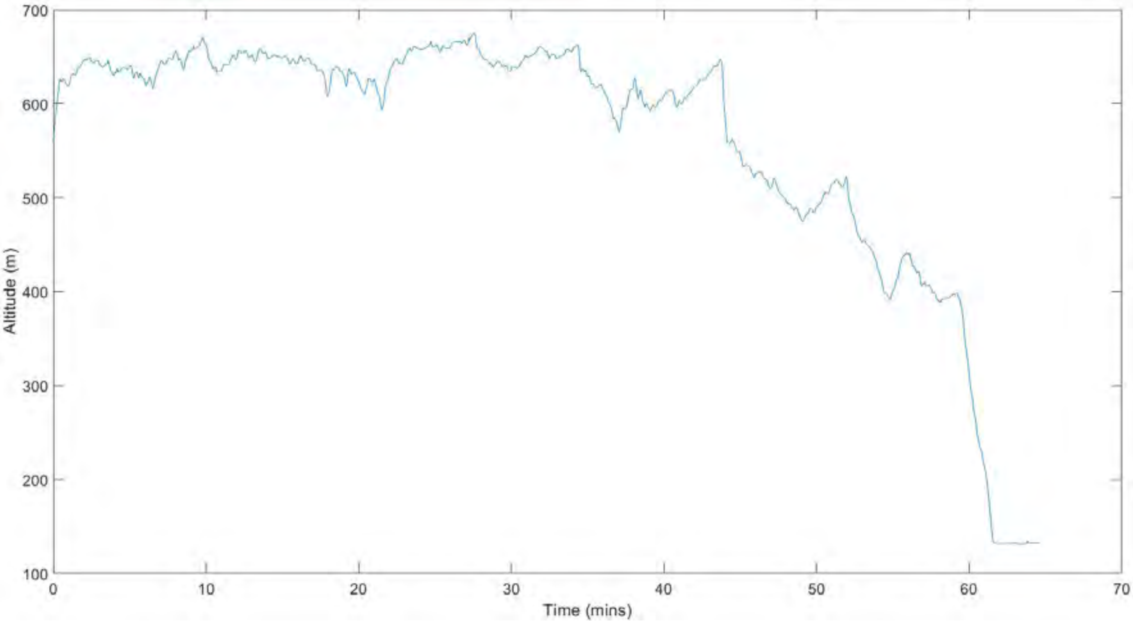

Figure 4.14: Actual elevation profile of airborne receiver as measured by the GNSS receiver

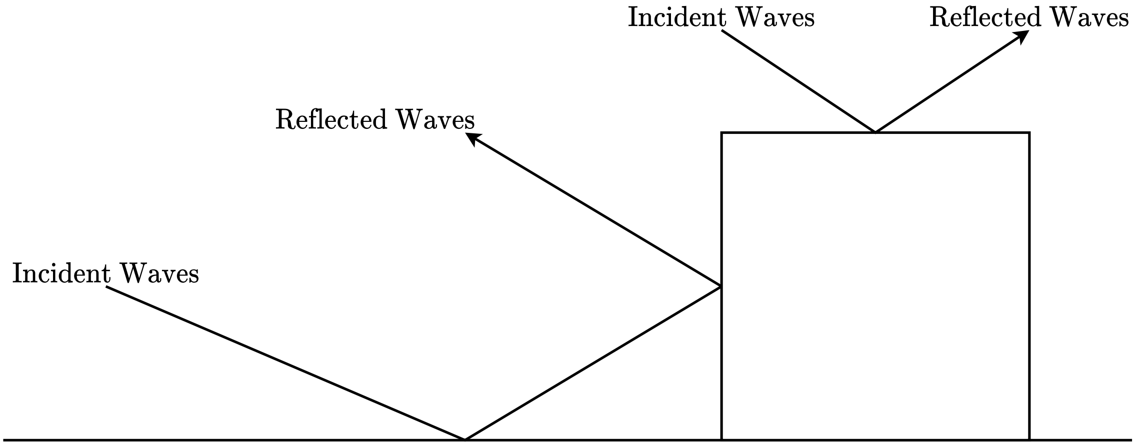

Figure 4.15: Diagram depicting the approximate reflection of incident waves on surfaces approximately parallel and perpendicular to the incident direction

4.5.1 Target Area Results

This section presents the results from the Bruntingthorpe target areas specified and shown in Section 4.3.2. For each of the target areas a series of comparison images between ground truth aerial imagery and the corresponding DVB-T SAR image of different sub-regions are shown, roughly in accordance with the different features and potential targets identified for each area.

For all of the SAR image results shown for the full target scenes the scene size is 10 km in the range direction and 4 km in the cross-range direction, whilst the image size is 2000 pixels in width by 1600 pixels in height, resulting in 5 meters per pixel in range and 2.5 meters per pixel in cross-range. The range resolution, which for a monostatic geometry is dependent only on the bandwidth, has a fixed theoretical value of approximately 20 meters. The cross-range resolution is dependent on the aperture length. Each image is processed with a fixed integration time of 4 seconds, however, the actual length of the synthetic aperture is dependent on the speed and any acceleration of the aircraft during the integration period. Each result is accompanied by a table showing the scene and aperture parameters, including the aperture length.

4.5.2 Bruntingthorpe

Figure 4.16 shows a SAR image of the Bruntinthorpe target scene overlaid with an aerial ground truth image of the scene. The important scene and aperture parameters, including integration time, are shown in Table 4.5. Immediately noticeable are returns across the entire image which appear to outline fields, the M1 motorway running down the image at approximately 1 km in range, as well as the airfield in the centre of the image. This is due to the presence of foliage, primarily trees, which surround these areas. Trees were planted around the entirety of the aerodrome in order to reduce the noise pollution of aircraft taking off and landing on the runway. Apart from the airfield the outlining effect of the signal returns is more prominent at shorter ranges between 0 and 3 km in range. Comparing the returns from a forest area, located at 2550 m in the X direction and 1250 m in the Y direction, to a similarly sized forest area at a greater range, located at 9175 m in the X direction and 1655 m in the Y direction, it is evident that the returns from the closer forest are higher in intensity as well as the density of returns.

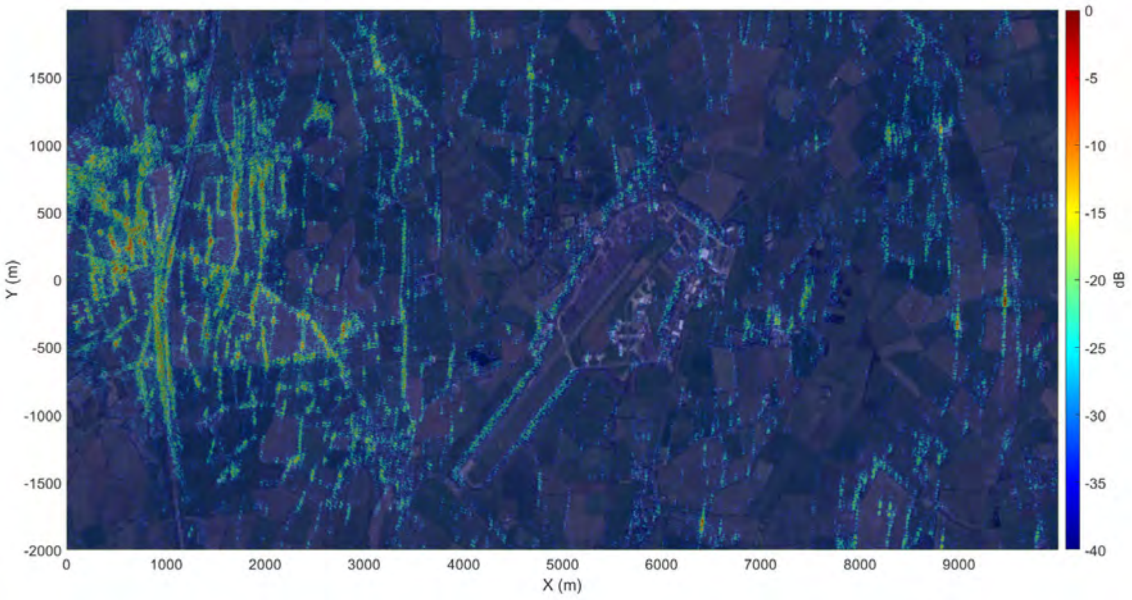

Figure 4.16: A DVB-T SAR image of the Bruntingthorpe target area superimposed onto aerial ground truth imagery

A comparison between a SAR image of the Bruntingthorpe air museum and surrounding aircraft hangers, as shown in Figure 4.12a, and a ground truth aerial image of the same area is shown in Figure 4.17. A forested region, which is part of the trees surrounding the airfield, is observable as a region of strong returns, labelled as 2 in the figure. The large hangers to the right of these trees do not appear to be present as distinct returns in the corresponding SAR image. A similar region of trees in the upper part of the image (not labelled), does not appear as strong in intensity in comparison. The air museum itself, contained within two large hangers in the region marked 3 in the figure, do not seem to have any strong returns associated with them. The returns visible in the region marked as 3 are more likely due to the trees within that region. The regions labelled 1, 4, and 5, show strong returns from buildings as opposed to trees. Although these buildings vary in size as seen from above, and appear much smaller than the aircraft hangers within the airfield, their height and material are not known and may explain the reason why these buildings are visible in the SAR image while others are not. For example, a taller building made from metal would be expected to produce stronger returns than a shorter building made from brick. Another possible explanation for the visibility of some buildings and not others is the effects of shadowing, where objects or terrain in front of buildings block the transmit signal from reaching them or the reflected signal from reaching the receiver. Given the extremely shallow angle of incidence of the transmit signal, shadowing is highly likely.

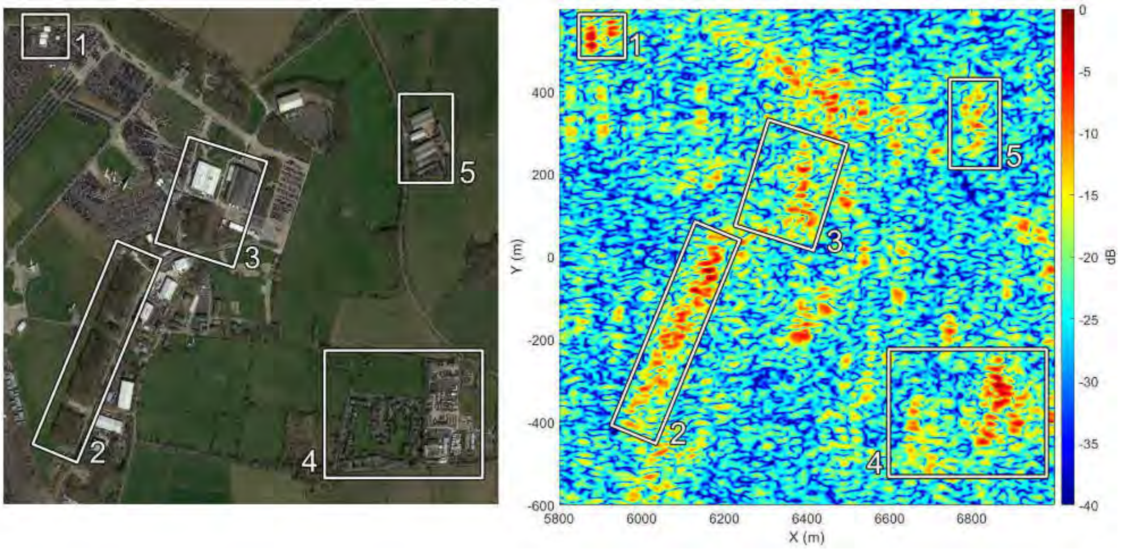

Figure 4.17: A side-by-side view showing aerial imagery of a sub-region of the Bruntingthorpe target area containing the air museum, next to a DVB-T SAR image of the same area. Regions of interest have been highlighted with numbered white boxes

To the south-east of the air museum is an area of the airfield with multiple parked aircraft which are part of the museum, as shown in Figure 4.12b. Figure 4.18 shows a side-by-side comparison of a SAR image of this area with the corresponding ground-truth aerial imagery of the same area. Unlike with buildings and trees, the locations of aircraft within the airfield can change and may not correspond exactly with the positions as they are shown in the ground-truth imagery. Returns in the regions labelled 1, 2, and 3 in the figure most likely correlate with the locations of the parked aircraft, although no specific aircraft features can be determined from the shape of the returns. Other strong returns in the image in the top-left, bottom-left, and right coincide with the the surrounding trees of the airfield. The runway itself and the car parking area to the north of the airfield, which sometimes contains vehicles as shown in the ground truth image, are not visible within the SAR image.

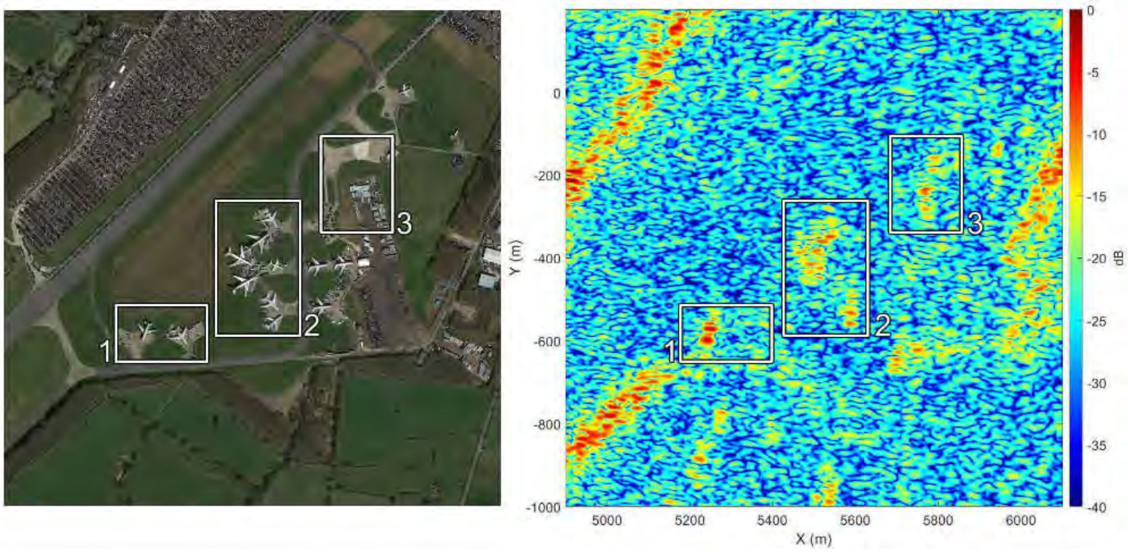

Figure 4.18: A side-by-side view showing aerial imagery of a sub-region of the Bruntingthorpe target area containing a group of parked aircraft, next to a DVB-T SAR image of the same area. Regions of interest have been highlighted with numbered white boxes

A comparison of the Peatling Pools area aerial ground truth imagery and corresponding SAR imagery is shown in Figure 4.19. The trees which surround the airfield are visible as a line of dense returns following the general shape of the forests. The pools themselves do not appear to reflect any DVB-T signals back towards the receiver, as expected. Regions labelled 1 and 2 in the figure show strong returns around the pools of water which can be attributed to trees.

Figure 4.20 shows a side-by-side comparison of an aerial image of a sub-region of the Bruntingthorpe target area, surrounding four wind-turbines, with a SAR image of the same sub-region. The four wind turbines are each highlighted with a numbered white circle in both the SAR image and the ground truth reference. Two forested regions are also highlighted with numbered white rectangles. The wind turbines appear as multiple strong returns clustered in a small area, possibly due to the rotation of the turbine blades. The upper forested region, labelled as 5, appears as a region of strong returns comparable in strength to the wind turbines. The other forested region, labelled as 6, appears noticeably weaker in intensity, which is likely due to a combination of the size of the forest and the topography of the landscape.

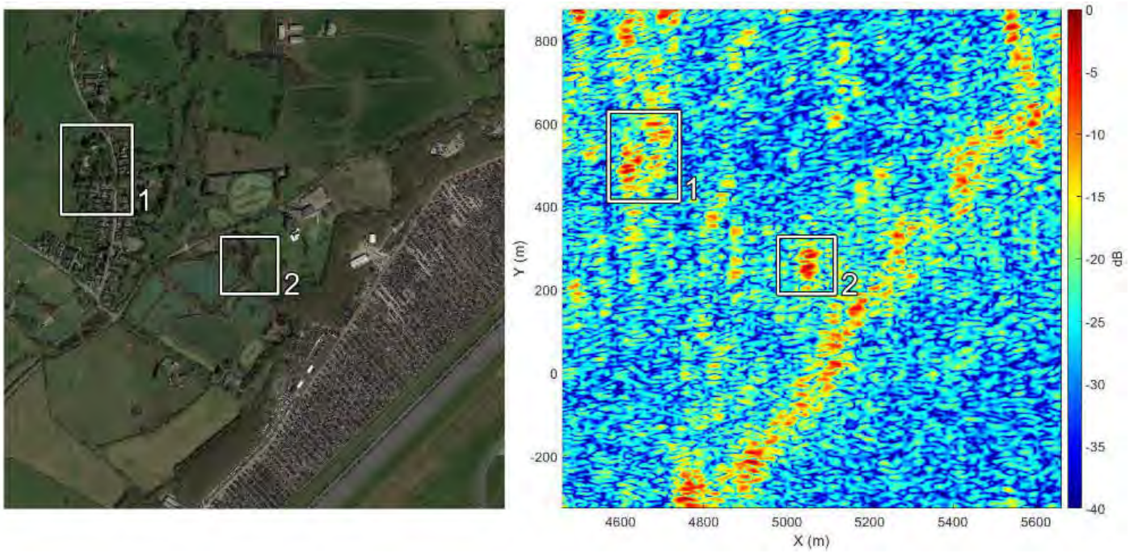

Figure 4.19: A side-by-side view showing aerial imagery of a sub-region of the Bruntingthorpe target area containing a series of water ponds, next to a DVB-T SAR image of the same area. Regions of interest have been highlighted with numbered white boxes

Also noticeable in the comparison are returns from individual trees and hedgerows within and bordering fields.

4.5.3 Comparison of Range Compression Techniques

For the images shown up to this point, range compression was performed by matched filtering, i.e. cross-correlating, the surveillance channel with reference channel. This is possible because the data was recorded with two separate antennas; one recording only the direct signal, and the other recording only the radar signal. However, a DVB-T SAR system using a single receiver channel recording both the direct and radar signals is possible, where range compression is performed by auto-correlating the recorded signal. Figure 4.21 shows a comparison of a quasi-monostatic DVB-T SAR image of a 6 km by 4 km region of the Bruntingthorpe target area produced with auto-correlation (4.21a) and cross-correlation (4.21b) range compression schemes. Overall, visually the images appear almost identical, with an almost identical number and density of returns, with the notable exception of a line of running

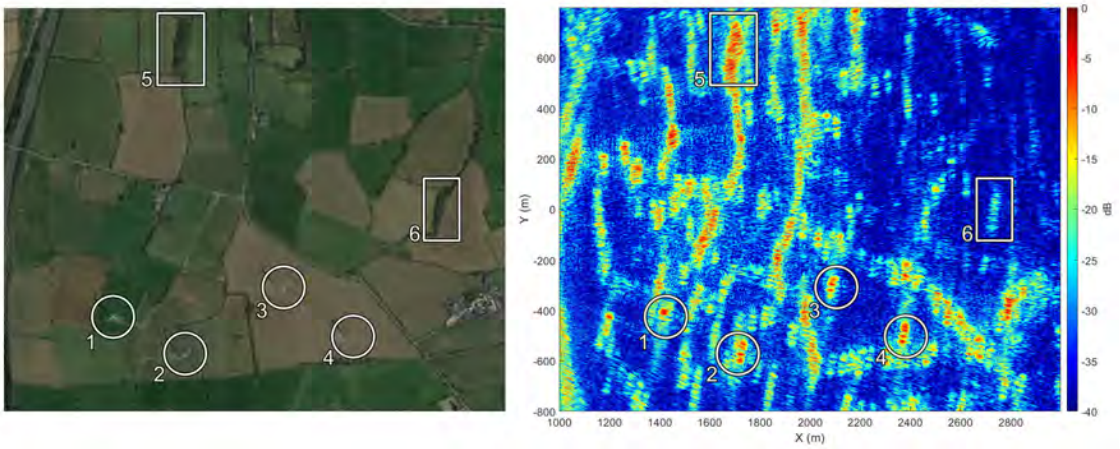

Figure 4.20: A side-by-side view showing aerial imagery of a sub-region of the Bruntingthorpe target area containing four wind turbines, next to a DVB-T SAR image of the same area. Regions of interest have been highlighted with numbered white boxes

across the auto-correlated image, which corresponds to the side-lobes of the direct signal.

The mean background level of the images is also different, with a slight increase in background level when range compression is performed via auto-correlation. Specifically, for the normalised SAR images shown, the auto-correlated result has a measured mean background level of -42.1 dB, while the cross-correlated result has a measured mean background level of -45.4 dB, an increase of approximately 3 dB. For a typical cross-correlation range compression scheme the direct signal is recorded through the front plate of a separate patch antenna, however, for an auto-correlation range compression scheme the direct signal is recorded through the back plate of the same patch antenna which records the radar signal. The measured difference in gain between cross-correlation and auto-correlation range compression schemes is due to a 3 dB difference in gain measured between a signal entering the front plate of the patch antenna compared to the same signal entering the back plate of the patch antenna.

Table 4.5: Table of scene and aperture parameters for the Bruntingthorpe target area.

Parameter	**Value**	**Unit**
Measurement Number	1	
Aperture Time	30	seconds
Integration Time	4	seconds
Aperture Length	256	meters
Mean Aircraft Speed	64	meters/second
Mean Aircraft Altitude	634	meters
Aperture Start	(52.5038, -1.2033)	(latitude, longitude)
Aperture End	(52.5061, -1.2026)	(latitude, longitude)
Aperture Centre	(52.5049, -1.2030)	(latitude, longitude)
Scene Bottom-Left	(52.4873, -1.2085)	(latitude, longitude)
Scene Top-Right	(52.5055, -1.0529)	(latitude, longitude)
Bistatic Angle	0.3972	degrees
Distance to Transmitter	49.5	km
Transmitter Grazing Angle	0.34	degrees

4.5.4 Point Spread Function Analysis

In an ideal scenario, the functionality of the image formation algorithm can be confirmed by imaging a point-like target and analysing the resulting Point Spread Function (PSF) within a SAR image. This is usually achieved in monostatic SAR by placing a calibrated target, such as a corner reflector, within the target scene at a known location. However, due to the large size requirements of a corner reflector for UHF frequencies, and problematic scattering effects due to the bistatic nature of the passive geometry, a suitable calibrated target could not be placed within the target scene. Instead, a point-like target already in the target scene was selected from the SAR imagery for analysis. A wind turbine in the Bruntingthorpe target area, located at (52.486487, -1.066874) in latitude and longitude, has a point-like response due to the 8 km range from the receiver and the spatial resolution. It should be noted that the wind turbine is not an actual point-target, and the possible rotation of the turbine blades could result in a more complex scattering environment. However, for a large turbine such as this one at a distance of nearly 10 km and with a spatial

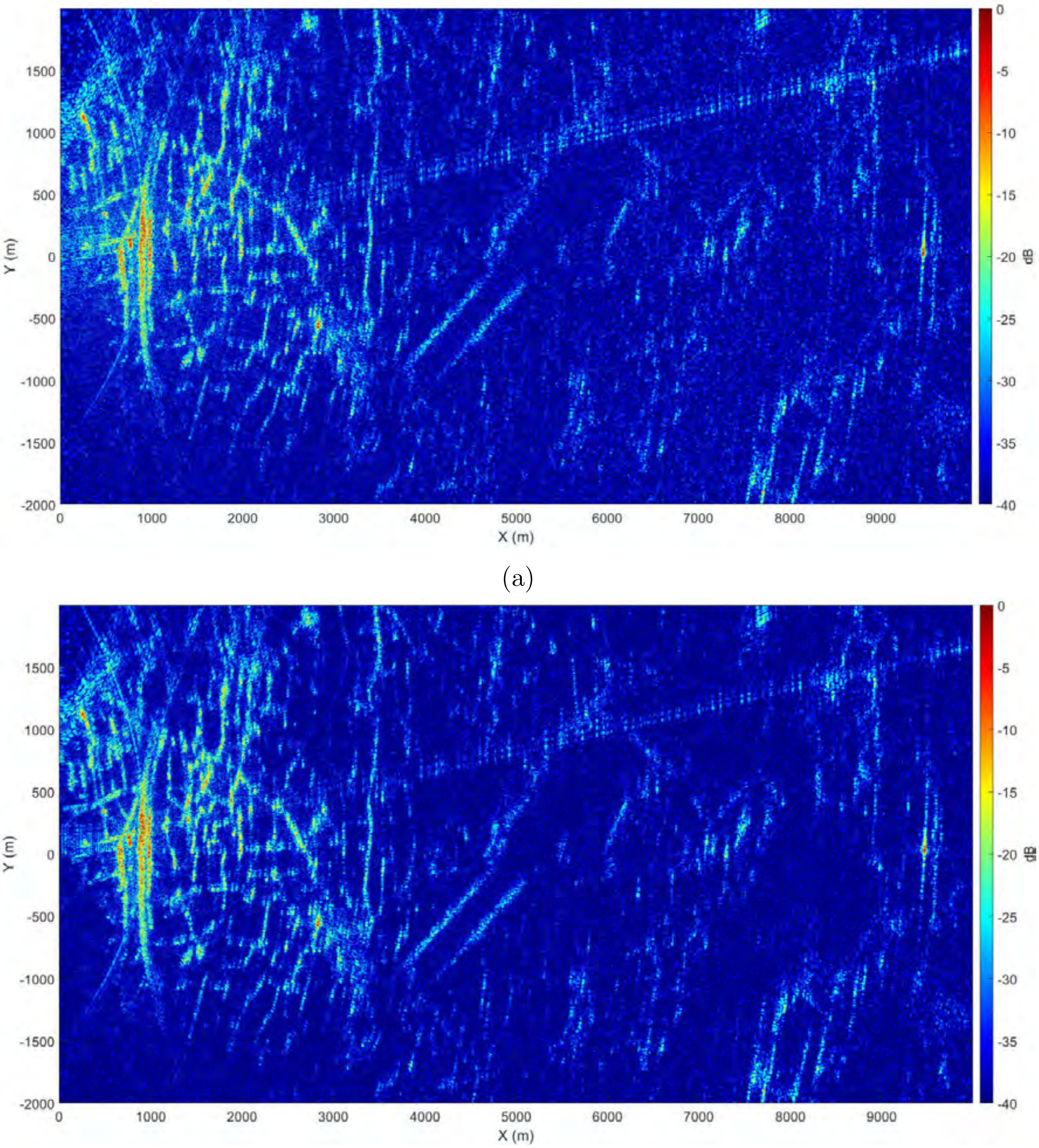

(a)

(b)

Figure 4.21: A comparison between DVB-T SAR images range compressed using (a) an auto-correlation scheme, and (b) a cross-correlation scheme

resolution of approximately 20 m, for the purposes of this analysis, returns from the wind turbine can be considered point-like.

Figure 4.22a shows an extracted PSF of the wind turbine from a full SAR image of the Bruntingthorpe target area with an aperture length of approximately 93 m. Figure 4.22b shows an image of a simulated PSF using the DVB-T SAR simulator shown in Chapter 3, with the same range and cross-range location and the same aperture length. Figures 4.22c and 4.22d are graphs of the corresponding range and cross-range profiles respectively for both the extracted and simulated PSF's and shows a strong coincidence, confirming the validity of the simulation. As can be seen in Figure 4.22c, the peak to null width is approximately 20 m, which is consistent with the expected range resolution of 19.7 m. The side-lobe levels around the main peak of the extracted PSF, in the range profile, are lower than the simulated PSF. The lower sidelobe levels of the extracted PSF are likely due to the complex scattering components of the wind turbine target which deviate from the model of a point-like target. However, the locations of the extracted PSF side-lobe peaks match very well to the locations of the simulated PSF. For the cross-range profiles, the extracted and simulated PSF's match up extremely well in both peak locations and peak intensities, with the first side-lobe peaks 13 dB lower than the main peak, consistent with a sinc-like return. The cross-range resolution, measured from the peak-to-null width of the main peak is approximately 40 m, which is consistent with the expected value of 39.6 m, given from Equation 2.37.

4.5.5 Effects of Noise on the Reference Channel

A degradation in image quality could result from a decrease in the SNR of the direct signal. This effect can be simulated by adding noise to the reference channel and can be used to investigate the possibility of long-range imaging, as increasing the distance between the transmitter and the scene results in a decrease in direct signal SNR. Similarly, depending on the acquisition geometry, a DVB-T SAR receiver may record the direct signal through the side-lobes of the receiving antenna, or from the side-lobes of the transmitting antenna, also resulting in a reduction in direct signal SNR.

Presented here is a simulation of the impact of these effects on SAR imagery using measured data from the quasi-monostatic measurement campaign. Measured data is

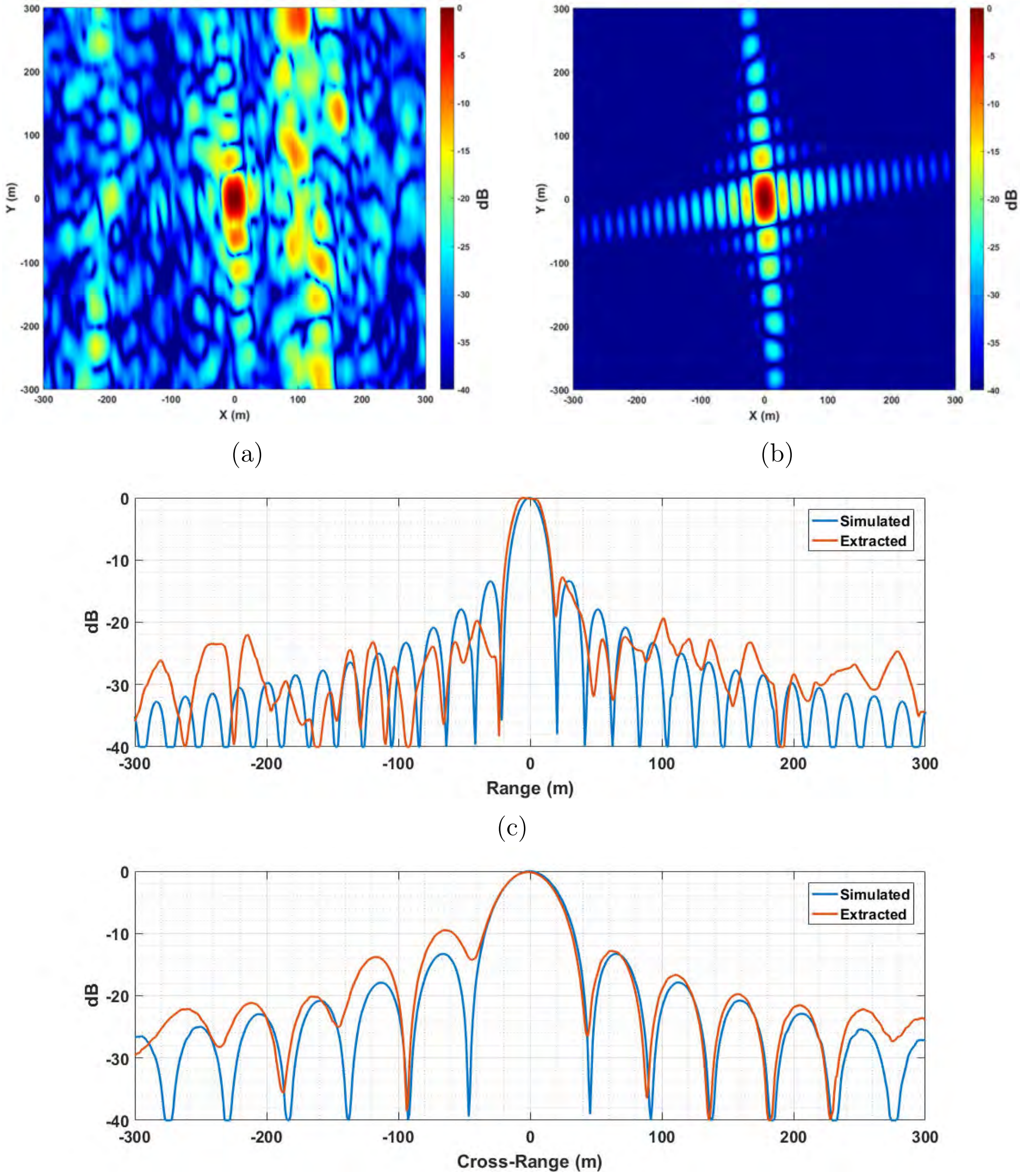

(a)

(b)

(c)

(d)

Figure 4.22: Images showing (a) an extracted PSF from aerial DVB-T SAR imagery, (b) a simulated PSF with the same parameters, (c) a plot of the range profiles of the extracted and simulated PSFs, (d) a plot of the cross-range profiles of the extracted and simulated PSFs

combined with added white Gaussian noise on the reference channel, thus reducing the direct signal SNR. Range compression via matched filtering is then performed by cross-correlating the radar channel with the noisy reference channel, and image formation is performed by backprojection. Although for the analysis presented here the range compression was performed with a cross-correlation of the reference and radar signals, range compression via auto-correlation would give as good a result. Figure 4.23 shows two plots of a segment of the measured DVB-T signal from the reference channel of the receiver. The first, Figure 4.23a, is unchanged and has a measured SNR of 14 dB, where the SNR of the direct signal is measured in frequency space assuming that the gaps between successive DVB-T channels is pure noise. In the second plot, Figure 4.23b, white Gaussian noise has been added in order to emulate an SNR of -30 dB.

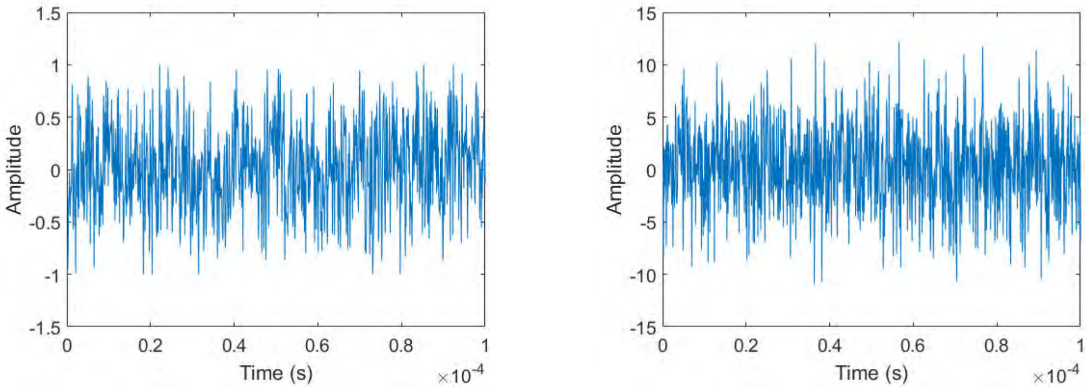

(a) (b)

Figure 4.23: Plots of the received signal for a single DVB-T symbol with (a) no additional added noise, and (b) with additional noise to emulate an SNR of -30 dB

Figure 4.24 shows a comparison of four DVB-T SAR images of a 2 km by 2 km region of the Bruntingthorpe target area, each with a different amount of added noise to the direct signal. Figure 4.24a has no additional noise and acts as a control while Figures 4.24b, 4.24c, and 4.24d have added noise in order to emulate a direct signal SNR of -10 db, -20 dB, and -30 dB respectively. The image SNR is measured by taking the ratio of the mean image intensity to the mean background level, and therefore includes any signal processing gains from the image formation algorithm. The SNR is then actually (Signal + Noise) / Noise, which is effectively the same as SNR within experimental error. For each image, the colourscale is normalised to the maximum intensity within each image. With an emulated direct signal SNR of -10 dB, treelines and field boundaries are still observable, but some of the previously visible individual trees located within fields are obscured by noise. At an emulated

-20 dB of direct signal SNR some of the field boundaries are no longer visible. The trees lining the embankments of the M1 motorway, previously visible on the left side of the image, are now lost to noise. Any individual trees are now indistinguishable from the background. With added noise emulating -30 dB of direct signal SNR only the brightest returns are distinguishable from noise, corresponding to clusters of trees or small forests. Figure 4.25 shows a plot of the mean background level of the SAR image against the emulated direct signal SNR as the noise power added increases. In general, as the added noise power increases the mean background level increases, resulting in a decrease in overall image contrast. Between –5 dB and -30 dB of emulated direct signal SNR, the relationship is approximately linear.

4.5.6 Extended Dwell Times

The wind turbine used in Section 4.5.4 for PSF analysis was utilised to investigate the effects of extending the integration time, and hence the dwell time on target. Although the airborne receiver was operated as a broadside SAR system with no steering of the receive antenna, due to the large area of observation, the majority of targets within the scene were illuminated for the entire duration of the synthetic aperture. Therefore, the system performed closer to a SAR operating in spotlight mode as opposed to stripmap mode. The cross-range resolution, as given by Equation 2.37, for a spotlight mode SAR improves with increasing synthetic aperture length. The effects of increasing the aperture length for a given target scene were investigated and the results are shown in Figure 4.26. As the length integration time was increased, thus increasing the synthetic aperture length, the cross-range resolution improved, as expected, up to around 16 seconds integration time (755 m aperture length), at which point the cross-range resolution remained constant at around 9 m. This is likely because the wind turbine, in reality, is not a point target, and at 16 seconds integration time the resolution cell is smaller than the extent of the target. Another possibility is the accumulation of motion errors causing a

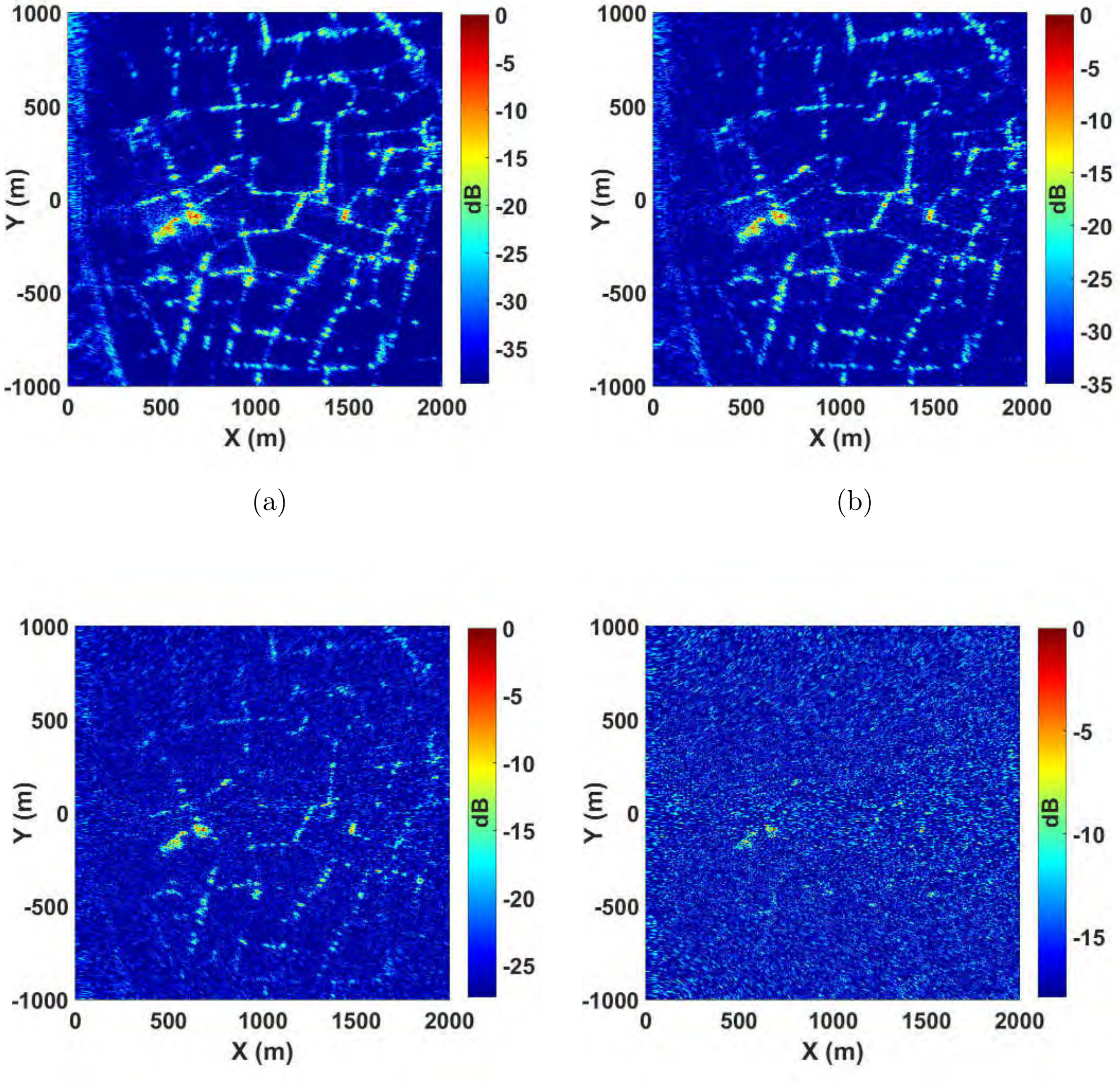

(a)

(b)

(c)

(d)

Figure 4.24: Extracts of back-projected SAR image with (a) Direct signal SNR of 14 dB (b) Direct signal with added noise to emulate SNR of 10 dB, (c) Direct signal with added noise to emulate SNR of 20 dB, (d) Direct signal with added noise to emulate SNR of 30 dB

decrease in cross-range resolution due to defocusing.

4.6 Conclusions

This chapter has demonstrated the development of a DVB-T receiver system from an initial design into a flight-ready system, and has also shown the first results of a

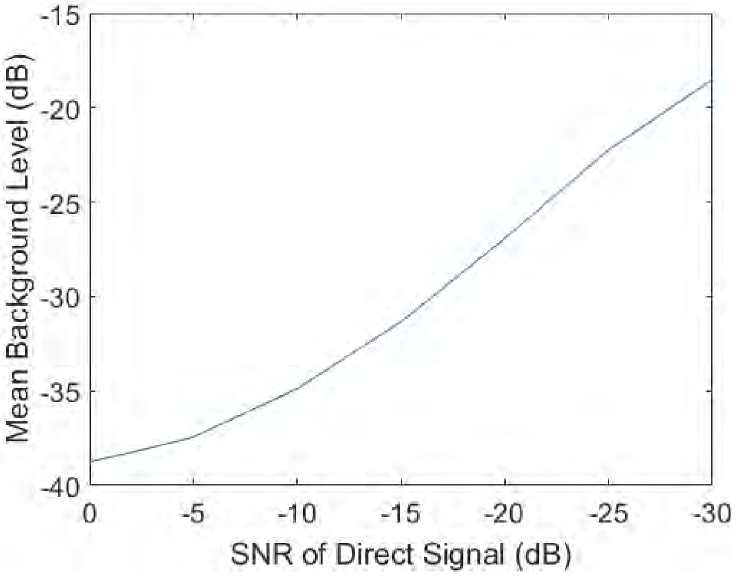

Figure 4.25: Graph showing the mean background level of the image in Figure 4.24a against the direct signal SNR with added noise before matched filtering

quasi-monostatic measurement campaign designed to validate the developed receiver system and image formation algorithm.

The initial DVB-T SAR receiver, developed originally for ground-based measurements, was modified for use on a Cessna 172N aircraft. For this purpose, a set of patch antennas, which could fit within the windows on the inside of the aircraft, were built and tested. A new, smaller, and more accurate positioning system was acquired and a set of RF front-end chains were developed and tested. The updated receiver system was tested and validated with a ground-based vehicle trial designed to directly compare the initial and updated receiver systems, and the results confirmed the validity of the updated system.

An airborne measurement campaign was conducted and a set of quasi-monostatic measurements for DVB-T SAR image formation were recorded at four different target locations, identified as areas with targets of interest such as trees, buildings, airfields, water bodies, and wind turbines, amongst other targets. The measured data was processed into quasi-monostatic SAR images which were then analysed. A comparison of DVB-T SAR imagery with ground truth aerial imagery was performed in order to further validate the receiver system and image formation algorithm, and also to begin to identify the kinds of returns observable for a known set of targets. A comparison of range compression techniques was presented and showed no meaningful difference between an auto-correlation scheme compared to a cross-correlation scheme. Additionally, an analysis of the point spread function of a point-like wind turbine target was performed by comparing the extracted PSF to a simulated version with the same parameters. Graphs of range and cross-range profiles for the extracted and simulated targets showed a good correspondence and validates the simulation. The performance of the image formation algorithm with the effects of added noise on the reference channel was also investigated and showed that imaging was still possible with an emulated direct signal SNR of up to -15 dB. This result demonstrates the possibility of long-range imaging up to four times greater than the results shown, representing a distance of 200 km from the transmitter. Finally, the effects of increasing the dwell time on the cross-range resolution were investigated and showed that a doubling of the dwell time equated to a halving of the cross-range resolution, as expected, up to a dwell time of around 16 seconds at which point the relationship no longer held. This is likely due to the accumulation of motion errors over a longer aperture or possibly due to the cross-range resolution becoming smaller than the target size, resulting in no further gains of resolution with increasing dwell time since the wind turbine target was not a true point target.

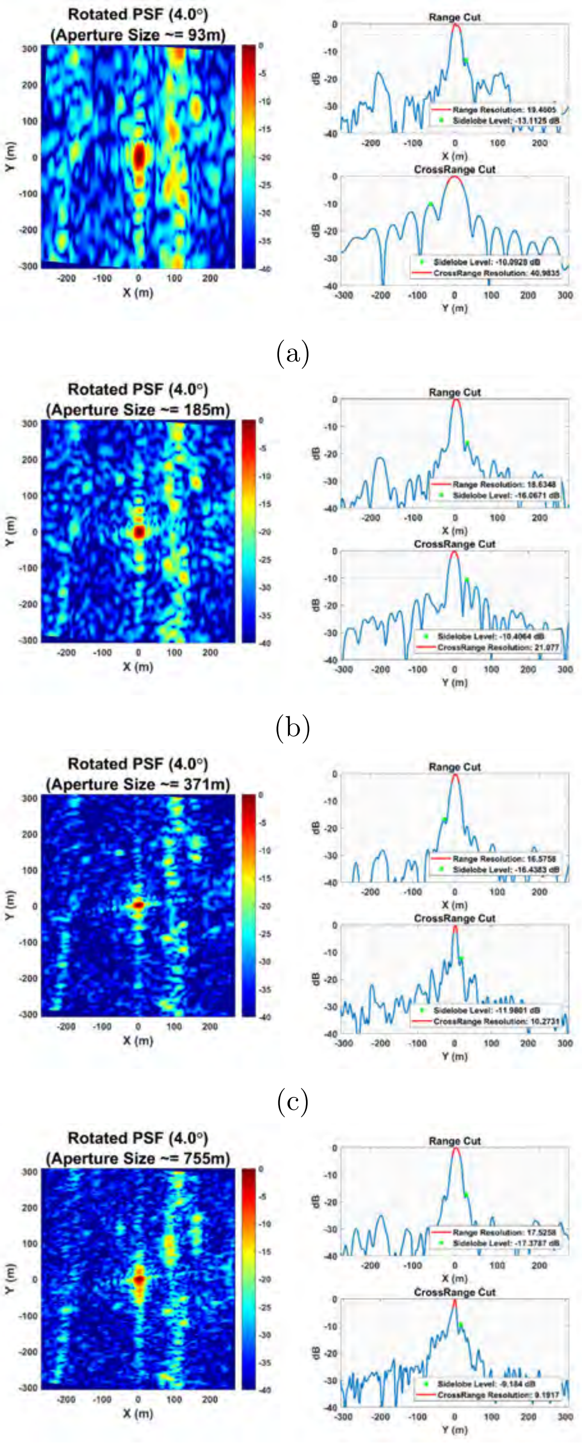

(a)

(b)

(c)

(d)

Figure 4.26: Images showing the effect of increasing dwell time on cross-range resolution for an extracted PSF of a wind turbine at 10 km range in the Bruntingthorpe target area: a) 1s integrated b) 2s integrated c) 4s integrated d) 8s integrated. For each sub-plot, the extracted PSF is shown as an image with axes of x and y in meters, the range cut is shown as a graph of intensity (dB) on the y-axis versus x position on the x-axis, and the cross-range cut is shown as a graph of intensity (dB) on the y-axis versus y position on the x-axis.

Chapter 5

Bistatic Airborne Measurements

5.1 Introduction

Since DVB-T SAR is a passive system, the geometry of the radar could be in a bistatic configuration with the target scene to be imaged. Therefore, it is important to understand the properties of bistatic DVB-T SAR imagery. This chapter presents the experimental methodology for the collection and formation of aerial DVB-T SAR imagery in a bistatic configuration, as well as the analytical and numerical analysis of SAR image properties with changing bistatic angle. The results and analysis are presented in three parts. The first part shows a comparison of quasi-monostatic DVB-T SAR imagery with differing flight altitudes, and hence differing grazing angles between the receiver and the target scene. Features and targets are visually identified, using ground truth aerial imagery, and comparisons of relative intensity, spread of target returns, and the amount of noise and speckle are commented on. The second part details a similar analysis but for a comparison of DVB-T SAR imagery with differing bistatic angles generated from apertures with similar altitudes. Part three presents a numerical analysis of average intensity and contrast over a multitude of images with varying bistatic angles and varying altitudes.

5.2 Experimental Campaign

An experimental campaign was designed to collect DVB-T radar data in order to form bistatic SAR imagery. The aim was to investigate the features of bistatic DVB-T SAR imagery of a known target scene to attempt to understand how returns from particular targets in a primarily rural area, such as forests, buildings, fields, wind turbines, and bodies of water, are affected by changes in the bistatic angle and the grazing angle between the receiver and the scene.

5.2.1 Receiver Equipment and Aircraft

The receiver equipment used for the bistatic measurement campaign was unchanged in design and implementation from the receiver used during the quasi-monostatic campaign described in Chapter 4. The aircraft used was another Cessna 172N Skyhawk, although not the exact same aircraft that was used before. The setup within the aircraft was the same, with the receiver equipment mounted within a vibration resistant box placed on the rear seats of the aircraft, and the pilot and an operator occupying the front two seats.

5.2.2 Target Scene

From the results of the first flight campaign, shown in Section 4.5.2, Bruntingthorpe Aerodrome was chosen as a suitable target area for the bistatic campaign. The target scene is a mostly rural area of ground defined by a north-orientated 10 km by 6 km rectangle encompassing the airfield, as well as some fields, farms, roads and small villages. Figure 5.1 shows an aerial image of the target scene, while Table 5.1 summarises the main parameters of the target scene, where the distance to the transmitter and transmitter grazing angle are measured from the centre of the image scene.

Figure 5.1: Aerial image of the Bruntingthorpe target scene used for the bistatic airborne measurement campaign

The main feature of the target scene, and the reason this particular scene was chosen for the bistatic airborne campaign, is the Bruntingthorpe aerodrome at its centre. As shown in the quasi-monostatic airborne campaign in Chapter 4, the trees outlining the airfield result in returns which highlight the shape of the airfield and allow it to be easily recognised in a SAR image. This allows for easy alignment with aerial ground truth imagery and the identification of other targets relative to the location of the airfield.

For the quasi-monostatic measurements presented in Chapter 4, the target scenes were defined relative to the measurement aperture as determined by the flight path of the aircraft during the integration time. A local Cartesian axis was defined such that the aperture direction, or cross-range axis, was orientated along the y-direction, the down-range axis was orientated along the x-direction, and the z-direction was defined to be perpendicular to x and y directions and pointed upwards away from

Table 5.1: Table of target scene parameters.

Parameter	**Value**	**Units**
Scene Width	10	km
Scene Height	6	km
Bottom Left	(52.469210, -1.202000)	(latitude, longitude)
Bottom Right	(52.469210, -1.054866)	(latitude, longitude)
Top Left	(52.523119, -1.202000)	(latitude, longitude)
Top Right	(52.523119, -1.054866)	(latitude, longitude)
Scene Centre	(52.496142, -1.128470)	(latitude, longitude)
Distance to Transmitter	49.26	km
Transmitter Grazing Angle	0.34	degrees

the ground. The origin of the local coordinate system was defined as the centre of the measurement aperture. The image scene was then defined as a rectangular area, usually 10 km in the x-direction and 4 km in the y-direction, orientated with the coordinate axes. Therefore, for two different measurements with flight paths that did not align, it was not possible to define the same target scene. To allow for the comparison of bistatic measurements of the same area, the target scene was defined as a fixed north-orientated area. Figure 5.2 shows the elevation topology of the target scene.

5.2.3 Flight Route

The planned flight route for the second campaign is shown in Figure 5.3, while the planned flight route aircraft altitude profile is shown in Figure 5.4. The launch point for the aircraft was again Coventry Airport. The flight path takes the aircraft demonstrator system around the target scene along six straight line segments, which form a half-hexagon trajectory from an aerial view. Five of the straight line segments were used to capture bistatic radar measurements, while the longest segment, which was in a forward scatter configuration resulting in a loss of resolution, was used to ascend or descend the aircraft. This allowed for the complete set of measurements along the five measurement segments to be repeated at different altitudes, increasing

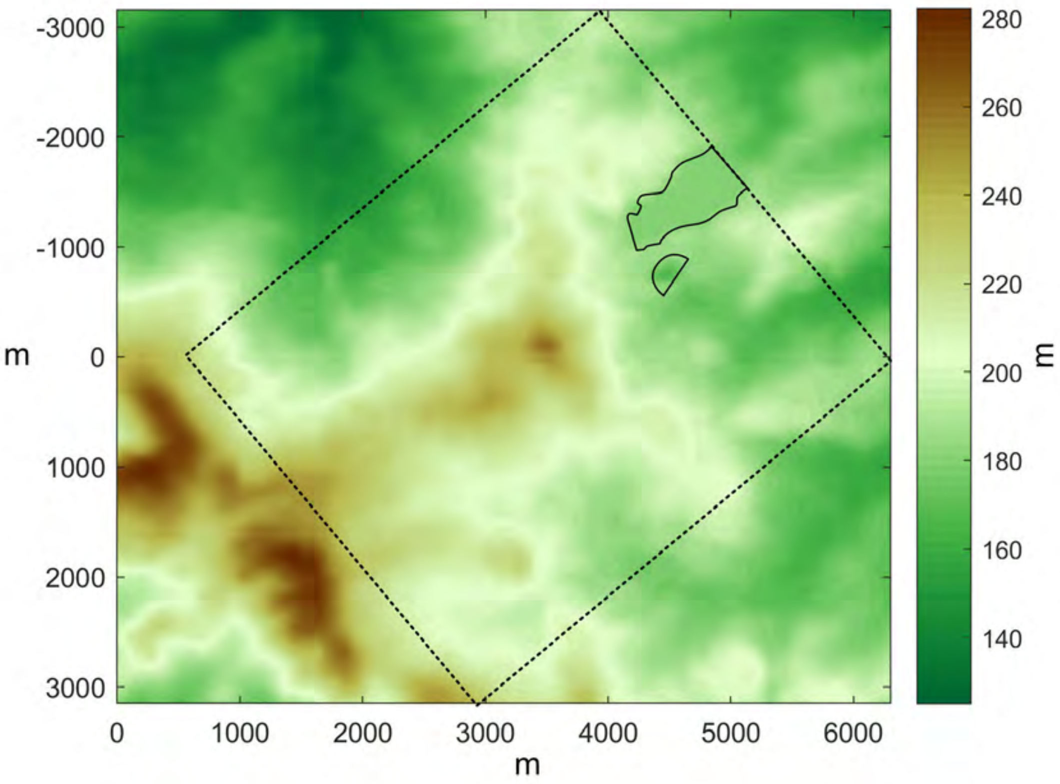

Figure 5.2: Elevation map of the Bruntingthorpe target area imaged for the bistatic measurement campaign

the total range of bistatic angles at which measurements were recorded.

5.3 Data Acquisition

Table 5.2 summarises the measurements from the bistatic airborne trial. In total, twenty-five measurements were recorded on 24 August 2018, constituting 328 GB of raw IQ data. The measurements are organised by the straight line segments of the flight path that the aircraft was traversing, with the segments numbered from one to five as shown in Figure 5.5. Five measurements were recorded for each of the five flight path segments, for a total of 25 measurements. Measurements were recorded at four possible altitudes: approximately 700 m, 900 m, 1100 m, and 1300 m. Due to the flight trajectory of the aircraft a measurement could not be recorded for every

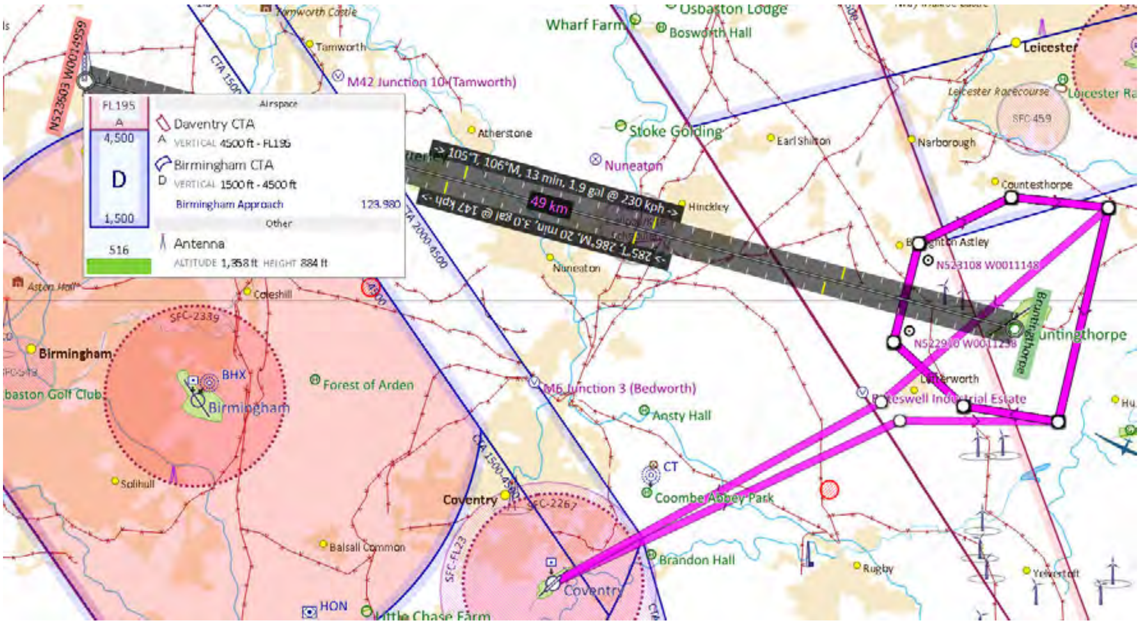

Figure 5.3: Planned flight route for the bistatic airborne measurement campaign shown in the SkyDemon application

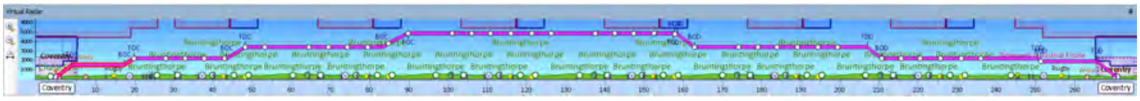

Figure 5.4: Planned altitude profile for the bistatic airborne measurement campaign shown in the SkyDemon application

altitude for each flight segment, therefore for some segments there are repeated measurements at the same altitude. The second column of the table indicates the segment of the flight route the aircraft was on during the measurement, while the last column shows the average altitude of the aircraft over the whole measurement.

5.4 Bistatic SAR Image Formation

The image formation algorithm used to process bistatic measurements into SAR imagery was the same backprojection technique used for generating monostatic imagery as described in Section 3.8 but with a modification to the definition of the image scene. Previously the image scene was defined within a Cartesian coordinate system such that the y-axis aligned with the aperture direction and the x-axis

Table 5.2: Table of measurements.

Measurement	**Path**	**Start Time**	**Recording Length (s)**	**Average Altitude (m)**
1	3	14:40:37	74.1081	694.26
2	4	14:42:22	51.5899	692.10
3	5	14:43:55	46.3340	725.60
4	1	14:49:37	87.9493	940.93
5	2	14:51:41	86.6124	974.57
6	3	14:53:43	57.1343	972.75
7	4	14:55:22	40.7372	976.07
8	5	14:56:36	46.4781	942.52
9	1	15:02:42	84.2662	1115.45
10	2	15:04:44	70.2546	1103.03
11	3	15:06:32	64.3695	1099.96
12	4	15:08:17	46.8451	1087.98
13	5	15:09:36	51.9307	1108.05
14	1	15:15:16	127.9592	1239.39
15	2	15:17:48	70.2415	1235.06
16	3	15:19:32	68.9046	1251.05
17	4	15:21:23	43.4635	1272.61
18	5	15:22:43	40.0294	1250.83
19	1	15:28:34	82.3525	1087.82
20	2	15:30:36	79.1937	1072.91
21	3	15:32:24	64.9462	1118.26
22	4	15:34:00	61.3810	1082.27
23	5	15:35:27	41.6416	1117.54
24	1	15:40:51	97.4389	954.90
25	2	15:42:57	80.5044	969.48

aligned with the down-range direction, with the aperture centre as the origin. The image scene within this coordinate system was then a rectangle with a specified length and width in range and cross-range respectively. Since the bistatic measurements were of the same area in object space, a fixed coordinate system which was independent of the chosen aperture direction was used for image formation. This allows for a simpler comparison of images of the same target scene generated with different apertures.

The image scene was first defined as a three-dimensional array of cells describing the ground surface to be imaged, with latitude and longitude coordinates defined

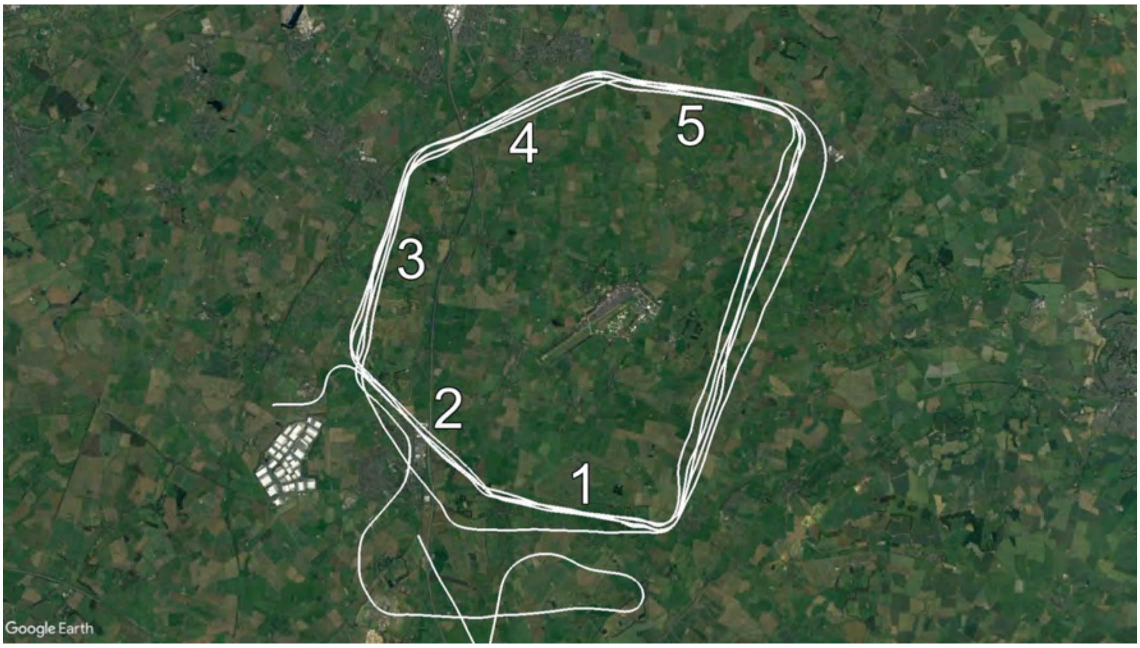

Figure 5.5: Actual flight route of the airborne platform as measured by the GNSS receiver. The different flight segments are labelled from 1-5

by the lower-left and upper-right corners of a rectangular region, and with altitude coordinates extracted from a digital elevation map of the same rectangular region. The scene, as defined in latitude longitude and altitude, was then transformed into a "local" Cartesian coordinate system with the transmitter as the origin point. The local coordinate system was defined such that the y-axis pointed north, the x-direction pointed east, and the z-direction pointed towards the centre of the earth in keeping with a right-handed coordinate system.

For the position of the radar demonstrator, provided by recorded measurements from the Spatial FOG GNSS receiver, the latitude longitude altitude coordinates underwent a series of pre-processing steps. The positional data was first transformed into a coordinate system aligned with the aperture direction, but with the transmitter as the origin. This allowed for the data to be smoothed in the y-direction, which pointed along the aperture direction, by fitting the data to a first order polynomial. Since the aircraft was known to be flying at an almost constant speed along the aperture direction during the measurement process, the expected curve describing the position along the aperture against time is a straight line. Smoothing, using the

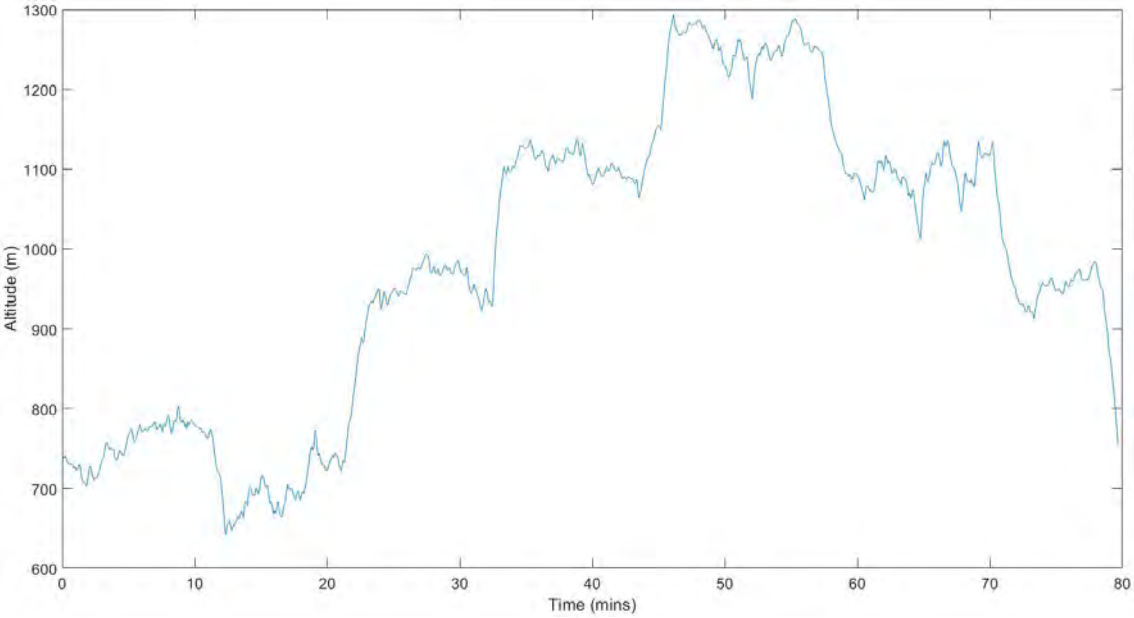

Figure 5.6: Actual altitude profile of the airborne platform as measured by the GNSS receiver

same process as described in Section 3.11, was applied to the positional data along the aperture and had the effect of mitigating the defocusing resulting from motion errors caused by inaccurate positional measurements from the GNSS receiver. A Kalman filter could also have been used, but it was found that a first order approximation of the position along the aperture was sufficient to produce focused SAR imagery. After smoothing, the positional data was then transformed into the same local coordinate system as the image scene ready for backprojection.

5.5 Results and Analysis

Due to the quantity of data, only the best images are shown for visual qualitative analysis. For the numerical analysis of average intensity and contrast, the full set of data was processed into SAR images. All of the images presented in this chapter were obtained using the backprojection algorithm with a cross-correlation matched filter. No additional processing, including autofocus techniques such as map drift, were included.

The collected data was formed into images using the image formation process described in Section 5.4. Rather than processing a full measurement as a single aperture, each measurement was split into a series of sub-apertures, each with 4329 DVB-T symbols which corresponds to 4 seconds of integration time. This allowed for a larger set of images to be produced, covering a range of bistatic angles from 4 to 140 degrees at four different flight altitudes. Processing shorter apertures also reduced the effects of motion errors which cause defocusing when accumulated over longer apertures. The physical length of each sub-aperture was dependent on the speed of the aircraft, which varied along different measurement paths depending on the direction of the prevailing winds on the day of the trial. For example, for the measurements recorded along paths 3, 4, and 5, the aircraft was travelling faster than for the measurements recorded along paths 1 and 2, suggesting a west to east prevailing wind.

For the comparisons shown in Sections 5.5.1 and 5.5.2, the processed SAR images were generated with 2000 pixels in width and 1200 pixels in height. With a scene spanning 10 km in width and 6 km in height, this corresponds to 5 meters per pixel in both directions. For the numerical analysis shown in Section 5.6, the image resolution for SAR images of the full target scene was decreased to 1000 pixels in width and 600 pixels in height in order to reduce the processing time, resulting in 10 meters per pixel in both directions. For SAR imagery of sub-regions of the target scene in Section 5.6, the image resolution was chosen to be 1000 pixels in width and 1000 pixels in height to correspond to the square sub-regions which each had a width and height of 1 km, resulting in 1 meter per pixel. The spatial resolution of the resulting SAR imagery is dependent on the bistatic angle and the synthetic aperture length. Equation 2.10 gives the range resolution for a particular bistatic angle, with a resolution of 19.7 m for the monostatic case. Equation 2.37 gives the cross-range resolution for particular aperture length at a particular range. The aperture length of each measurement is approximately 200 m, giving a theoretical cross-range resolution of 10 meters at 5 km, i.e. the centre of the image scene.

The altitude of the aircraft for a particular SAR image was determined by taking the mean of the altitude as measured by the GNSS receiver over the length of the aperture used to produce the image. Similarly, the aperture length was determined by the positional data from the GNSS receiver at the start and end of the aperture. The bistatic angle of an image is taken to be the angle between a line connecting the transmitter to the centre of the target scene and a line connecting the centre of the target scene to the centre of the aperture for that particular image. Because the bistatic angle can vary greatly over a SAR image, a bistatic angle map is shown where appropriate. The bistatic angle map is an image with the same dimensions as the corresponding SAR image of the target scene, however, rather than showing intensity, the bistatic angle map shows the bistatic angle at each pixel of the corresponding SAR image. The grazing angle of an image refers to the angle between the centre of the aperture and the ground plane at the centre of the target scene. There is another grazing angle, which is that between the transmitter and the ground plane at the centre of the target scene. Since both the transmitter and target scene are fixed, this value is constant for all images with a value of 0.34 degrees. Therefore, from this point forward, the term grazing angle refers to the receiver grazing angle. Figure 5.7 demonstrates the geometry and the definitions of the different angles. The bistatic angle is denoted as β, the grazing angle to the receiver is denoted γ_r, and the grazing angle to the transmitter is denoted γ_t.

5.5.1 Quasi-monostatic Imagery at Different Altitudes

Figure 5.8 shows a comparison of four quasi-monostatic SAR image results, produced from segment number 3 of the flight trajectory as shown in Figure 5.5, each corresponding to a different flight altitude, as shown in Table 5.3. All of the images shown are processed with an integration time of 4 seconds, corresponding to 4329 DVB-T symbols. The length of each aperture is dependant on the speed of the aircraft and is shown in the second column of Table 5.3. The first column shows

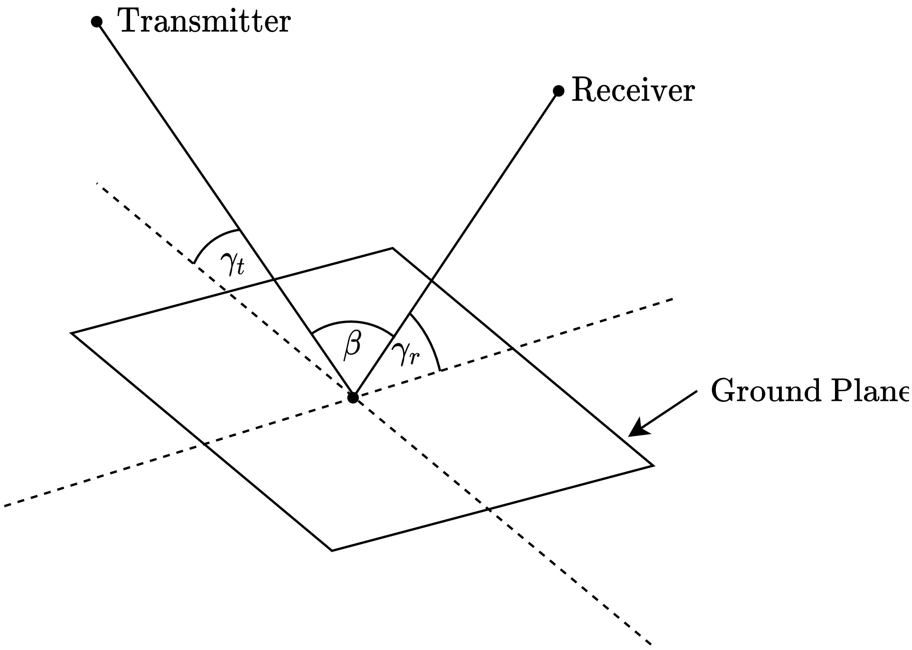

Figure 5.7: Diagram of the geometry of the bistatic experimental configuration showing the definitions of bistatic angle, transmitter grazing angle, and receiver grazing angle

the measurement number followed by, after a hyphen, the centre of the aperture in seconds relative to the start of the measurement. The SAR images are shown in dB and are normalised to the maximum intensity within the image, while the dynamic range is artificially clipped to -40 dB in order to more clearly observe the strongest returns amongst the background.

Table 5.3: Table of quasi-monostatic varying altitude measurements

Measurement	**Average Altitude (m)**	**Aperture Length (m)**	**Bistatic Angle (degrees)**	**Grazing Angle (degrees)**
1-49	694	228	5.31	6.85
6-42	972	218	5.41	9.16
11-32	1100	260	4.18	11.01
16-54	1251	215	9.96	12.82

Each aperture has been chosen such that the aperture centres are as close to each other as possible in latitude and longitude, given the trajectories of the aircraft during each measurement. Figure 5.9 shows a close-up aerial image depicting the

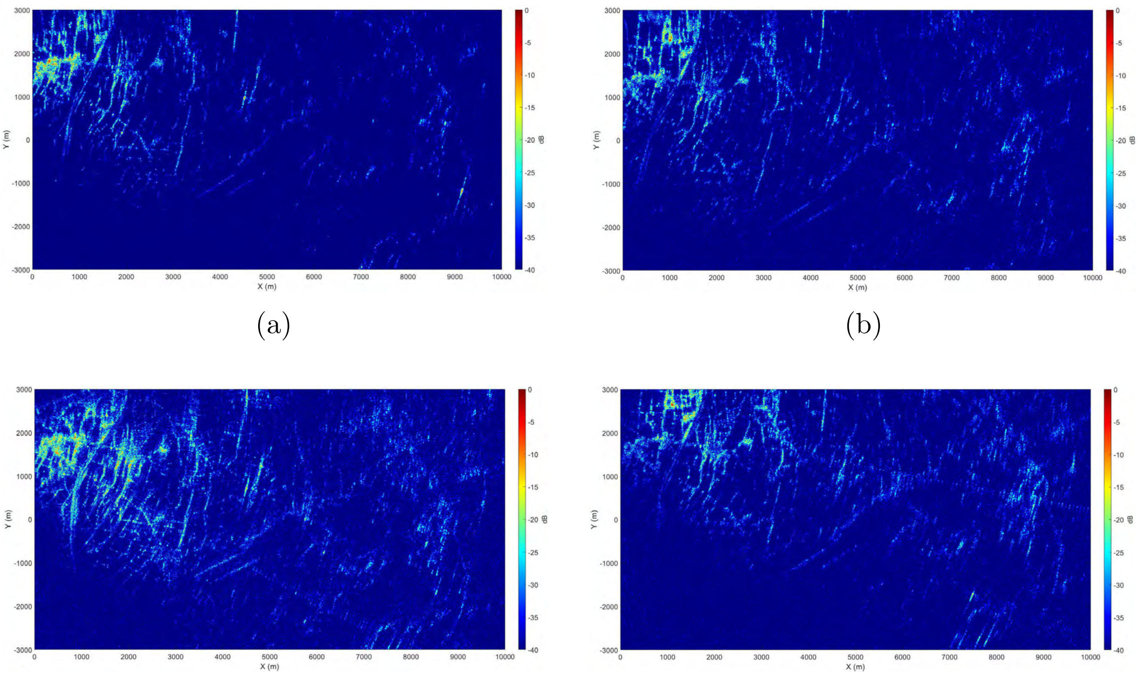

(a) (b)

(c) (d)

Figure 5.8: Quasi-monostatic DVB-T SAR images of the bruntingthorpe target area from segment 3 of the flight route, with altitudes of: (a) 694 m, (b) 972 m, (c) 1100 m, (d) 1251 m

flight paths of the receiver for each measurement, as well as the location of the aperture centre which was used to generate the images. The flight paths are labelled with the corresponding measurement number as shown in Table 5.2.

The first image result, a larger version of which is shown in Figure 5.10, is similar to the results shown in Figure 4.16 from the set of quasi-monostatic airborne measurements, described in Chapter 4. This is because of the similar target scene and quasi-monostatic geometry, as well as a similar flight altitude of approximately 700 m. The main difference between this result and the one shown in Chapter 4 is the aperture location, which in these results is located further to the west. Also, although the image scene is very similar, the image scene for the results shown in Chapter 4 is aligned to the aperture direction whilst the images shown here are north-aligned. The flight altitude of 694 m corresponds to a receiver to ground grazing angle of 5.31 degrees. On the left side of the figure the M1 motorway is visible as two lines of returns, which slightly curve, at approximately 800 m in the x-direction.

Figure 5.9: Aerial image showing the flight trajectories for the quasi-monostatic measurements and locations of aperture centres

These returns correspond to the trees and hedges which line each embankment of the motorway. Also due to the surrounding trees, Bruntingthorpe airfield is clearly outlined at approximately 5 km in the x-direction and -1 km in the y-direction. A point-like target is visible at (9100 m, -1800 m) in x and y respectively, and has been identified as a wind turbine, which was shown in Section 4.5.4 of Chapter 4, with a location in latitude and longitude coordinates of: 52.486517, -1.066848.

With an average flight altitude of 972 m, Figure 5.11 shows a larger version of Figure 5.8b. Immediately noticeable is that the amount of speckle and background noise is comparatively higher relative to the 694 m flight altitude in Figure 5.10. Returns from close-range targets such as the M1 motorway and surrounding fields and buildings are relatively stronger and more prominent. A forested area, located at (2500 m, 1800 m) in x and y respectively, is more clearly defined and closer to the ground truth shape, as opposed to Figure 5.10. This is also true for other forested areas located below the airfield at approximately (7000 m, -1100 m). However, far-range targets appear weaker in intensity, such as the wind turbine at (9100 m, -1800 m) which is now approximately 10 dB lower in intensity.

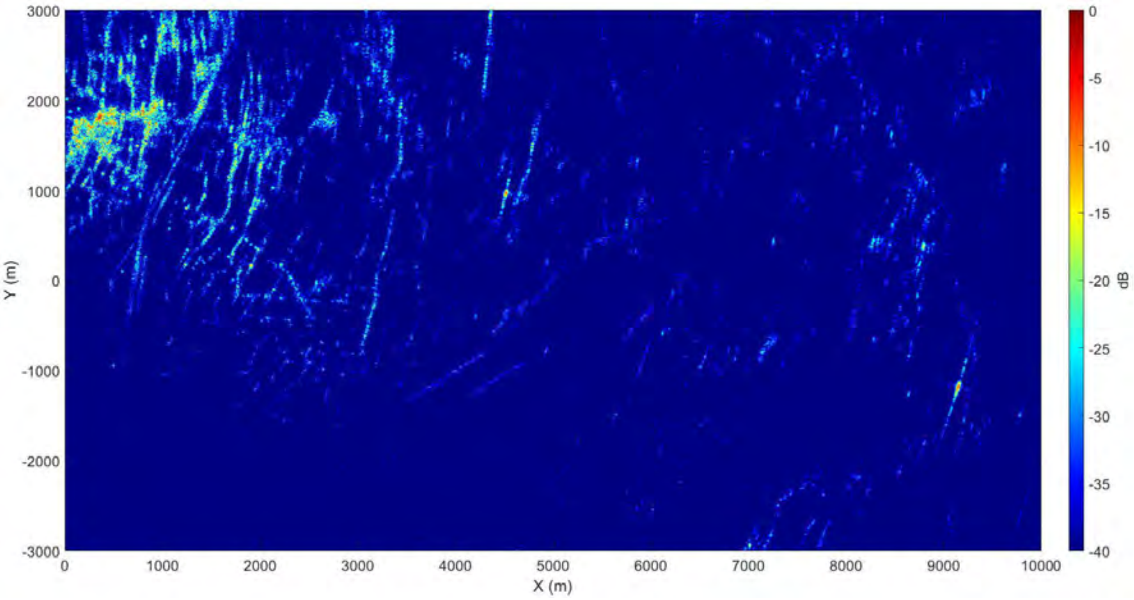

Figure 5.10: Quasi-monostatic DVB-T SAR image of the Bruntingthorpe target area with an aircraft altitude of 694 m

Figure 5.12, a larger version of Figure 5.8c, shows a SAR image of the target scene from a quasi-monostatic configuration and with an average aircraft altitude of 1100 m. This corresponds to a grazing angle between the receiver and the ground of 11 degrees. The features of the image are very similar to Figures 5.10 and 5.11, which were generated with lower aperture altitudes. Many of the same targets can be observed, including the outline of the airfield and the M1 motorway, as well as field boundaries at the near-range. Far-range targets appear more defined and easier to observe than in Figure 5.11. In general, returns appear to be more broad, especially in the 0 to 1 km range region, which may suggest that the image is not as focused as the previous images, and overall the image appears to have more speckle.

Figure 5.13 shows a larger version of Figure 5.8d, which shows a quasi-monostatic DVB-T SAR image with an aircraft altitude of 1251 m, corresponding to a receiver to ground grazing angle of 12.47 degrees. The features of the image appear shifted upwards in comparison to the previous images, which could be due to an inaccuracy in the measurements of the receivers position, however the image is still primarily in focus. The airfield and field boundaries that could be observed in previous imagery is

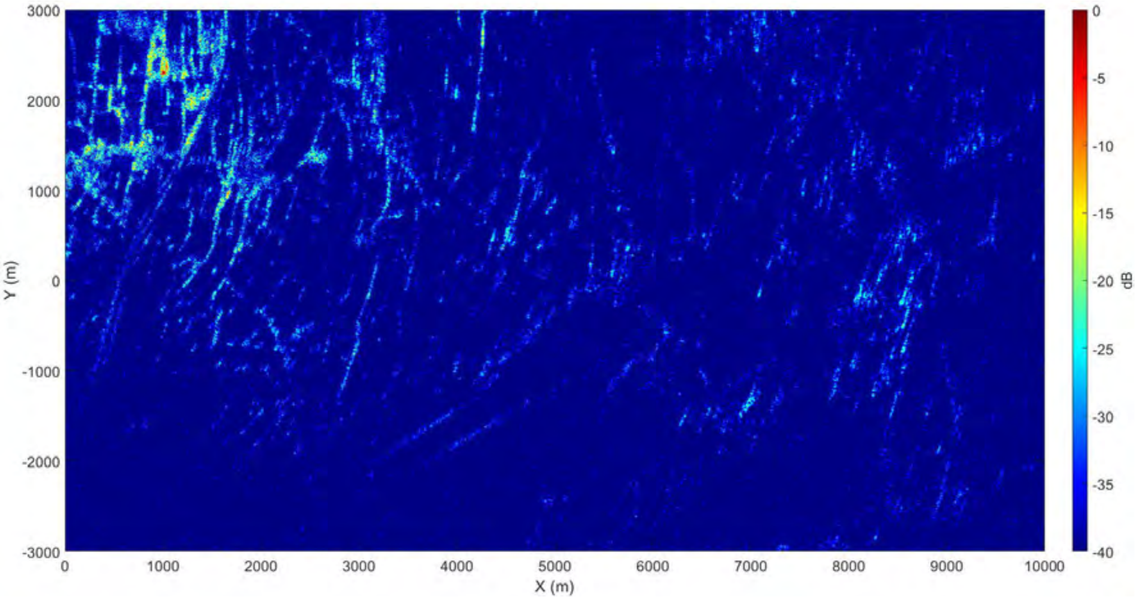

Figure 5.11: Quasi-monostatic DVB-T SAR image of the Bruntingthorpe target area with an aircraft altitude of 972 m

still visible, although the returns are not as broad as those in Figure 5.12, suggesting a more in-focus image. Background speckle and relative intensity is on the same order of magnitude as Figure 5.11 from visual observation. As with the other quasi-monostatic images, no target returns appear in the lower-left region outside of the main beam of the receiving antenna.

5.5.2 Bistatic Imagery at Constant Altitude

Figure 5.14 shows a comparison of five DVB-T SAR images with varying bistatic angles but with similar altitudes. Each image is processed with an aperture consisting of 4329 DVB-T symbols, corresponding to 4 seconds of dwell time, at an altitude of approximately 1100 m. The exact aperture length is dependent on the speed of the aircraft and is detailed in Table 5.4, which also includes the bistatic and grazing angles, measured at the centre of the image, as well as the latitude and longitude coordinates of the centre of the processed apertures. The bistatic angle is prefixed with a plus or minus indicating whether the bistatic angle is measured on the left side or the right side of the baseline respectively. The table also shows

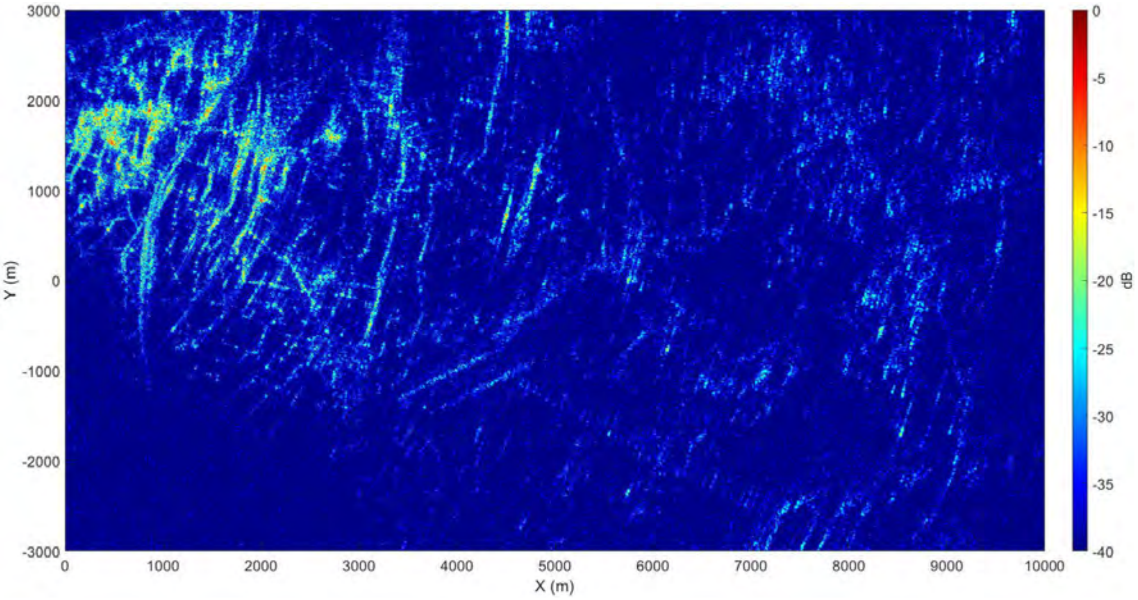

Figure 5.12: Quasi-monostatic DVB-T SAR image of the Bruntingthorpe target area with an aircraft altitude of 1100 m

the measurement number the aperture was extracted from, as well as the start time of the aperture relative to the beginning of the measurement. Figure 5.15 shows a comparison of the bistatic angle maps for each of the five images.

Table 5.4: Table of bistatic constant altitude measurements

Measurement	**Average Altitude (m)**	**Aperture Length (m)**	**Bistatic Angle (degrees)**	**Grazing Angle (degrees)**
9-2	1116	169	-109.82	11.48
10-22	1102	185	-50.13	11.23
11-16	1100	233	+7.13	10.77
12-26	1087	254	+59.05	11.69
13-38	1110	246	+112.06	10.02

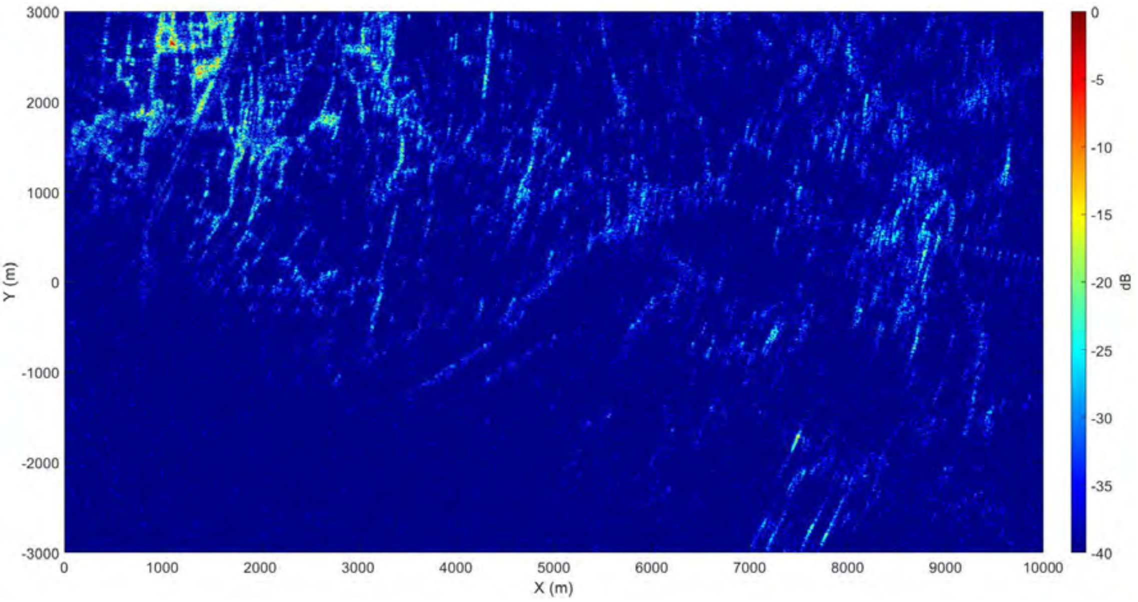

Figure 5.13: Quasi-monostatic DVB-T SAR image of the Bruntingthorpe target area with an aircraft altitude of 1251 m

Figure 5.16, a larger version of Figure 5.14a, shows a bistatic image generated from a 169 m long aperture with an average altitude of 1116 m, a bistatic of 109.82 degrees, and a grazing angle of 11.48 degrees at the centre of the image. The aperture used to generate the image is a sub-section of measurement 9, recorded along path 1 of the flight route. The bottom-left of the image is defocused, with a strong return spread over a large area. This is explained by the bistatic angle within this region as shown by the bistatic angle map in Figure 5.15a. As can be seen from the bistatic angle map, the bistatic angle increases from 110 degrees in the centre to around 170 degrees in the bottom-left region, thus approaching a forward scatter geometry resulting in a loss of resolution and imaging capability. The defocusing in the bottom-left region, as well as partially on the left side of the image, is also partly explained by the 50 degree 3 dB beamwidth of the receiving antenna, which for the processed aperture, places the bottom-left and bottom-right regions outside of the main beam of the antenna.

A very faint outline of the airfield can be observed at the centre of the image, with a series of defocused target returns visible along the lower-right edge of the

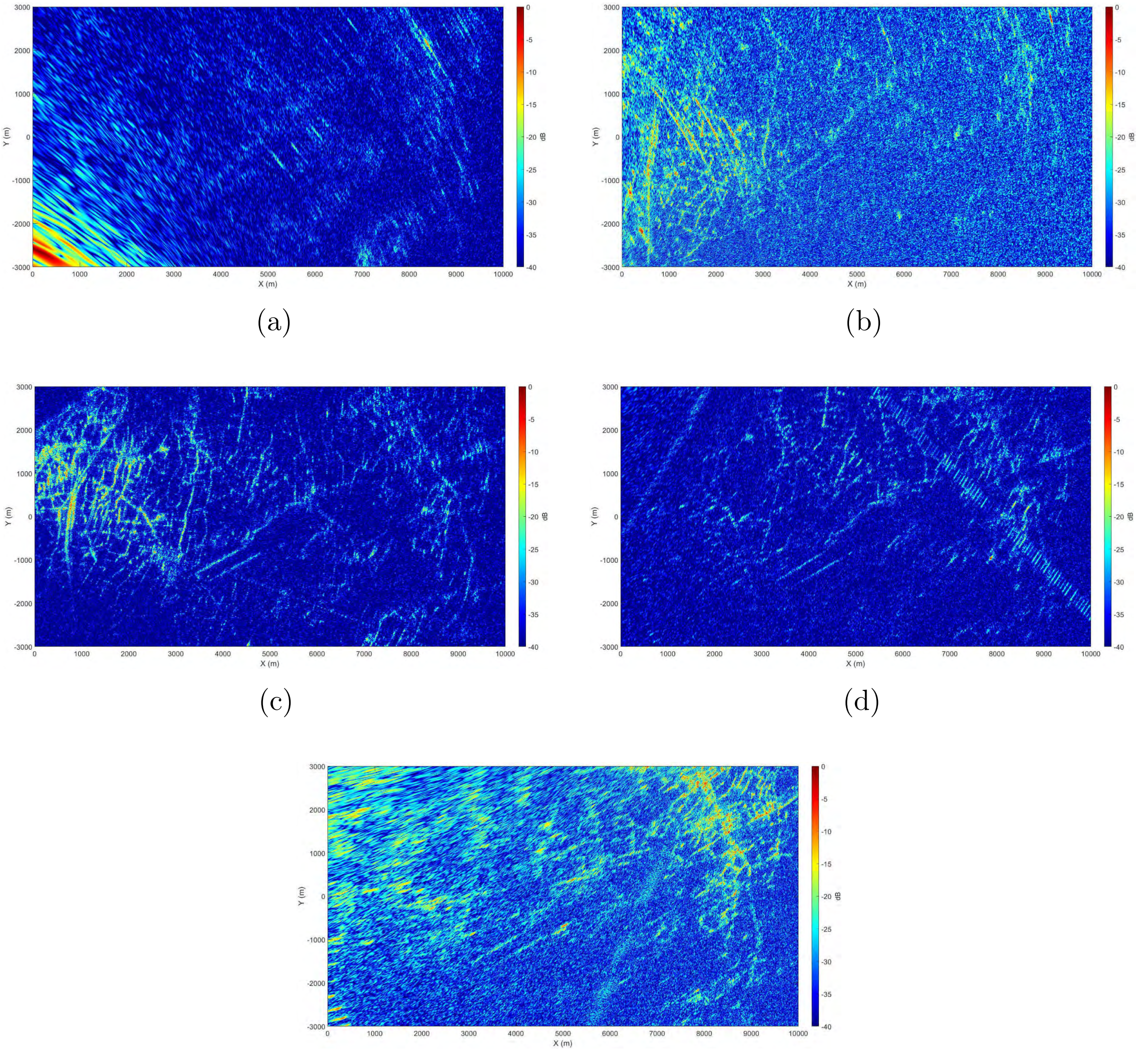

(a) (b) (c) (d) (e)

Figure 5.14: Bistatic DVB-T SAR images of the Bruntingthorpe target area from all five flight segments, with a constant altitude of approximately 1100 m, and with bistatic angles of: (a) 109.82°, (b) 50.13°, (c) 7.13°, (d) 59.05°, and (e) 112.06°

aerodrome, possibly originating from large aircraft hangers, or perhaps large aircraft, which can be observed in the ground truth imagery shown in Figure 5.1. A small region of the image between 6.5 km and 8 km in X and -2 km and -3 km in Y appears to be the most "in-focus", when visually inspecting the spread of the target returns in this region and comparing them to returns of the same targets from other focused imagery. This coincides with the region of the image which has the lowest bistatic angle whilst being within the main beam of the receiving antenna. Another possible cause of defocusing in regions of the image which are not in forward scatter configuration is the inaccurate positioning of the receiver.

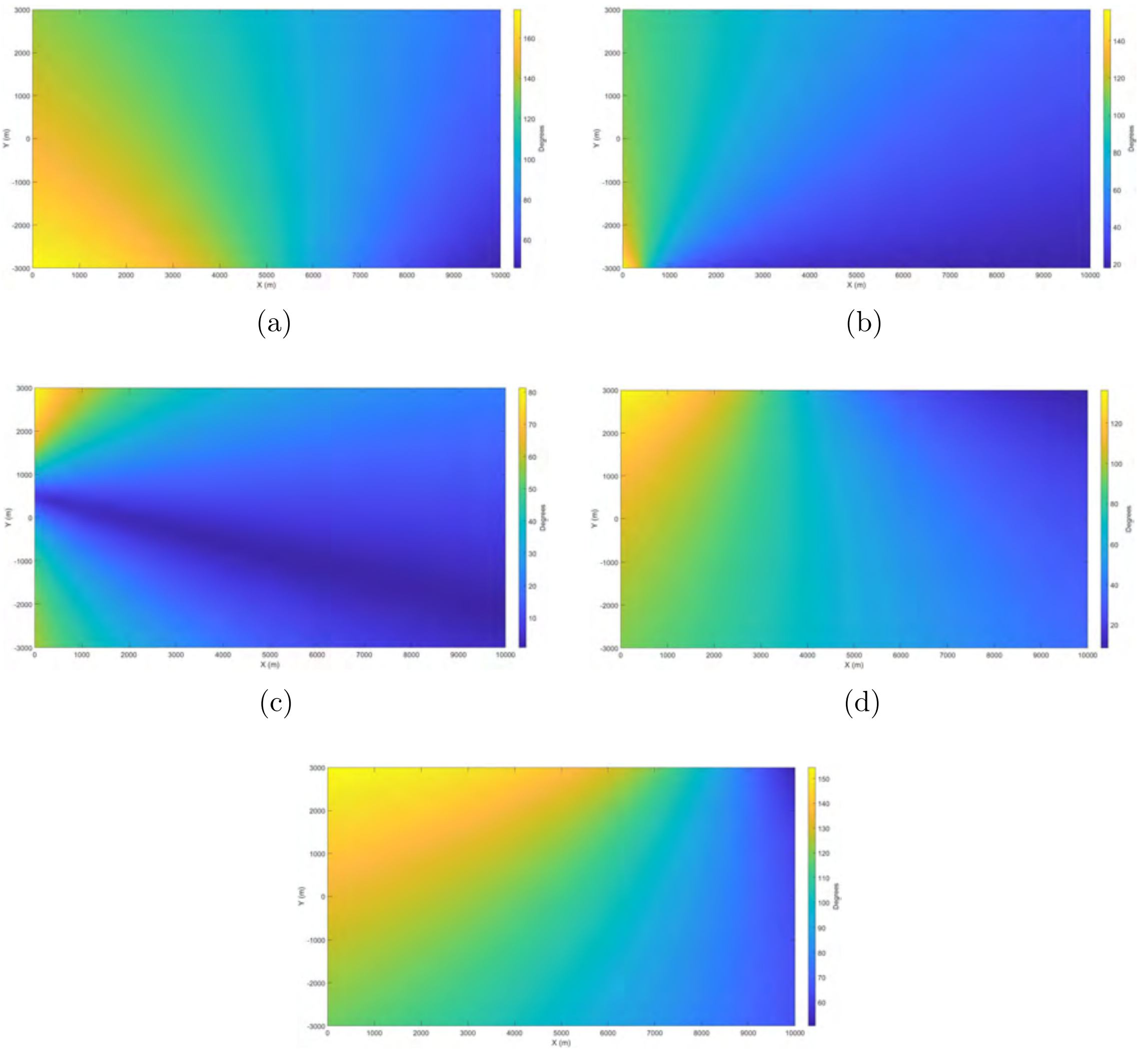

(a) (b)

(c) (d)

(e)

Figure 5.15: Bistatic angle maps of the Bruntingthorpe target area from all five flight segments, with a constant altitude of approximately 1100 m, and with bistatic angles of: (a) 109.82°, (b) 50.13°, (c) 7.13°, (d) 59.05°, and (e) 112.06°

A strong return can be seen at coordinates (8380 m, 2180 m) within the image, spread across several range and cross-range resolution cells. Comparison with ground truth imagery suggests that a possible source of this return could be from one of several large farm buildings in the area surrounding the village of Shearsby, located within the same region, using the outline of the airfield to approximately align and orientate the ground truth imagery. Due to the lack of structure in regions where stronger returns are not visible, only a small amount of information about the imaged scene can be extracted visually from the resulting image. Not shown here for brevity are the SAR images from other apertures extracted from measurement 9, because

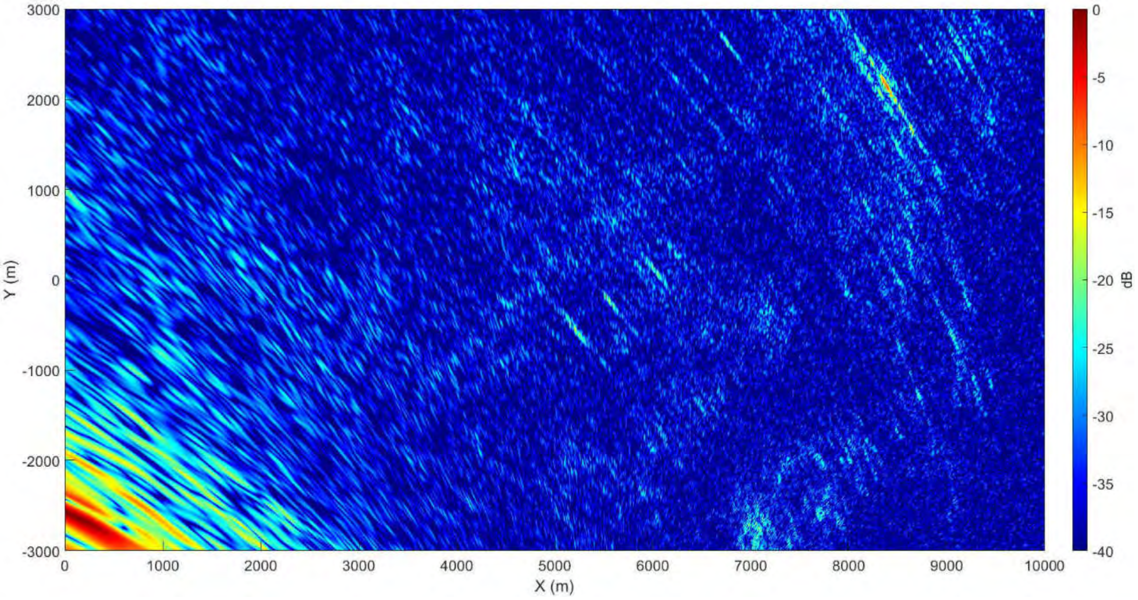

Figure 5.16: Bistatic DVB-T SAR image of the Bruntingthorpe target area with an aircraft altitude of 1116 m and a bistatic angle of 109.82 degrees

all other processed images are either equivalent in detail to Figure 5.16 or present a completely defocused image in which no details can be extracted.

Figure 5.17, a larger version of Figure 5.14b, shows a bistatic image of the target scene formed with an aperture 185 m in length, 1102 m in altitude, a bistatic angle of 50.13 degrees, and a receiver grazing angle of 11.23 degrees. The aperture is a sub-section of measurement 10, which was recorded along flight path 2. The majority of the strongest returns are located on the left side of the image where the M1 motorway can be seen at approximately 570 m in the X direction and spans vertically from -3 km to 1 km in the Y direction. To the right of the M1 motorway are a collection of returns corresponding to field boundaries as well as the village of Gilmorton, located between approximately 2 km and 3 km in X and -1.2 km and -0.6 km in Y. Based on the shape of returns outlining field boundaries, and by comparing them to the ground truth imagery, a strong return at coordinates (1831 m, 388 m) and another weaker return at coordinates (2081 m, 152 m) can each be attributed to wind turbines. Both returns appear spread out over multiple resolution cells suggesting that they are defocused or affected by some form of interference. Two

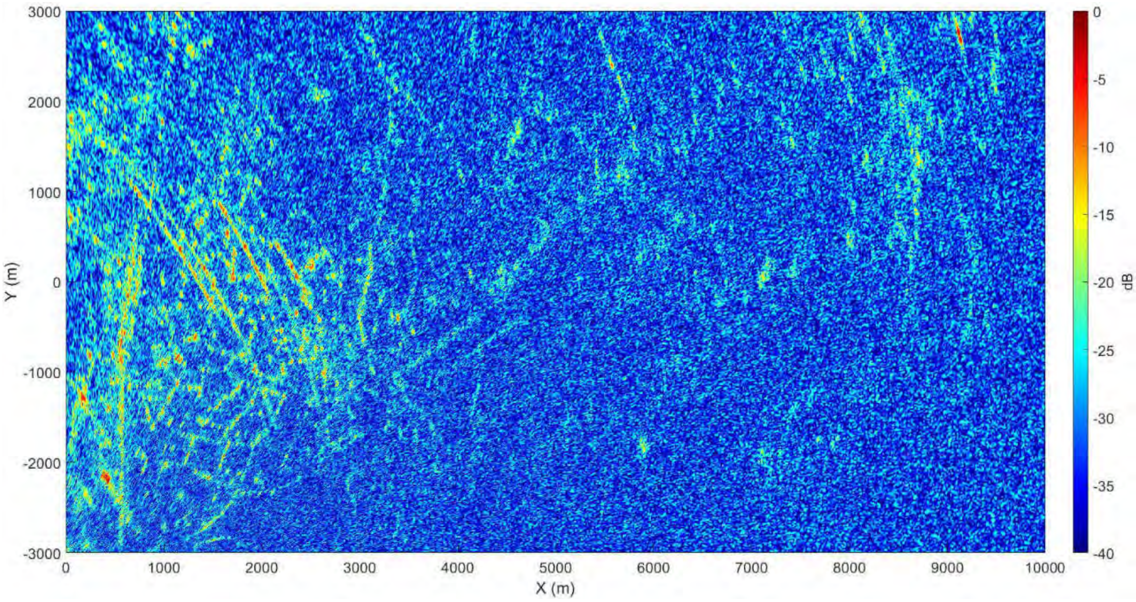

Figure 5.17: Bistatic DVB-T SAR image of the Bruntingthorpe target area with an aircraft altitude of 1102 m and a bistatic angle of 50.13 degrees

other wind turbines located nearby in the ground truth imagery cannot be visually located in the SAR image due to the presence of multiple strong returns in the same area.

The airfield, located in the centre of the image, can be seen as a an outline of returns predominantly on the northern side of the airfield. Unlike Figure 5.16, no strong returns are visible along the southern edge of the airfield where the aircraft hangers are located. At coordinates (2600 m, 2070 m) there is a patch of returns which, when compared with ground truth imagery, corresponds to the location of a small forested area. This is also true for similar patches located at (4600 m, 1625 m), (5903 m, -1835 m), (7125 m, -1960 m), and (7140 m, 38 m). In the top right of the SAR image are a collection of returns that appear to have some structure and may correspond to field boundaries or a group of wooded areas located near the village of Shearsby, however, no specific targets can be identified. A large and strong return can be seen at coordinates (9125 m, 2745 m), spread over multiple resolution cells, suggesting that the target returns are either defocused or from a large object. Another point-like target is visible, located at coordinates (5575 m, 2420 m), which is not observed in Figure 5.16.

Using the airfield to judge alignment, it is evident that the SAR image in Figure 5.17 is distorted in comparison to Figure 5.16, resulting in a shift of target locations between images. The exact form of the transformation describing this distortion is difficult to determine, but by comparing the relative size and orientation of the outline of the airfield, the transformation appears to correspond to a rotation and a skew with a transformation origin at the location of the receiver. This distortion is likely the result of inaccurate positional data from the GNSS receiver. Realigning the images reveals that the return at coordinates (9125 m, 2745 m) is likely from the same target as the return located at (8380 m, 2180 m) in Figure 5.16.

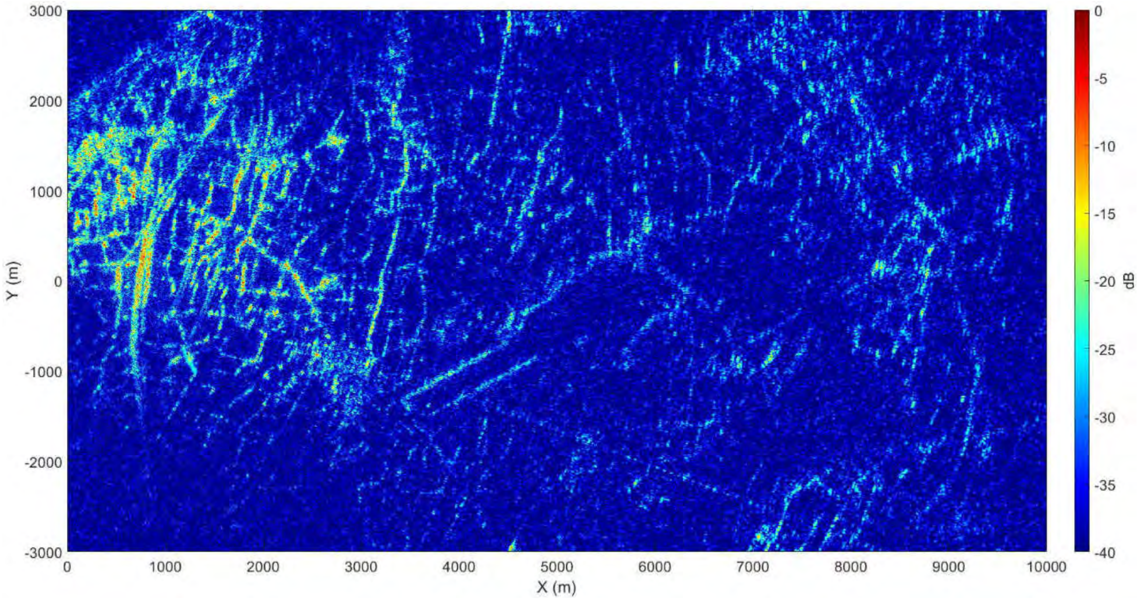

Figure 5.18: Bistatic DVB-T SAR image of the Bruntingthorpe target area with an aircraft altitude of 1100 m and a bistatic angle of 7.13 degrees

Figure 5.18, a larger version of Figure 5.14c, shows a SAR image of the target scene using a 233 m aperture from measurement 11, which was recorded along flight path 3. The aperture geometry is in a quasi-monostatic configuration with a bistatic angle of 7.13 degrees, an altitude of 1100 m, and a grazing angle of 10.77 degrees. Many of the features are the same as those shown and discussed for Figure 5.12, but the main features are summarised here for completeness.

In comparison to Figures 5.16 and 5.17, more features and target returns can be observed throughout the image. Field boundaries and the airfield can be clearly identified, as well as the M1 motorway, and a vertical line of trees and bushes to the left and above the airfield. The amount of speckle is significantly reduced in comparison to Figure 5.17, and target returns can be seen in the bottom-right region of the image which were not visible before. On the contrary, there are no target returns in the bottom-left region of Figure 5.18, as well as in the very top-left of the image. This is due to these areas being outside of the main beam of the receiving antenna.

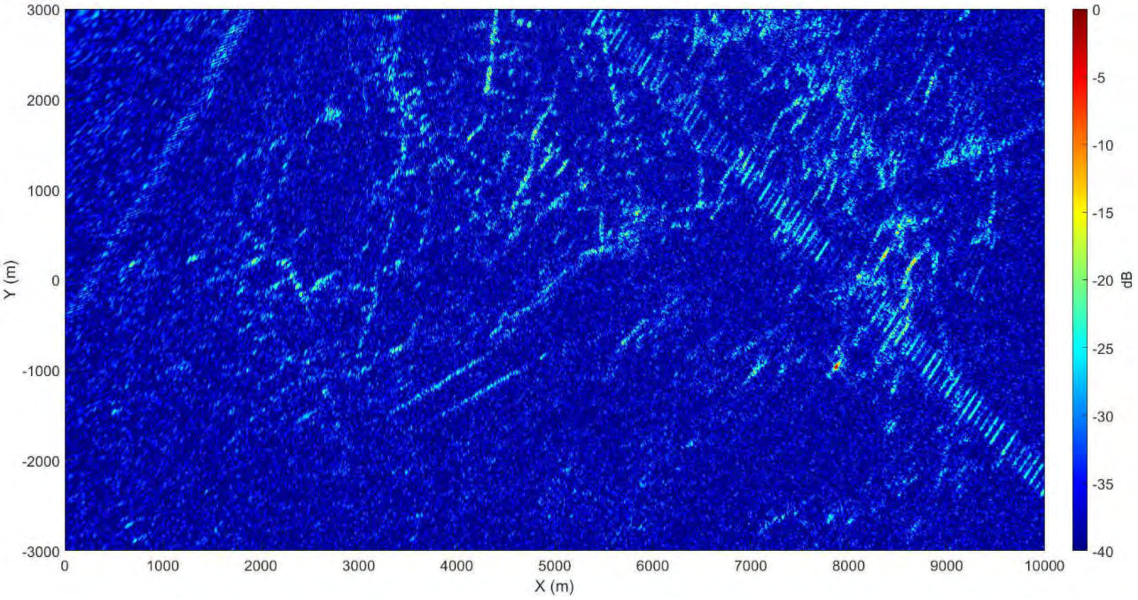

Figure 5.19: Bistatic DVB-T SAR image of the Bruntingthorpe target area with an aircraft altitude of 1087 m and a bistatic angle of 59.05 degrees

Figure 5.19, an enlarged copy of Figure 5.14d, shows a bistatic DVB-T SAR image generated using an aperture with length 254 m at an altitude of 1087 m, with a configuration resulting in a bistatic angle of 59.05 degrees and a grazing angle of 11.69 degrees. The aperture represents a sub-section of measurement 12, which was recorded along flight path 4. The bistatic angle is similar to that of Figure 5.17, however, the geometry is different, in that the receiver is located on the opposite side of a line extending from the transmitter to the centre of the target scene. This geometry means that the transmitter illuminates the front side of the reference channel receiving antenna as opposed to the back face. An artefact is visible as a line of returns in the upper-right quadrant of the image and is due to direct signal interference.

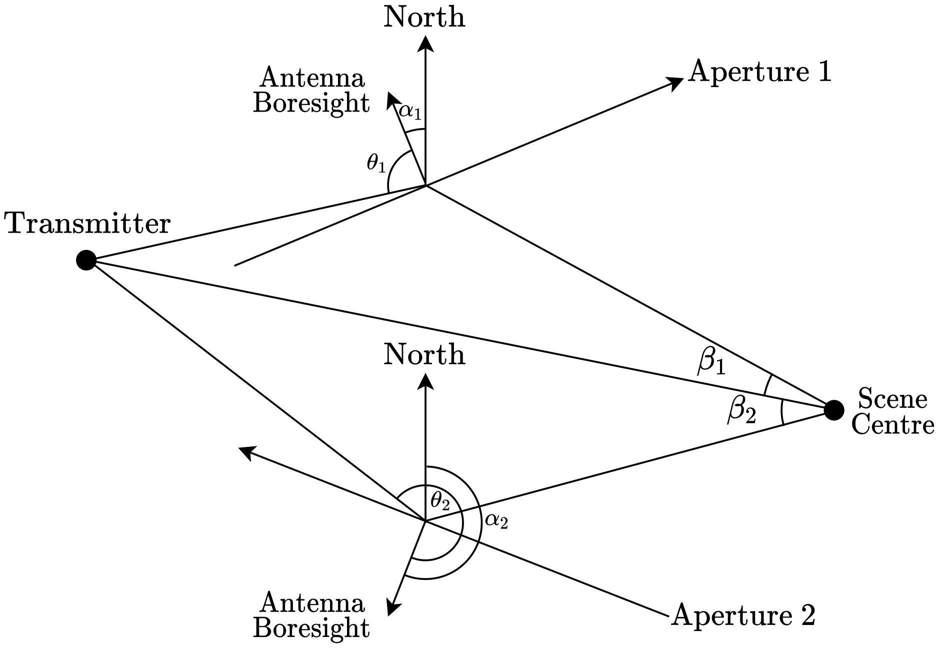

Figure 5.20: Diagram showing the difference in look angles between different flight segments with similar bistatic angles. An artefact due to direct signal interference is visible as a line in the upper-right quadrant of the image.

Figure 5.20 demonstrates the difference in geometry between the two apertures with similar bistatic angles but on opposite sides of the transmitter to scene line. The two apertures are labelled as Aperture 1 and Aperture 2 and represent apertures along flight paths 4 and 2 respectively. The corresponding bistatic angles to the target scene centre are labelled as β_1 and β_2 and are similar. However, the angle between a line connecting the transmitter to the receiver, and the look direction of the reference channel receiving antenna, θ_1 and θ_2, is very different due to the location of the transmitter and the direction of motion of the receiver along each aperture. For Aperture 1, representing flight path 4, the direct signal from the transmitter is received by the front face of the reference channel patch antenna as $|\theta_1| < 90°$. Whereas for Aperture 2, $|\theta_2| > 90°$, and therefore the direct signal from the transmitter is received on the back face of the reference channel patch antenna.

By the same reasoning, the direct signal will be received on the back face of the antenna for flight paths 1 and 2, and on the front face for flight paths 3, 4 and 5, based on the geometry of the scene and location of the transmitter. However, as previously stated, the patch antennas have a main beam width of 50 degrees, and thus for the cases where the direct signal is received by the front face of the antenna, the direct signal is expected to be received outside of the main beam for flight path 5. Therefore, only for flight paths 3 and 4 is the direct signal received by the main beam of the reference channel antenna. This partly explains the reduced background levels in Figures 5.18 and 5.19, as well as the presence of direct signal interference in the form of an artefact within the images.

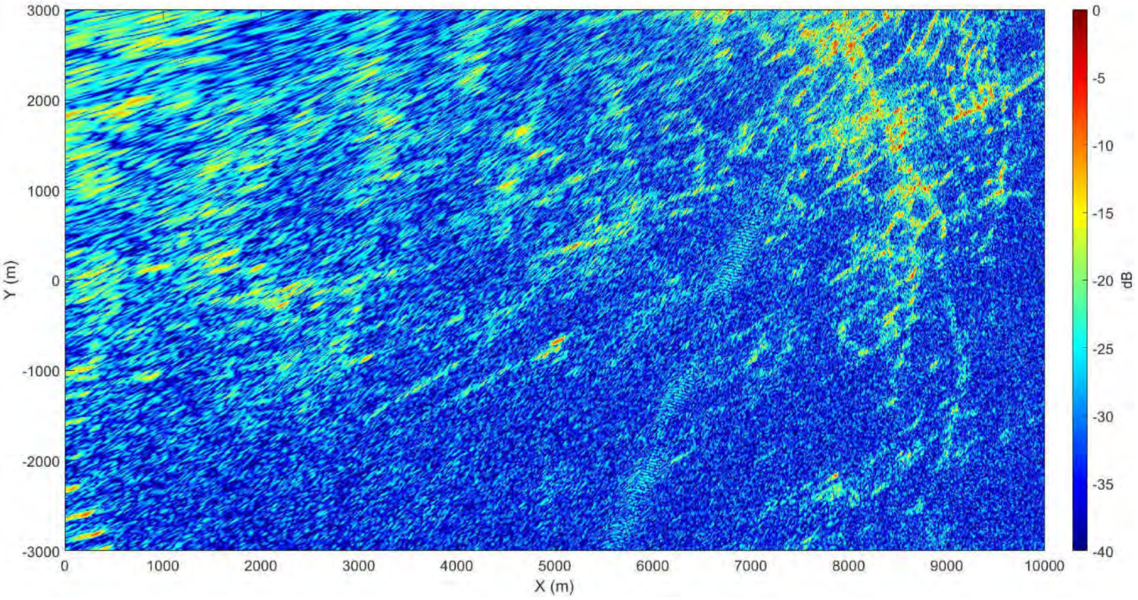

Figure 5.21: Bistatic DVB-T SAR image of the Bruntingthorpe target area with an aircraft altitude of 1110 m and a bistatic angle of 112.06 degrees

Finally, Figure 5.21 shows an enlarged version of Figure 5.14e, which itself shows a bistatic SAR image of the target scene from a 246 m long aperture with an altitude of 1110 m. The aperture was extracted from measurement 13, which was recorded along flight path 5, and the geometry results in a bistatic angle of 112.06 degrees and a grazing angle of 10.02 degrees. Due to the geometry of receiving antenna with respect to the target scene, objects in the upper-right region of the image display a higher contrast than in the upper-left of the image. Targets in the upper-left of the image are completely defocused, which is explained by the bistatic angle map of the measurement, shown in Figure 5.15e. The bistatic angle map shows that the bistatic angle increases from around 100 degrees in the centre of the image, to around 150 degrees in the upper-left corner, approaching a forward scatter configuration. The bistatic angle at the centre of the image is similar to the bistatic angle at the centre of the image shown in Figure 5.16, however, unlike Figure 5.16, more in-focus target returns can be observed in the upper-right region of the image. This is likely due to the angle between the transmitter and the antenna look direction, resulting in the direct signal being received by a side-lobe of the reference channel antenna. The outline of the airfield is also visible, with a strong return from a source along the lower edge of the airfield. Comparison with the ground truth imagery suggests that this could be from either an aircraft hanger, or one or more of the parked aircraft.

5.6 Numerical Analysis of Bistatic DVB-T SAR Imagery

Up to this point in the thesis DVB-T SAR imagery has been analysed visually by describing the shape, relative size, and density of returns and comparing them to the likely targets that produced them using a combination of ground truth imagery and intuition. This section presents a numerical approach to analysing bistatic returns from known targets by calculating how values such as intensity and standard deviation change over varying bistatic angle.

For the numerical analysis each measurement, listed in Table 5.2, was split into equal length sub-apertures of 4 seconds, corresponding to 4329 DVB-T symbols. In total, after image formation, this produced 404 DVB-T SAR images. The generated SAR images were manually filtered by visual inspection and comparison to ground truth imagery to determine whether the image was in-focus and not distorted due to errors. Images that were out of focus or heavily distorted were discarded. For each of the resulting images the aperture altitude, bistatic angle, receiver grazing angle, mean intensity, maximum intensity, minimum intensity, and image standard deviation were measured and recorded.

5.6.1 Intensity and Standard Deviation Definitions

As shown in Section 2.2.3, a SAR image is a two-dimensional array of cells, where each cell corresponds to a point in the target scene, and where the value of each cell is a complex value representing the magnitude and phase of the received signal from the corresponding point after matched filtering and integration over the synthetic aperture. The magnitude of this complex value is called the intensity and is a function of the radar-cross-section of targets located within the cell, as well as propagation affects, atmospheric attenuation, and gain from the receiving antenna, receiver system, and image formation.

For bistatic imagery the RCS depends on the aspect angles to both the receiver and the transmitter. In general, the bistatic RCS can be categorised into three different regions depending on the bistatic angle:

1. Pseudo-monostatic
2. Bistatic
3. Forward Scatter

The first region, pseudo-monostatic refers to an effective equivalence between a monostatic and bistatic radar for small bistatic angles. There is no standard definition for the bistatic angle below which can be considered quasi-monostatic, however, Willis [39] explains that for bistatic angles typically less than 5 degrees this equivalence holds. As the bistatic angle increases, the start of the bistatic region refers to bistatic angles for which the equivalence theorem fails and the target RCS is reduced in comparison to the monostatic case. This reduction in RCS is due to a combination of three main factors[39]:

1. Changes in the bistatic angle causing changes in relative phase between discrete scattering centres
2. Changes in radiation from discrete scattering centres. For example, when a discrete scattering centre is reflected away from the receiver.
3. Changes in the existence of discrete scattering centres caused by shadowing.

These factors usually contribute to an overall reduction in RCS with increasing bistatic angle. Assuming that effects other than reflectance are constant over the target scene, and by normalising the intensity of a SAR image by the maximum intensity within the image, the relative intensity of an image cell over different bistatic angles can be used to analyse meaningful information about a target.

Standard deviation is also a useful metric for analysing SAR imagery. Given an N by M image of cells, where each cell represents an intensity, the two-dimensional standard deviation of image cell intensities is given by:

$$SD = \sqrt{\frac{1}{MN}\sum_{i=0}^{N-1}\sum_{j=0}^{M-1}(I_{ij} - \bar{I})^2} \tag{5.1}$$

where $\bar{I}$ is the average intensity of the entire image and I_{ij} are the intensities of the i-th and j-th image cell. The two-dimensional standard deviation can be thought of as the measure of the dispersion or spread of intensity over the image. Therefore, standard deviation provides a method of determining whether a SAR image is correctly focused.

5.6.2 Full Target Scene

Figure 5.22 shows a plot of the average intensity over DVB-T SAR imagery of the full target scene against the bistatic angle. The average intensity is calculated by taking the mean value of each image cell and then normalising to the maximum value across all images. The results show a negative correlation between bistatic angle and image intensity. That is, the image intensity decreases approximately linearly with increasing bistatic angle, with an approximately 10 dB decrease from 0 to 70 degrees. The intensity of a target with changing bistatic angle is highly dependent on the shape of the target, as demonstrated by the spread in intensity shown in Figure 5.22. For example, for a spherical target the highest intensity would occur at a bistatic angle of 0 degrees and decrease for increasing bistatic angle. However, a target with a more complex shape may have a higher RCS at a higher, non-zero, bistatic angle. The results show that on average, across the full image containing many different targets, the average RCS decreases with increasing bistatic angle.

Figure 5.23 shows a plot of the standard deviation for DVB-T SAR imagery of the full target scene as the bistatic angle increases. The results show a similar negative correlation as with the intensity, with an approximately linear relationship. The standard devaition decreases by approximately 20 dB from 0 to 70 degrees in bistatic angle, and the maximum span of the results is approximately 5 dB. This shows that, on average, targets appear more defocused for larger bistatic angles.

5.6.3 Sub-regions of Full Target Scene

Figure 5.25 shows an aerial image of the target scene with four sub-regions highlighted with a white outline. Each region contains a particular type of target which represent different SAR image textures.

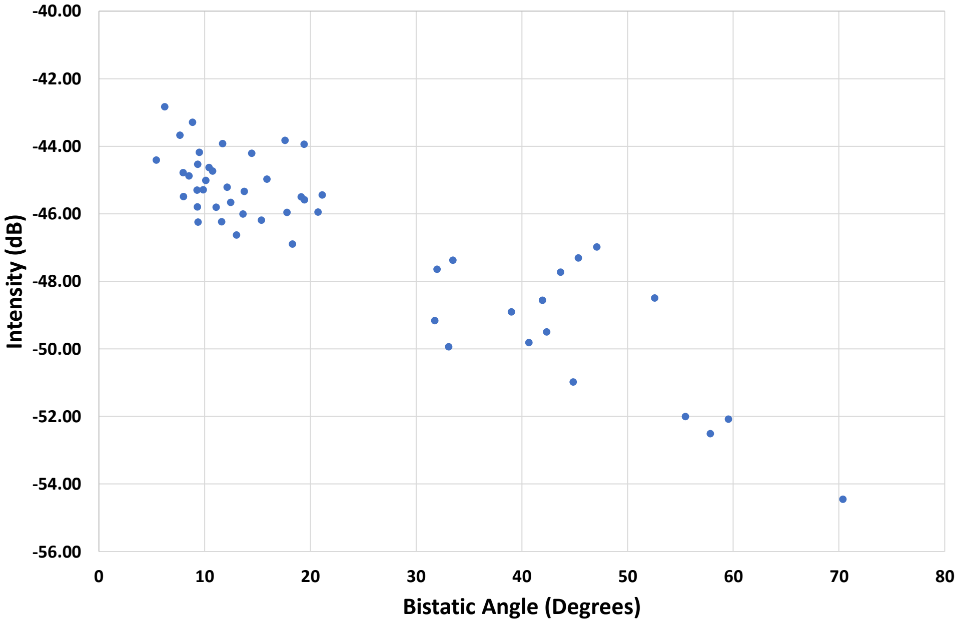

Figure 5.22: Graph of image intensity against increasing bistatic angle for DVB-T SAR imagery of the full target scene

1. The first region encompasses a village, which is formed of predominantly one and two story closely spaced buildings, and represents a built-up or urban area.
2. The second region contains mostly empty fields with a small number of sparsely scattered vegetation, including trees and hedgerows.
3. The third region represents a collection of primarily woodland areas with some fields in-between.
4. The fourth region contains a wind turbine surrounded by fields.

The process for numerical analysis of image intensity and standard deviation was repeated for each of the four regions, close-up images of which can be seen in Figure 5.25. The range of bistatic angles varies for each target region due to the location of the region relative to the platform trajectory. For example, the region containing

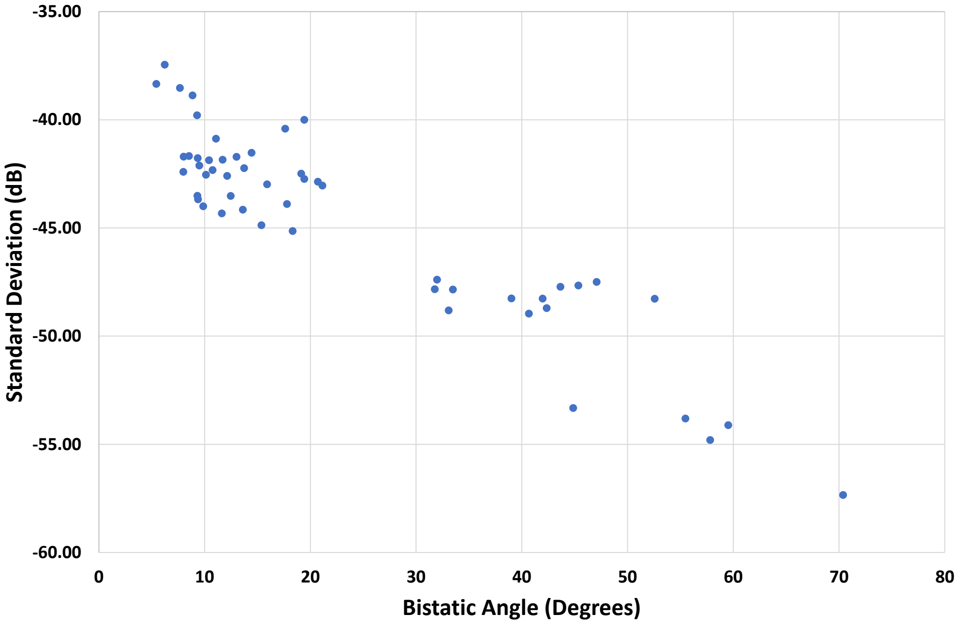

Figure 5.23: Graph of image standard deviation against increasing bistatic angle for DVB-T SAR imagery of the full target scene

the buildings is closer to the flight path, and hence closer to the synthetic apertures, and therefore has a larger range of bistatic angles from approximately 10 to 140 degrees. In contrast, the wind turbine target area which is located further from the flight route has a range of bistatic angles from around 5 to 80 degrees. For each set of results for each target region, the results were independently filtered to include only the in-focus results, which also contributes to the range of bistatic angles for a particular region.

For all four regions the correlation between bistatic angle and intensity, as well as the correlation between bistatic angle and standard deviation, is negative. The main difference between the different regions is the span of the results for intensity and standard deviation. For the region encompassing the buildings, there is a span of up to 10 dB for intensities at the same bistatic angle, as shown in Figure 5.26a, and up to nearly 20 dB for standard deviation measurements, as shown in Figure 5.26b.

Figure 5.24: Aerial image of the target area with the locations of four smaller target areas, used for numerical analysis, indicated by white boxes

This is due to the complex structure of the target region, which contains many buildings with different shapes and orientations which reflect differently from one another, however the specific bistatic RCS is not known for any particular target.

For the region containing fields, although still a negative correlation with increasing bistatic angle, the average intensity and standard deviation has a greater variance at the lower bistatic angles. The span is again around 10 dB for intensity, and around 15 dB for standard deviation. Results appear more concentrated at higher bistatic angles, particularly for measurements of the average standard deviation in Figure 5.27b. This behaviour can be explained somewhat by the fact that the fields are effectively parallel with the incident waves, and thus are expected to reflect the majority of the energy away from the incident direction. At low bistatic angles the average intensity is comparable to the buildings region, shown in Figure 5.26a, but at higher bistatic angles the average intensity is 3-5 dB is comparatively higher, as shown in Figure 5.27a.

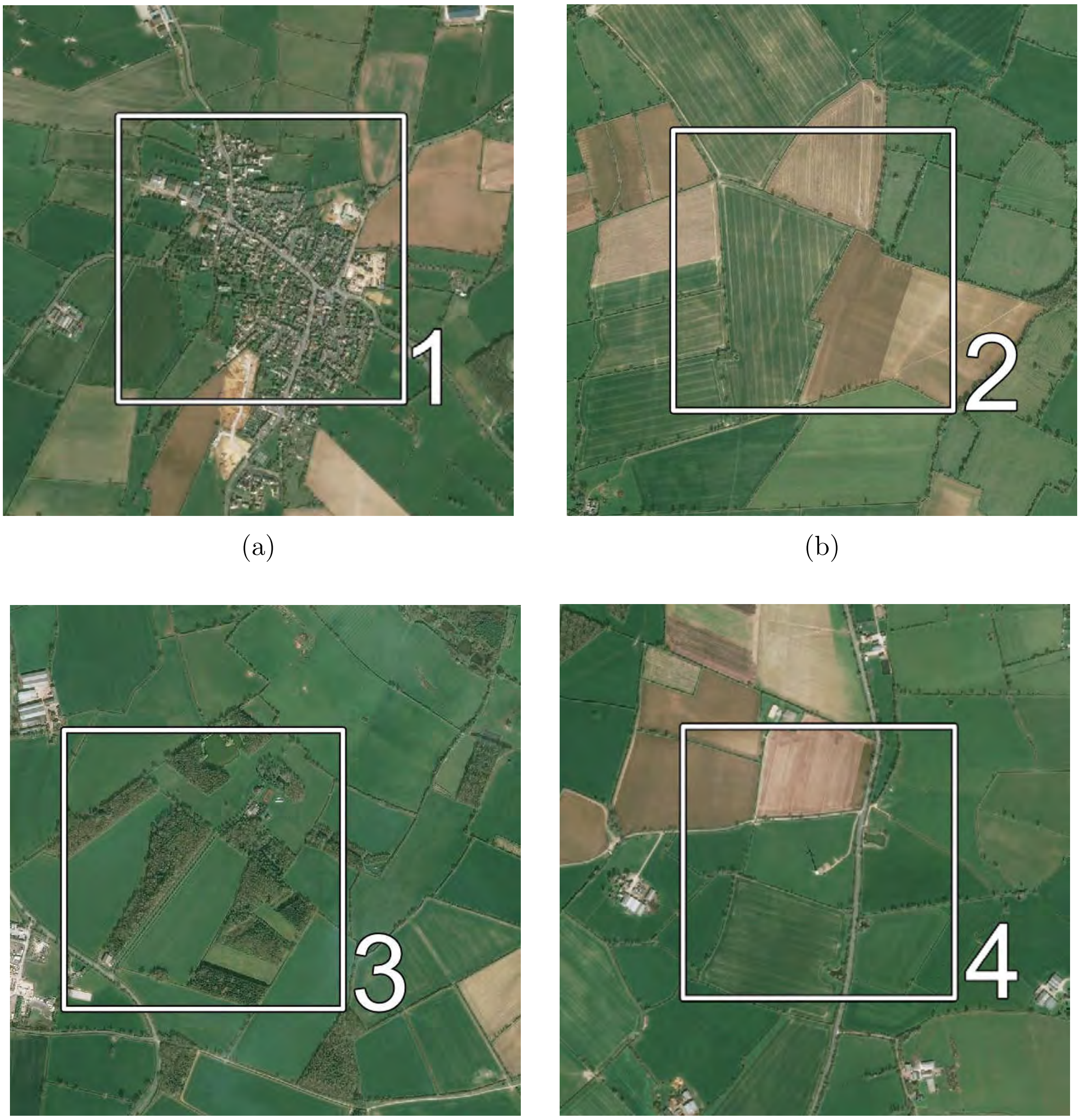

(a) (b)

(c) (d)

Figure 5.25: Images of the the four target sub-regions imaged with the DVB-T SAR system for numerical analysis

Similar results can be seen with the forested region, although with a smaller span of approximately 8 dB and an overall increase of approximately 3 dB in average intensity and standard deviation across all bistatic angles in comparison to Figure 5.26a, the region containing buildings. For average standard deviation, which is a measure of the spread of target returns and is an indication for the focus of an image, the results are more concentrated, with a maximum span of approximately 8 dB. It should be noted that due to the location of the forested region relative to the flight route, the range of bistatic angles, in comparison to the buildings and fields regions, is lower, ranging from approximately 4 to 95 degrees. The concentration, and higher average values, of results for both intensity and standard deviation can be explained in part by the fact that forested regions produce strong returns at all bistatic angles measured, as was observed in Section 5.5.2.

Finally, for the region containing the wind turbine, the results for average intensity are approximately 5 dB lower for smaller bistatic angles, in comparison to the average intensity of the fields region shown in Figure 5.27a. Comparison with the fields region is important since the primary targets other than the wind turbine are the fields which surround it. However, unlike the fields region, the span of the results for average intensity show less dispersion and the same is true for the standard deviation. The results also suggest a non-linear relationship between average intensity and standard deviation with increasing bistatic angle. The results for image standard deviation for the wind turbine region, shown in Figure 5.29b, demonstrate the least dispersion of all the regions, but with lower average values at higher bistatic angles. Although the wind turbine has been shown to behave similar to a point-like target in quasi-monostatic imagery, in realty the wind turbine is a complex target with a non-trivial bistatic RCS. Therefore, although these results provide an idea of the general behaviour, it is not possible from this initial analysis to determine the cause of the observed behaviour in intensity and standard deviation for larger bistatic angles.

Figure 5.30a shows the results of average intensity versus bistatic angle for all four of the regions, plotted onto the same axes. It can be seen from this graph that the average intensity of the wind turbine is around 10 dB lower than the other regions. This is most likely due, in part, to the increased distance between the receiver and the target as well as the bistatic scattering properties of the turbine. Similarly, Figure 5.30a shows the average standard deviation versus bistatic angle for all four regions, plotted onto the same graph. There is a much greater spread in the measured standard deviation for all targets at all bistatic angles. As with intensity, the standard deviation of the wind turbine is much lower than for other targets. Due to the number of factors that could influence the measured intensity and standard deviation, an investigation of bistatic scattering for different types of target is required in order to understand the observations made on the results presented, and could be the subject of further work on the topic of DVB-T SAR.

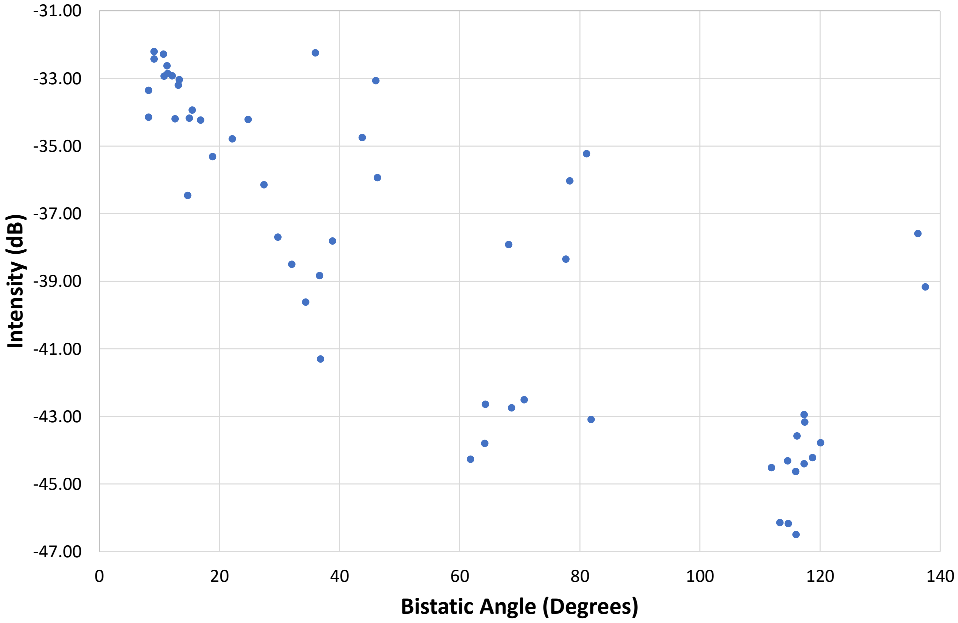

(a)

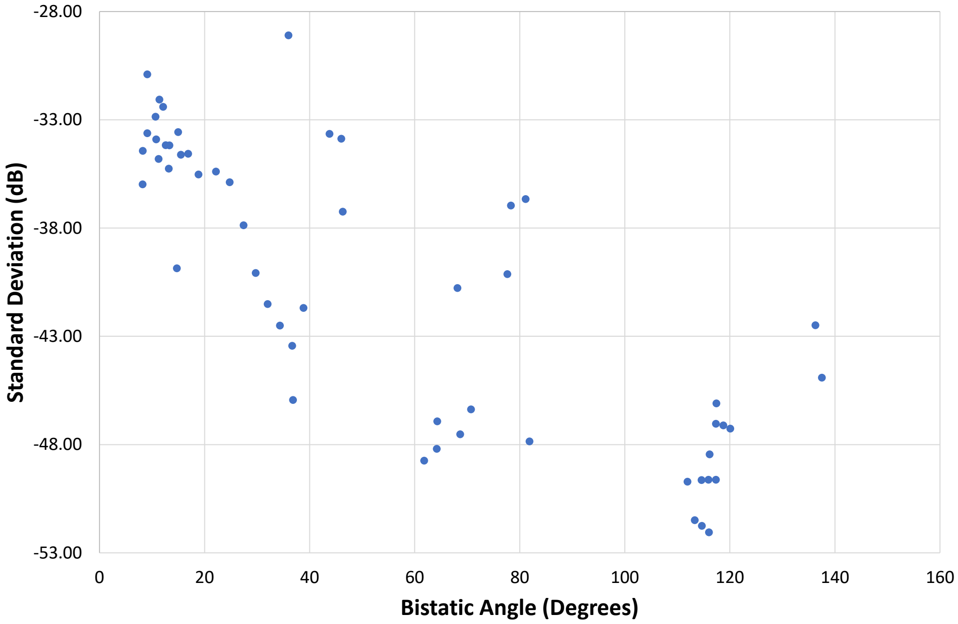

(b)

Figure 5.26: Graphs of (a) image intensity and (b) image standard deviation, against increasing bistatic angle for DVB-T SAR imagery of a region 1 in Figure 5.25, containing primarily buildings

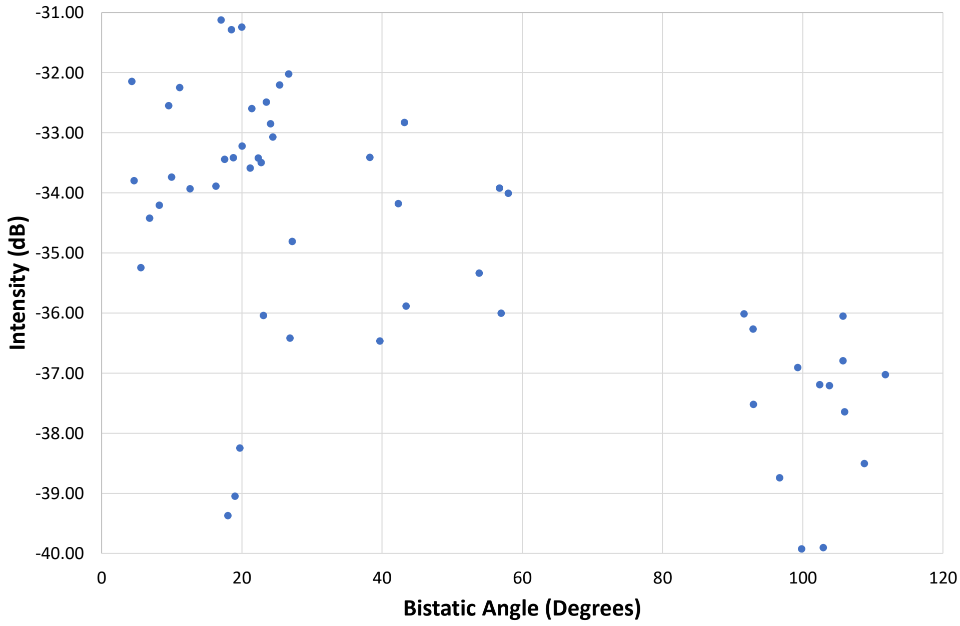

(a)

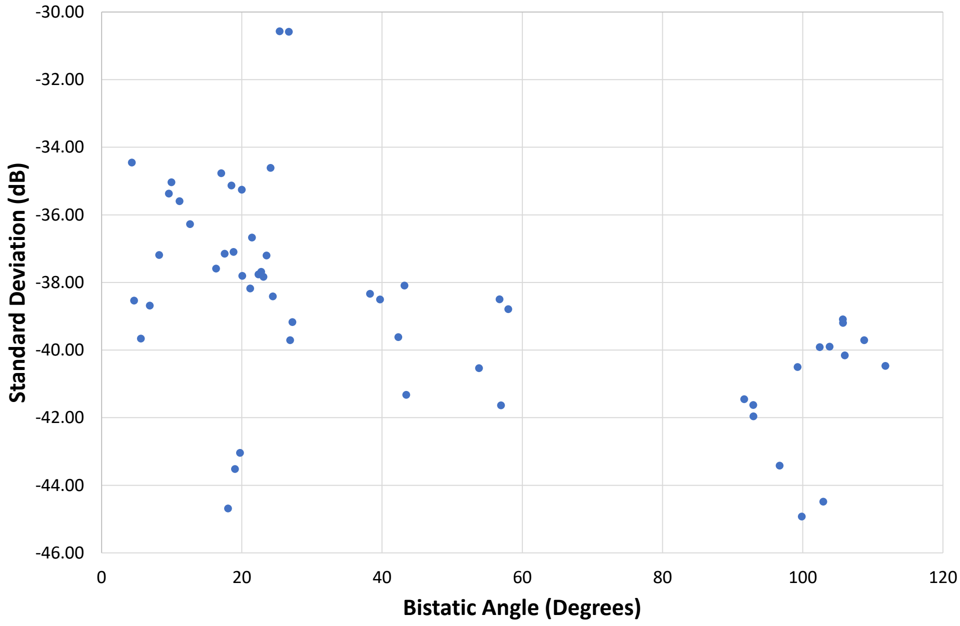

(b)

Figure 5.27: Graphs of (a) image intensity and (b) image standard deviation, against increasing bistatic angle for DVB-T SAR imagery of a region 2 in Figure 5.25, containing primarily fields

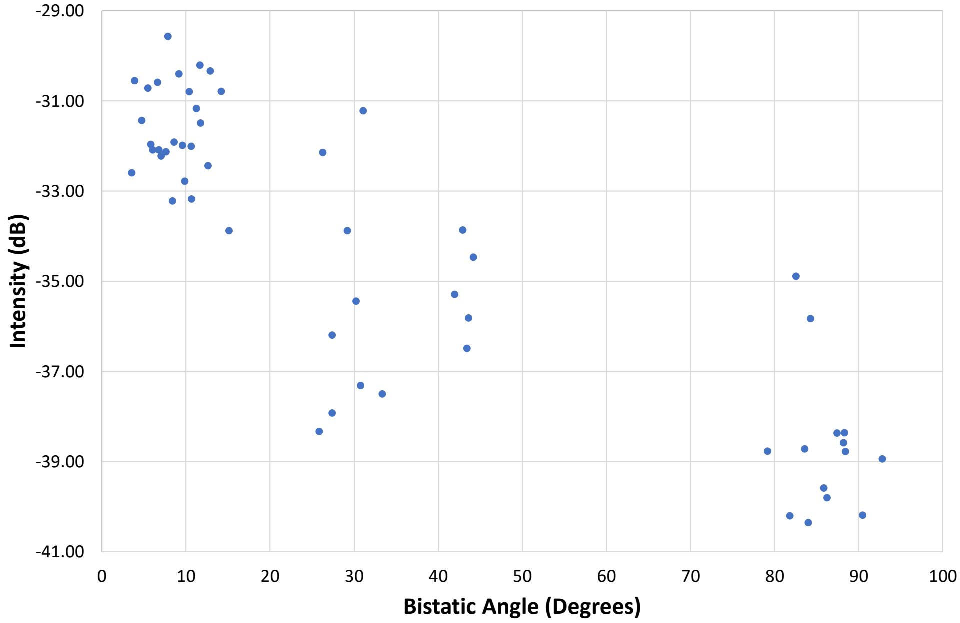

(a)

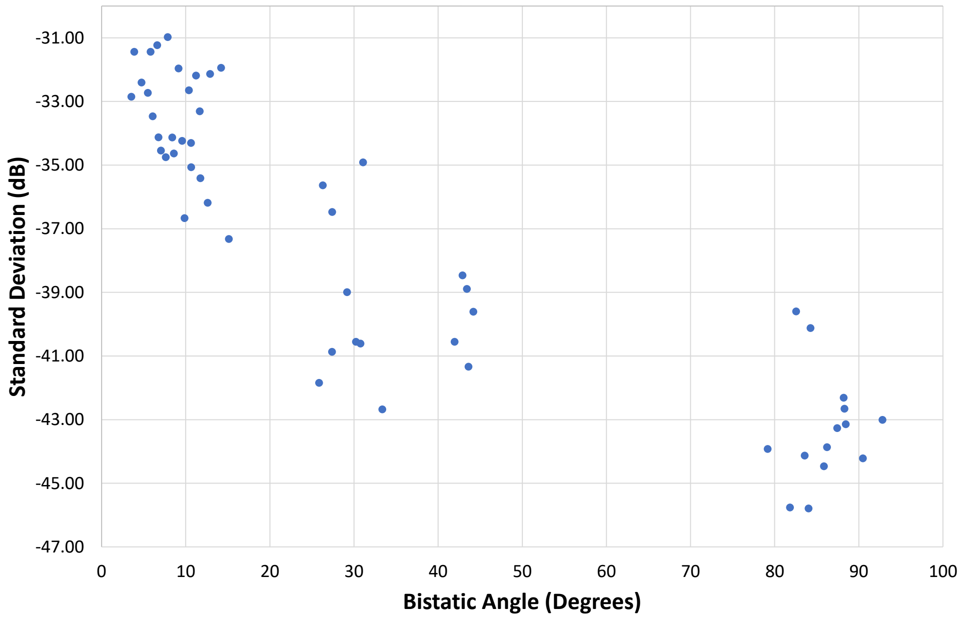

(b)

Figure 5.28: Graphs of (a) image intensity and (b) image standard deviation, against increasing bistatic angle for DVB-T SAR imagery of a region 3 in Figure 5.25, containing primarily forests

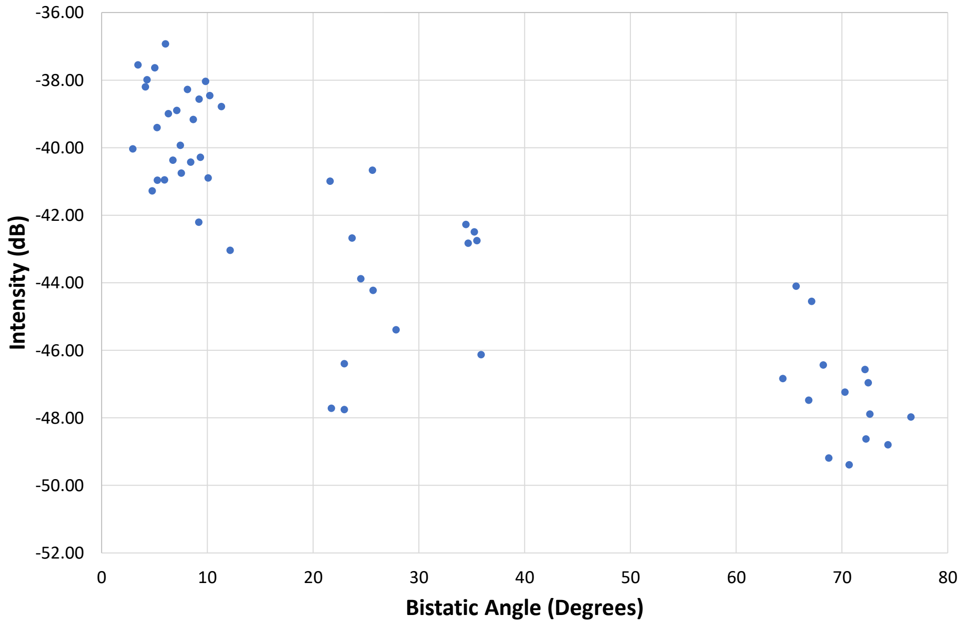

(a)

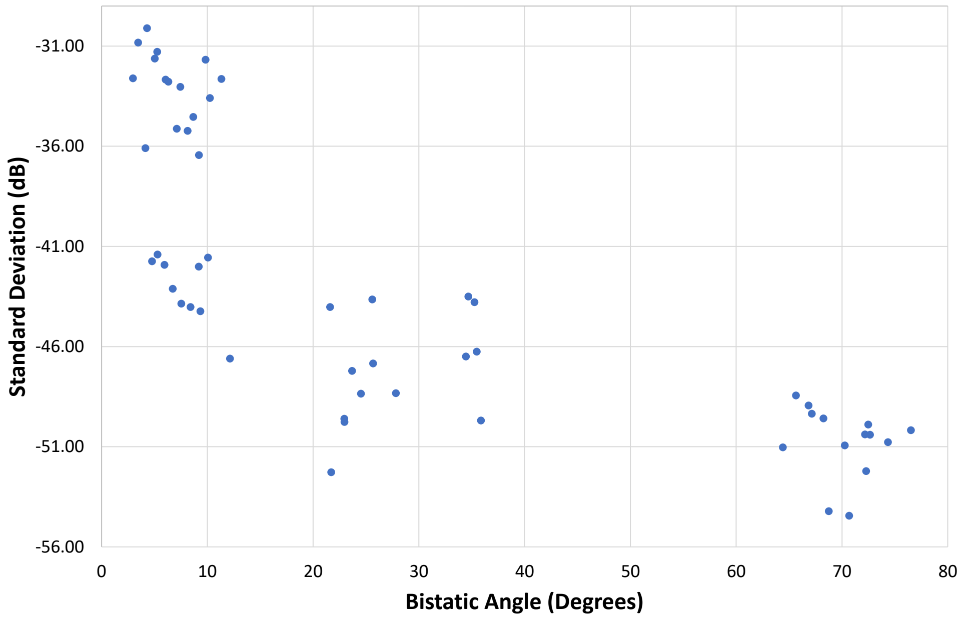

(b)

Figure 5.29: Graphs of (a) image intensity and (b) image standard deviation, against increasing bistatic angle for DVB-T SAR imagery of a region 4 in Figure 5.25, containing a single wind turbine

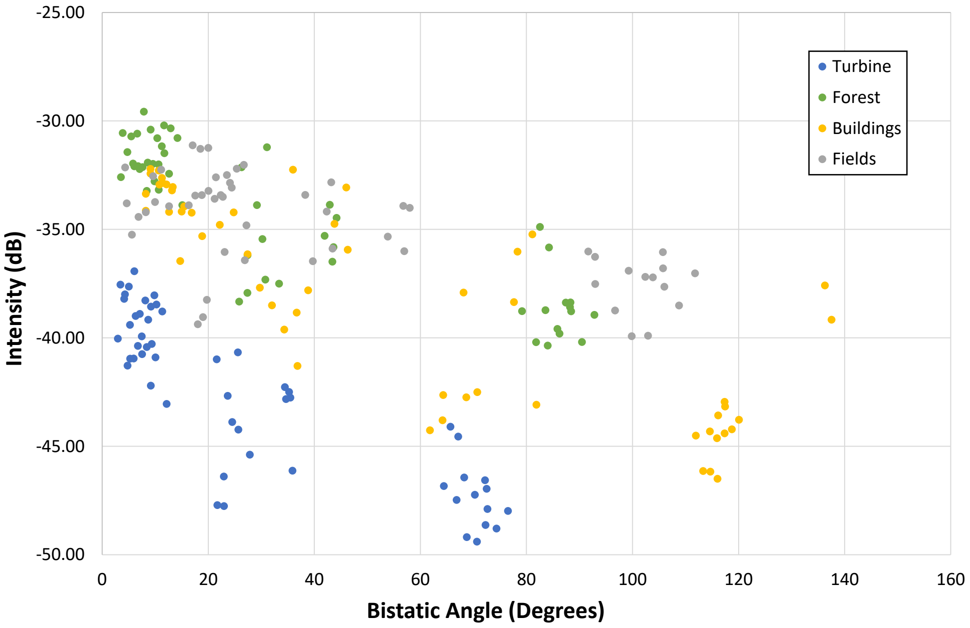

(a)

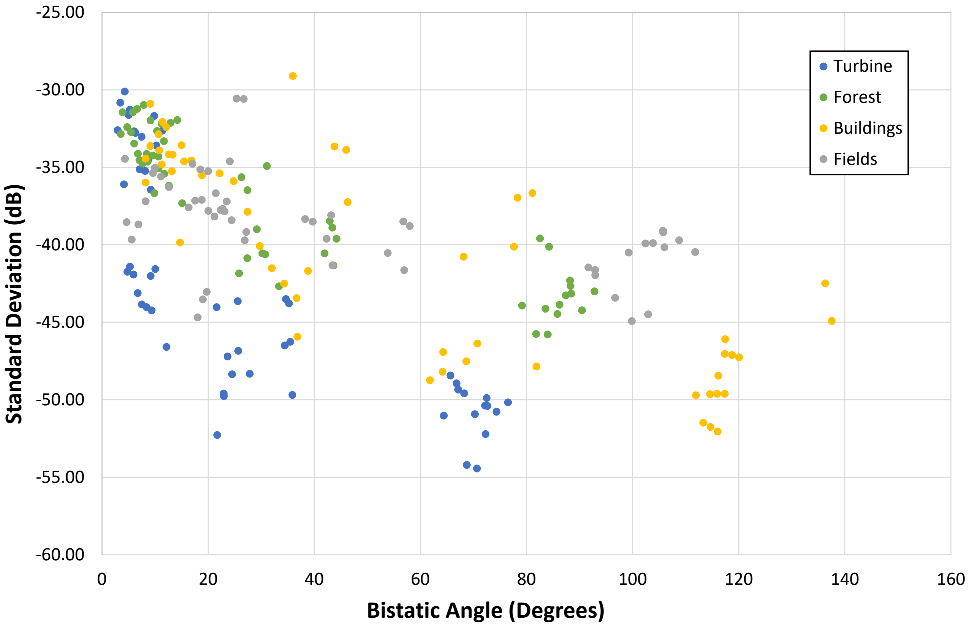

(b)

Figure 5.30: Graphs of (a) image intensity and (b) image standard deviation, against increasing bistatic angle for DVB-T SAR imagery for all four regions in Figure 5.25, plotted on the same axes.

5.7 Conclusions

In this chapter, bistatic DVB-T SAR image results have been presented and analysed. An airborne measurement campaign was performed and SAR imagery was generated of the Bruntingthorpe target area with a range of bistatic angles from 4 to 140 degrees, and a range of altitudes from 700 to 1300 m. Quasi-monostatic imagery with varying altitudes, and hence varying receiver grazing angles, was visually analysed and compared with ground truth imagery, as well as with results from the quasi-monostatic results shown in Chapter 4. Bistatic imagery at a constant altitude was analysed visually, with bistatic angle maps used to explain the observability of returns at high bistatic angles.

Also presented in this chapter was an initial numerical analysis of bistatic DVB-T SAR imagery. The entire dataset of measurements were processed into SAR images with an integration period of 4 seconds, and the resulting collection of images was filtered down by comparison with ground truth aerial imagery to check image focus. The remaining images were analysed by measuring and plotting the average intensity and contrast against the bistatic angle. This process was repeated for four unique target regions, each containing primarily a single type of target; a group of buildings, an area of fields, a cluster of forests, and an area containing a solitary wind turbine. The graphs were commented on, and it was found that for the full target scene, and all of the sub-regions, the average intensity and contrast both decreased with increasing bistatic angle but with a different dispersion of results depending on the targets being imaged.

Chapter 6

Conclusion and Future Work

6.1 Summary and Conclusions

This thesis has provided a systematic theoretical and experimental study of DVB-T-based Synthetic Aperture Radar imaging in order to determine under what circumstances the technology can produce useful and usable imagery.

Chapter 2 presented the background theory relating to radar, SAR, and the DVB-T waveform. The DVB-T signal was simulated in order to investigate the ambiguity function, which demonstrated the ambiguities caused by pilot carriers within the signal.

In Chapter 3, the theoretical constraints of a DVB-T SAR system were investigated by examining how the power budget, spatial resolution, and sensitivity of the system change with increasing range and bistatic angle. It was found that these constraints allow for imaging with a receiver as far as a low-earth orbit, but that the imaging capability of the system from a resolution perspective is highly dependent on the bistatic geometry of the system. The potential impact of multiple transmitter interference on DVB-T SAR imagery was investigated by simulating a point target illuminated by two DVB-T transmitters. The locations and output power of the two transmitters were taken from real-world examples in the UK. In this case, the Sutton Coldfield transmitter and the next closest transmitter with the same frequency, located in Chesterfield, were chosen. A simulation of the measured signal reflected from a point target showed that multiple transmitters resulted in ambiguities appearing after range compression. However, after image formation via backprojection, no ambiguities could be observed in the resulting SAR imagery. This result was confirmed with a comparison to a simulation of the same point target response but with a single transmitter, and no visual effects of multiple transmitter interference on the resulting imagery could be observed. Following on from the demonstration of pilot carrier ambiguities in Chapter 2, the effects of these carriers on the image formation process was investigated. It was found that the process of image formation suppresses the ambiguities caused by the pilot carriers due to the mismatch between the range histories of pilot ambiguities and real targets. The development of an image formation algorithm, based on backprojection, was presented, including the data processing steps required to generate focused imagery. An initial DVB-T receiver system was designed and built using a USRP, Yagi antennas, and a TOPCON GNSS receiver. Finally, a ground-based measurement campaign was conducted, the results of which verified the image formation algorithm and DVB-T receiver operation, while also demonstrating the capabilities of a ground-based vehicular platform for SAR imaging. In addition, the DVB-T SAR images of the Bartley Reservoir target area, which contained a hill with a highest point of approximately 100 m above the measurement aperture, demonstrated the effects of non line-of-sight propagation of the DVB-T signal, with returns from a row of electricity pylons visible behind the hill.

Chapter 4 showed the evolution of the initial DVB-T receiver system, developed in Chapter 3 for ground-based proof-of-concept measurements, into a flight-ready demonstrator system. This involved changing the Yagi antennas to patch antennas, changing the TOPCON GNSS receiver to the Spatial FOG GNSS receiver, and developing a set of RF front-end chains. Testing of these new components, both individually and as parts of the full flight-ready receiver system, was conducted on the ground. Results were compared with the initial receiver system to confirm the working operation of the new system. The flight-ready system was mounted within a Cessna 172N SkyHawk aircraft and flown around four target areas to collect a set of quasi-monostatic measurements. These measurements were then converted into DVB-T SAR imagery using the image formation algorithm presented in Chapter 3. A visual analysis of the quasi-monostatic DVB-T SAR imagery was performed by comparison to ground-truth aerial imagery, and the informational potential of the imagery was demonstrated and confirmed through the identification of real world targets. The results also demonstrated that quasi-monostatic imagery could be formed with aperture lengths up to 256 m at distances up to 50 km from the transmitter. To further validate the receiver system and image formation algorithm, a point spread function analysis was performed on a point-like wind turbine target located approximately 10 km from the receiver. A sub-region of the image containing the wind turbine return was extracted and compared with a simulated version of a point target at the same range. Comparisons of the range and cross-range profiles of the extracted and simulated target returns showed good correspondence, thus validating the receiver system. The effects of noise on the direct signal were investigated, providing an indication of the performance of the system at longer ranges. It was found that the majority of returns could still be distinguished from imagery with added noise to the direct signal, emulating a direct signal SNR of up to -15 dB. The effect of extending the integration time, which results in an improvement in cross-range resolution, was also investigated. It was found that doubling the integration time halved the cross-range resolution, as expected, however, only up to around 16 seconds integration time, at which point there were no further improvements, likely due to the accumulation of motion errors over longer apertures causing defocused imagery.

Chapter 5 presented a bistatic airborne measurement campaign and the visual and numerical analysis of bistatic DVB-T SAR image results. The DVB-T receiver system was flown in a Cessna 172N aircraft around the Bruntingthorpe target area, shown in Chapter 4. A set of bistatic airborne measurements was recorded, with bistatic angles ranging from 4 to 140 degrees, and with an aircraft altitude ranging from 700 to 1300 m. The recorded measurements were used to produce a set of DVB-T SAR images using the image formation algorithm shown in Chapter 3, but modified to generate imagery of a fixed target area independent of the aperture direction. This allowed for direct comparison of the bistatic SAR imagery of the target area. Firstly, a visual analysis and comparison of quasi-monostatic DVB-T SAR imagery of the target area, with differing flight altitudes, and hence differing receiver grazing angles, was shown. The level of detail, and the number and locations of returns, was similar across all of the compared images, with only the background level differing between them. It is not possible to conclude from these results whether the small change in background level observed was a direct result of the changing receiver grazing angle. Secondly, a visual analysis and comparison of bistatic DVB-T SAR imagery, with a constant flight altitude, was shown. As well as the identification of targets within the imagery, an explanation for the lack of target returns between images was provided by using maps of the bistatic angle across the image, as well as the receiver beamwidth. Thirdly, an initial numerical analysis of bistatic DVB-T SAR imagery was performed. The relationship between average image intensity and bistatic angle, and the relationship between image contrast and bistatic angle, were shown for the full target area, and for four sub-regions containing different types of targets: buildings, fields, forests, and a wind turbine. These initial results showed a negative correlation between both intensity and bistatic angle, as well as between contrast and bistatic angle. The behaviour of the results for intensity and contrast with increasing bistatic angle was commented on, and an attempt was made to explain the findings using intuition about the expected behaviour of the interaction of incident DVB-T signals on the different types of target. However, because the target regions are complex in structure, the exact RCS governing the behaviour was not known.

In summary, this thesis has presented the first systematic theoretical and experimental study of DVB-T SAR image formation, comprising of the development of simulations and signal processing algorithms, as well as a series of ground-based and airborne trials. This thesis has provided a comprehensive catalogue of quasi-monostatic and bistatic images that confirm the feasibility of DVB-T SAR, investigated the informational potential of this imagery, and provided a first attempt to further understand the attributes of images that can be formed at higher bistatic angles.

6.1.1 Future Work

Throughout the thesis, a number of observations were made that require further investigation to explain. In Chapter 4, monostatic SAR imagery of the Bruntingthorpe target area was shown and target features were identified. However, a pair of large aircraft hangers within the airfield did not produce observable returns within the SAR imagery despite possessing qualities that would be expected to do so, notably, the large size and presumably metallic composition of the structures. In addition, Chapter 4 showed that other targets within the SAR imagery, including forested areas and buildings, varied in intensity. Similarly, data analysed in Chapter 5, showed that intensity of the returns varied at different bistatic angles. In both of these cases, observation of these returns alone was not sufficient to identify any correlation between physical properties, or scene geometry, and observed intensities. While this thesis has provided the first systematic study of DVB-T SAR, showing its feasibility as an imaging technology, a phenomenological study, applying theoretical models to the collected experimental data to make quantitative predictions, is required in order to understand these findings. Specifically, bistatic scattering models at UHF, as well as a more in-depth study of propagation and effects of geometric distortion, such as shadowing, are required to explain the observations made in this thesis. A possible approach to this study could be the use of calibrated targets with a known theoretical RCS placed into the scene to provide a method of numerically measuring and quantifying target intensity with varying bistatic angle. Furthermore, a controlled target could be placed in different configurations and geometries to investigate the effects of shadowing and possible indirect propagation or foliage penetration, typical of UHF frequencies.

Another point for further research was identified in Section (4.5.6), where the effects of increasing the dwell time on target for monostatic imagery were investigated. It was found that increasing the dwell time, thus increasing the aperture length, improved the cross-range resolution up to a dwell time of 16 seconds, at which point the cross-range resolution ceases to improve. One possible reason suggested for this discrepancy was the non-coherent scattering of the wind turbine used as a point-like scatterer when analysing longer dwell times, which could be further investigated by measuring the bistatic scattering properties of known targets as part of a phenomenological study. Another possible reason for a plateau in measured cross-range resolution with increasing dwell time is the effects of motion errors. It was also hypothesised that motion errors are the primary contributor to observable defocusing in produced SAR imagery. Further work could investigate the cause of defocusing and ways of correcting these errors.

Bibliography

---

[1] M. A. Richards et al., eds. *Principles of modern radar.* Raleigh, NC: SciTech Pub, 2010. ISBN: 978-1-891121-52-4 978-1-891121-53-1 978-1-891121-54-8 978-1-61353-201-0.

[2] C. A. Wiley. “Synthetic Aperture Radars”. In: *IEEE Transactions on Aerospace and Electronic Systems* AES-21.3 (1985), pp. 440–443.

[3] S. Paloscia et al. “The Sensitivity of Cosmo-SkyMed Backscatter to Agricultural Crop Type and Vegetation Parameters”. In: *IEEE Journal of Selected Topics in Applied Earth Observations and Remote Sensing* 7.7 (2014), pp. 2856–2868.

[4] M. Tanguy et al. “Development of a methodology for flood hazard detection in urban areas from RADARSAT-2 imagery”. In: *2014 IEEE Geoscience and Remote Sensing Symposium.* 2014, pp. 3342–3345.

[5] U. Wegmuller et al. “Nonuniform Ground Motion Monitoring With TerraSAR-X Persistent Scatterer Interferometry”. In: *IEEE Transactions on Geoscience and Remote Sensing* 48.2 (2010), pp. 895–904.

[6] D. C. Mason et al. “Flood Detection in Urban Areas Using TerraSAR-X”. In: *IEEE Transactions on Geoscience and Remote Sensing* 48.2 (2010), pp. 882–894.

[7] M. Salehi, M. R. Sahebi, and Y. Maghsoudi. “Improving the Accuracy of Urban Land Cover Classification Using Radarsat-2 PolSAR Data”. In: *IEEE Journal of Selected Topics in Applied Earth Observations and Remote Sensing* 7.4 (2014), pp. 1394–1401.

[8] A. S. Komarov and D. G. Barber. “Sea Ice Motion Tracking From Sequential Dual-Polarization RADARSAT-2 Images”. In: *IEEE Transactions on Geoscience and Remote Sensing* 52.1 (2014), pp. 121–136.

[9] A. Renga et al. “SAR Bathymetry in the Tyrrhenian Sea by COSMO-SkyMed Data: A Novel Approach”. In: *IEEE Journal of Selected Topics in Applied Earth Observations and Remote Sensing* 7.7 (2014), pp. 2834–2847.

[10] A. Renga and A. Moccia. “Use of Doppler Parameters for Ship Velocity Computation in SAR Images”. In: *IEEE Transactions on Geoscience and Remote Sensing* 54.7 (2016), pp. 3995–4011.

[11] R. Raney. “RADARSAT-Canada’s national radar satellite program”. In: *IEEE Antennas and Propagation Society Newsletter* 25.3 (June 1983), pp. 4–8. ISSN: 2168-0329. DOI: `10.1109/MAP.1983.27682`.

[12] S. Buckreuss, R. Werninghaus, and W. Pitz. “The German satellite mission TerraSAR-X”. In: *IEEE Aerospace and Electronic Systems Magazine* 24.11 (Nov. 2009), pp. 4–9. ISSN: 0885-8985. DOI: `10.1109/MAES.2009.5344175`.

[13] P. Snoeij et al. “Sentinel-1 radar mission: Status and performance”. In: *IEEE Aerospace and Electronic Systems Magazine* 25.8 (Aug. 2010), pp. 32–39. ISSN: 0885-8985. DOI: `10.1109/MAES.2010.5552610`.

[14] M. Virelli, A. Coletta, and M. L. Battagliere. “ASI COSMO-SkyMed: Mission Overview and Data Exploitation”. In: *IEEE Geoscience and Remote Sensing Magazine* 2.2 (June 2014), pp. 64–66. ISSN: 2473-2397. DOI: `10.1109/MGRS.2014.2317837`.

[15] H. D. Griffiths and N. R. W. Long. “Television-based bistatic radar”. In: *Communications, Radar and Signal Processing, IEE Proceedings F* 133.7 (Dec. 1986), pp. 649–657. ISSN: 0143-7070. DOI: `10.1049/ip-f-1.1986.0104`.

[16] Asem Salah et al. “Experimental study of LTE signals as illuminators of opportunity for passive bistatic radar applications”. In: *Electronics Letters* 50 (2014), pp. 545–547. DOI: `10.1049/el.2014.0237`.

[17] K. Kulpa et al. “The concept of airborne passive radar”. In: *2011 MICROWAVES, RADAR AND REMOTE SENSING SYMPOSIUM*. 2011, pp. 267–270.

[18] B. Dawidowicz et al. “Detection of moving targets with multichannel airborne passive radar”. In: *IEEE Aerospace and Electronic Systems Magazine* 27.11 (2012), pp. 42–49.

[19] F. Colone et al. “A Multistage Processing Algorithm for Disturbance Removal and Target Detection in Passive Bistatic Radar”. In: *IEEE Transactions on Aerospace and Electronic Systems* 45.2 (2009), pp. 698–722.

[20] C. Coleman and H. Yardley. “Passive bistatic radar based on target illuminations by digital audio broadcasting”. In: *IET Radar, Sonar Navigation* 2.5 (2008), pp. 366–375.

[21] J. E. Palmer et al. “DVB-T Passive Radar Signal Processing”. In: *IEEE Transactions on Signal Processing* 61.8 (2013), pp. 2116–2126.

[22] K. Kulpa et al. “Passive radar for strategic object protection”. In: *2011 IEEE International Conference on Microwaves, Communications, Antennas and Electronic Systems (COMCAS 2011)*. 2011, pp. 1–4.

[23] D. Poullin. “Passive detection using digital broadcasters (DAB, DVB) with COFDM modulation”. In: *IEE Proceedings - Radar, Sonar and Navigation* 152.3 (2005), pp. 143–152.

[24] D. W. O’Hagan et al. “A multi-frequency hybrid passive radar concept for medium range air surveillance”. In: *IEEE Aerospace and Electronic Systems Magazine* 27.10 (2012), pp. 6–15.

[25] Michail Antoniou and Mikhail Cherniakov. “GNSS-based bistatic SAR: a signal processing view”. In: *EURASIP J. Adv. Sig. Proc.* 2013 (2013), p. 98.

[26] F. Santi, M. Antoniou, and D. Pastina. “Point Spread Function Analysis for GNSS-Based Multistatic SAR”. In: *IEEE Geoscience and Remote Sensing Letters* 12.2 (2015), pp. 304–308.

[27] C. Prati et al. “Passive geosynchronous SAR system reusing backscattered digital audio broadcasting signals”. In: *IEEE Transactions on Geoscience and Remote Sensing* 36.6 (1998), pp. 1973–1976.

[28] L. Cazzani et al. “A ground-based parasitic SAR experiment”. In: *IEEE Transactions on Geoscience and Remote Sensing* 38.5 (2000), pp. 2132–2141.

[29] S. Brisken et al. “Passive radar imaging using DVB-S2”. In: *2017 IEEE Radar Conference (RadarConf)*. 2017, pp. 0552–0556.

[30] M. Antoniou et al. “Experimental Demonstration of Passive BSAR Imaging Using Navigation Satellites and a Fixed Receiver”. In: *IEEE Geoscience and Remote Sensing Letters* 9.3 (2012), pp. 477–481.

[31] A. Evers and J. A. Jackson. “Experimental passive SAR imaging exploiting LTE, DVB, and DAB signals”. In: *2014 IEEE Radar Conference*. Cincinnati, OH, 2014, pp. 0680–0685. DOI: `10.1109/RADAR.2014.6875677`.

[32] D. Gromek et al. “Initial results of passive SAR imaging using a DVB-T based airborne radar receiver”. In: *2014 11th European Radar Conference*. Oct. 2014, pp. 137–140. DOI: `10.1109/EuRAD.2014.6991226`.

[33] L. M. H. Ulander et al. “VHF/UHF bistatic and passive SAR ground imaging”. In: *2015 IEEE Radar Conference (RadarCon)*. May 2015, pp. 0669–0673. DOI: `10.1109/RADAR.2015.7131080`.

[34] D. Gromek, K. Kulpa, and P. Samczyński. “Experimental Results of Passive SAR Imaging Using DVB-T Illuminators of Opportunity”. In: *IEEE Geoscience and Remote Sensing Letters* 13.8 (Aug. 2016), pp. 1124–1128. ISSN: 1545-598X. DOI: `10.1109/LGRS.2016.2571901`.

[35] P. O. Frölind. "Results of airborne passive SAR ground and sea target imaging using DVB-T signals". In: *2016 IEEE Radar Conference (RadarConf).* May 2016, pp. 1–4. DOI: `10.1109/RADAR.2016.7485125`.

[36] L. M. H. Ulander et al. "Airborne passive SAR imaging based on DVB-T signals". In: *2017 IEEE International Geoscience and Remote Sensing Symposium (IGARSS).* Fort Worth, TX, July 2017, pp. 2408–2411. DOI: `10.1109/IGARSS.2017.8127477`.

[37] Merrill I. Skolnik, ed. *Radar handbook.* 2nd ed. New York: McGraw-Hill, 1990. ISBN: 978-0-07-057913-2.

[38] Chris Oliver and Shaun Quegan. *Understanding synthetic aperture radar images.* eng. The SciTech radar und defense series. OCLC: 845399713. Raleigh, NC: SciTech Publishing, Inc, 2004. ISBN: 978-1-891121-31-9.

[39] Nicholas J. Willis. *Bistatic radar.* Edison, NJ: SciTech Publishing, 2005. ISBN: 978-1-891121-45-6.

[40] Bernard Mulgrew, Peter M. Grant, and John Thompson. *Digital signal processing: concepts and applications.* eng. 2. ed. OCLC: 248760104. Basingstoke: Palgrave Macmillan, 2003. ISBN: 978-0-333-96356-2.

[41] Mehrdad Soumekh. *Synthetic aperture radar signal processing with MATLAB algorithms.* New York: J. Wiley, 1999. ISBN: 978-0-471-29706-2.

[42] M. A. Richards. *Fundamentals of radar signal processing.* Second edition. New York: McGraw-Hill Education, 2014. ISBN: 978-0-07-179832-7.

[43] *Digital Video Broadcasting (DVB); Framing structure, channel coding and modulation for digital terrestrial television.* 1997. URL: `https://pdfs.semanticscholar.org/cde9/8a0be0311505aee20afe13c1578819a4ca0f.pdf` (visited on 12/12/2016).

[44] Mikhail Cherniakov and David V Nezlin. *Bistatic radar: principles and practice.* English. OCLC: 839221144. Chichester: John Wiley, 2007. ISBN: 978-0-470-02630-4.

[45] R. Saini and M. Cherniakov. "DTV signal ambiguity function analysis for radar application". In: *IEE Proceedings - Radar, Sonar and Navigation* 152.3 (2005), pp. 133–142.

[46] H. Kuschel et al. "On the resolution performance of passive radar using DVB-T illuminations". In: *11-th INTERNATIONAL RADAR SYMPOSIUM*. 2010, pp. 1–4.

[47] F. Colone, D. Langellotti, and P. Lombardo. "DVB-T Signal Ambiguity Function Control for Passive Radars". In: *IEEE Transactions on Aerospace and Electronic Systems* 50.1 (2014), pp. 329–347.

[48] B. Ferrell. "Ultrawideband foliage penetration measurements". In: *Proceedings of 1994 IEEE National Radar Conference*. 1994, pp. 80–84.

[49] J. Young, M. Poirier, and B. Ferrell. "VHF/UHF ultra-wideband measurements of scattering targets in foliage". In: *IEEE Antennas and Propagation Society International Symposium 1992 Digest*. 1992, 586 vol.1–.

[50] H. Kuschel and D. Schneider. "Propagation modeling for VHF/UHF-radar detection of targets behind a forest". In: *Proceedings of the 1998 IEEE Radar Conference, RADARCON'98. Challenges in Radar Systems and Solutions (Cat. No.98CH36197)*. 1998, pp. 325–330.

[51] *Predicted coverage of public service and commercial digital television multiplexes following switchover*. en. Sept. 2016. URL: `https://www.ofcom.org.uk/tv-radio-and-on-demand/information-for-industry/guidance/tech-guidance/dttcoverage` (visited on 09/23/2020).

[52] *Sutton Coldfield (Birmingham, England) Full Freeview transmitter*. en. URL: `https://ukfree.tv/transmitters/tv/Sutton_Coldfield` (visited on 09/13/2020).

[53] *TheBigTower Sutton Coldfield Transmitter*. URL: `https://www.thebigtower.com/live/SuttonColdfield/` (visited on 09/14/2020).

[54] *Elevation Finder.* URL: `https://www.freemaptools.com/elevation-finder.htm` (visited on 09/14/2020).

[55] F. Canini et al. "Use of Digital-Television terrestrial (DTV) signals for passive radars". In: *11-th INTERNATIONAL RADAR SYMPOSIUM.* June 2010, pp. 1–4.

[56] P. Wojaczek et al. "The application of the reciprocal filter and DPCA for GMTI in DVB-T - PCL". In: *International Conference on Radar Systems (Radar 2017).* 2017, pp. 1–5.

[57] Y. Fang et al. "Improved Passive SAR Imaging With DVB-T Transmissions". In: *IEEE Transactions on Geoscience and Remote Sensing* (2020), pp. 1–11.

[58] *Get Elevations - Bing Maps.* en-us. URL: `https://docs.microsoft.com/en-us/bingmaps/rest-services/elevations/get-elevations` (visited on 09/19/2020).

[59] J. Rosado-Sanz et al. "Design of a broadband patch antenna for a DVB-T based passive radar antenna array". In: *2017 IEEE 17th International Conference on Ubiquitous Wireless Broadband (ICUWB).* 2017, pp. 1–5.

Appendix A

Quasi-monostatic Airborne Campaign - Additional Target Areas

A.1 Quasi-Monostatic Target Areas

Advanced Structural Dynamics Evaluation Centre (ASDEC)

The Advanced Structural Dynamics Evaluation Centre (ASDEC) is a research facility owned by Horiba MIRA located at coordinates (52.5619, -1.4558) in latitude and longitude, 30 km from Birmingham and 20 km from Leicester. The primary feature of this target area is a set of test tracks, used by Horiba MIRA as a proving ground, surrounding and within a former airfield. Next to the test tracks are a group of large buildings, as shown in Figure A.2a. East of the test facility is a solar array occupying a 200 m by 400 m space, shown in Figure A.2b.

Figure A.1: Aerial image of the ASDEC target area

Tatenhill Airfield and St George's Park

Figure A.3: Aerial image of Tatenhill Airfield and St George's Park target area

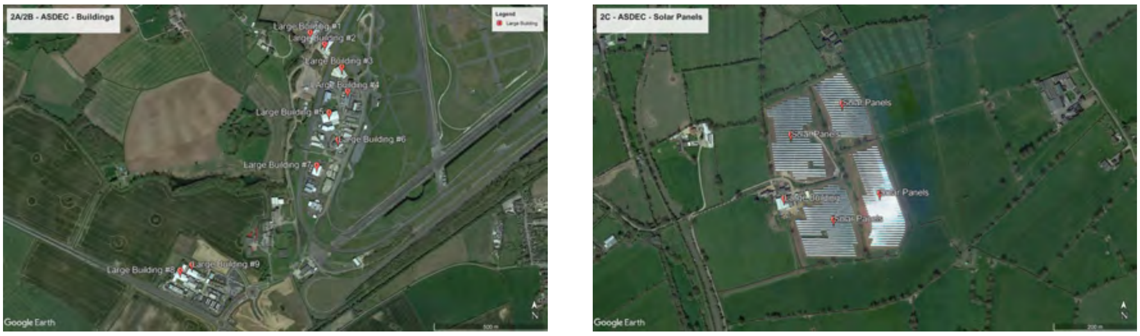

(a) A group of large buildings within the ASDEC target area

(b) An array of solar panels east of the test facility

Figure A.2: Two sub-regions of the ASDEC target area showing different potential targets of interest

Tatenhill airfield is located at coordinates (52.813577° latitude, -1.766236° longitude), 134 m above mean sea level, and about 9 km west of Burton upon Trent, Staffordshire, England. Figure A.3 shows an aerial image of the airfield and surrounding scene as well as the path of the aircraft during the trial, shown as a white line. The airfield is comprised of three intersecting runways, however only the east-west runway, with a length of 1190 m, remains operational whilst the other two, the north-south and southwest-northeast runways, are now used for aircraft parking. Located on the north-south runway are a complex of aircraft hangers, with twenty-six smaller hangers on the north side and another two larger hangers on the south side. To the north-east of the operational runway are a series of buildings housing the Tatenhill Flying School. The airfield is encircled by a road and forested regions can be found along the north-eastern edge and along the southern edge of the airfield. Another large forested region is located approximately 500 m to the west of the airfield. As well as the airfield, the surrounding area is also home to St George's Park, which contains a collection of paths, buildings, fields, small woodland areas and a small water body. Figure A.4b shows a close-up aerial image of the park area.

(a) (b)

Figure A.4: Aerial images of sub-regions of the tatenhill target area showing a close-up of (a) the airfield runways, and (b) the buildings within St George's Park

National Memorial Arboretum

Figure A.5: Aerial image of the National Memorial Arboretum target area

The fourth and final target area encompasses a region containing the the National Memorial Arboretum, located at (52.727808° latitude, -1.731431° longitude) in latitude and longitude. This area contains many potential targets including some that are not present in the other target areas.

The largest targets in the scene are a group of large buildings flanking the A38 road,

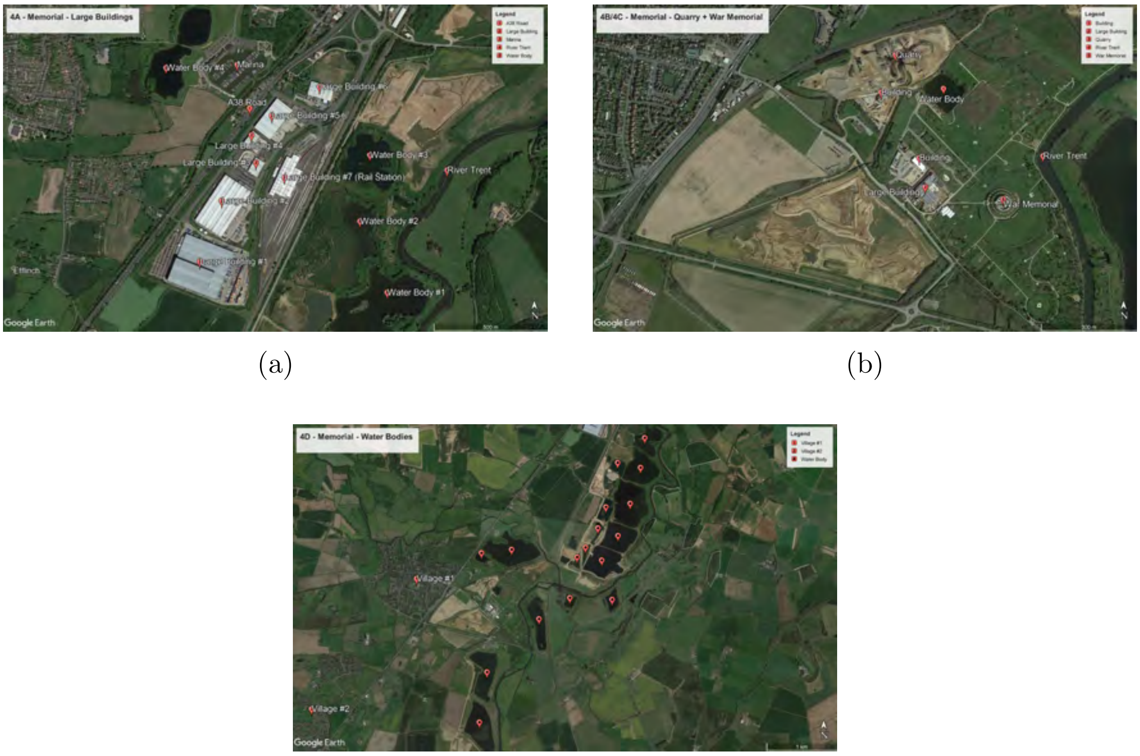

(a)

(b)

(c)

Figure A.6: Aerial images of three sub-regions of the memorial target area showing close-up imagery of: (a) a group of large buildings, (b) the Memorial Arboretum, (c) a series of large bodies of water the largest of which is a distribution centre for the company Argos. Behind these buildings is Bombardier a train depot and a series of rail tracks. As well as many roads, surrounding these buildings are a marina and several large bodies of water. Figure A.6a shows a close-up aerial image of the large buildings and surrounding area with targets of interest labelled. The bodies of water are not expected to act as targets themselves, as they are likely to reflect radio away from the receiver, but instead act as regions where no returns are expected in the final imagery.

Closer to the flight path of the aircraft, and labelled as B and C in Figure A.5, are the war memorial itself and a quarry. The war memorial, located next to the river Trent, is an interesting shape and is surrounded by foliage which is expected to be visible on DVB-T SAR imagery of the area. The quarry is recessed into the ground and may not have direct line-of-sight to the transmitter but appears to contain large metallic machinery which is expected to be highly reflective to DVB-T signals. Also in the area are some large buildings and bodies of water, as shown in Figure A.6b which highlights the different features of the area.

On a larger scale the memorial target scene is also home to many very large bodies of water located next to, and on both sides of, the river Trent which meanders through the target scene. Also within the target scene are a multitude of forested regions, which are outlined in white in Figure A.6c, which also indicates the locations of the bodies of water.

A.2 Quasi-Monostatic SAR Image Results

A.2.1 ASDEC

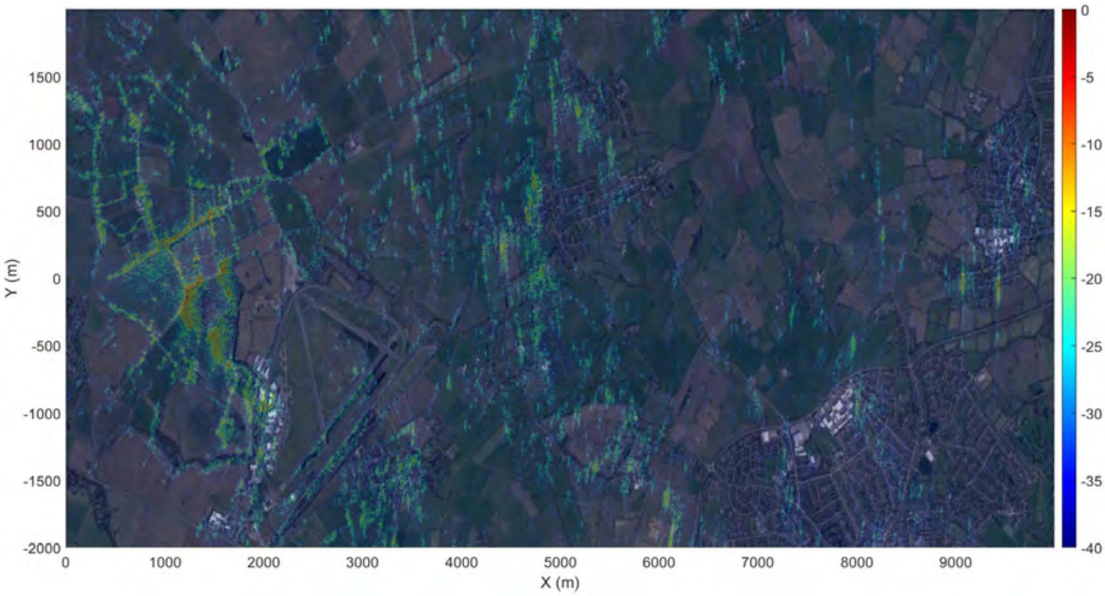

Figure A.7: A DVB-T SAR image of the ASDEC target area superimposed onto aerial ground truth imagery

Figure A.7 shows a SAR image of the ASDEC target area overlaid with an aerial image of the scene. As with the SAR image of the Bruntingthorpe target scene, shown in Figure 4.16, field boundaries are distinguished by strong returns from surrounding trees and hedgerows. Strong returns can also be observed from forested areas to the north-west and south of the test track. However, the test track itself is not visible in the SAR image as the incident radio waves from the transmitter are reflected away from the receiver. Returns from possible targets are sparsely scattered beyond a range of approximately 6 km. Hinckley village can be seen in the bottom-right of the image scene but only a small number of returns can be observed which do not appear to directly correspond to any particular targets but are likely the result of reflections from buildings orientated in such a way as to reflect incoming radio waves towards the receiver. Multipath reflections of the incoming radio waves from multiple buildings before propagating to the receiver is also possible. Table A.1 summarises the main parameters of the ASDEC target scene used for image generation.

Figure A.8 shows a comparison between a close-up aerial image of the large buildings shown in Figure A.2a, with the corresponding SAR image of the same area. Not all of the buildings appear as returns in the SAR image, however, three regions labelled as 1, 2 and 3 show a series of returns which correspond to the buildings shown in the ground truth imagery. The region labelled 4 shows the returns from a line of trees visible only by the shadow that they cast in the aerial imagery, but easily observable in the SAR image.

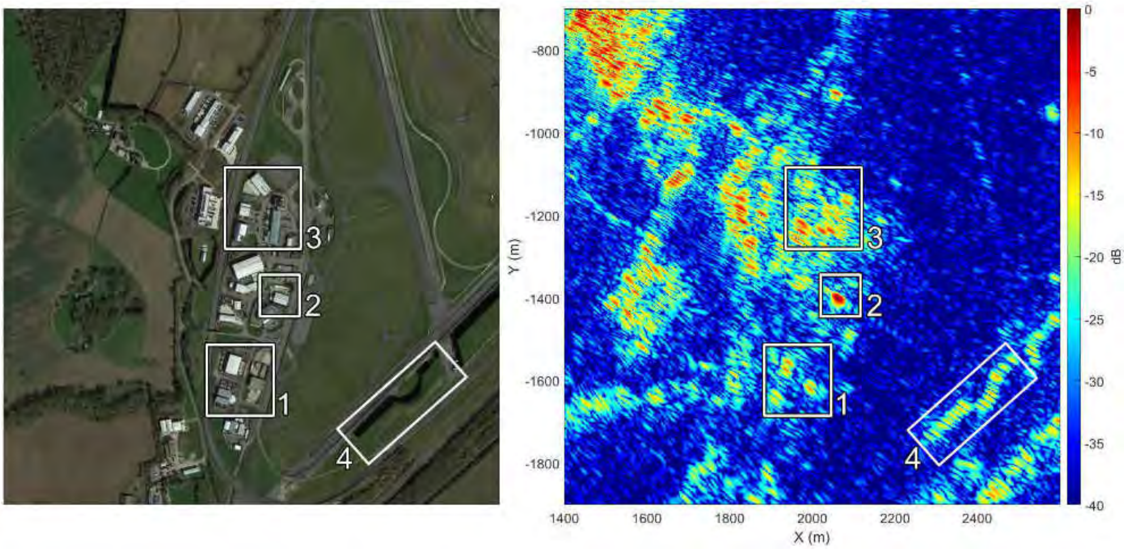

Figure A.8: A side-by-side view showing aerial imagery of a sub-region of the ASDEC target area containing a group of large buildings, next to a DVB-T SAR image of the same area. Regions of interest have been highlighted with numbered white boxes

Figure A.9 shows a comparison of an aerial image of an area within the ASDEC target scene which contains multiple solar panels, with the corresponding SAR image of the area. Disregarding the returns from trees, there do appear to be some weaker returns from the first area containing solar panels, labelled as 1 in the figure, however, the second area containing solar panels, labelled as 3, does not appear to produce any significant returns. This may be due to many factors, including the orientation of the solar panels as well as their composition. Since solar panels are designed to absorb light, it is possible that the incident radio waves were absorbed by the panels or simply that they were reflected away from the receiver.

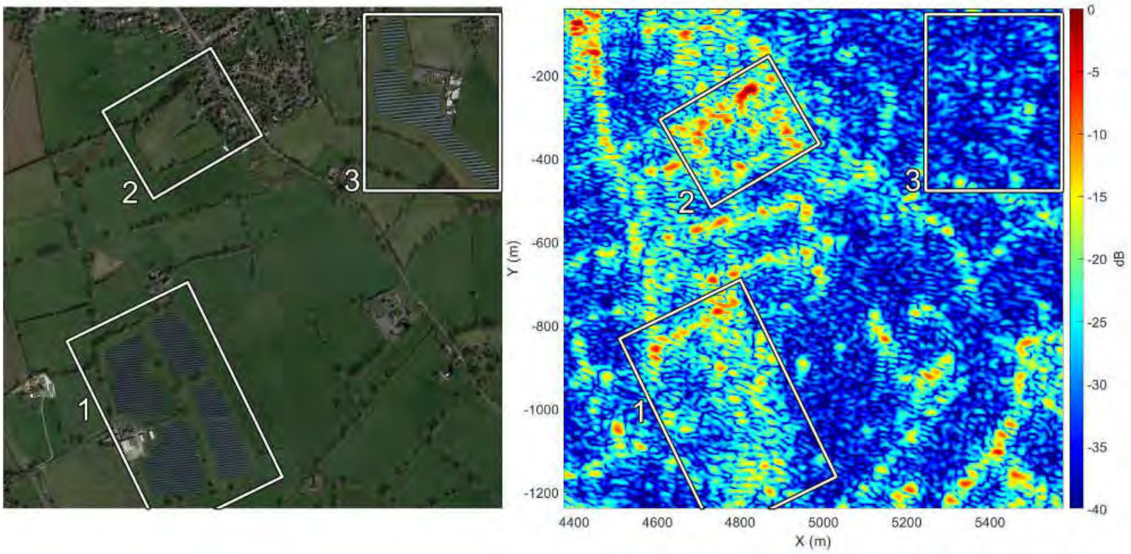

Figure A.9: A side-by-side view showing aerial imagery of a sub-region of the ASDEC target area containing an array of solar panels, next to a DVB-T SAR image of the same area. Regions of interest have been highlighted with numbered white boxes

Table A.1: ASDEC Scene Parameters.

Parameter	**Value**	**Unit**
Measurement Number	4	
Aperture Time	20	seconds
Integration Time	4	seconds
Aperture Length	220	meters
Mean Aircraft Speed	55	meters/second
Mean Aircraft Altitude	636	meters
Aperture Start	52.5667, -1.4865	latitude, longitude
Aperture End	52.5687, -1.4862	latitude, longitude
Aperture Centre	52.5677, -1.4863	latitude, longitude
Scene Bottom-Left	52.5499, -1.4898	latitude, longitude
Scene Top-Right	52.5748 -1.3364	latitude, longitude
Bistatic Angle	0.2164	degrees
Distance to Transmitter	23.8	km
Transmitter Grazing Angle	0.72	degrees

A.2.2 Tatenhill

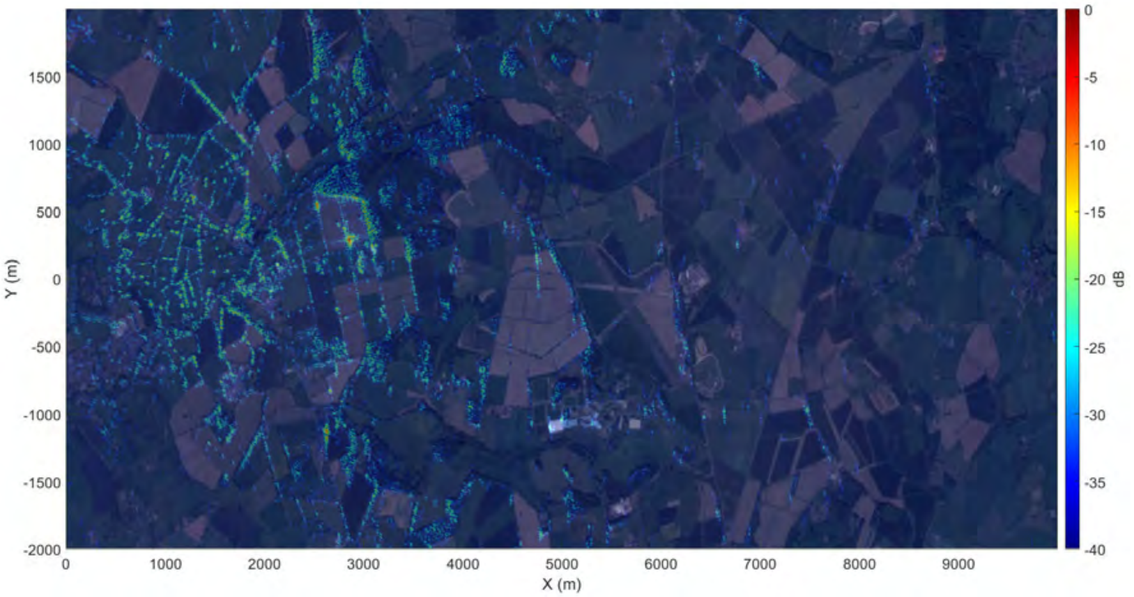

Figure A.10: A DVB-T SAR image of the Tatenhill target area superimposed onto aerial ground truth imagery

Figure A.10 shows a DVB-T SAR image of the Tatenhill Airfield target area overlaid with an aerial ground truth image of the target scene. As with the imagery of the other target scenes, field boundaries can be identified due to the surrounding trees and hedgerows. Although this particular target area is closer to the Sutton Coldfield transmitter than any of the others, returns appear sparsely past 5 km in range from the aperture. In the SAR image of the full scene the airfield does not appear to have many returns, however, Figure A.11 shows a comparison of a SAR image of just the airfield next to a aerial image of the same area. Although the runway itself is not visible, an aircraft hanger at coordinates (5551, -312) in range and cross-range is highlighted with a strong return, and a cluster of hangers in the upper-right section of the image are also visible.

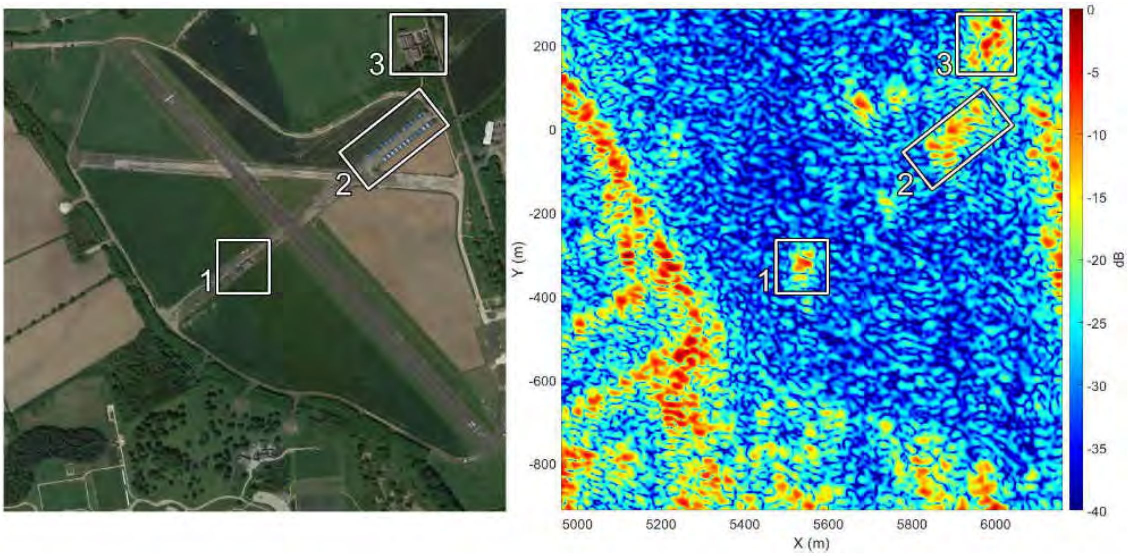

Figure A.11: A side-by-side view showing aerial imagery of a sub-region of the ASDEC target area encompassing the airfield, next to a DVB-T SAR image of the same area. Regions of interest have been highlighted with numbered white boxes

Figure A.12 shows a side-by-side comparison of a SAR image of St George's Park with ground truth aerial imagery of the same area. The regions marked as 1 and 2 show the locations and SAR responses of isolated patches of trees in otherwise empty fields. The regions marked 3 and 5 show returns from the buildings within the park, while returns within the region marked as 4 could be attributed to a building or a nearby cluster of trees.

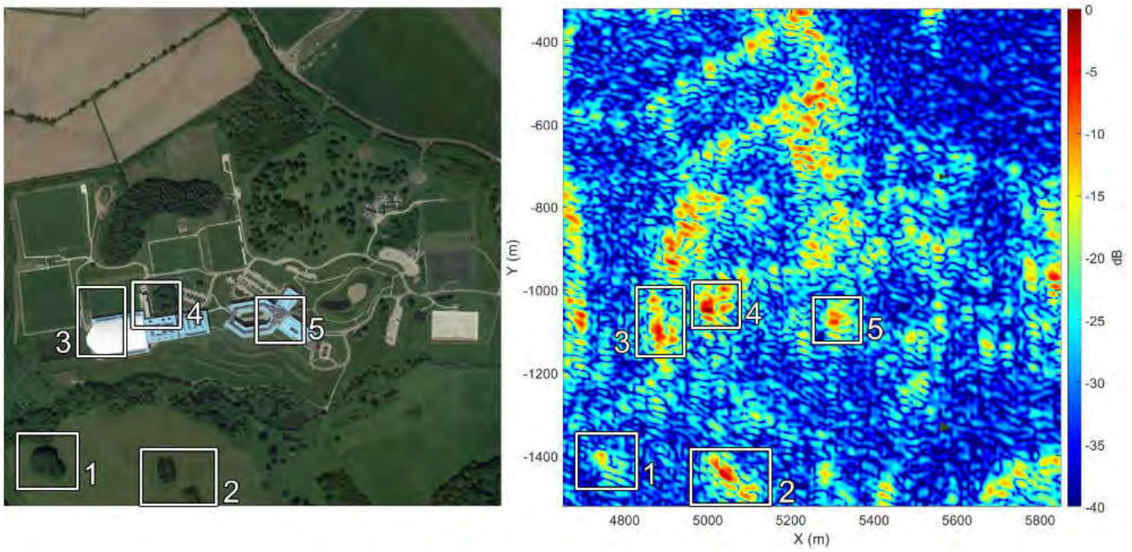

Figure A.12: A side-by-side view showing aerial imagery of a sub-region of the ASDEC target area containing St George's Park, next to a DVB-T SAR image of the same area. Regions of interest have been highlighted with numbered white boxes

Table A.2: Table of scene and aperture parameters for the Tatenhill target area.

Parameter	**Value**	**Unit**
Measurement Number	7	
Aperture Time	40	seconds
Integration Time	4	seconds
Aperture Length	189	meters
Mean Aircraft Speed	47	meters/second
Mean Aircraft Altitude	652	meters
Aperture Start	52.7649, -1.7926	latitude, longitude
Aperture End	52.7656, -1.7952	latitude, longitude
Aperture Centre	52.7652, -1.7938	latitude, longitude
Scene Bottom-Left	52.7578, -1.7668	latitude, longitude
Scene Top-Right	52.8544, -1.7598	latitude, longitude
Bistatic Angle	0.1668	degrees
Distance to Transmitter	23.9	km
Transmitter Grazing Angle	0.72	degrees

A.2.3 Memorial

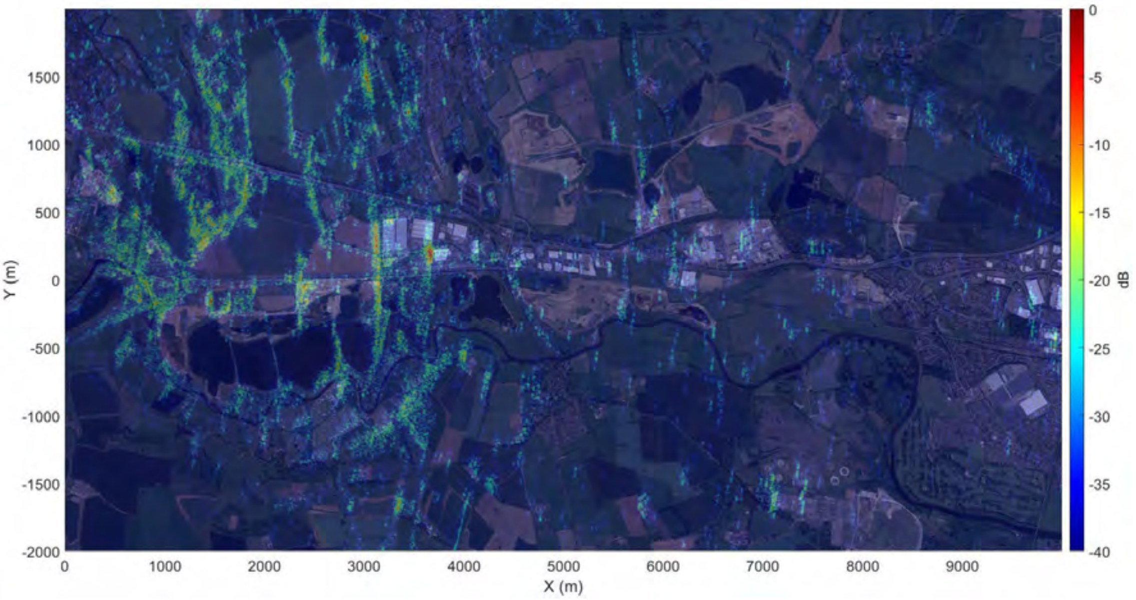

Figure A.13: A DVB-T SAR image of the Memorial target area superimposed onto aerial ground truth imagery

Figure A.10 shows a DVB-T SAR image of the National Memorial Arboretum target area overlaid with an aerial ground truth image of the target scene. Due to the location of the aperture, the memorial itself is only just visible on the far left of the image. However, a group of large water bodies and a group of large buildings are easily observed in the ground truth imagery. The water bodies do not produce any returns in the SAR imagery, however the thin strips of land between the water bodies are visible as thin lines of returns. As with the other target areas, forested regions are highlighted by strong patches of returns which clearly outline field boundaries and the A38 road, which has trees on its embankments. The strongest returns are from the group of large buildings at approximately 3500 m in range and 250 m in cross-range. The edge of the building closest to the aperture shows a strong line of returns due its perpendicular orientation relative to the incident DVB-T signal.

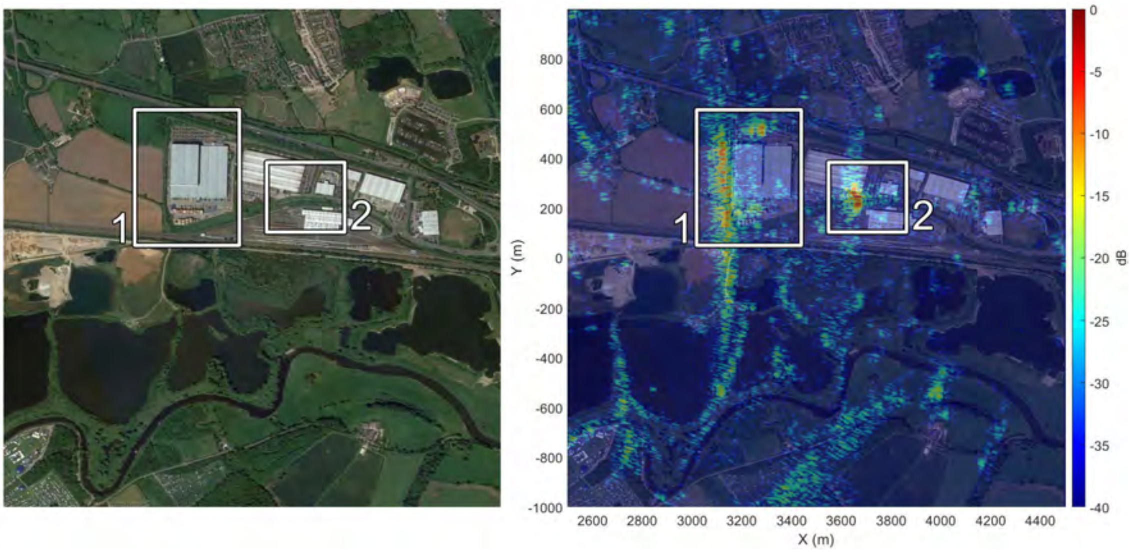

Figure A.14: A side-by-side view showing aerial imagery of a sub-region of the Memorial target area encompassing a group of large warehouses and buildings, next to a DVB-T SAR image of the same area. Regions of interest have been highlighted with numbered white boxes

Figure A.12 shows a side-by-side comparison of a close-up SAR image of the group of large buildings, next to ground truth aerial imagery of the same area. The target scene is a 2 by 2 km sub-region of the target area shown in Figure A.13. The region indicated as 1 marks the location of the patch of returns due to the largest building, which is also the closest building to the aperture.

The region labelled 2 shows the location of the strongest returns in the image which appear to be caused by another of the large buildings. However, the exact origin is difficult to determine due to the misalignment with the ground truth imagery, possibly due to geometric distortions such as foreshortening or layover.

Table A.3: Memorial Scene Parameters.

Parameter	**Value**	**Unit**
Measurement Number	11	
Aperture Time	40	seconds
Integration Time	4	seconds
Aperture Length	184	meters
Mean Aircraft Speed	46	meters/second
Mean Aircraft Altitude	618	meters
Aperture Start	52.7238, -1.7195	latitude, longitude
Aperture End	52.7238, -1.7220	latitude, longitude
Aperture Centre	52.7234, -1.7207	latitude, longitude
Scene Bottom-Left	52.7173, -1.6929	latitude, longitude
Scene Top-Right	52.8140, -1.6976	latitude, longitude
Bistatic Angle	0.1412	degrees
Distance to Transmitter	15.6	km
Transmitter Grazing Angle	1.01	degrees

Appendix B

DVB-T Parameters

Table B.1: Continual pilot carrier locations, adapted from [43]

2K Mode							**8K Mode**						
0	48	54	87	141	156	192	0	48	54	87	141	156	192
201	255	279	282	333	432	450	201	255	279	282	333	432	450
483	525	531	618	636	714	759	483	525	531	618	636	714	759
765	780	804	873	888	918	939	765	780	804	873	888	918	939
942	969	984	1050	1101	1107	1110	942	969	984	1050	1101	1107	1110
1137	1140	1146	1206	1269	1323	1377	1137	1140	1146	1206	1269	1323	1377
1491	1683	1704					1491	1683	1704	1752	1758	1791	1845
							1860	1896	1905	1959	1983	1986	2037
							2136	2154	2187	2229	2235	2322	2340
							2418	2463	2469	2484	2508	2577	2592
							2622	2643	2646	2673	2688	2754	2805
							2811	2814	2841	2844	2850	2910	2973
							3027	3081	3195	3387	3408	3456	3462
							3495	3549	3564	3600	3609	3663	3687
							3690	3741	3840	3858	3891	3933	3939
							4026	4044	4122	4167	4173	4188	4212
							4281	4296	4326	4347	4350	4377	4392
							4458	4509	4515	4518	4545	4548	4554
							4614	4677	4731	4785	4899	5091	5112
							5160	5166	5199	5253	5268	5304	5313
							5367	5391	5394	5445	5544	5562	5595
							5637	5643	5730	5748	5826	5871	5877
							5892	5916	5985	6000	6030	6051	6054
							6081	6096	6162	6213	6219	6222	6249
							6252	6258	6318	6381	6435	6489	6603
							6795	6816					

Table B.2: TPS carrier locations, adapted from [43]

2K Mode					**8K Mode**							
34	50	209	346	413	34	50	209	346	413	569	595	688
569	595	688	790	901	790	901	1073	1219	1262	1286	1469	1594
1073	1219	1262	1286	1469	1687	1738	1754	1913	2050	2117	2273	2299
1594	1687				2392	2494	2605	2777	2923	2966	2990	3173
					3298	3391	3442	3458	3617	3754	3821	3977
					4003	4096	4198	4309	4481	4627	4670	4694
					4877	5002	5095	5146	5162	5321	5458	5525
					5681	5707	5800	5902	6013	6185	6331	6374
					6398	6581	6706	6799				

Appendix C

Front-end Components Specification

Component	**Supplier (Model Number)**	**Specifications**
Low Noise Amplifier	Mini-Circuits. (ZFL-700+)	$F_1 - F_u$:250-700 MHz, Gain: 30 dB, NF: 2.0 dB
Band Pass Filter	Mini-Circuits. (RBP-650+)	Pass Band (Loss <7dB): 624 - 680 MHz, Stop Bands (Loss >20 dB): 520 MHz & 760 MHz, Stop Bands (Loss>35 dB): 520 MHz & 810-1000 MHz